UNIVERSITY OF LEEDS

Novel Approaches to Blast Protection for Armoured Fighting Vehicles

Joseph Matthew Anthony Wilson

University of Leeds

School of Physics and Astronomy

Submitted in accordance with the requirements for the degree of

Doctor of Philosophy

February, 2020

Intellectual Property Statement

The candidate confirms that the work submitted is his own, except where work which has formed part of jointly-authored publications has been included. The contribution of the candidate and the other authors to this work has been explicitly indicated below. The candidate confirms that appropriate credit has been given within the thesis where reference has been made to the work of others.

J. Wilson and J. Pittard. "The Contribution of Perforated Plate Aperture Geometry to Shock Mitigation: A Numerical Simulation Approach". In: *Unpublished, under publication embargo.* 2019.

Acknowledgements

To the people who made this project possible, especially my supervisors Professor Ben Varcoe and Dr Samantha Pugh, and Dr Cam Johnston (retired), Stuart Jones and Chris Livesey of BAE Systems: This work has given me the opportunity to push past what I thought possible of myself, and I thank you for it. My thanks too to both the staff of the School of Physics at the University of Leeds and the Advanced Research Computing team for their help and support, especially Dr Anne Ghesquiere for endless editorial assistance and Dr Julian Pittard for his advice on theory and understanding, often kindly delivered in response to my entirely unexpected visit.

To my Mother and Father, and to Nazira and Said Karodia, I have no words; the brevity of this sentiment must stand in inverse proportion to my gratitude, and I hope it is sufficient. There are many others that I have cause to thank, so many that I cannot list you all. You know who you are; I was profuse with thanks at the time, and it remains to this day.

Finally to my dear fiancée Cherise Stanley who has stood by (or sometimes endured) me through the countless obstacles, both personal and professional, that I have encountered in my life over the last four years. I love you dear, and am eagerly anticipating our future together.

Abstract

Modern fighting vehicles and their crews require enhanced protection against the detonation of buried explosive charges, a threat which includes shock-waves, high gas pressures, and the rapid ejection of the earth above the charge. This thesis seeks a novel means of providing that protection. It selects an approach based on the use of perforated plates. These plates contain multiple apertures which allow the partial transmission of a shock, disrupting the shock structure and interfering with the flow of detonation products. Computational fluid dynamics (CFD) in ANSYS FLUENT and multi-physics simulations in AUTODYN are applied to study the utility of this scheme in defending against the complex blast environment of a buried charge. The CFD research progresses from the development of a shock modelling technique through to the simulation of rigid 3-dimensional perforated plates of fixed porosity and varying hydraulic ratio and a study of their contribution to shock mitigation. A novel modification to the scheme based on the incorporation of a post-barrier flow divertor into the target structure is proposed and investigated. Comparison is made to existing research; contrary to experimental observations, the numerical simulations indicate that the shape of the perforations influences the mitigation capabilities of the plates. A reduction of 41-32% in the peak pressure acting on a target surface is observed when the separation between the plate and the target surface is large. The highest mitigation is provided by plates with the smallest apertures. This is reduced to 23-24% when the distance is reduced. The flow divertor approach yields little additional protection. The multi-physics simulations progresses from the simulation of the detonation of a buried charge through to the impact of the detonation on a flat plate, and then to a novel examination of the fluid-structure interactions involved when perforated plates defend a target from a buried charge. The scheme is found to provide a 23.5% minimum reduction in the vertical deflection of a solid witness plate, and scales well against varying blast conditions. It is shown that the primary loading on the target is from the gaseous detonation products, with the plate protecting against the majority of the ejecta. Perforated plates are demonstrated to be effective in defending against shock-waves and the detonation of buried charges.

Contents

List of Figures

LIST OF FIGURES

List of Tables

LIST OF TABLES

Abbreviations

ALE	Arbitrary Lagrange-Euler	NATO	North Atlantic Treaty Organization
ANFO	Ammonium Nitrate	ODE	Ordinary Differential Equation
AUSM	Advective Upstream Splitting Method	PE4	Plastic Explosive-4
ARC	Advanced Research Computing	PETN	Pentaerythritol Tetranitrate
BAE	British Aerospace Engineering	PICO	Participants, Interventions, Comparisons, Outcomes
C4	Composition-4	PRISMA	Preferred Reporting Items for Systematic Review and Meta-Analysis
CAD	Computer-Aided Design	PU	Polyurea
CFD	Computational Fluid Dynamics	RANS	Reynolds-Averaged Navier Stokes
CFL	Courant-Friedrich-Lewy	RHA	Rolled Homogeneous Armour
CONWEP	Conventional Weapons	RK4	4th Order Runge-Kutta
DNS	Direct Numerical Simulation	RPPL	Rigid-Perfectly Plastic Locking
EOS	Equation of State	SCDM	SpaceClaim Direct Modeller
FCT	Flux-Corrected Transport	SLIC	Simple-line Interface Calculation
FVS	Flux-Vector Splitting	SPH	Smooth Particle Hydrodynamics
GUI	Graphical User Interface	SST	Shear-Stress Transport
HPC	High-Performance Computing	STANAG	Standardization Agreement
IED	Improvised Explosive Device	TNT	Trinitrotoluene
JWL	Jones-Wilkins-Lee	UDF	User-Defined Function
LLNL	Lawrence Livermore National Laboratory	ZND	Zel'dovich-Neumann-Döring
MUSCL	Monotonic Upwind Scheme for Conservation Laws		

Chapter 1

Introduction

1. INTRODUCTION

The intention of this PhD thesis is to apply numerical simulations to answer a question posed by BAE Systems, a major manufacturer of arms and fighting vehicles. The question arose in part from a curious and unexpected observation; a small half-kilogram explosive charge, placed within an enclosed steel box filled with air, will completely destroy the surrounding container. The same charge placed within the same box, but now fully surrounded by sawdust, will not. An comparison of the two outcomes is shown in Figure 1.1. In light of this behaviour, the question posed by BAE Systems is thus; "Is there a novel methodology by which armoured fighting vehicles can be protected against the detonation of buried explosives?". This thesis suggests that there is, and that an approach based on controlling the blast through a novel geometric approach holds significant promise.

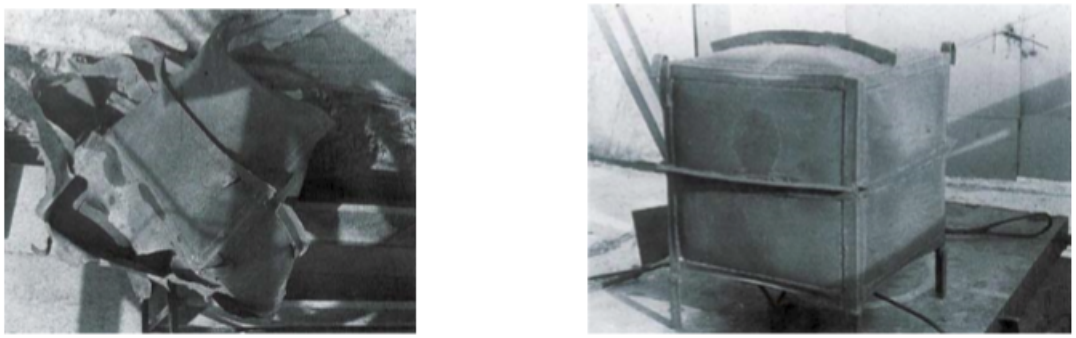

(a) (b)

Figure 1.1: A comparison of the detonation of a 0.5 kg RDX charge within a steel box. The box is 0.7m to a side, with walls 3mm thick. In a), the box was filled with air, in b), sawdust at a density of $100 kgm^{-3}$. Taken from the work of Vitali Nesterenko [1]

The primary objective of any defensive scheme is to protect the occupants from harm. This thesis examines the contemporary literature on blast defence to establish a conceptually novel means by which this objective can be accomplished, and investigates the most promising in detail.

The recent conflicts in Afghanistan and Iraq are notable for the extensive use of

ambush weaponry in the form of the Improvised Explosive Device, or "IED". The use of these devices beneath a vehicle involves the detonation of significant quantities of explosives at very close ranges, in a complex and enclosed environment. The extensive damage such blasts can cause is reflected in the casualty figures; Bird and Fairweather, in their study of fatality rates in both theatres [2], note that in 2006 from January 1st to September 17th, three in five coalition deaths in Iraq were as a consequence of IED attacks. Likewise, in Afghanistan over the period October 2001 - September 17th 2006, a quarter of fatalities are attributed to such causes. Contrary to detonations in air, the enclosure of the charge in soil introduces an additional threat posed by the ejection of the surrounding earth. To protect against this event, a defensive scheme must be capable of mitigating both the initial pressure wave of the detonation and the associated impact of the ejected mass, conceptually referred to as a "sand-slug" or "soil slug". A scheme capable of mitigating a complex blast event such as this is of significant value, both as protection for vehicles and in the broader scope of blast defence.

1.1 Research Rationale

The current paradigm for the defence of infantry vehicles against under-vehicle blast is the V-hull, in which the underside of the vehicle is shaped to deflect the incoming blast and ejecta. However, the results of Nesterenko [1] (as shown in Figure 1.1) indicate that enhanced mitigation of a detonation can be achieved without reliance upon increasingly thick and heavy armour or bulky blast deflection structures. While investigation of the alternatives can be carried out experimentally, the physical investigation of blasts is stymied by two primary considerations:

- The danger posed by explosives requires that they be handled with extreme caution. The financial cost of carrying out physical tests and the facilities required are significant.

- Explosives are destructive, which places limits on applicable experimental methods. Investigative tools must either be highly insensitive to blast or placed at sufficient distance to prevent their destruction. Potentially novel and complex mitigation dynamics, while present in the experiment, may be impossible to quantify or even discern with such an approach.

The alternative to the experimental approach is to instead simulate the detonation and subsequent dynamics through the mathematical representation of the relevant phenomena. The range of applications for which numerical methods are suitable has grown in conjunction with both the expanding processing power of modern computers, and the increasing fluency by which relevant phenomena can be described mathematically. While this permits the extraction of parameters and insight which would be inaccessible to a physical experiment, there is an associated disadvantage. Depending on the techniques applied, physical validity may be lost in the translation from real phenomena to numerical construct. Despite this concern, numerical methods have two critical advantages over experimentation:

- Simulations are, by comparison, financially cheap to perform, and allow rapid and inexpensive refinement of designs and investigative techniques.
- The nature of simulation provides immediate and full access to the dynamics of the system.

Such an approach allows for the investigation and optimisation of design factors long before a physical prototype exists, and it is here that the work in this thesis is applied.

The detonation of buried charges is highly complex and the dynamics are strongly influenced by a range of factors including:

- Charge size, shape and composition
- The material properties of the soil around the charge
- The depth at which the charge is buried

To ensure repeatable and reliable experimentation, a standard testing methodology is provided in the form of NATO Standardisation Agreement (STANAG) 4569 and the associated documentation on the testing of vehicles against landmine threat [3] and IED threat [4]. Throughout this thesis, this documentation is referred to collectively as STANAG 4569. Particular attention is given to annexes C and D in [3] and annex D1 in [4], which address the specific methodological requirements for the testing of prospective protection schemes. The objective of developing and testing approaches

under STANAG 4569 requirements is the protection of the crew. The principal threats to the crew are [5]

- Deformation or rupture of the floor of the vehicle
- Shock transmission into the vehicle
- The vertical acceleration of the vehicle.

These factors are directly related to the loading exerted on the underside of the vehicle by the blast. The proposal is therefore to develop a novel protective approach that minimises this loading. Given the limited space and harsh operating conditions under a vehicle, the chosen approach cannot be overly fragile or bulky, and should be effective against a range of charge sizes. Reuse-ability in the aftermath of a blast is not feasible. A new scheme that meets these criteria will achieve the objectives of the project and provide significant scope for further novelty in blast defence. In searching for a means of achieving these objectives, the nature of the problem must first be understood. In Section 1.2, the mechanics of a blast are described, first in the simplified case and then as applied to a buried charge.

1.2 Blasts

1.2.1 Detonation

A detonation is the rapid release of chemical energy by an explosive material. The process is precipitated by a shock-front passing through the material, which releases stored energy at an extremely high rate. A shock-front is a transient wave moving faster than the local sound-speed that marks the boundary of a sharp discontinuity in material variables. Across a shock-front, the density, pressure and temperature change near instantaneously from their initial unshocked values to a post-shock state. Mass, momentum and energy are conserved across the shock-front, as expressed by the ideal gas Rankine-Hugoniot relationships [6]:

$$\rho_1 u_1 = \rho_2 u_2 = m \tag{1.1a}$$

$$\rho_1 u_1^2 + p_1 = \rho_2 u_2^2 + p_2 \tag{1.1b}$$

$$h_1 + \frac{u_1^2}{2} = h_2 + \frac{u_2^2}{2} \tag{1.1c}$$

In the above equations, the subscripts 1 and 2 refer to the condition behind and in front of the wave respectively. ρ is the fluid density, u is the particle velocity, and h is the enthalpy (the internal energy plus pV, where p is pressure and V is volume) per unit mass. The relationship between the initial and final material parameters for a shocked material is given by the Hugoniot curve (shown in Figure 1.2), which describes all the possible post-shock states that can be achieved in a given material with initial conditions P_0, V_0. A shock-front travelling through the material with a fixed velocity describes a straight line in P-V space which connects the initial and final states on the curve [6]. This line is known as the Rayleigh line. In a detonating explosive, the Chapman-Jouget point is the point at which the Rayleigh line is tangent to the Hugoniot curve, and defines the detonation speed and associated initial P-V state of the detonation products. P-V graphs for both the case of a generic shocked material and the specific case of a shock travelling through an explosive material are shown in Figure 1.2.

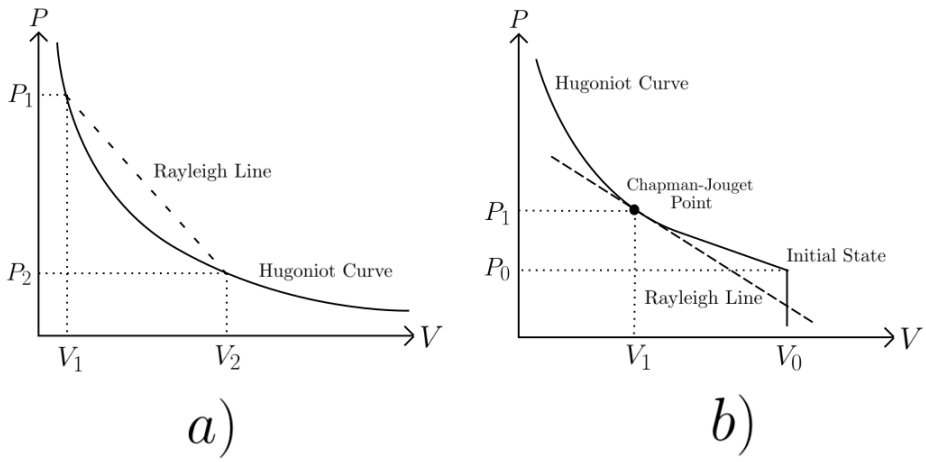

Figure 1.2: Hugoniot curves and associated Rayleigh lines for a) the general case of a shock propagating in a material and b) the specific case of a shock travelling through an explosive material. In b), only the detonation branch is presented.

This theory is the simplest analytical model for a detonation, and presumes that the reaction is initiated immediately by the passage of the shock. The more recent model

of Zel'dovich-Neumann-Döring (ZND) introduces further physical fidelity to the detonation process by incorporating an approximation to the behaviour of the chemistry; under this model, the shock does not precipitate an immediate and full conversion of the reactant mass to detonation products. Instead, the reaction occurs in hysteresis in the high-density post-shock region, which serves to accelerate the subsonic flow in the wake of the initial shock. This sustains the incident shock-front as it passes through the reactant matter [7].

At close range, the structure of the blast is highly unstable. Fišerová [8] gives a qualitative description of the instability of the near-field blast as "fingers of fire". An example of this instability can be seen in Figure 1.3. Despite the disparity in charge size, the two fireballs are seen to be similar in the structure of the irregularities at their surface. The result of irregular blast loading can be clearly seen in Figure 1.4, in which a perforated plate is applied directly to the surface of a deformable witness plate and then exposed to a close-range detonation. The resulting depth of the dimples are used to determine the local blast loading, and reveal an irregular pattern.

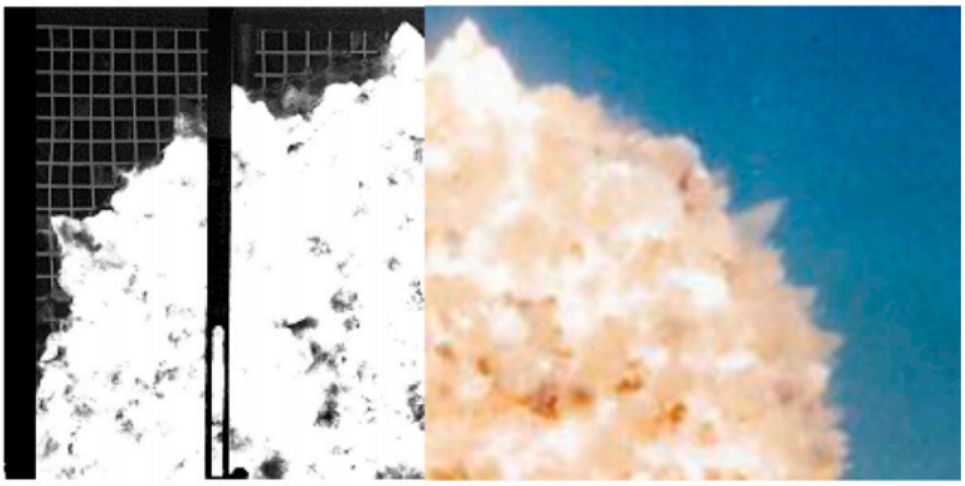

Figure 1.3: Still images of the fireballs created from (left) the detonation of 113g of PETN and (right) 4.7 kilotonnes of ANFO. From the work of Andrew Tyas [9].

At a distance from the detonation, the pressure wave arrives as a sharp peak followed by a steady decay and subsequent negative pressure. The idealised model is given

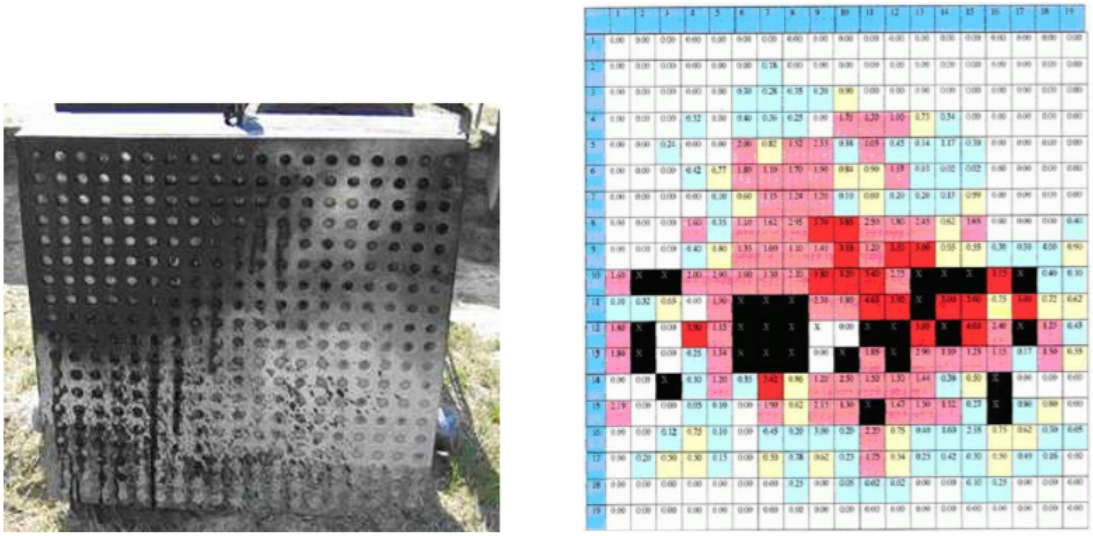

Figure 1.4: a) A mine dimple gauge used to evaluate the blast loading exerted by a landmine and b) the associated spatial "scorecard" of dimple deflections corresponding to the regions of greatest loading. In b), the distribution of the blast load can be seen to be highly irregular. Adapted from the work of Darina Fišerová [8].

by the Friedlander equation

$$P(t) = P_0 + P_s\Big(1 - \frac{t}{T_s}\Big)e^{-\frac{bt}{T_s}} \tag{1.2}$$

where P_0 is the initial (unshocked) atmospheric temperature, P_s is the peak overpressure of the blast, b is a wave-shaping parameter given as a function of P_s, t is time and T_s is the duration of the positive "overpressure" that exceeds P_0. The corresponding pressure structure is shown in Figure 1.5, and the structure as applied to a spherical air-blast is shown in Figure 1.6.

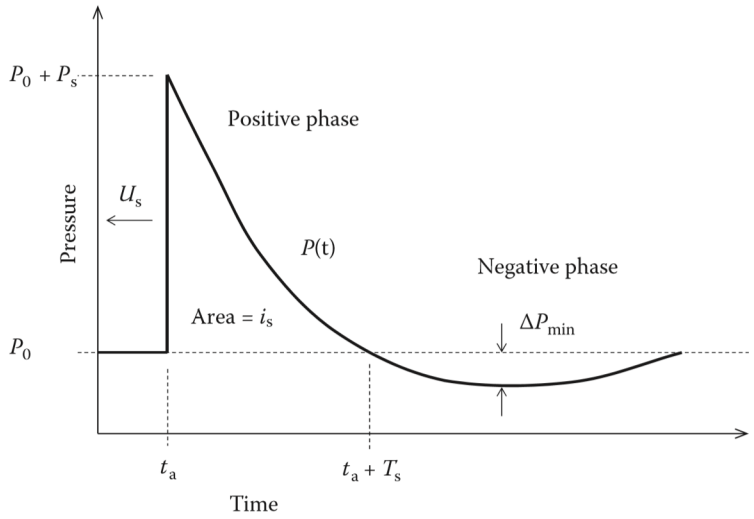

Figure 1.5: Depiction of the curve described by the Friedlander equation for an arbitrary blast wave. From the book "*Armour: Materials, theory and design*" by Paul Hazell [10].

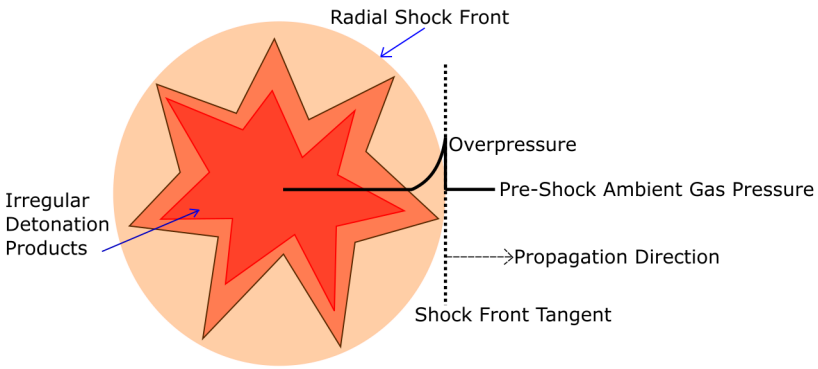

Figure 1.6: Depiction of an air blast, the associated irregular detonation products, the spherical shock-wave and the structure of the pressure wave and propagating shock-front. Adapted in part from the work of Lahiri and Ho [11]

On encountering a flat surface, the shock-wave reflects, The pressure behind the reflected wave is significantly higher than that of the incident wave. For a planar shock-wave of initial pressure jump p_1 striking a flat surface at zero incidence (where the plane of the incident shock-wave and the surface are fully parallel, as shown in Figure 1.7), the reflected peak pressure p_r can be shown to be [12]

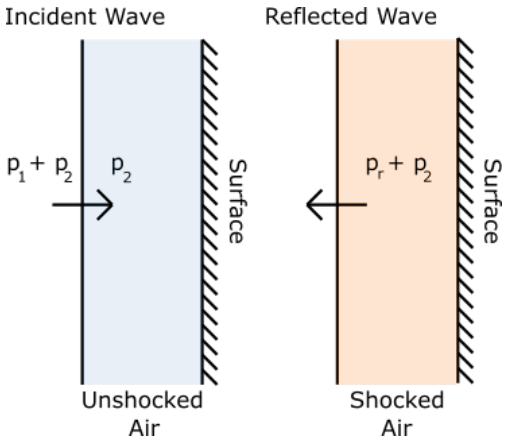

Figure 1.7: Depiction of the reflection of a planar shock striking a surface at zero incidence. The shock is initially moving from left to right; the reflected shock is moving from right to left. Adapted from the book "*Blast and Ballistic Loading of Structures*" by Smith and Hetherington [12].

$$p_r = 2p_1\Big[\frac{7p_2 + 4p_1}{7p_2 + p_1}\Big]. \tag{1.3}$$

or, as a jump ratio expressed as a function of the Mach number M of the reflected wave [6],

$$\frac{p_r}{p_1} = (1 + \frac{\gamma - 1}{2}M^2)^{\frac{\gamma}{(\gamma-1)}} \tag{1.4}$$

where γ is the ratio of specific heats (1.4 for air). Equation 1.3 imposes a limit to the maximum reflection pressure; if p_2 is small compared to p_1, the maximum value of p_r that can be reached is $8p_1$. The incident and reflected shocks and the respective pressure conditions are shown in Figure 1.3.

However, the above assumes that the heat capacity of the gas remains constant. If the temperature increase on reflection is sufficient to ionise the component gas, the heat capacity will change, and the reflection pressure can be significantly (up to 20 p_1) higher [12]. The total impulse transferred to a target by a shock-wave is the integral of the pressure acting on the surface over time, or

$$I = \int_{t_a}^{t_a+T_s} p(t)dt \tag{1.5}$$

where I is the impulse and $p(t)$ is the function describing the pressure over time.

1.2.2 Buried charge dynamics

In Section 1.2.1, shocks are considered as a phenomena occurring in a gaseous medium. If a charge detonates beneath the ground, an intensely high-pressure, high-temperature region is formed in a small volume enclosed by soil. The progression of the blast within the soil is shown in Figure 1.8. Commentary on the stages of the detonation shown in Figure 1.8 is given below:

(a) The initial shock-front is transmitted to the surrounding material, compressing it. The soil in the immediate vicinity within 2 to 3 radii of the charge is totally crushed, and does not meaningfully influence the propagation of the shock. In the region of 3-6 charge radii, the soil undergoes a plastic deformation, compressing and subsequently compacting. Beyond this limit, stress waves propagate outwards, with the soil responding elastically to their transit. [13]

(b) The compressive stress waves from the initial detonation reach the air-soil interface. The compression wave will partially reflect at this interface [13], with the greater part of the energy being directed back downwards towards the origin of the blast [14]. The remainder of the wave is transmitted to the air above as a shock-wave. This initial shock will strike the vehicle first, exerting a minor loading [14].

(c) Within the ground, the interaction of the reflected compression wave travelling back through the compressed soil and the pressure exerted by the expanding gas void from the detonation will serve to fracture and spall the region of soil directly above the charge [13, 14], accompanied by a bulging rise in the soil.

(d) With the shattering of this body (the “soil cap”), the gaseous detonation products begin to vent through the gaps left by the fracture. The high pressure gases within the detonation void will now vent preferentially upwards through the path of least resistance, and the detonation products are released directionally towards the vehicle [15]. The combination of the sudden rise in the soil and the venting of detonation gases initiates a second air shock, which is driven and sustained by the venting gases. Depending on the chemistry of the explosive, further energy release

can occur within this time-frame as the products are exposed to the surrounding atmosphere, a process known as "afterburning" [16, 17]. The soil cap above the

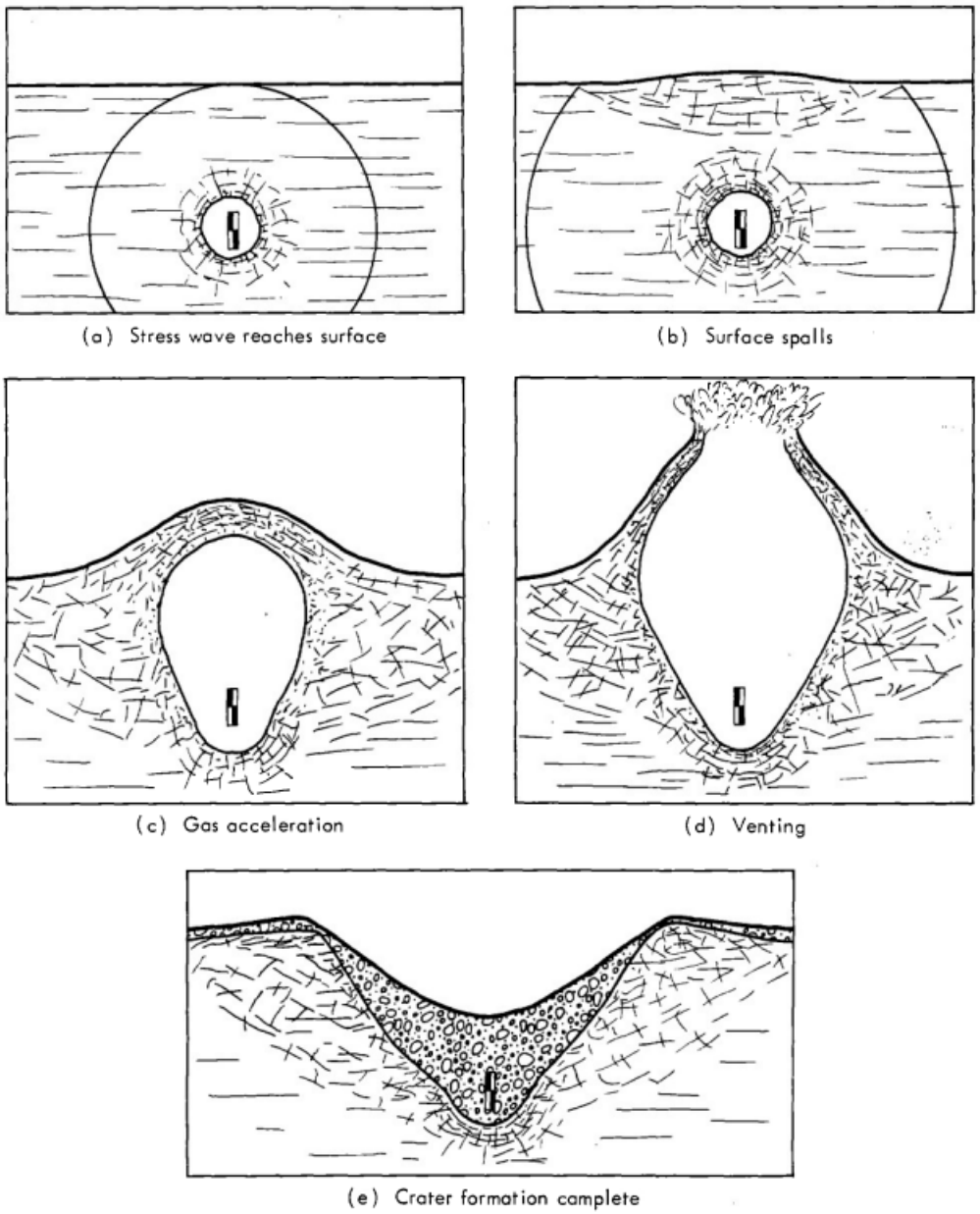

Figure 1.8: Progression of stress waves, soil response and excavation of a detonating buried charge. Taken from the work of Major Stanley Johnson et al [15].

detonation separates from the surrounding soil and is ejected upwards towards

the underside of the vehicle. While the initial volume of material ejected as a soil cap itself is noted by Bergeron et al [13] to be quite small, the continued outflow of gas from the initial detonation void will continue to erode the edges of the crater and propel quantities of material upwards. The total mass ejection over time can constitute as much as 1-2 cubic meters of material [13], travelling at speeds ranging between 357-894 ms^{-1} [14]. The ejected mass tends to take a conical form with an internal angle ranging from $60° - 90°$ with sharper angles resulting from deeper burial depths [13].

(e) Assuming the sand-slug does not penetrate the vehicle, the ejecta will fall back into the crater, partially re-filling it.

Characterisation of the detonation of a buried charge is a complex task. Soil and sand are both structurally complex materials with highly variable mechanical properties. Bergeron et al [13], Held et al [18], Denefeld et al [19] and Hlady [20] provide experimental characterisation of such detonations across a range of burial depths and surrounding material. Across these works, it is shown that the outcome of a detonation is strongly influenced by:

- The depth at which the charge is buried
- The water content of the soil
- The grain size and structure of the soil
- The cohesiveness of the soil

Laine and Sandvik [21] provide a numerical model for the material response of dry sand to detonation, which is extended by Fišerová [8] to incorporate varying moisture content and soil cohesion. For a deeply-buried mine, the gaseous detonation products of the charge may not breach the surface soil, with the detonation instead excavating a subterranean void (or "camouflet"). While the stress waves from the detonation will reach the surface and partially transmit into the air, this scenario poses significantly less threat to a vehicle.

Assuming that the burial depth is not sufficient to create a camouflet, the gas expansion phase of the detonation takes place some 5-10 ms after charge detonation

with the soil ejection continuing over a period of 50-100 ms [14]. Bouamoul indicates that the primary loading dynamics of a typical mine-blast event occur within 4-5ms of detonation [22]. A large collection of x-ray photographs of the surface upheaval from real buried charge tests for varying overburden, soil composition and charge size parameters can be found in the work of Bergeron et al [13]; several of these are shown in Figure 1.9.

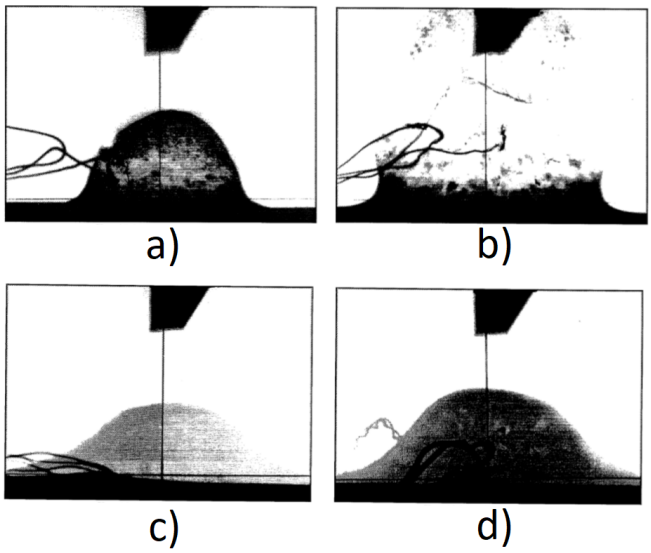

Figure 1.9: X-ray photographs of a buried charge detonation. a) and b) display the surface upheaval at 100.9μs and 201.9μs for the detonation of a 100g C4 charge with an overburden of 3cm of silica sand. c) and d) show the same phenomenon at 451μs and 526.1μs for the same charge at a burial depth of 8cm. Taken from the work of Bergeron et al [13]. Despite the considerably later time shown, the bulging soil cap over the deeper charge has not yet ruptured, unlike the cap over the shallower charge.

These images serve to highlight that while buried charge detonations will have similar features, the ultimate outcome can vary significantly with respect to the progress of the detonation and the threat posed to the vehicle. It is for this reason that STANAG 4569 provides definitive severity rankings for charge mass, burial depth and soil composition. Threat level 4, the "worst-case scenario" with regards to these parameters [3, 4], involves the detonation of a 10 kg Trinitrotoluene (TNT) blast mine concealed with an overburden of 10 cm of water-saturated sandy gravel.

Bergeron et al find that the highest air-shock velocities are encountered when the charges are laid flush with the surface with no overburden of material [13]. They also find that the burial depth strongly affects both the time over which the shock rises to peak pressure and the maximum attainable pressure. The maximum air pressure is seen to vary by a factor of 19 in comparisons between identical charges which are either surface-flush or buried at 80mm. Likewise, the ejection velocity of the soil cap also decreases with increased burial depth [13]. In examining the role of burial depth on impulse transfer, Held [18] determined that the total momentum imparted to a flat plate by the detonation of a 5 kg mine surrogate is 90% greater for the case of a charge buried at 100 mm, compared to the surface-laid and surface-flush cases. Taylor indicates that the slug contributes approximately half of the loading on a surface above the charge [23]. It is apparent that the slug loading is significant, and consequently the specific case of a buried charge detonation differs significantly from other blast events.

1.2.3 Vehicle response to mine blast loading

The conditions present in the region directly above the charge in the aftermath of the detonation have now been established. Assuming a vehicle is present above the blast, two primary threats are now approaching the underside with considerable velocity. While the arrival time of each is notionally separate and is described accordingly, they can overlap [5].

The first threat is the arrival of the shock-front. At close ranges, the shock-front is highly irregular even for surface laid charges, and the nature of the gas venting through the soil exacerbates this condition [8]. The shock will strike and subsequently reflect from any part of the vehicle in its path, exposing these parts to a transient pressure condition which is sustained by the continued flow of the detonation gases. This pressure loading imparts a sharp impulse transfer to the vehicle, with both local and global consequences. Locally, components exposed directly to the pressure will experience elastic and plastic deformation, an event that occurs within approximately 5 ms after detonation [5]. Bouamoul indicates that a flat steel plate mounted above a buried charge will reach maximum velocity at between 1-2ms after detonation. Deformation of components is not necessarily an undesirable consequence as strain modes will absorb some of the energy of the blast, but excessive deformation of the floor of the vehicle

(the "floor-pan") is to be avoided. Even if the floor pan is not fully ruptured, the sudden deformation of the floor poses a significant risk to occupants in contact with the surface at the moment of deformation [10]. In modern vehicles, this pressure loading is addressed by the inclusion of a V-shaped hull. The V-hull presents an angled surface to the blast; aside from deflecting the soil ejecta, the absence of flat or concave surfaces prevents the full reflection and maximum pressurisation of the shock as described in Equation 1.3. Such a design is clearly visible in the construction of the Leopard personnel carrier, a highly innovative mine-resistant vehicle from the Rhodesian bush war of 1964-1979, which can be seen in Figure 1.10.

Figure 1.10: A Leopard infantry carrier used in the Rhodesian bush war. The heavily V-shaped hull is displayed, alongside other defensive adaptations to landmine blast. Taken from the work of Ramasamy et al [14]

On a global level, tensile and compressive waves will travel into and through the rigid structure of the vehicle with a typical maximum velocity of 5000 ms^{-1} [5], where they can subsequently deform other components and rupture weld-lines [14]. Damage to sensitive components can also occur as a result of high-frequency (>1Khz) vibrations imparted to the structure. Low-frequency vibrations also pose a threat to the crew [24]. The second global effect is the transient vertical acceleration of the vehicle, which begins 10-20 ms after detonation. Upon reaching a peak height some 100-300 ms after the initiation of the acceleration the vehicle will then fall back to the ground, potentially landing in the crater left by the detonation [5].

The second threat, the arrival of the ejected soil cap, arrives shortly after the air

shock. This high velocity ejecta strikes the underside of the vehicle, transferring momentum first to the local impact point and then to the rest of the vehicle. If the slug is arrested by the vehicle structure without penetrating, then the constituent material will eventually fall back into the crater left by the initial blast. While the time-frame over which the initial slug transfers momentum to the structure is short when compared to the gas shock, the time-frame over which ejected material continues to be launched at the vehicle by the gas contained in the detonation void is significantly longer, and the total material impact phase may be some 20-100 ms longer than the total gas interaction [14].

1.3 A review of novel methods in the literature

1.3.1 Review strategy

To assess the existing state of the literature to determine the most promising avenues of research and the relevant methodological approaches, a structured approach to literature surveying was adapted from the Preferred Reporting Items for Systematic Review and Meta-Analysis (PRISMA) review methodology. PRISMA is an effort on the part of an international group of medical researchers to standardise the process of reporting in systematic reviews and meta-analyses of medical literature [25]. Central to the scheme is the notion of a "PICO" (Participants, Interventions, Comparisons and Outcomes) table, which is used to construct search terms for use in literature databases. Successive rounds of selection criteria are then applied to the literature presented as a result of these search terms, with the intention that the search strategy should be methodical, repeatable, and return as much relevant literature as possible. Furthermore, and of especial importance with regards to the formation of a new defensive scheme, the use of a review protocol of this type captures the broadest range of applicable literature. By adopting a structured approach, gaps in the literature with respect to significant phenomena can be more readily identified. A description of the modified PRISMA review protocol applied in this work is described in greater detail in appendix A.

The literature acquired through the PRISMA-based survey can be grouped into distinct categories based on the fundamental conceptual approach. The three predominant

categories are the mitigation of blasts through:

- The use of deformable structures
- Through fluidic means
- Control of the shock through geometric arrangements

On the basis of this literature review, a geometric approach to blast mitigation based on flat, perforated plates was selected as being the most promising candidate with respect to the suitability criteria. Additional summaries of the other techniques discovered in the course of the review are also presented for the purposes of comparison.

1.3.2 Mitigation by deformable materials

A deformable material is intended to reduce the load transferred to a target by compressing or distorting, with some of the energy of the blast being expended in doing work on a sacrificial deformable structure. In the literature regarding the use of deformable materials in generic blast defence several distinct approach categories can be discerned, although with some overlap:

1. Foam-based mitigation, in which compressible foams are applied to the target surface, [26–36].
2. Sandwich plates, wherein a deformable material is inserted between a face and backing plate, [37–45].
3. Impedance mismatching, in which multiple material interfaces are employed to reflect and dampen the shock, [24, 46–50].

Foam-based mitigation

A foam-based approach to blast defence involves the addition of a layer of foam cladding to a surface and a thin rigid cover plate intended to both protect the softer material from wear and to ensure even distribution of the blast load [26, 32, 33]. The primary type of protective foam in the literature is that of a metallic aluminium foam, with a secondary focus on conventional plastic foams. The concept is shown in Figure 1.11.

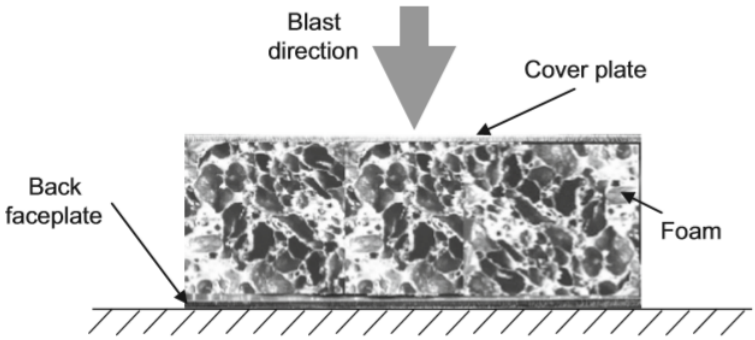

Figure 1.11: The predominant concept behind foam-based blast mitigation. Taken from the work of Karagiozova et al. [33]

On interaction with a blast aluminium foam compacts and plastically deforms, with the shock propagating throughout the foam and driving a wave of compaction throughout the material. A common model applied in the study of foams as blast mitigators is that of the Rigid-Perfectly Plastic Locking (RPPL) mode based on the work of Hanssen [51], in which the foam behind the transient shock-front compacts to the point of maximum density. The initial state and subsequent blast-driven compaction of an aluminium foam are shown in Figure 1.12. The stress-strain behaviour proposed by this model is shown in Figure 1.13, where the region under the plateau corresponds to shock energy expended in progressively compressing the foam to a densification limit; after compression, stresses on the compressed foam propagate as they would in a solid.

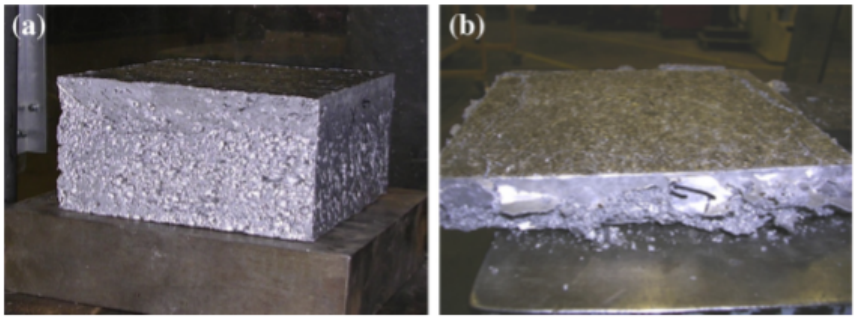

Figure 1.12: An aluminium foam of initial thickness 75mm, a) before and b) after a detonation event. Taken from the work of Wu and Sheikh [31].

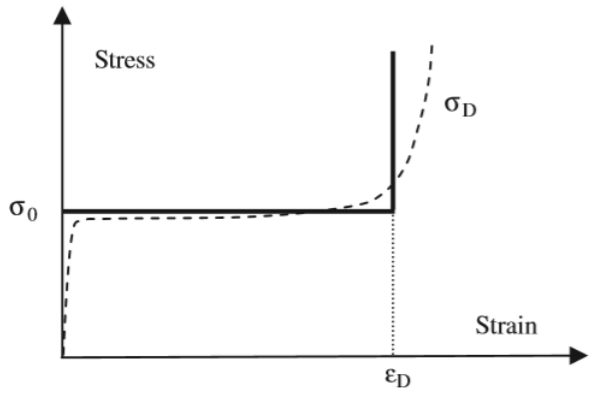

Figure 1.13: Stress-strain curve for a shock propagating through foam under the hypothetical RPPL mode (solid line) and in general practice (dashed line). σ_D is the stress in the densified material, and σ_0 is the initial elastic deformation response. ε_D is the densification strain, the critical strain value at which point the foam has reached maximum density. Taken from the work of Ma and Ye [32].

Foams are capable of enhancing blast mitigation but several authors [36, 49, 52–54] note that, depending on the intensity of the blast loading, the densification of foam materials under shock can actively enhance shock loading on a structure. This is particularly the case in which the blast is sufficiently intense that the foam reaches full compaction before the blast is fully expended. This behaviour is not limited to foams; Nesterenko [1] notes that the thickness of a sawdust barrier must be between 6-8 times greater than the diameter of the charge in order to avoid amplifying the loading.

Sandwich plates

The sandwich panel concept involves the layering of deformable materials which are usually enclosed between a front and back face-plate. In several cases foams are incorporated into the design, although extra materials are included. The best example of the distinction between sandwich plates and pure-foam approaches is the use of lattice-structured metal cells, which incorporate arrangements of metal folded into topologically regular structures, which are then sandwiched between a front and back plate to protect the arrangement and spread the blast loading across multiple loading points on the lattice. A simulated example of such an arrangement is presented in Figure 1.14, with the associated real deformation of such a plate under blast load shown

in Figure 1.15.

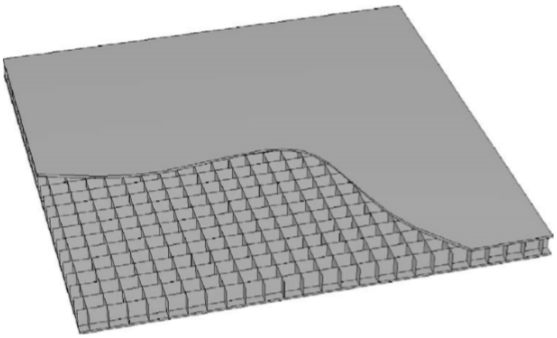

Figure 1.14: A square-honeycomb type lattice cell plate with cutaway face-plate. Taken from the work of McShane, Radford, Deshpande and Fleck [55]

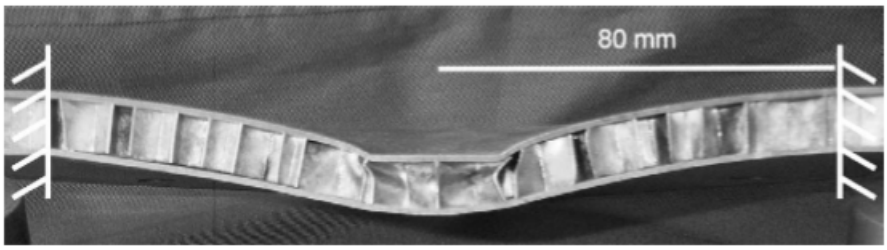

Figure 1.15: Deformation of a real square-honeycomb structure of the type shown in Figure 1.14. Taken from the work of McShane, Radford, Deshpande and Fleck [55]

A second categorical approach is the use of layers of nano-composites [56]. On a structural level, a nano-composite is a soft matrix material (typically a polymer) in which harder structures are embedded. An image of such a distribution in polyurea (PU) is given in Figure 1.16, in which the microscopic construction of the material can be seen. Polyurea is a strain-hardening material which stiffens under increasing load, a behaviour attributed to this variable domain structure.

The use of a fully-composite face and back-plate significantly reduces the effectiveness of such structures in mitigating one of the key threats. This was indicated in

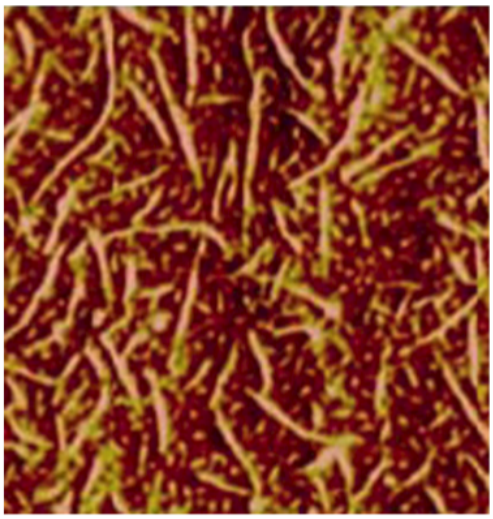

Figure 1.16: Tapping-Mode Atomic Force Microscope image of polyurea, in which long, thin, hard structures are embedded in a softer surrounding material. Taken from the work of Grujicic et al [56]

conversations with Dr Cam Johnston of BAE Systems during which Dr Johnston indicated that fully composite schemes had a tendency to disintegrate during mine blast loading tests [57].

Impedance mismatching

On encountering the interface between two materials with varying sound-speeds a travelling shock-wave will partially reflect, with the remaining fraction of the shock transmitting into the new material. Manipulation of this behaviour for the purpose of shock mitigation is known as "impedance mismatching", the contribution of which to the mitigation of shocks is already indicated in several of the foam and sandwich plate schemes above [32, 39]. Bergeron et al [13] identify the attenuating effects of impedance mismatching as an experimental factor in the measurement of the shock overpressure of a mine detonation, citing the discontinuity in density between the steel exterior of a pressure transducer housing and the plastic inserts into which the transducers themselves were mounted. A depiction of multiple reflections and shock transmissions occurring in 1-dimension for a system of discrete elements is shown in Figure 1.17.

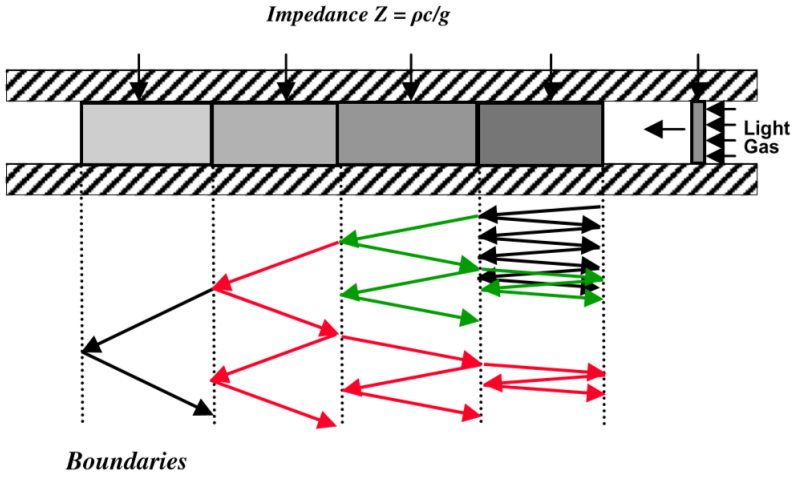

Figure 1.17: An impact plate travelling right to left strikes an array of masses with varying shock impedance. The reflection and transmission of the transient shock at each interface over time is shown. Taken from the work of Hui and Dutta [46]

Conclusions on deformable materials

While demonstrably effective at mitigating air shocks, foam-based approaches display potentially undesirable blast amplifying behaviours, especially under loading from the detonation of larger charges, which makes them unsuited to defending against a range of blasts. On a broader level, deformable materials show positive blast mitigating effects, although in all examined studies the loading of a sand-slug is absent. The majority of deformable schemes are reliant in some way on the use of a face-plate intended to spread the loading over multiple points of the defensive structure; while effective against pressure loading over the face, the localised slug impact may prove harder to disperse. Finally, a scheme where the defensive capabilities are based on deformation is unsuited to the underside of a vehicle based on the possibility of incidental impact during regular operation, which will degrade the protective capabilities ahead of time.

1.3.3 Mitigation by Fluids

The use of water as a mine-blast mitigating agent (in the form of water-filled tyres) has historical precedence [14]. Water is an attractive substance for blast mitigation because it is cheap, fire-suppressant and abundant in nature. Two broadly different

applications of fluids in blast mitigation can be discerned from the literature:

1. Mitigation of shocks by means of aerosolised water, [58–60]

2. The absorption and redirection of blast momentum, [61–66]

Aerosolised water

When suspended in aerosol form, droplets of water struck by the initial shock will fragment into "child" droplets with greater surface area. This process is shown in Figure 1.18. This fragmenting process will extract a portion of the kinetic energy of the shock. Moreover, in the region following the shock in which high-temperature detonation products are present, these child droplets will absorb a fraction of the thermal energy, although the scale of the droplets is indicated by Adiga et al to strongly influence thermal absorption [59]. Schwer and Kailasanath [60] indicate that the presence of water can also directly quench the secondary reaction of initially unconsumed explosive material in the air, especially if the chemistry of the charge is highly oxygen deficient.

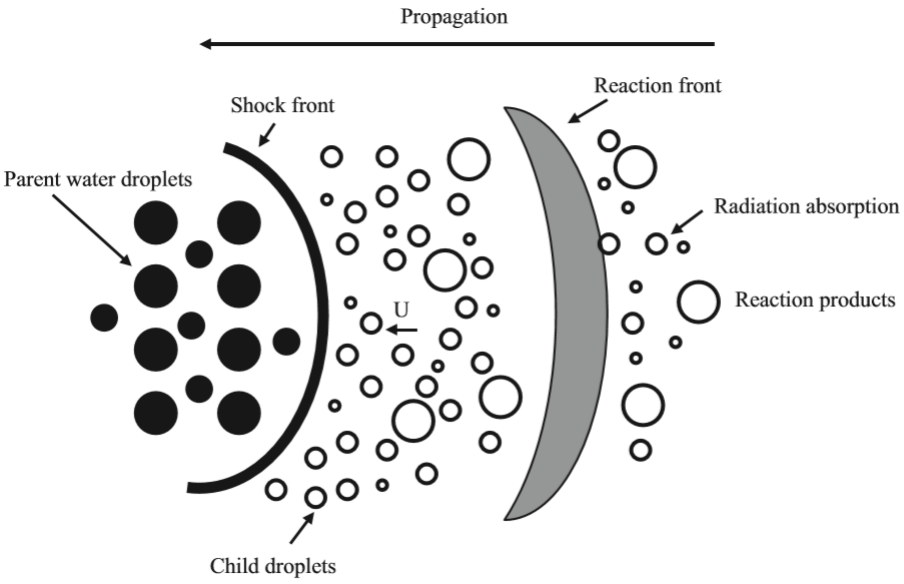

Figure 1.18: The interaction of a reaction-driven shock-wave with water droplets. Taken from the work of Adiga et al [59].

Water filled vessels

The intention behind the use of water-filled vessels is to provide an incompressible and highly deformable medium to the blast. On impact from the blast, water is ejected from the vessel at speed, carrying momentum away from the vehicle. The concept is shown visually in Figure 1.19. According to several authors [61, 63, 67], imposing a gap between the water vessel and the impact target yields superior performance to the case in which the vessel is in direct contact.

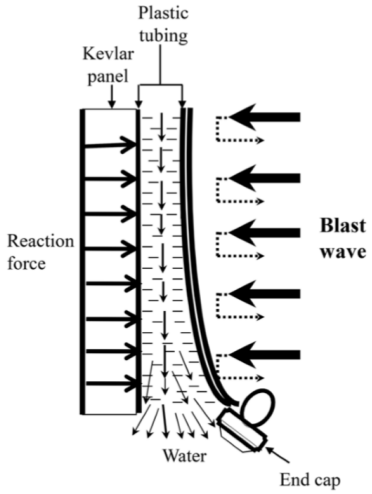

Figure 1.19: The blast-energy redirection concept of Chen et al. Taken from the work of Chen et al [66].

Conclusion on fluids

Fluidic approaches also show shock mitigating properties. While no adverse consequences to the use of a fluidic scheme can be seen in the literature, similar issues to their practical use in the underside of a vehicle can be foreseen. The approach requires large quantities of water be carried in a vessel beneath the vehicle; leakage or evaporation of the fluid over time is a particular concern, as this will impair the blast mitigating properties. Furthermore, the aerosol approach faces the difficulty of identifying a blast event and dispersing sufficient water in the extremely short time-frame available.

1.3.4 Mitigation by Geometric arrangements

In the literature regarding the use of geometric arrangements in generic blast defence, two distinct approach groupings or categories can be discerned. These categories are:

1. The use of flat grids or perforated plates, [68–71]
2. The use of angled baffles or geometric shapes, [72–79]

Much of the literature on the topic is focused upon the defence of enclosed spaces such as corridors and ducts, and frequently features the use of laboratory shock-tubes and numerical simulation as an investigative technique.

Perforated plates are flat metal plates containing a number of perforations or apertures of various sizes. A key parameter of interest is the "porosity" (referred to here as ε) of the plate, which refers to the ratio of the total area of the plate which is open to the flow to the obstructed area. Britan et al [68] examined flat perforated plates in which ε is fixed at 40% of the total surface area of the plate ($\varepsilon = 0.4$). By holding the porosity constant but changing the shape of the individual apertures, they were able to study the effects of a varying hydraulic ratio D_h on the mitigation of shocks.

$$D_h = \frac{4S}{\Pi} \tag{1.6}$$

In Equation 1.6, D_h is defined as the ratio of the area of the open surface area S to the aperture perimeter Π. The plate designs of Britan et al with their respective hydraulic ratios are shown in Figure 1.20.

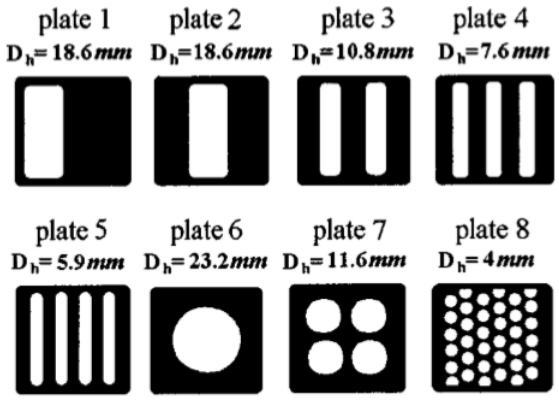

Figure 1.20: The $\varepsilon = 0.4$ plate designs applied in the work of Britan et al [68].

These plate designs are exposed to experimental shock-tube driven shocks of Mach strength $M = 1.435$ and 1.58. The mitigation of these shocks is given as

$$k = \frac{\Delta p}{\Delta p_i}, \tag{1.7}$$

where Δp is the peak pressure jump downstream of the barrier and Δp_i is the peak pressure of the incident shock prior to the barrier. k is a dimensionless measure of shock mitigation. The pressure mitigation downstream of the barrier as a function of distance normalised to the hydraulic ratio x/D_h (where x is the downstream distance) is presented in Figure 1.21. Significant reductions in pressure are observed in the downstream region near the barrier, with the shock overpressure rapidly returning to a plateau of intensity further downstream. The particular shape of the aperture is largely immaterial to the intensity of the downstream shock at sufficient distance, with the majority of the pressure reduction occurring in the region $0 < x/D_h < 7$. Plate designs with lower hydraulic ratios therefore achieve maximum mitigation of the shock in a shorter distance.

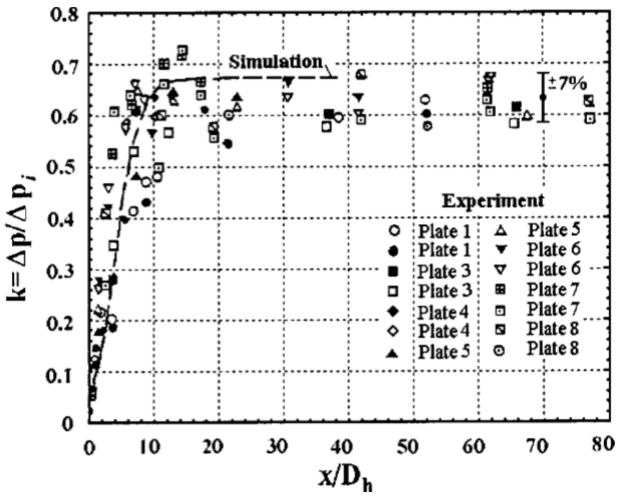

Figure 1.21: Downstream mitigation of shocks as a function of hydraulic-ratio normalised distance. Taken from the work of Britan et al [68].

Examinations of the flow-field in the immediate region behind perforations of varying porosity and angle are provided by Chaudhuri et al [79] and Berger et al [73]. As the flow following the initial shock-wave passes through the openings in a barrier, tur-

bulent vortices are shed (cast off) from the barrier lip. The formation of vortices from the edge of apertures of different cross-section is shown in Figure 1.22, alongside the downstream structure of the shock.

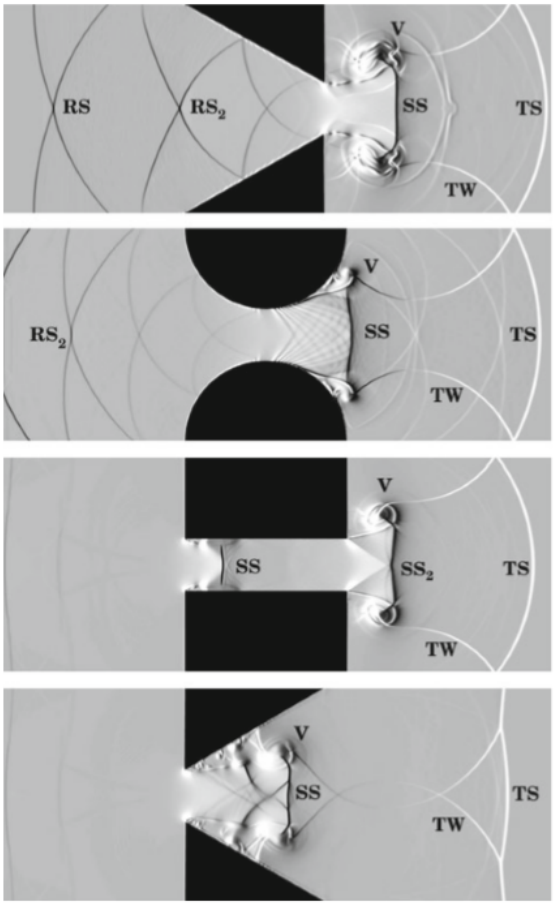

Figure 1.22: Numerical Schlieren (shadowgraph) photography images of shocks passing through perforations. *TS* refers to the transmitted shocks, *RS* to the reflected shock, *SS* to the secondary shock, *V* to the vortex and *TW* to the transverse wave. Taken from the work of Chaudhuri et al [79].

In Figure 1.22, the 4th image shows a diverging aperture structure, in which the perforation becomes wider in the downstream direction. This aperture configuration [73, 79] provides enhanced shock mitigation when compared to other aperture types. Berger et al attribute the superior shock mitigation of this design to two causes:

- The rarefaction of the transmitted shock. The downstream divergence of the

barrier ensures that the shock is constantly expanding in this region, rather than being continually focused as in the case of the converging aperture.

- The positioning of the shed vortices is pulled towards the central symmetry line, into the path of the flow. The interference of these vortices with the aperture flow serves to extract momentum through turbulent mixing.

This can be seen explicitly in Figure 1.23. Berger et al demonstrate that for porosities lying between 0.1-0.7, the angle of the barrier exerts a significant influence on the mitigation of shocks, with the mitigation of downstream pressure increasing by 10% for the diverging barrier geometry when compared to the converging geometry. While the effect is most pronounced for a diverging barrier, vortex shedding is present across all barrier configurations. For a barrier of fixed porosity, a decrease in hydraulic ratio inherently represents a corresponding increase in the total perimeter of the aperture. As vortices are shed from the edge of apertures, an increase in total aperture perimeter is anticipated to increase vortex production and the associated turbulent mixing.

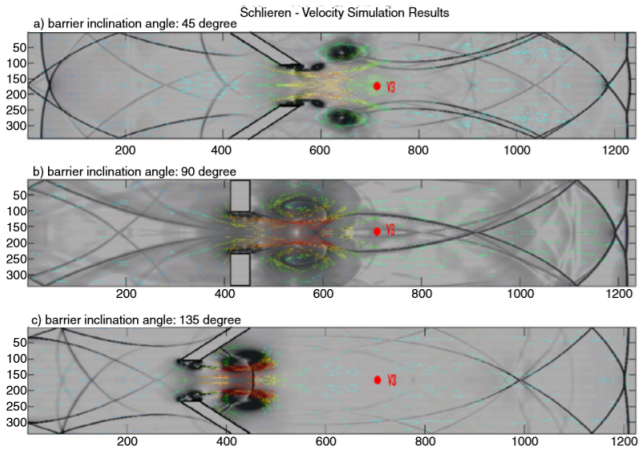

Figure 1.23: Numerical Schlieren photography images of shocks passing through shock baffles of varying angle from left to right, corresponding to a) converging b) flat and c) diverging barrier configurations. Vortices can be seen as the dark circular regions close to the rear of the barrier . Taken from the work of Berger et al [73].

The role of fluid viscosity and turbulence in the vortex shedding process is addressed in the work of Britan et al [68], who performed a 2-dimensional numerical simulation

of a shock striking a thin obstruction in a shock-tube. Both the viscid and inviscid cases are considered, with the conclusion that inviscid simulations produce excessive and unphysical vorticity throughout the downstream flow. This is shown in Figure 1.24, where an extensive vortex street can be seen shedding from the barrier lip. The gas viscosity is identified as the primary mechanism by which the shed vortices are dissipated, and is critical to the successful simulation of this particular mechanism of action.

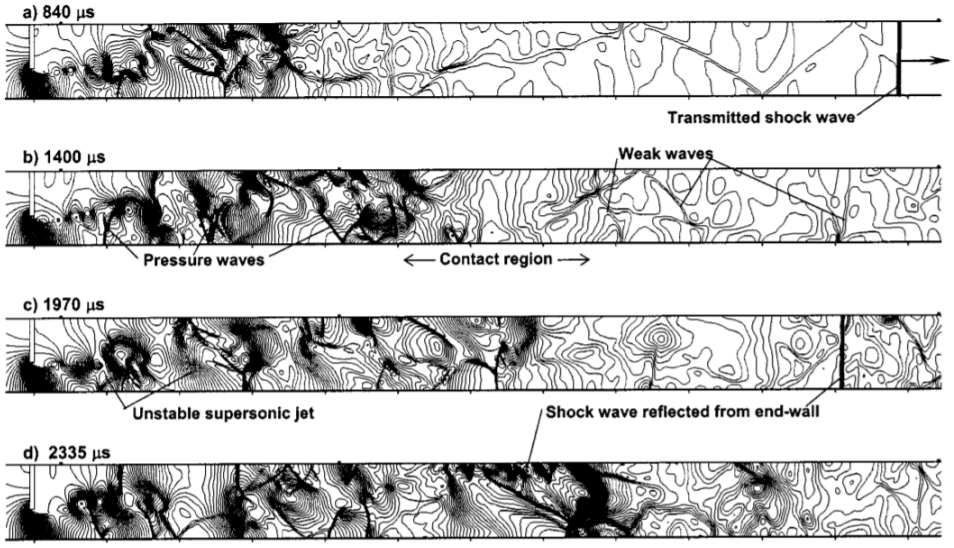

Figure 1.24: Numerical density contours for the inviscid flow downstream of a single-aperture barrier. The excessive vorticity is visible in the dense agglomerations of contours. Taken from the work of Britan et al [68].

In the above, the effects of barrier porosity and their relation to shock mitigating flow mechanisms is shown. However, a real defensive scheme will be exposed to both shock and slug loading and may deform considerably, with possible consequences for the efficacy of the scheme. Empirical evidence for the success of perforated plates in mitigating blasts is therefore desirable. Langdon et al present two papers on this topic. In the first paper [69], circular perforated plates (see Figure 1.25) with a porosity of $\varepsilon = 0.13$ are clamped within an explosive-driven shock-tube in which the shock-front is generated by the detonation of small charges of PE4 (a composite plastic explosive) ranging from 9-21 g. A 1.6mm mild steel witness plate was placed behind both single

and double layer configurations of the perforated plate.

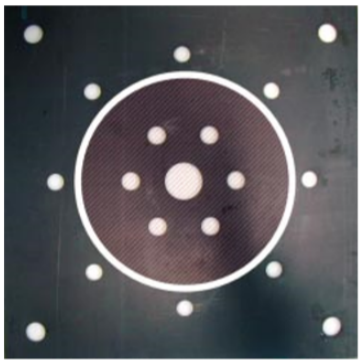

Figure 1.25: The single perforated plate design applied in the work of Langdon et al [69]. Only the large central circular section is exposed to the shock.

The ratio of the permanent deflection of the protected witness plate to the unprotected case serves as the measure of mitigation. The experimental arrangement for the dual-plate experiment is shown in Figure 1.26. The stand-off distance between individual plate arrangements remains fixed.

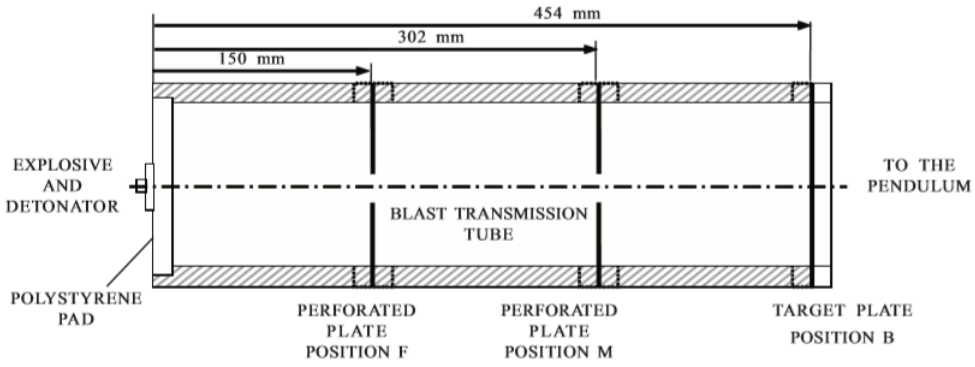

Figure 1.26: The placement and stand-off distances of explosive, perforated plates and witness plate for the dual-barrier approach of Langdon et al. Taken from the work of Langdon et al [69].

In [69], Langdon et al do not state a specific mechanism of action as to how the perforated plates serve to mitigate the shock. Mechanical "petalling" failure of the plate,

in which it ruptures and deforms outwards in the manner of flower petals (see Figure 1.27), was observed for higher charge masses. Despite this,the permanent deflection of the witness plate was reduced by between 65-75% for the case in which a single perforated plate was applied, rising to 90-95% for the case in which two sequential plates were placed between the charge and the rear plate.

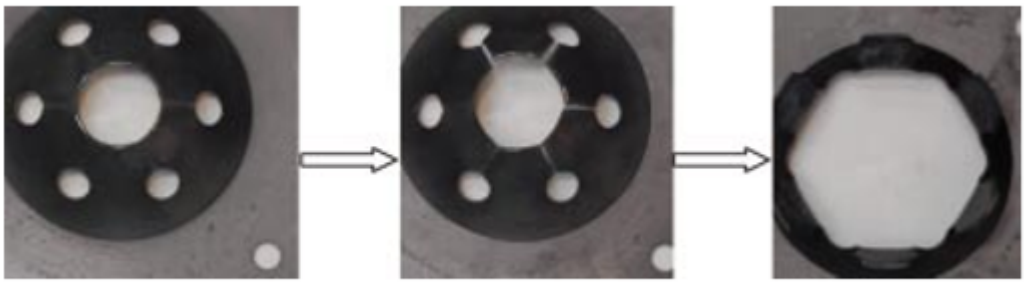

Figure 1.27: Deformation and failure of the initial-placement (position F, see Figure 1.26) perforated plate by the blast generated by charges of a) 13.5 b) 15.0 and c) 20 g of PE4. Taken from the work of Langdon et al [69].

Langdon et al [70] made a following attempt to investigate the mechanism of action through numerical simulation and associated experimentation. Single-aperture perforated plates of varying ε and two deformation behaviours, deformable (thickness 1.6mm) and nominally rigid (thickness 25mm) were exposed to the detonation of PE4 charges ranging from 5-21g. The permanent deflection of thin witness plates was applied as a measure of mitigation. The deformation profile of the witness plate for higher-porosity ($\varepsilon = 0.5 - 0.25$) perforated plates was similar to that of the unprotected case, with reduction in peak deflections beginning at $\varepsilon = 0.25$. More significant reductions in deflection were observed for the lower porosities. Variation in the thickness of the perforated plates was observed to have minimal effect on witness plate deflection. Numerical studies were executed in ANSYS AUTODYN as 2-dimensional simulations with axial symmetry and porosities ranging from $\varepsilon = 0.75 - 0.04$, with the results rotationally extended to 3 dimensions. Unlike the numerical approaches seen in [68, 73, 79], AUTODYN does not include a turbulence model in its solutions of the flow dynam-

ics. The effects of momentum extraction through turbulent mixing noted in [68, 73, 79] are therefore not replicated in [70]. The simulation arrangement is shown in Figure 1.28.

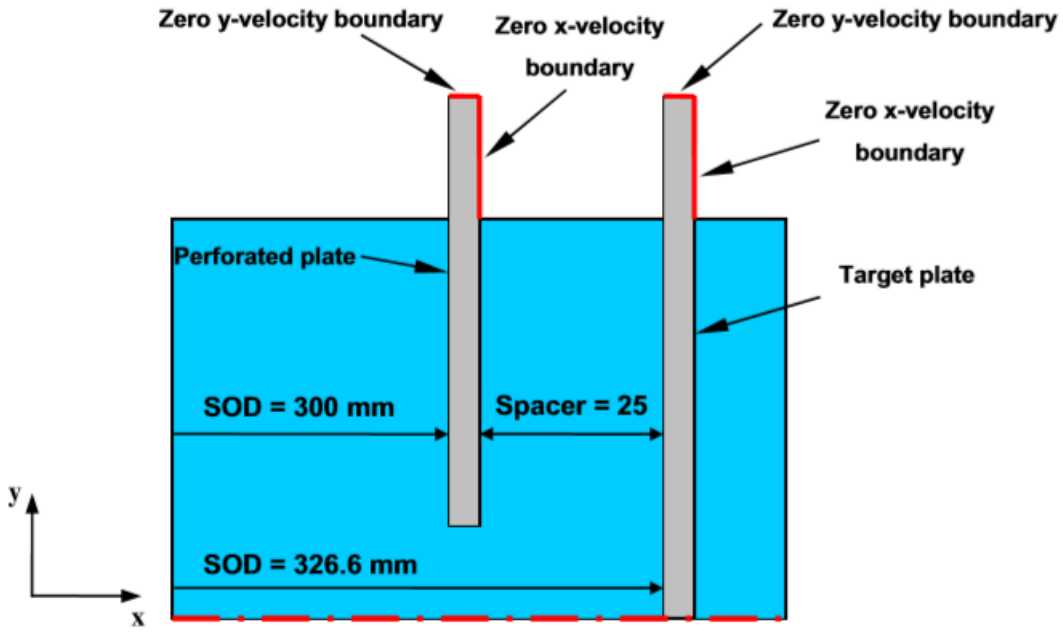

Figure 1.28: AUTODYN simulation arrangement for an investigation into the mechanisms of perforated plate defence. The dashed red line indicates the axis of rotational symmetry. Taken from the work of Langdon et al [70].

Impulse measurements from the front and rear of the witness plate were recorded, as were the mid-point deflections and pressure conditions exerted on the witness. For porosities $\varepsilon = 1 - 0.25$, no discernible impact was made on the duration of the applied loading, although the loading duration does begin to increase as the porosity grows smaller, reaching a maximum at 50% for the $\varepsilon = 0.04$ case. However, the response time of the witness to loading was noted to consistently increase with decreasing porosity. It was also noted that a high-pressure condition remained at the surface of the witness even after the plate had reached an equilibrium position. Decreasing the porosity beyond $\varepsilon = 0.5$ decreased the mid-point deflection of the witness, but also applied greater loading to the perforated plate, resulting in the induction of tearing deformation at the clamped edge, a behaviour also seen in the experimental studies (see Figure 1.29).

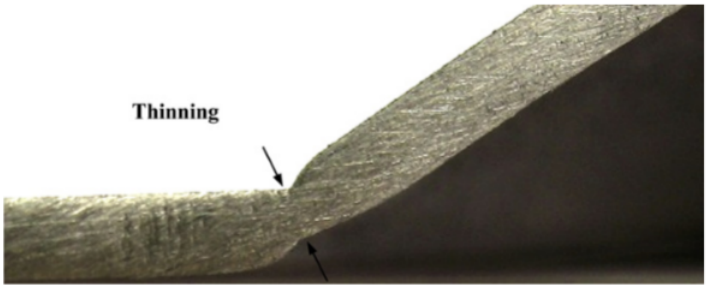

Figure 1.29: Thinning indicative of the onset of tearing at the clamped plate edge for a plate of porosity $\varepsilon = 0.11$. Taken from the work of Langdon et al [70].

Conclusion on geometric means

Geometric approaches based on the use of perforated grids or plates show demonstrable shock-mitigation properties. Several points are in favour:

- Contrary to the other approaches, a significant component of the mitigation arises from the behaviour of the flow itself; the role of the perforations is to disrupt the initial shock and introduce flow characteristics which are unfavourable to the shock-wave and gas flow, rather than attempting to directly absorb the energy of the blast.
- Perforated plate approaches may therefore scale well against blasts of varying intensity
- Perforated plates are, at a base level, simply metal plates with holes in them, and are likely to be comparatively insensitive to operating conditions under a vehicle. Depending on the particular arrangement, they may potentially be lighter and occupy less space than alternative schemes.

These points are tempered by the following considerations:

- A perforated plate will be structurally weaker than a solid plate. This may be offset by the flow through the apertures reducing the pressure loading on the perforated plate.

- While potentially beneficial from the perspective of shock mitigation, the perforations also provide opportunity for solid ejecta to pass through the apertures and strike the hull.

- While certain aspects of the way in which perforated plates mitigate shocks are known, a cohesive understanding of their dynamics (especially with respect to complex mine and IED blasts) remains elusive.

On the basis of the above, the decision was made to investigate perforated plate-type geometries as a means of protecting vehicles against blast. Such schemes offer the potential for comparatively simple, practical, durable and effective protection. The requirement of empty space behind the protective modification lowers the weight of the scheme and yields significant scope for innovation with respect to adaptations and modifications that can further enhance blast mitigation. Finally, the suggested mechanisms of action by which perforated plate-type schemes act to mitigate shocks may meet the requirement for performance against a range of threat intensities. However, the unknown factors in the approach must be addressed before a full recommendation can be made.

1.4 Formulation of research objectives

The particular shape of the apertures present in a given barrier is seen to exert little influence over the intensity of the downstream shock at sufficient distance. However, it is also shown that the majority of the pressure recovery occurs in the region $0 < x/D_h < 7$. The downstream spatial length of this region is highly dependent on the hydraulic ratio D_h, and the general pressure recovery in this region is indicated to be largely comparable between designs. Assuming a constant plate porosity, this suggests that smaller individual aperture sizes with lower hydraulic ratios will provide equivalent mitigation to larger apertures while requiring less downstream distance in which to effect the same reduction in shock. In optimising the design and striking a balance between the minimisation of the plate-hull spacing and the protection offered to the vehicle, an understanding of the flow field in the immediate post barrier region and the ways in which it can be manipulated to greatest effect is sought.

The literature regarding the role of geometric schemes in the mitigation of shocks is entirely absent the effects of the solid ejecta of a buried charge blast. While anticipated in the cases in which the defence of corridors and ducts is the objective of the study, it is also absent in the works by Langdon et al [69, 70] in which defensive perforated plates are suggested to be plausible options for mine blast mitigation. Indeed, the literature in general is devoid of studies in which perforated plates as defensive schemes are examined outside of shock-tubes or shock-tube like environments. Aside from the results presented by Langdon et al in [70], no consideration is given to the deformation of the perforated plate or the consequences for the flow field and associated blast mitigation. Further to this is the observation by Langdon et al in [69] that difficulty lies in establishing the relative contribution made to the mitigation resulting from the perforated nature of the plate when considered against the effects of deformation. This thesis therefore proposes two primary objectives:

1. To attempt to isolate the specific contribution of the porous nature of perforated plates to the mitigation of shocks, and examine ways of manipulating the flow-field to greatest effect

2. To examine the performance and dynamics of perforated plates in simulated mine-blast scenarios

Two simulation types are performed to this end:

1. The 3-dimensional simulation of a planar shock striking a fully rigid barrier. Analysis of the downstream pressure and flowfield yields insight into the contribution of barrier design to the mitigation of shocks. Comparison is made to the experimental works of Britan [68]. A novel divertor scheme intended to re-direct the post-barrier flow is also investigated.

2. The simulated detonations of a buried charge. A flat perforated plate is imposed between the detonation and a solid witness plate; the deformation of the witness is taken as a measure of protection. Comparison is made to two alternatives: a single thick plate, and a solid protective plate at the same spacing as the perforated plate.

1.5 Thesis structure

The remainder of this thesis is directed towards achieving these objectives. The following Chapters and the manner in which their contents achieve these goals are summarised below:

In Chapter 2, The theory of numerical simulation as applied to the objectives of the project is presented. Particular consideration is given to the differences between multi-physics simulation and pure computational fluid dynamics, and the relevance of these differences to the approaches adopted in the investigation.

In Chapter 3, a modelling methodology for 3-dimensional examinations of the flow field downstream of a perforated barrier is developed. The techniques and models suitable for the generation and study of shock interactions with a fully-rigid perforated plate are examined, alongside considerations of the spatial resolution of the simulation.

In Chapter 4, The techniques derived in Chapter 3 are applied to the full 3-dimensional simulation of shock interaction with perforated plates of varying hydraulic ratio within a shock-tube like environment. The case in which the downstream distance is sufficient to allow the transmitted shock to return to return to a planar form is compared to the case in which the end-wall of the tube is placed in close proximity to the barrier. The concept of a post-barrier flow divertor is also examined. The numerical model is compared to previous results in the literature.

In Chapter 5, A simulation approach for the dynamics of buried charge detonations is sought. Appropriate problem geometry and material models are selected. The effect of spatial resolution on the accuracy of the blast prediction is investigated.

In Chapter 6, The approach developed in Chapter 5 is applied to the simulation of a buried charge detonation and the associated impact on a target protected by a perforated plate scheme. A range of perforation configurations and charge configurations are considered and compared to alternative solid-plate arrangements.

In Chapter 7, The results of the previous 4 Chapters are combined and an as-

sessment of the potential use of perforated plates as a protective scheme in defending against IEDs and mines is made. Deficiencies in the available modelling approaches and their impact on the project are considered.

In Chapter 8, The thesis closes with a summary of the findings. Proposals are made for relevant future work

Chapter 2

Modelling Methodologies

As described in the first Chapter of this thesis, there are two research objectives, summarised as:

- The modelling of a shock striking a perforated plate and and investigation of the downstream flow
- The modelling of the blast and slug loading from a buried charge detonation, and its interaction with a perforated plate defence scheme.

The geometry and physics of both problems are highly complex and analytical solutions cannot be applied. However, the complex geometry of the problem can be broken into smaller pieces, and local solutions to the governing equations can be found. This process of spatial decomposition or "meshing" is shown in Figure 2.1, in which two pipes may be seen meeting at a box. The flow of a real fluid through this domain will be complex and cannot be solved in a single equation. Instead, the domain is broken into individual elements or "cells". Flow variables are passed between each cell and its neighbours according to a discrete form of the governing flow equations. The combination of all the individual solutions will approximate to the true large-scale behaviour of the system.

Figure 2.1: A complex geometry as a) a continuous volume , and b) broken into a mesh of smaller volumes or "cells".

This is the numerical approach. The equation sets are large, and solutions are only

feasible through computers. The codes that find solutions to systems of equations of this type are known as "solvers". While modern solver packages are highly capable, there is no single solver which includes all the possible physics that may be present in a real experiment. The choice of solver is governed by the relevant phenomena of interest.

For the first objective, in the absence of plate deformation, the problem is a matter of fluid dynamics alone, with the following major considerations:

1. Fluid viscosity and the presence of turbulence
2. Spatial resolution of the shock and flow structure
3. Accurate prediction of downstream pressure

For the second objective, fluids and solids must interact, with the dynamics of the problem being driven by a detonation. This requires a simulation which is capable of combining multiple solution techniques and material models. These phenomena and the most important consideration for each are:

1. Detonation dynamics:
    - Empirical vs theoretical models of detonation
2. Solid body dynamics:
    - Accurate models for material deformation
3. Fluid dynamics:
    - The flow of multiple materials in the same volume

The role of fluid viscosity and turbulence is explicitly identified as a major contributing factor to the mitigation potential of perforated plates, and a range of suitable simulation techniques are present in modern solvers for computational fluid dynamics. However, these codes are extremely limited with respect to the prediction of solid body deformation. Likewise, the codes which are capable of combining fluid-solid interaction for the simulation of a buried charge detonation do not contain the capability to model the turbulent behaviour of the flow. It is for this reason that the two research objectives are investigated with two different solvers. The CFD solver FLUENT is applied to the

modelling of the flow-field behind a fully-rigid perforated plate, while the multi-physics solver AUTODYN is applied to the simulation of buried charge detonation. Both solvers are developed and maintained by ANSYS Inc. Within these packages, there are two solution approaches which are used extensively in this work:

- The Eulerian approach, in which the cells into which the computational domain is split are fixed in space. As the simulation progresses in time, material and flow properties are transferred between cells according to the laws of conservation of mass, momentum and energy.
- The Lagrangian approach, in which material is embedded in the mesh. If the material deforms, so does the mesh. Mass is automatically conserved, and solutions are sought for the equations of motion for the points or "nodes" that define each mesh element.

The difference between the two approaches is shown in Figure 2.2, in which a tungsten penetrator moving at $1500ms^{-1}$ has struck a $4mm$ thick mild steel plate. The plate is modelled using both Eulerian and Lagrangian meshes. A cross-section of both is shown in which the numerical grid is displayed to highlight the difference. The spatially fixed nature of the Euler approach makes it ideal for modelling materials which are expected to undergo significant deformation such as fluids, or solids experiencing very high strain rates. This is demonstrated in Figure 2.2, in which the deformed plate material and the undeformed mesh in which the material resides may be seen on the left. Likewise, it is clear from the deformation of the Lagrangian mesh in Figure 2.2 that this approach is unsuitable for the modelling of fluids. The requirement that material remain within the mesh will very quickly lead to the "tangling" of mesh elements under large deformations. The Lagrangian approach is therefore better suited to the modelling of solid bodies for which smaller but more accurate deformation is required, or where the location of material interfaces must be known precisely. This Chapter begins with a description of the Eulerian approach and the modelling of fluids. The FLUENT-specific aspects of the Eulerian (or "finite-volume") approach are described in the context of this work. The Lagrangian and Eulerian solvers in AUTODYN are then described , alongside the method by which the solvers may interact. A brief summary of how FLUENT and AUTODYN are used to construct and solve problems is given.

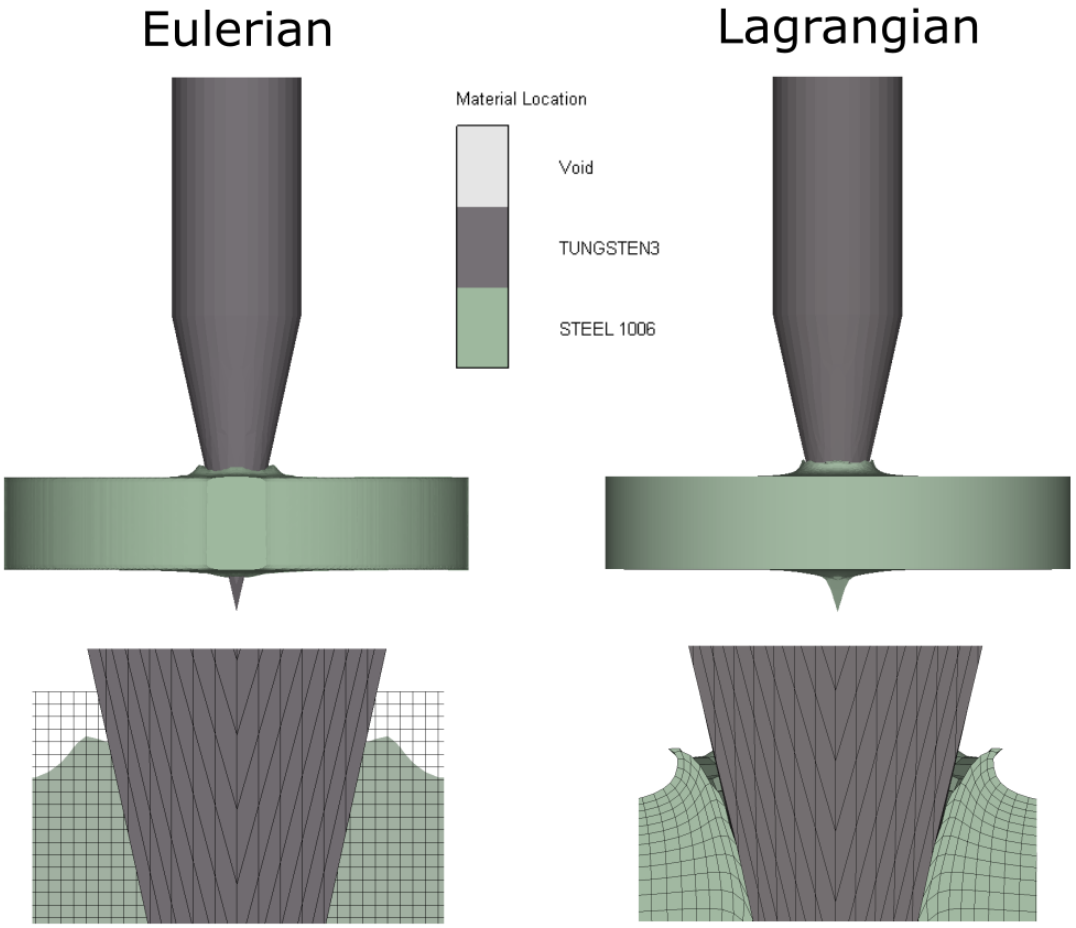

Figure 2.2: The penetration of a mild steel plate by a small tungsten penetrator at $t = 6\mu s$ after initial contact. The tungsten penetrator is modelled with a Lagrangian mesh, while the target plate is modelled with an Eulerian mesh (left) and a Lagrangian mesh (right). The Eulerian mesh is spatially fixed and material deformation is a consequence of transport between cells, while the cells of the Lagrangian mesh are visibly deformed with the material.

2.1 The Euler Approach

The Euler approach is predominant in the simulation of fluid mechanics. The most complete description of the behaviour of a fluid is given by the compressible, viscid Navier Stokes equations. These equations represent the transfer of mass, momentum and energy and are usually written in a conservation form suited to the transfer of material between spatially fixed elements. The initial equations are given in Table 2.1.

Table 2.1: The Compressible Viscid Navier Stokes Equations [80, 81]

Conservation Law	Equation
Mass	$\frac{\partial \rho}{\partial t} + \nabla \cdot (\rho \mathbf{u}) = 0$
Momentum	$\frac{\partial \rho u}{\partial t} + \nabla \cdot (\rho u \mathbf{u}) = -\frac{\partial p}{\partial x} + \frac{\partial (\tau_{xx})}{\partial x} + \frac{\partial (\tau_{yx})}{\partial y} + \frac{\partial (\tau_{zx})}{\partial z} + \rho F_x$
	$\frac{\partial \rho v}{\partial t} + \nabla \cdot (\rho v \mathbf{u}) = -\frac{\partial p}{\partial y} + \frac{\partial (\tau_{xy})}{\partial x} + \frac{\partial (\tau_{yy})}{\partial y} + \frac{\partial (\tau_{zy})}{\partial z} + \rho F_y$
	$\frac{\partial \rho w}{\partial t} + \nabla \cdot (\rho w \mathbf{u}) = -\frac{\partial p}{\partial z} + \frac{\partial (\tau_{xz})}{\partial x} + \frac{\partial (\tau_{yz})}{\partial y} + \frac{\partial (\tau_{zz})}{\partial z} + \rho F_z$
Energy	$\frac{\partial \rho E}{\partial t} + \nabla \cdot (\rho E \mathbf{u}) = \rho \dot{q} + \nabla \cdot (k \nabla T) - \nabla (p \mathbf{u})$
	$+ \frac{\partial (u \tau_{xj})}{\partial x} + \frac{\partial (v \tau_{yj})}{\partial y} + \frac{\partial (w \tau_{zj})}{\partial z} + \rho \mathbf{F} \cdot \mathbf{u}$
Ideal Gas	
Equation of state	$p = (\gamma - 1) \rho e$

In Table 2.1, ρ is the fluid density, t the time, u, v, w the velocity components in the x, y, z axes, $\mathbf{u}$ the total velocity vector, p the pressure and F_i the body forces (electromagnetic or gravitational) acting on the fluid within a cell, where $\mathbf{F}$ is the combined vector of such. E is the sum of internal (e) and kinetic energy $E = (e + \frac{u^2}{2})$, k the coefficient of thermal conduction , T the temperature, and $\dot{q}$ the rate of change in heat energy. S_E represents sources of thermal energy. The τ_{ij} terms are components of the viscous stress tensor:

$$\Pi = \begin{pmatrix} \tau_{xx} & \tau_{yx} & \tau_{zx} \\ \tau_{xy} & \tau_{yy} & \tau_{zy} \\ \tau_{xz} & \tau_{yz} & \tau_{zz} \end{pmatrix} \tag{2.1}$$

Here τ_{ij} simply refers to the notion of viscous stress, which is in direct proportion to the strain rate of the fluid; a computationally tractable approximation is introduced

later in this Section. The momentum equations are of particular interest, as they represent a means of solving for the motion of the flow; in order from left to right, the terms relate the local and convective acceleration to the pressure gradient and viscous forces acting on an infinitesimal fluid body. The application of Gauss' law to the equations of Table 2.1 and collection of the terms lying under the resulting surface and volume integrals allows the entire system of equations to be expressed as [80]

$$\frac{\partial}{\partial t}\int_V \mathbf{W}dV + \oint \mathbf{s}\cdot[\mathbf{F}-\mathbf{G}]dA = \int_V \mathbf{H}dV \tag{2.2}$$

where **W,F,G,H** are column vectors of the fluxes of flow quantities

$$\mathbf{W} = \begin{Bmatrix} \rho \\ \rho u \\ \rho v \\ \rho w \\ \rho E \end{Bmatrix} \tag{2.3a}$$

$$\mathbf{F} = \begin{Bmatrix} \rho\mathbf{v} \\ \rho\mathbf{v}_{ijk}u + p\hat{i} \\ \rho\mathbf{v}_{ijk}v + p\hat{j} \\ \rho\mathbf{v}_{ijk}w + p\hat{k} \\ \rho\mathbf{v}_{ijk}E + p\mathbf{v} \end{Bmatrix} \tag{2.3b}$$

$$\mathbf{G} = \begin{Bmatrix} 0 \\ \tau_{xi} \\ \tau_{yi} \\ \tau_{zi} \\ \tau_{ij}v_j + \mathbf{q} \end{Bmatrix} \tag{2.3c}$$

$$\mathbf{H} = \begin{Bmatrix} 0 \\ \rho F_x \\ \rho F_y \\ \rho F_z \\ \rho(uF_x + vF_y + wF_z) + \rho\frac{dq}{dt} \end{Bmatrix} \tag{2.3d}$$

In the case where the flow is inviscid (and thus absent the viscid stress terms), the Navier Stokes equations become the inviscid Euler equations. In the set of vectors described in Equation 2.3b, the vector column **F** is written in a compact form that encompasses the orthogonal flux vectors characterised by the unit vectors $\hat{i}, \hat{j}, \hat{k}$. $\mathbf{v}_{ijk}$ is the velocity component u, v, w corresponding to the relevant unit vector, and E is the total energy $E = \rho(e + \frac{\mathbf{u}^2}{2})$. The fluxes described by column **F** are the fluxes of convective quantities, whose value is dependent on the fluid velocity. Column **W** contains the fluxes of scalar quantities, and column **G** contains the viscous fluxes. Column **H** contains body forces. The decomposition of the governing equations into flux vectors also permits a modular approach to their solution, in which different calculation methodologies may be applied to each vector column. Solution for the transport of these flux quantities at cell interfaces over time may be accomplished in two ways; through time implicit, or time explicit techniques.

However, there is an associated cost in adopting the finite volume approach; in calculating transport in flux form, the spatial distribution of quantities within the cell is lost. The flux at cell interfaces must be reconstructed to allow accurate transport of flow variables. For the purposes of simulating shockwaves, preservation of the shock discontinuity without excess diffusion (broadening of the shock interface over successive timesteps) must also be achieved. This is accomplished through "upwind" schemes.

2.1.1 Upwind Schemes for Shock Simulation

Upwinding schemes are flux transport methodologies in which the direction of propagation of information throughout the system is explicitly accounted for. The method of characteristics is applied; at cell interfaces, solutions are sought for the function in (x, t) space $x = x(t)$ along which the advection equation for a flux ϕ:

$$\frac{\partial \phi}{\partial t} + u_x \frac{\partial \phi}{\partial x} = 0 \tag{2.4}$$

reduces to the ordinary differential equation:

$$\frac{dx}{dt} = u_x \tag{2.5}$$

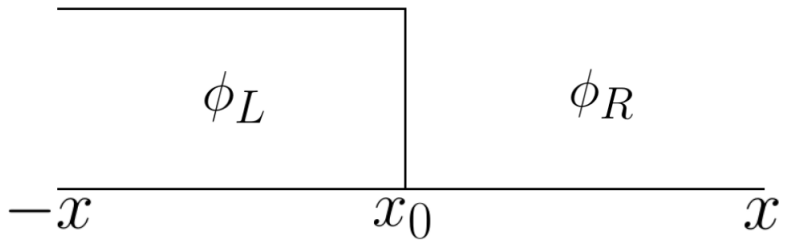

Figure 2.3: The general initial condition of the Riemann problem at $t = 0$. The initial discontinuity in ϕ is centred on x_0, and is expected to propagate from left to right

which yields the "characteristic velocity" u_x of a given flux variable. The Riemann problem is of particular importance in flow upwinding, and strongly informs the theoretical basis for upwind schemes, to the extent that these schemes are also known as Approximate Riemann Solvers [82].

The Riemann Problem

The Riemann problem describes an initial discontinuity in a gas, where the distribution of flux ϕ at $t = 0$ is described as

$$\phi(x, 0) = \phi_0(x) = \begin{cases} \phi_L & \text{if } x < 0 \\ \phi_R & \text{if } x > 0 \end{cases} \tag{2.6}$$

The spatial arrangement of ϕ is shown in Figure 2.3. This arrangement also describes the starting conditions for a physical shock tube, where the high pressure driver gas and low pressure driven gas are separated by a thin membrane. On bursting the membrane, a shock (initially centered at x_0) propagates into the driven section. From the initial boundaries of the problem, the characteristic line of the shock may be described as $x(t) = x_0 + u_x t$. However, a corresponding wave structure will also travel to the left, forming a rarefaction fan as gas expands into the lower pressure region. The position of discontinuities within the flow at a later time is shown in Figure 2.4

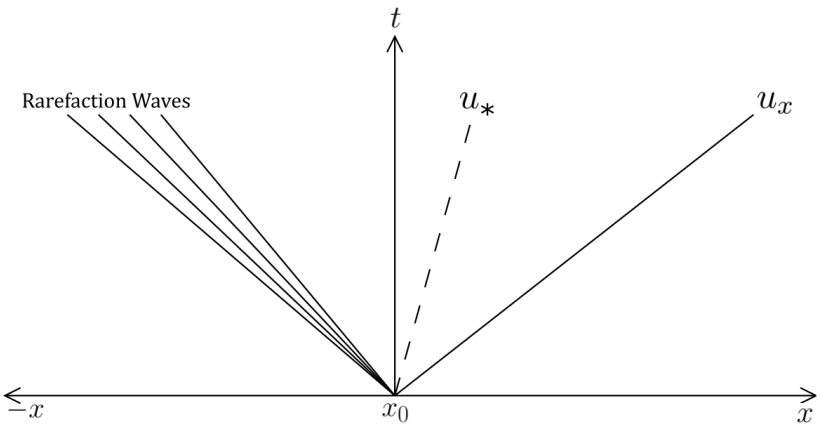

Figure 2.4: Characteristic lines for the Riemann problem at a later time t. The right-most line corresponds to the shock-front, propagating from left to right with characteristic velocity u_x. The dashed line represents the position of the contact discontinuity between the compressed and expanded gases, which moves in space with velocity u_* The leftmost cluster of lines represents a rarefaction fan moving to the left. The total region between the left-most and right-most characteristic lines is the "domain of dependency". [82, 83]

The relationship between the Riemann problem and the dynamics of a shock tube is used in the shock tube test of Sod [84], in which the numerical simulation of the initial shock-tube problem of a given scheme is compared to the analytic solution. This test is applied when selecting an appropriate upwind scheme in Chapter 3. Of particular importance are

- Accurate spatial prediction of the discontinuities in the flow
- The suppression of unphysical oscillations at flow discontinuities.

Flux differencing and flux splitting

Both AUTODYN and FLUENT are capable of applying upwind schemes in the solution of shock dynamics. Equation 2.4 may be written as [83]

$$\mathbf{U}_t + \mathbf{F}(\mathbf{U}_x) = 0 \tag{2.7}$$

where $\mathbf{U(x,t)}$ is a vector of conserved scalar variables and $\mathbf{F}(\mathbf{U})$ the corresponding vector of convective variables. Toro [83] identifies two primary approaches by which the upwind direction of the flow may be established, with Equation 2.7 as a starting point. These are:

- The Godunov (or Flux-differencing) approach
- Flux-vector splitting (FVS)

Both approaches give rise to a wide variety of numerical flux calculation schemes. The original first-order scheme of Godunov is based directly on solutions to the Riemann problem. The assumption is made that the value of a given flux is a constant average across the cell; taken as a system, the flow variables are represented as a piecewise distribution over the domain. The discontinuity created at the cell interface is solved along the characteristic lines as a solution to the Riemann problem, thus preserving the correct flow direction. The original Godunov method forms the basis for a range of competing flux differencing schemes; the flux-differencing approach focused on in this work is the higher-order scheme of van Leer [85]. This method is applied in both FLUENT in the form of the Monotonic Upstream-centered Scheme for Conservation Laws (MUSCL), and the multi-material Euler solver in AUTODYN (with modifications).

The alternative is to determine the upwind and downwind directions of the flow by "splitting" $\mathbf{F}(\mathbf{U})$ into two fluxes; the upwind $\mathbf{F}^+(\mathbf{U})$ and the downwind $\mathbf{F}^-(\mathbf{U})$. Determination of the split flux is accomplished by finding the eigenvalues of the Jacobian matrix $\mathbf{A}(\mathbf{U})$, which is defined as

$$\mathbf{A}(\mathbf{U}) = \frac{\partial \mathbf{F}}{\partial \mathbf{U}} \tag{2.8}$$

The eigenvalues λ_i of $\mathbf{A}(\mathbf{U})$ are positive in the upwind direction (λ_i^+) and negative in the downwind (λ_i^-). This splits the flux exactly around the discontinuity in eigenvalues represented by the shock-front, preserving the discontinuity over time. As with the Godunov scheme, the FVS approach contains a range of implementations, of which this thesis is interested in one; the Advective Upstream Splitting Method (AUSM) of

Liou[1] and Steffen [87].

FLUENT permits the application of both the MUSCL and AUSM schemes in a single simulation; MUSCL may be applied to the transport of scalar and turbulent fluxes, while AUSM may be applied to the convective flux. In Chapter 3, the performance of the combined MUSCL/AUSM approach in FLUENT is examined as a shock-tube solver method.

The Van Leer scheme

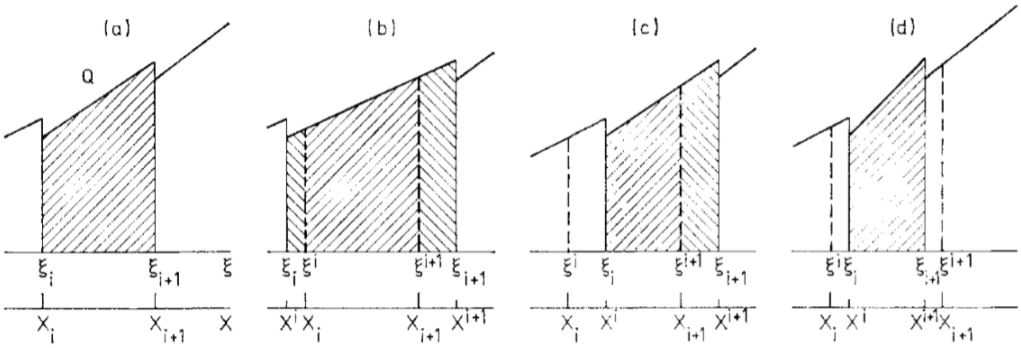

Figure 2.5: The possible final states of the initial Lagrangian transport step for a given 1D cell in the Van Leer scheme. X_i, X_{i+1} denote the limits of the fixed Eulerian mesh while X^i, X^{i+1} describe the final positions of the original cell contents after the deformation. a) describes the initial state of the material in the cell; in b), the material is transported both left and right. In c), the material deforms inwards to the cell on the left, and intrudes rightwards into the next cell. In d), the material is compressed inwards into the cell. Remapping follows, with the fixed mesh updated with the new material contents. Taken from the work of Van Leer [85]

Under the scheme of Van Leer, the distribution of flux within a cell is assumed to be linear. Transport for a cell is performed in two steps; in the first, the material within the cell deforms as though contained in a Lagrangian cell element. On completion of the Lagrangian step, the distorted material is mapped back to the spatially fixed Eulerian mesh. The deformation stage in 1- dimension is shown in Figure 2.5. The

[1]Sadly recently departed; an excellent and informative historiography of the AUSM method may be found in [86]

method of characteristics exploited by the original Godunov scheme is incorporated into the second-order accurate Lagrangian scheme[1], and thus the upwinding property is preserved [85].

The Van Leer scheme also suppresses oscillations in regions where the average flux value in a sequence of cells is monotonic (constantly increasing or decreasing, as anticipated at discontinuities) by limiting the slope of the flux distribution within the cell, as shown in Figure 2.6. With the flux limiter method applied in ANSYS, the MUSCL scheme is spatially accurate to third-order [80].

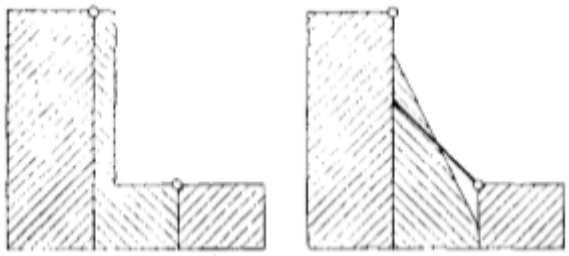

Figure 2.6: Flux limitation as applied to a shock-front; in the left image, the actual shock structure in 1 dimension is shown. In the right image, the limited flux (heavy line) that prevents the unphysical oscillation that would be generated by the discontinuity between flux distributions. [85]

The AUSM+ scheme

Under the AUSM+ scheme, the flux-splitting method outlined in Section 2.1.1 is further modified; the vector $\mathbf{F}$ in Equation 2.3b may be decomposed into convective and pressure terms. In 2 dimensions, the x-axis flux vector may be represented as

$$\mathbf{F}_x = u \begin{pmatrix} \rho \\ \rho u \\ \rho v \\ \rho E \end{pmatrix} + \begin{pmatrix} 0 \\ p \\ 0 \\ 0 \end{pmatrix} \tag{2.9}$$

[1] An approach which also overcomes the Godunov order-barrier theorem

where the convective terms are treated as scalar quantities (akin to **W** in Equation 2.3a) and the pressure flux obeys the acoustic wave speed. These two flux columns are discretised separately. At cell interfaces, the flux of both columns is calculated from the splitting of the advective Mach number $M_{1/2} = M_L^+ + M_R^-$, where M_L^+ and M_R^- are the wave speeds. The scalar and pressure fluxes are calculated using different 4th-order polynomial formulations for the splitting [80]. Decoupling of the pressure and scalar terms allows upwinding of the scalar flux according to the correct flow velocity, while allowing the pressure shock to propagate correctly [87–89].

2.1.2 Mesh Types

The creation of a suitable mesh for Eulerian flows is highly dependent upon the physics of interest. The two types of mesh construction applied in this thesis are:

1. Structured meshes, in which the cells obey an orderly distribution in space and have regular "connectivity" (each cell face connects exactly to the face of a neighbour).
    - The relationship between cells may be expressed via i, j, k indices corresponding to spatial arrangement.
    - Maintaining the connectivity relationship poses problems for complex geometries.
    - Cannot be locally refined, as this will violate connectivity at the edge of the refinement zone.
2. Unstructured meshes, in which cells are not required to have regular connectivity
    - Highly flexible in fitting the mesh to complex geometry, especially curved surfaces .
    - Lack of connectivity requires that the position of cells relative to one another be stored explicitly in memory, and is correspondingly computationally expensive when compared to structured meshes.
    - Variability in the mesh construction may result in cells with high skewness, in which faces or cell shapes may deviate from the "ideal" equilateral shape, with implications for the accuracy of flux transport. [80]

FLUENT admits the use of unstructured meshes, while AUTODYN only permits structured meshes for the Euler solver.

2.2 FLUENT Modelling techniques

The work in FLUENT is directed towards the solution of viscid, turbulent, compressible and transient (time-unsteady) flow. While FLUENT is suitable for an extensive range of modelling scenarios, this Section focuses on the methods most appropriate for the simulation of a shock-tube like environment.

FLUENT is capable of applying two primary solver formulations on the basis of the flow parameter used to calculate the pressure field. The velocity field in both cases is solved from the momentum equations:

- The pressure-based solver, in which the pressure field is calculated directly
- The density-based solver, in which the pressure field is calculated indirectly, from the equation of state

As compressible flows are characterised by a varying density, the density based formulation with a compressible ideal gas equation of state is applied, implemented in FLUENT as

$$\rho = \frac{p_{op} + p}{\frac{R}{M_w}T} \tag{2.10}$$

where p_{op} is the operating pressure (the average pressure of the flow), p is the static pressure (defined with respect to the operating pressure), R is the gas constant $8.314 J\,(mol\,k)^{-1}$ and M_w the molecular weight of the gas. T is the temperature, is provided from solution of the energy equation given in Table 2.1 . As the aim is to model the complex geometry of a perforated plate, an unstructured mesh approach is applied. A means of calculating the flux at cell interfaces for cells of notionally arbitrary shape is required. This is accomplished through a Green-Gauss nodal gradient reconstruction

$$\bar{\phi}_f = \frac{1}{N_f}\Sigma_n^{N_f}\bar{\phi}_n \tag{2.11}$$

where $\bar{\phi}_f$ is the average flux at a cell face, N_f represents the number of nodes lying on a given face and ϕ_n is the flux value at the face nodes [90–92]. The accuracy of the flux reconstruction can be impaired if a cell is highly skewed. For tetrahedral meshes, the FLUENT manual recommends that the average value of the cell skewness should be below 0.33, with no cells exceeding a skewness of 0.95 [93]. The automatic meshing feature in ANSYS constrains the maximum and average cell skew to lie within these tolerances.

2.2.1 Time-stepping in FLUENT

Time-stepping for unsteady flow in FLUENT is performed using the 4th-order Runge-Kutta (RK4) method. To solve the general ODE $\frac{d\phi}{dt} = f(\phi, t)$ along the characteristic line over a fixed time-step Δt from an initial timestep n, the Taylor series around $\phi(t_n + \Delta t)$ is approximated to through combinations of first order derivatives of $\phi(t_n + \Delta t)$ [94]. The RK4 approximation is given by

$$\phi_{n+1} = \phi_n + \frac{1}{6}(c_1 + 2c_2 + 2c_3 + c_4) \tag{2.12}$$

where

$$c_1 = \Delta t f(\phi_n, t_n) \tag{2.13a}$$
$$c_2 = \Delta t f(\phi_n + \frac{1}{2}\Delta t, t_n + \frac{1}{2}c_1) \tag{2.13b}$$
$$c_3 = \Delta t f(\phi_n + \frac{1}{2}\Delta t, t_n + \frac{1}{2}c_2) \tag{2.13c}$$
$$c_4 = \Delta t(\phi_n + h, t_n + c_3) \tag{2.13d}$$

The method is time-explicit; values of ϕ at the later time-step ϕ_{n+1} are not present in $f(\phi, t)$. The time stability of explicit schemes is dependent upon the Courant-Friedrich-Lewy (CFL) condition which, in 1-dimension, requires that $C < 1$ for

$$C = \frac{(u+a)\Delta t}{\Delta x} \tag{2.14}$$

where u is the maximum propagation velocity of information through the system, a is the sound-speed of the gas, Δt is the time-step, and Δx is the distance across the smallest element in the simulation. This condition can be obeyed either by selecting a fixed time-step such that information in the flow does not propagate further than the smallest Δx in the discrete mesh, or it can be managed automatically by FLUENT over the course of a simulation. As significant variations in maximum flow velocity are expected over the course of the simulations, a fixed minimum time-step will frequently be much smaller than required by the CFL condition. Automatic time-stepping is applied in the FLUENT simulations unless otherwise stated.

2.2.2 Turbulence Modelling

Turbulence is a state of unsteady flow in which the velocity of the flow field fluctuates chaotically as a function of both time and space [95], and arises explicitly as a consequence of fluid viscosity. The transition from laminar (steady) to turbulent flow occurs rapidly when the dimensionless Reynolds number of the flow (the ratio of inertial to viscous force) exceeds a critical value. The Reynolds number is calculated as

$$Re = \frac{\rho u L}{\mu} \tag{2.15}$$

where ρ is the fluid density, u the velocity of the fluid (relative to a nearby boundary such as a wall), L is the characteristic linear dimension of the flow (in meters) and μ is the dynamic viscosity of the fluid (units of $Pa\,s$). The dependence of the Reynolds number on L and the flow properties means that the value of Re_{crit} for a given flow will vary.

While turbulent flows are locally chaotic, the Kolmogorov hypothesis describes a generic structure for the turbulent flow field. Within the flow, the kinetic energy attributed to the turbulence is passed from eddies (regions of swirling and rotating flow) with the largest characteristic lengthscales down through progressively smaller eddies until it reaches the dissipative lengthscale at which inertial and viscous forces are balanced.

At this scale, the kinetic energy of the turbulence is dissipated thermally.

In practice, the eddies at the dissipative lengthscales are both very small and rotate very fast. Resolution of these eddies in time and space requires an exceptionally fine mesh and small timesteps and is extremely computationally expensive. This DNS (Direct Numerical Simulation) approach to the modelling of turbulence is therefore usually reserved for fundamental research into turbulence [95].

With respect to computation, Britan et al [68] also provide a relevant insight regarding the mesh scale. In the inviscid simulation, the flow downstream of the barrier changes considerably as the spatial resolution increases. This can be seen in Figure 2.7.

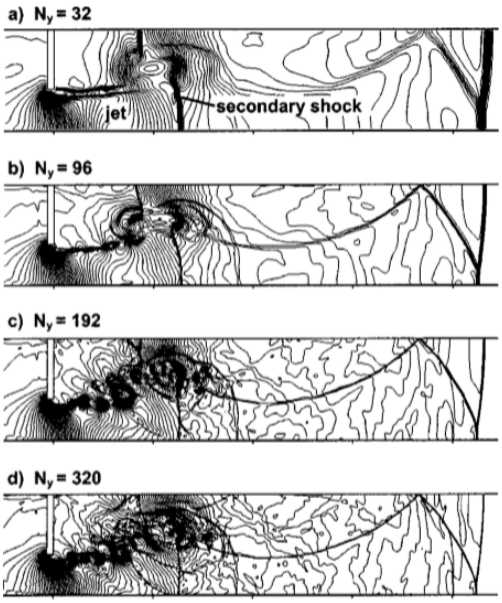

Figure 2.7: The increasingly complex downstream flow field as a property of increasing spatial resolution. In a) through d), the number of cells spanning the domain in the vertical axis is increasing, with a concomitant increase in the density of shed vortices

While this progressively increases the resolution of the shock-front and reduces the numerical smearing[1] present in lower-resolution meshes, the structure of the down-

[1]Broadening of the shock interface

stream flow varies indefinitely as a function of mesh density. Aside from the sharp increase in computational resources required to solve the problem (especially if expanded to 3-dimensions), achieving a flow state which is mesh-independent is critical to achieving consistent results.

An alternative to the DNS approach is to treat the chaotic nature of turbulence as a statistical phenomenon [95]. This is achieved through Reynolds averaging, by decomposing the flow velocity at a 3-dimensional point $\mathbf{x}$, $u(\mathbf{x},t)$, into a mean flow $\overline{u(\mathbf{x},t)}$ and a fluctuating component $u'(\mathbf{x},t)$, or:

$$u(\mathbf{x},t) = \overline{u(\mathbf{x},t)} + u'(\mathbf{x},t) \tag{2.16}$$

Substituting this value into the Navier Stokes equations yields the Reynolds-Averaged Navier Stokes equations or RANS. In RANS formulation, the momentum equation is now [81]

$$\frac{\partial \rho\overline{u_i}}{\partial t} + \nabla\cdot(\rho\overline{u_i}\overline{\mathbf{u}}) = \frac{\partial \overline{p}}{\partial x} + \mu\nabla\cdot(\nabla(\overline{\mathbf{u}})) - \rho\Big[\frac{\partial(\rho\overline{u'^2})}{\partial x} + \frac{\partial(\rho\overline{u'v'})}{\partial y} + \frac{\partial(\rho\overline{u'w'})}{\partial z}\Big] \tag{2.17}$$

In Equation 2.17, the viscous stress terms τ_{ij} in the original Navier-Stokes equations are now expressed as $\tau_{ij} = -\rho\overline{u_i'u_j'}$, where $\overline{u_i'u_j'}$ are the Reynolds stresses. To close the system of equations, a suitable relationship must be found for $\overline{u_i'u_j'}$. The approach for the RANS modelling of Newtonian fluids is to do this via the Boussinesq hypothesis (Equation 2.18), under which the viscous stresses are assumed to be proportional to the mean velocity gradients.

$$\tau_{ij} = -\rho\overline{u_i'u_j'} = \mu_t\left(\frac{\partial\bar{u}_i}{\partial x_j} + \frac{\partial\bar{u}_j}{\partial x_i}\right) - \frac{2}{3}\rho k\delta_{ij} \tag{2.18}$$

In Equation 2.18, two new terms are introduced; μ_t, the turbulent viscosity, and k, the turbulent kinetic energy. δ_{ij} is the Kronecker delta. These new terms allow closure of the Navier-Stokes equations and form the basis of the "2-equation" $k-\varepsilon$ and $k-\omega$ turbulence models. ε represents the dissipation rate of k, while ω represents the specific dissipation rate, analogous to the ratio of ε to k [95]. Both of these models are commonly applied to the simulation of turbulent flows and the $k-\varepsilon$ models are used extensively in the literature on the numerical simulation of perforated plates [68, 73, 79]. For both models, the production of turbulent kinetic energy (G_k) is

$$G_k = -\rho\overline{u_i' u_j'}\frac{\partial u_j}{\partial x_i} \tag{2.19}$$

which is evaluated in FLUENT [93] as

$$G_k = \mu_t S^2 \tag{2.20}$$

where S is the mean rate of strain tensor $\sqrt{2S_{ij}S_{ij}}$, and

$$S_{ij} = \frac{1}{2}\Big(\frac{\partial u_j}{\partial x_i} + \frac{\partial u_i}{\partial x_j}\Big). \tag{2.21}$$

For both models, μ_t is [95]

$$\mu_t = \frac{C_\mu k^2}{\varepsilon} \tag{2.22}$$

Where C_μ is a model constant. The above provides a means of calculating the two values k and μ_t required to close the RANS equations. Transport of k, ε and ω in this work is performed using the MUSCL scheme. Summaries of the $k-\varepsilon$ and $k-\omega$ models and their variants are given in Tables 2.2 and 2.3. Extensive discussion of the implementation of these models in FLUENT is not given here, but can be found at [90]. Here, descriptions are given to illustrate the salient differences between models. The models examined in this work are summarised in Tables 2.2 and 2.3.

Table 2.2: The $k-\varepsilon$ models examined in this work

Model	Notes
Standard	- The original $k-\varepsilon$ model of Launder and Spaulding [96]. - Assumes the flow is fully turbulent. The calculation of ε is fully empirical [90, 95]. - Noted to over-predict the spreading of round jets [95, 97], and is insensitive to the effects of adverse pressure gradient and the corresponding boundary layer separation [90]. - Inaccuracies arise from the underlying hypothesis to the calculation of μ_t and from the empirical nature of the ε equation [95]

Realisable	- Constrains the Reynolds stresses to physically "realisable" values, and applies a different formulation for the turbulent viscosity and ε calculations in an effort to correct the errors of the standard model. [93] - Derived from the exact equation for the transport of mean-square vorticity fluctuations. - Superior to the standard model for vorticity and rotation of flow.

Table 2.3: The $k-\omega$ models examined in this work

Model	Notes
$k-\omega$	The model of Wilcox [98]. Superior in the near-wall treatment, but produces erroneous results in the free-stream as ω is constrained to be non-zero. [95]
$k-\omega$ SST	- The Shear-Stress Transport (SST) model of Menter [99], which blends the $k-\varepsilon$ and $k-\omega$ models to overcome the free-stream issues with the original $k-\omega$ model. [95] - μ_t is calculated using a blending function which is reliant upon the distance to the nearest wall and allows transition from $k-\omega$ in the near-wall to $k-\varepsilon$ function in the free-stream. [93]

It should be noted that the flow-fields produced by the time-averaging approach of the RANS are entirely absent the structures present in "real" turbulent flows. The effects of turbulence on the flow are ersatz and entirely reproduced by the relevant transport equations. The application of the 2-equation RANS models in simulating the shock interaction with a rigid perforated plate has three purposes:

- To provide a means of reaching mesh convergence for the results of the simulation,
- To suppress the unphysical excess vorticity observed by Britan et al [68] in the inviscid case, and

- To simulate the turbulent mixing and associated momentum extraction identified by Berger et al [73] and Chaudhuri et al [79]

While it was previously noted that prior simulation work in this field utilises a 2-equation approach, these works universally apply a $k-\varepsilon$ based formulation. The simulation of flows through perforated plates in shock-tube like conditions is anticipated to involve a range of flows and turbulence conditions, with both free-stream and wall bounded effects present within the model. Given the identified issues with $k-\varepsilon$ and the original $k-\omega$ model then in this work the performance of several $k-\varepsilon$ and $k-\omega$ models are compared with respect to flow structure, pressure prediction and computational tractability,

Boundary Layers

The introduction of viscidity requires that the flow be treated with care at boundaries to the flow. Bounded flows are inescapable in the gas-dynamic work in this thesis; even if the edges of the shock channel are treated as outflows or symmetry conditions, the inside of the barrier apertures represent. To retain verisimilitude simulations must account for, at minimum, wall boundary effects in the aperture. Assuming a smooth, non-moving wall as a limit to the flow environment, at this boundary the flow velocity is constrained to be nil. Close to the wall (as a function of distance to the wall y), as the local flow velocity is low, the Reynolds stresses are low and viscous stress dominates; the flow in this region is correspondingly laminar. Away from the wall, the velocity of the flow grows logarithmically in accordance with Von Karman's law of the wall, eventually transitioning into the free stream velocity. The significant velocity gradients in the near-wall region are a major generator of turbulence. The total shear stress acting on the fluid is the sum of viscous stresses and the Reynolds stress, and their relative contribution to the flow in the near-wall region can be expressed in dimensionless units of viscous length y^+ [95],

$$y^+ = \frac{\rho u_\tau y}{\mu} \tag{2.23}$$

where $u_\tau = \sqrt{\tau_w/\rho}$ is the friction velocity, τ_w the wall shear stress and μ the dynamic viscosity. τ_w is given by

$$\tau_w = \frac{1}{2} C_f \rho u_f^2 \tag{2.24}$$

where u_f is the expected free-stream velocity and C_f is the skin friction. For flows with $Re < 1 \cdot 10^9$, the Prandtl-Schlichting skin friction formula can be applied [100] which is calculated as

$$C_f = 0.455[\log_{10}(Re)]^{-2.58} \tag{2.25}$$

where Re is the Reynolds number in the free stream. This permits scale-independent assessment of the boundary layer in units of y^+; in the region $y^+ < 5$, the Reynolds stress is negligible and the flow is fully laminar. Over the transitional domain $5 < y^+ < 30$, the influence of viscosity decreases while the Reynolds stresses become dominant. In the region $30 < y^+ < 200$, the log-law applies. Resolution of this boundary can be achieved in two ways:

- Full numerical resolution of the boundary layer; to resolve the boundary layer for $y^+ = 1$ at high (supersonic) velocity, the first cell height will be extremely small.
- Wall functions, which use the scale-independent nature of boundary layer flows to approximate to a real boundary structure.

To capture the boundary layer behaviour through either approach, the mesh of the domain must be appropriately constructed. An "inflation layer" in which the first cell height at the boundary lies within an appropriate y^+ range with logarithmic growth in height for subsequent cells is applied in the mesh at wall boundaries. To calculate the first-cell height at the wall to a desired y^+ value, Equation 2.23 can be re-arranged to yield

$$y = \frac{y^+ \mu}{\rho u_\tau} \tag{2.26}$$

In simulating a transient shockwave and the associated flow, there are two obstacles that must be overcome:

- For full resolution of the boundary layer in a time-explicit calculation, obeying the CFL stability criterion will impose an extremely small time-step.

- The velocity of the transient flow-field over the domain will vary in space and time; a near-wall mesh with a suitable y^+ structure at time t_0 may not be valid at a later time t_n, regardless of the use of either full boundary layer resolution or standard wall functions.

To address this, the "enhanced" wall treatment models present in FLUENT are applied when using the 2-equation turbulence models [101, 102]. Under this approach, for the $k-\varepsilon$ models the limit between boundary and free-stream flow is calculated continuously throughout the simulation on the basis of a height-dependent Reynolds number

$$Re_y = \frac{\rho h \sqrt{k}}{\mu} \tag{2.27}$$

where h is the distance to the nearest boundary. In the h domain yielding $Re_y > 200$, the turbulence is calculated by the $k-\varepsilon$ model. Below this, the wall model of Wolfshtein [103] is applied over the appropriate spatial domain, regardless of mesh structure. For the $k-\omega$ simulations, the boundary layer is modelled through a method in which the laminar and log-law regions are blended according to the model of Kader [104]. For both models, the intention of the enhanced wall treatments is to provide a y^+-insensitive formulation, although it is recommended [90] that the near-wall region still be modelled with an inflation layer spanning a minimum of 10 cells.

2.3 AUTODYN Modelling Techniques

AUTODYN is a time-explicit solver for multiphysics which admits the use of multiple solution techniques within the same simulation. Interaction between solvers is accomplished through various coupling techniques. While supporting a range of solver types (including Smooth Particle Hydrodynamics (SPH) and Arbitrary-Lagrange-Euler (ALE) techniques), the multi-physics sections of this thesis apply a combination of Eulerian and solid-element Lagrangian solution methods.

2.3.1 Time-stepping in AUTODYN

Time-stability in AUTODYN is a function of the CFL condition. For gas-solid interaction, the significant difference in sound-speed between the two phases will cause the

Table 2.4: Fundamental equations of continuity for the Lagrange processor

Conservation Law	Equation
Mass	$\rho = \frac{m}{V}$
Momentum	$\rho\frac{\partial x^2}{\partial^2 t} = \frac{\partial \sigma_{xx}}{\partial x} + \frac{\partial \sigma_{xy}}{\partial y} + \frac{\partial \sigma_{xz}}{\partial z}$
	$\rho\frac{\partial y^2}{\partial^2 t} = \frac{\partial \sigma_{yx}}{\partial x} + \frac{\partial \sigma_{yy}}{\partial y} + \frac{\partial \sigma_{yz}}{\partial z}$
	$\rho\frac{\partial z^2}{\partial^2 t} = \frac{\partial \sigma_{zx}}{\partial x} + \frac{\partial \sigma_{zy}}{\partial y} + \frac{\partial \sigma_{zz}}{\partial z}$
Energy	$\frac{\partial e}{\partial t} = \frac{1}{\rho}(\sigma_{xx}\dot{\varepsilon}_{xx} + \sigma_{yy}\dot{\varepsilon}_{yy} + \sigma_{zz}\dot{\varepsilon}_{zz} + 2\sigma_{xy}\dot{\varepsilon}_{xy} + 2\sigma_{yz}\dot{\varepsilon}_{yz} + 2\sigma_{zx}\dot{\varepsilon}_{zx})$
General equation of state	$p = f(\rho, e)$

simulation to run very slowly if a global timestep is shared between the Lagrangian and Eulerian solvers. This is addressed through the use of sub-stepping, in which the Lagrangian solver performs multiple solution steps over the course of one Euler timestep. By default, AUTODYN adjusts the global time-step throughout the progress of a simulation in response to the evolving dynamics of the system.

2.3.2 Lagrangian Methods

The Lagrangian approach requires that solutions be found for the movement and deformation of the mesh. A Lagrangian mesh element is defined by multiple nodes describing the vertices of the cell. The deformation and movement of the mesh is produced by the movement of individual cell nodes, the accelerations of which are solved through a force-balance equation. The Lagrange solver technique applied in AUTODYN is ultimately based on the work of Wilkins [105]. The equations solved by the Lagrange processor are shown in Table 2.4.

As material is not transported between cells, the conservation of mass is trivial and density is calculated as the total mass divided by the current cell volume. The momentum conservation equations relate the change in momentum to the applied forces; in the Lagrangian formulation, these are equivalent to the material stresses σ_{ij}, which can be expressed in compact form through the Cauchy stress tensor:

$$\sigma_{ij} = \begin{bmatrix} \sigma_{xx} & \sigma_{xy} & \sigma_{xz} \\ \sigma_{yx} & \sigma_{yy} & \sigma_{yz} \\ \sigma_{zx} & \sigma_{zy} & \sigma_{zz} \end{bmatrix} \tag{2.28}$$

In the energy equation, the strain ε_{ij} represents the displacement of a cell node from an initial starting position; the product of $\sigma_{ij}\varepsilon_{ij}$ therefore corresponds to the work done in moving the node against a given stress. It is intuitive that multiple reference points are required to properly reconstruct the stresses within a cell. An example of the two solid element node distributions that may be applied in the Lagrangian solver is given in Figure 2.8

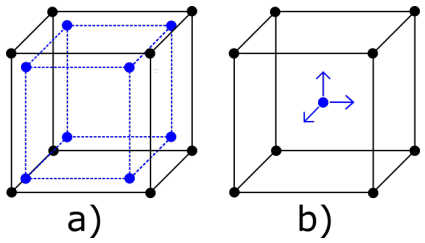

Figure 2.8: Two types of Lagrangian element. In a), one (blue) integration point is attached to each (black) node. In b), a single integration point is shared within the cell. It is clear from b) that a single integration point is only capable of calculating the hydrodynamic (normal) stresses; multiple integration points are required to properly capture the off-diagonal stress elements. If single integration points are used, the nodes defining the cell can deform without correctly dissipating energy, producing a characteristic "hourglassing" shape in the mesh. Throughout this thesis, all Lagrangian bodies are modelled as solid bodies with hexahedral eight-point integration cells.

Motion of the cell nodes is found through integration of the nodal accelerations; solutions are sought for the equation

$$\mathbf{Ma} + \mathbf{Cv} + \mathbf{Kx} - \mathbf{F} = 0 \tag{2.29}$$

where $\mathbf{a}$, $\mathbf{v}$, $\mathbf{x}$ are the vectors of (respectively) acceleration, velocity and displacement and $\mathbf{M}$, $\mathbf{C}$ and $\mathbf{K}$ are the associated matrices of mass, damping forces and stiffness. $\mathbf{F}$

represents externally applied loads. In the absence of damping forces, Equation 2.29 can be written as

$$\mathbf{Ma} = \mathbf{F} - \mathbf{Kx} \tag{2.30}$$

Defining $\mathbf{Kx} = \mathbf{I}$ where $\mathbf{I}$ represents the internal forces in the material. The internal forces are calculated from the displacement of the nodes from their position in the previous time-step. Solution for nodal accelerations is found by inverting the mass matrix. This is considerably faster than inverting the stiffness matrix; the stiffness matrix contains off-diagonal elements, while the mass matrix is a diagonal matrix containing only the scalar values of mass for each node. The acceleration is given by

$$\mathbf{a} = \mathbf{M}^{-1}(\mathbf{F} - \mathbf{I}) \tag{2.31}$$

On determining the accelerations, the new velocities and nodal displacements for the time-step can be found through time integration via a central difference scheme. The new stresses and strains are then calculated from the displacement. This is the time-explicit formulation of the Lagrangian solution method.

2.3.3 AUTODYN Euler Modelling

Unlike FLUENT, AUTODYN requires a structured mesh for the Euler domain. No turbulence transport equations are available in the calculation of fluid motion, and AUTODYN applies the inviscid Euler equations. Two distinct Euler solvers are available: The Flux-Corrected Transport (FCT) form of Boris and Book [106], and the Multi-Material Euler-Godunov form. Only gaseous materials with perfect-gas equations of state are permitted for use with the FCT-Euler solver, whereas the Multi-Material Euler-Godunov solver admits materials with strength models and variable equations of state. In this work, only the Multi-Material solver is applied.

The Multi-Material Scheme

The Multi-material Euler solver is based on the second-order accurate Godunov-type scheme for material transport as advanced by Van Leer [85]. The Lagrangian deformation stage described in Section 2.1.1 also permits the introduction of stresses into the Eulerian solution, which in turn allows solution of material models which require stress calculations.

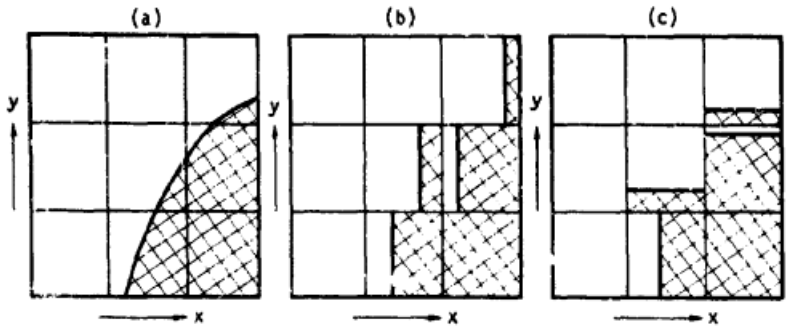

Figure 2.9: The SLIC method of interface reconstruction in 2 dimensions. The "true" fluid interface in a) is reconstructed from 1 dimensional topologies derived from sweeps in b) the x axis and c) the y axis. Taken from the work of Noh and Woodward. [107]

The presence of multiple materials within the same computational volume requires that the interface between materials be reconstructed within the cell. In AUTODYN, reconstruction of the material interface is performed with the Simple Line Interface Calculation (SLIC) of Noh and Woodward [107]. The method is shown in Figure 2.9.

2.3.4 Euler-Lagrange Coupling

To allow the Euler and Lagrange solvers to interact (and thus simulate the impact of gas and sand on a plate), AUTODYN applies the following technique; an Euler mesh is present throughout the entire computational domain. Bodies described with a Lagrangian mesh will therefore (either fully or partially) occupy some of the Euler cells. At the edge of the Lagrangian body, the exterior surface will only partially intersect an Eulerian volume. Stresses within the Euler cell will act over the intersecting Lagrangian face. This is shown in Figure 2.10. The process is reversible; if the motion of a Lagrangian mesh moves the surface into an Euler cell, the changing volume of the cell will produce stresses on the contents, driving the motion of material in the Euler mesh. However, if the volume of the Euler cell is reduced to a very small value, the CFL condition will require an extremely small global timestep.

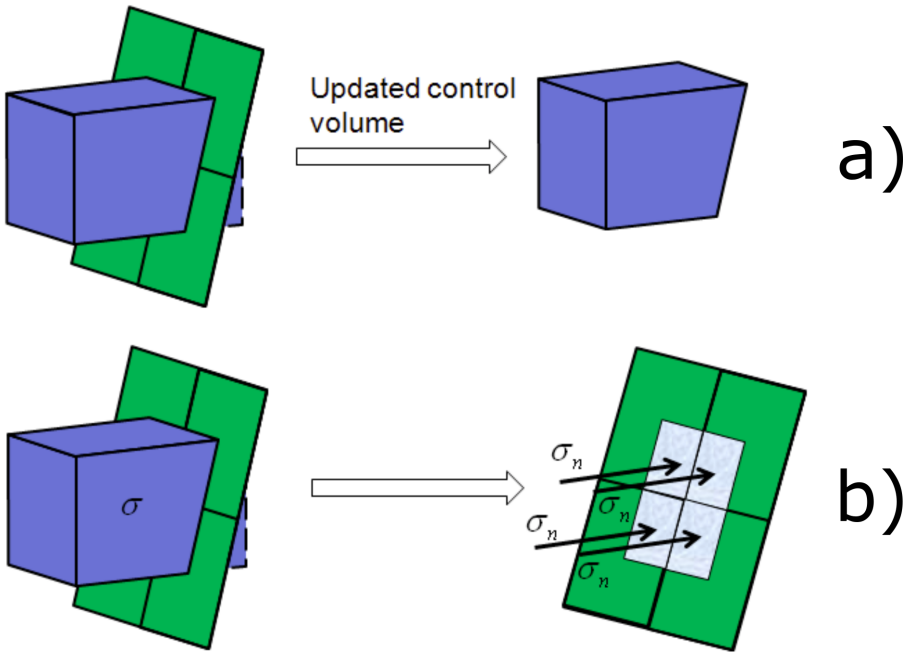

Figure 2.10: a) A Lagrangian (green) surface intersecting an Eulerian control volume (blue), with the consequences for the shape and volume of the Euler element and b) The normal stress forces exerted by a material in an Euler cell acting on the intersecting face of a Lagrangian surface. Taken from [108]

To counter this, Euler cells which are reduced beyond a set initial volume are merged with the nearest neighbour. In AUTODYN, this "cover-fraction" is set to half the initial cell volume by default, but can be altered [108].

2.3.5 Lagrange-Lagrange Coupling

Over the course of a simulation, if more than one Lagrangian body is present in the domain, then contact between the two bodies can occur. AUTODYN provides two principal methods by which collision between two Lagrangian bodies can be represented: the gap-contact method, and the trajectory-contact method. This work applies the trajectory-contact method with penalty forces. Under the trajectory-contact method, when two separate Lagrangian meshes meet and partially penetrate, forces are then applied to separate the two meshes. Under the penalty contact scheme, this penalty force is proportional to the penetration depth. The penalty force is Hookean, and is

calculated as

$$F_c = k_c x_{dp} \tag{2.32}$$

where k_c is a property analogous to spring stiffness (in this context known as the contact or penalty stiffness) and x_{dp} is the depth to which the surfaces are penetrated. Greater penetrations therefore produce greater penalty forces. While simple and computationally inexpensive, the force required to fully eliminate penetration cannot be known for any arbitrary contact condition. Alteration of the penalty stiffness such that the resultant force excessively separates the two bodies will result in unphysical oscillations as the two surfaces "bounce" back and forth until the dynamics driving the contact cease. If the penalty stiffness is too low, excessive penetration of the material interfaces will remain. To prevent unphysical oscillations, the penalty forces are set such that a small penetration remains at the end of the time-step. Subsequent time-steps will exert further (albeit proportionally smaller) forces to push the interfaces out of the penetration zone. This outcome, while preferable to unphysical oscillations, is still not perfectly physical, and is not fully conservative of kinetic energy given the requirement for multiple time-steps to converge on the correct contact position.

2.3.6 Stability Criteria

AUTODYN is time-explicit, and as such stability in time is ensured by obeying the CFL condition. However, certain other conditions can terminate a simulation early. While AUTODYN conserves mass and momentum, it has previously been established that certain calculation methodologies (such as the penalty contact interaction) do not fully obey the conservation of energy. AUTODYN therefore provides an assessment of the energy error, and is capable of terminating a simulation early if the energy error exceeds a pre-set value (5% by default). It is however possible to suspend termination and allow the simulation to run to completion. The energy error in AUTODYN is calculated as

$$E_{error} = \frac{E_c - E_r - W}{max(|E_c||E_r||E_k|)} \tag{2.33}$$

In Equation 2.33, E_c is the current energy (the sum of the current internal energy, kinetic energy and hourglassing energy). E_r is the reference energy, the value of the sum of the internal, kinetic and hourglassing energies at $t = 0$. E_k is the total kinetic

energy across the system. W represents the total work done within the system, and is calculated as

$$W = W_{cons} + W_{load} + W_{bf} + E_{erode} + W_{pen} \tag{2.34}$$

where W_{cons} is the work done by constraints imposed upon the system, W_{load} is the work done by loading conditions, W_{bf} is work performed by body forces, E_{erode} represents energy losses through erosion and W_{pen} is the work done by contact penalty forces (assuming the non-conservative penalty contact method is applied).

AUTODYN will also terminate early if the time-step becomes excessively small. This can be caused by Lagrangian elements decreasing in volume as elements deform (and thus reducing the global Courant number), or if excess material is transported into or from an Eulerian control volume. This is of particular importance in the modelling of blasts, as during the early phases of the detonation significant material transport between cells can occur.

2.4 Material Modelling

AUTODYN requires that materials in the simulation possess a constitutive mathematical model that describes their response to varying mechanical conditions. A successful material model will result in simulated bodies responding realistically to imposed loading. Material models are composed of several discrete parts, of which the core equations describe the following:

1. A strength and failure model, which describes the material response to stress and strain and specifies the conditions under which it will fail, and the manner in which it will do so. The relationship between stress and strain for a given material is typically derived experimentally, and parameters for a particular model formulation are derived. No single model is suitable for all materials, and AUTODYN contains common models for the simulation of a diverse range of substances.

2. An equation of state, which describes the relationship between pressure, density and energy.

Central to the failure of materials is the notion of the yield surface. Materials can fail due to a range of stress configurations, such as shear forces or tension. The yield surface describes a surface in the space defined by the stress tensor σ_{ij}. A material which contains a combination of stresses that reaches the yield surface will begin to experience plastic deformation, and may eventually fail completely. Materials with directionally-dependent responses to strain (such as sand) will possess a different yield surface to materials with an isotropic strain response (such as some metals). Specific material models are addressed in Chapter 5 alongside the relevant context of the simulations. With regards to the effects of detonation, two distinct approaches can be adopted in numerically simulating the effects of detonations on structural bodies:

1. Empirical blast loading
2. Full simulation of the detonation process

Under the first approach, the loading conditions applied to the body are derived from experimental analysis of real blasts; this is the approach adopted by tools such as CONWEP [11]. Under the second, the detonation process and associated loading is simulated directly, from the moment of detonation onwards. Within this category, two further distinctions can be drawn between empirical and theoretical approaches; theoretical models incorporate the chemistry of the detonation, while empirical models are derived from experimental data fitting. The Jones-Wilkins-Lee Equation of State (JWL-EOS) is a commonly applied empirical model for detonation. As applied in AUTODYN, it takes the form

$$p = A\Big(1 - \frac{\omega}{R_1 V}\Big)e^{-R_1 V} + B\Big(1 - \frac{\omega}{R_2 V}\Big)e^{-R_2 V} + \frac{\omega E}{V} \tag{2.35}$$

where A, B, R_1, R_2, ω are coefficients derived from experimentation. V is the ratio of expansion from the initial detonation product V_0 to a final state V_{final}. E is the energy released by the detonation per unit volume. JWL parameters for explosive material are derived from cylinder tests, in which the material is detonated within a copper cylinder. The motion of the cylinder wall is used to establish the expansion behaviour of the detonation [109]. Many of the explosive material models in AUTODYN are derived from the JWL-EOS testing work of Dobratz and Crawford at Lawrence Livermore National Laboratory [110]. In AUTODYN, the detonation reaction is initiated from a

point, with the detonation process spreading radially outwards through the material. The detonation reaction within a given cell can take two forms; either the full energy of the reaction is released instantaneously, or energy is released via a progressive "burning" of the material over multiple time-steps. The difference between the two approaches is phenomenologically akin to the difference between the Chapman-Jouget and ZND detonation models. In this work, the burn-over-time approach is applied in simulating the detonation process.

2.5 Simulation workflow

In this section, the generic workflow for the execution of a simulation in both FLUENT and AUTODYN is described. While the solvers are different, the process is conceptually the same:

1. Geometry definition:
    - AUTODYN and FLUENT: The geometry of the problem for both solvers is constructed in ANSYS SpaceClaim, a CAD tool for the preparation of simulation geometry.
2. Meshing:
    - FLUENT: Geometries for simulation in FLUENT are loaded into ANSYS meshing, a dedicated mesh creation GUI. Mesh sizing and construction type, inflation layers and boundary names (inlets, walls and outlets) are defined at this stage.
    - AUTODYN: Simulations for execution in AUTODYN are meshed in the ANSYS Explicit Dynamics environment. The Lagrangian mesh is specified by selecting the relevant body and applying a mesh size. The Eulerian mesh is defined at this point, either by specifying the total number of cells or the side length of the hexahedral elements. However, the Eulerian mesh is not generated at this stage, but at the time the simulation is imported into AUTODYN.

3. Pre-processing:

   - FLUENT: The completed mesh is loaded into the FLUENT preprocessor. Solution techniques and models, flow conditions, gauge locations and results output are selected here. The problem is then initialised, and ready to run.
   - AUTODYN: Simulations in AUTODYN are prepared in two stages; the ANSYS Explicit Dynamics environment is used to prepare the model. Material models, symmetry and boundary conditions, and detonation initiation points are assigned here. The completed set-up is then exported to the AUTODYN pre-processor, where measurement gauges, solver options and results output are set. The problem is then ready to run.

4. Solution:

   - FLUENT and AUTODYN: Solutions are either executed locally on the workstation used to create the simulation or submitted to ARC2, a HPC cluster at the University of Leeds.

5. Post-processing:

   - FLUENT: Output data files from the solution are opened in ANSYS CFD-Post for examination of the flow-field variables. Output files from pressure gauges are converted into comma-separated value (.csv) files in Excel.
   - AUTODYN: Postprocessing is performed within the AUTODYN GUI. Material status and location can be displayed and manipulated. Histories from the monitor gauges can be reviewed and saved as .csv files.

Chapter 3

Initial Shock Modelling

As noted in Chapter 1, previous work on the subject of the mitigating capabilities of perforated plates has seen frequent use of shock-tubes as a method of generating an air-blast surrogate. To investigate the mechanism of action by which a perforated plate mitigates shocks, a modelling methodology must be developed.

Flows in shock-tubes are internal flows, in the sense that they occur in a domain enclosed by walls. Even in the free-space case, a flow passing through the aperture of a plate will pass through a wall-bounded region. The consideration of wall boundary effects is therefore unavoidable. As noted in Chapters 1 and 2, the inviscid case produces non-physical results and so a suitable turbulence model must be determined. Selection of a methodology must also be made with respect to the sensitivity of a given approach to the mesh structure.

This chapter establishes a methodology for the simulation of shocks in partially obstructed channels. Validation of the flux transport and temporal discretisation schemes seen in Chapter 2 is accomplished by comparing the simulation of a 2-dimensional shock-tube environment to the 1 dimensional analytic solution for the Sod shock-tube problem. Comparison is made between a tetrahedral and triagonal mesh. An alternative means of shock generation to the full simulation of a shock-tube is presented. Turbulence models for the simulation of the flow through a partial obstruction are assessed on grids of varying resolution. The flow-field through a 2-dimensional double aperture is inspected.

3.1 Validation of flux models for shock simulation

To assess the MUSCL/AUSM flux transport and time-stepping models for their role in evaluating shock phenomena, a 2-dimensional shock-tube simulation was performed. Results for the density, internal energy, pressure and velocity across a shock moving with a velocity of Mach 1.5 were compared to the 1-dimensional analytic case.

3.1.1 Simulation setup

A 2-dimensional rectangular surface of length 500 mm and height 100 mm was defined in Spaceclaim Direct Modeller (SCDM). This surface is shown in Figure 3.1.

Figure 3.1: The 2-dimensional rectangular shock-tube

This surface was subdivided in ANSYS meshing into a regular mesh of quadrilateral cells 1 mm in length and height, containing 50000 elements in total. Initially an inviscid flow is considered, removing the need for a turbulence model, and no modification of the mesh at the boundaries of the flow is required. The structure of the mesh is displayed in Figure 3.2

A tetrahedral mesh of the same element side length is shown in Figure 3.3.

In comparing Figures 3.2 and 3.3, it can be seen that the cell interfaces in the quadrilateral mesh will be consistently parallel to the plane of shock-front moving from left to right, whereas the interfaces for the tetrahedral mesh will not. Complex geometry may be better captured through the use of triangular or tetrahedral elements, especially through circular apertures. It is therefore desirable to compare the performance of a quadrilateral square mesh against that of a tetrahedral mesh. An identical simulation is executed for a tetrahedral mesh with the same element side length, which generates a mesh of 104318 elements. In ANSYS Meshing, the limits of the domain are given identifying tags which identify them as particular boundary types such as walls, inlets and outlets. In this case, a symmetry boundary type is applied to the limits of the problem. The symmetry boundary type functions as a simplified stationary wall; no fluxes can transfer across the boundary, and the normal flux velocity and gradient at these boundaries are zero. The symmetry plane, as suggested by the name, is used in cases for which the problem is symmetric about the line described by the boundary.

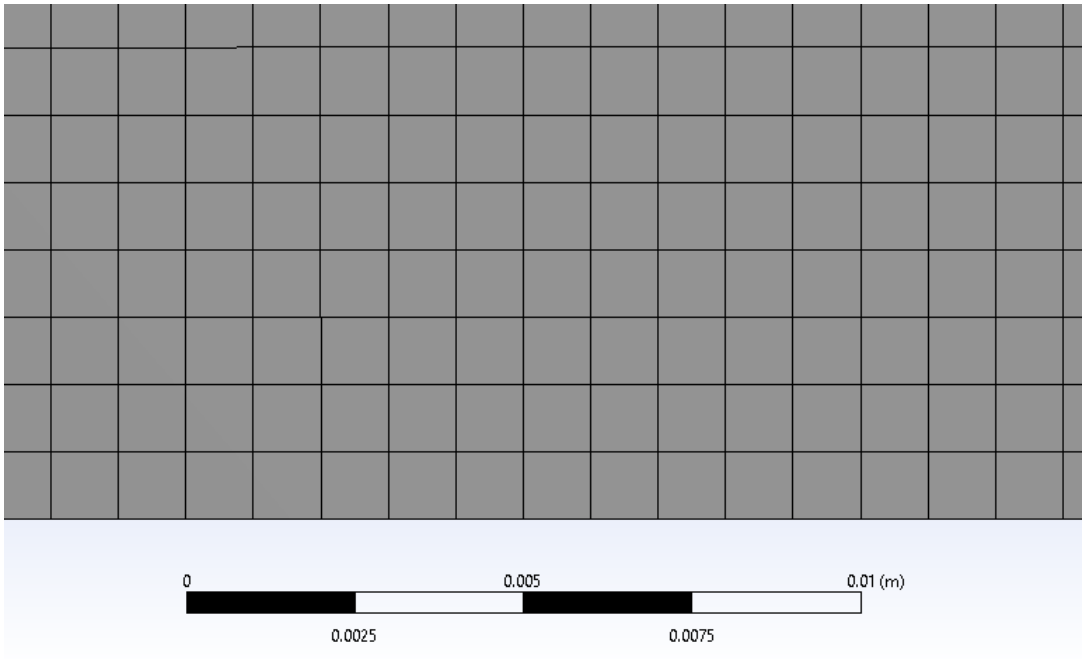

Figure 3.2: Regular quadrilateral mesh applied to the 2-dimensional shock-tube environment

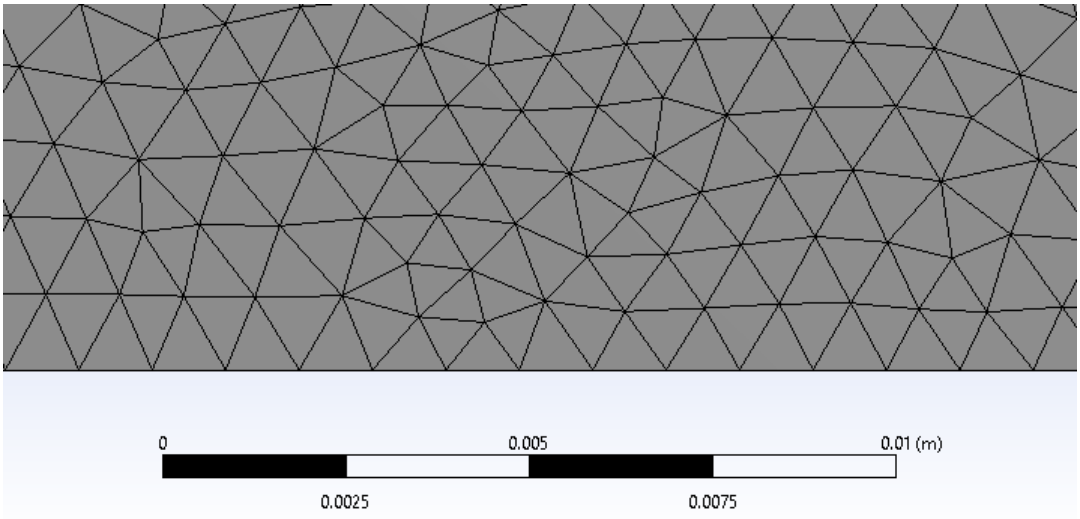

Figure 3.3: Unstructured tetrahedral mesh applied to the 2-dimensional shock-tube environment

Preprocessing

The mesh is imported into the FLUENT pre-processor. The first stage of preprocessing in FLUENT is to specify the solver type and time formulation; the applied solver is the density-based formulation and the time formulation is transient, as described in Section 2.2. The second stage is to define the models for turbulence and energy. Here, the fluid is modelled as inviscid, so no turbulence model is applied. As internal energy changes across the shocked and high pressure domains are anticipated, the energy equation described in Table 2.1 is applied.

The third stage requires that the material properties of the fluid(s) applied in the simulation be defined. A single species of gas (air) is used. For an inviscid gas simulation, FLUENT requires that the calculation method of 3 quantities be defined; the density, molecular weight and constant-pressure heat capacity C_p. Both C_p and molecular weight are taken as constant, where $C_p = 1006.43 J\,kg^{-1}$ and the molecular weight is $28.966 kg\,kmol^{-1}$. As this is a study of compressive flow, the compressible ideal gas equation of state described in Equation 2.10 is applied for the calculation of the flow density.

The fourth stage is to define the spatial and temporal methodologies to be applied in the solution. The scalar flux is calculated through the MUSCL scheme, while the convective flux is calculated through AUSM. Calculation of flux values at cell interfaces is performed using the Green-Gauss node based gradient evaluation method. The temporal formulation applied is a 4th-order Runge-Kutta explicit timestepping method with a user-specified time-step size. Details of the these solution schemes can be found in Chapter 2.

On definition of the solution methods, the solution may now be “initialised”, which applies the initial values across the domain and calculates the connectivity relationship between cells. No initial velocities are specified; the fluid in both driver and driven sections is static at $t = 0$. The temperature across the entire domain is initialised at 300 K. The gauge pressure is initialised at 0. The default ”operating pressure” in FLUENT is automatically defined as $101,325 Pa$. Variations in flow pressure (the “gauge pressure”) are defined relative to this value. On initialisation, the absolute pressure in the domain

(the sum of the operating pressure and gauge pressure) will also be $101,325Pa$. While seemingly trivial, this distinction is of significant importance in the following stage.

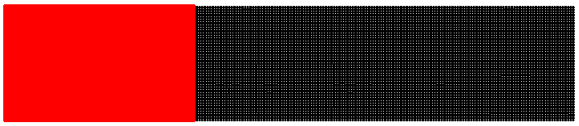

Figure 3.4: Cells marked (in red) for adaption to high pressure to create the initial conditions of the shock-tube

The entire domain now contains gas at constant pressure, temperature and density. To create the shock-tube driver section, the cells occupying the left of the domain up to 166 mm are added to a registry. The marked and unmarked cells are shown in Figure 3.4. These cells are then "patched", with the original pressure altered to a user-specified value. The pressure in the driver section can be calculated from the Rankine-Hugoniot jump equations by matching the pressure and velocity across the discontinuity [6]. The pressure calculation for the driver section (p_{driver}) is given in Equation 3.1

$$p_{driver} = p_{driven}\frac{2\gamma_{driven}M_s^2 - (\gamma_{driven}-1)}{\gamma_{driven}+1}\Big[1-\frac{(\gamma_{driver}-1)}{\gamma_{driven}+1}\frac{c_{driven}}{c_{driver}}\Big(M_s-\frac{1}{M_s}\Big)\Big]^{-\frac{2\gamma_{driver}}{\gamma_{driver}-1}} \tag{3.1}$$

where p_{driven} is the pressure of the driven gas (in this case, air at atmospheric pressure of $101,325Pa$) and γ_i is the ratio of specific heats. As both driver and driven sections are filled with air, this is a constant $\gamma = 1.402$. c_i is the speed of sound in the medium occupying the driven and driver sections ($c_1 = c_2 = 343ms^{-1}$) and M_s is the desired shock Mach number. A Mach number of $M = 1.5$ is selected. From Equation 3.1, the required driver section pressure is $710,421Pa$. The patch function in FLUENT can modify either the absolute pressure or the pressure relative to the operating pressure. To ensure that the correct pressure in this section is set, the patch function must either be set to alter the absolute pressure, or the operating pressure should first be subtracted from the intended absolute pressure. Under either approach, the gauge

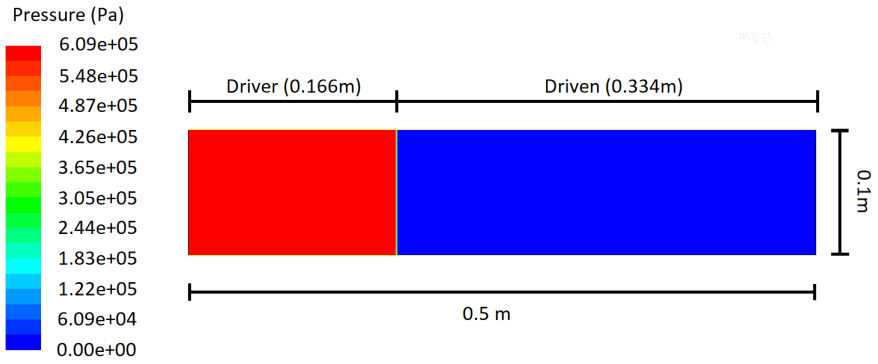

Figure 3.5: The initial pressure across the spatial domain for the 2-dimensional Sod shock-tube test

pressure in the driver zone will now register as $609,096Pa$. The pressure across the domain is shown in Figure 3.5. The temperature of the driver gas is the same as the driven gas, at $300\,K$

Output files are created to export simulation data for the density, x-velocity, internal energy and static pressure at intervals of 100 time-steps. As the grid and the velocity at which information is expected to propagate through the system are known, then a fixed time-step is applied. To obey the Courant stability criterion $C < 1$

$$C = \frac{(u+a)\Delta t}{\Delta x} \tag{3.2}$$

Then for the fixed, regular mesh where $\Delta x = 1mm$ and an anticipated maximum wave speed of $u = 521.2ms^{-1}$, the timestep applied must at maximum (for $C = 1$) be

$$\Delta t = \frac{\Delta x}{u} = 1.92 \cdot 10^{-6} \tag{3.3}$$

In practice, $C < 1$ is desirable to maintain stability in the unstructured tetrahedral mesh. Furthermore, a specific end-time across both simulations is required for the purposes of comparing the flow structure. The fixed time-step applied is 1×10^{-7}. The simulation is executed for 1500 such time-steps.

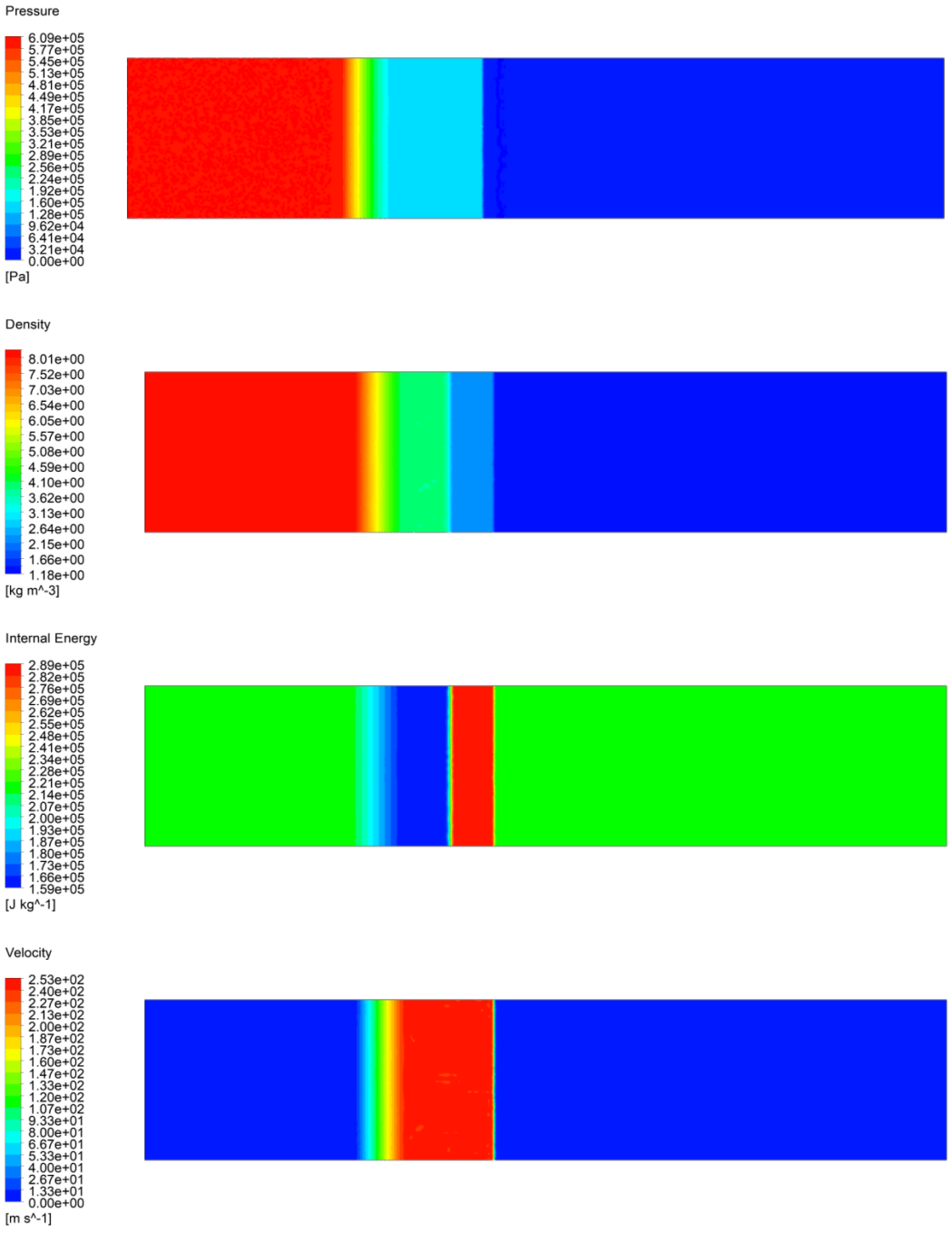

Figure 3.6: Distribution of pressure, density, velocity and internal energy across the 2-dimensional shock-tube domain at $t = 100\mu\,s$

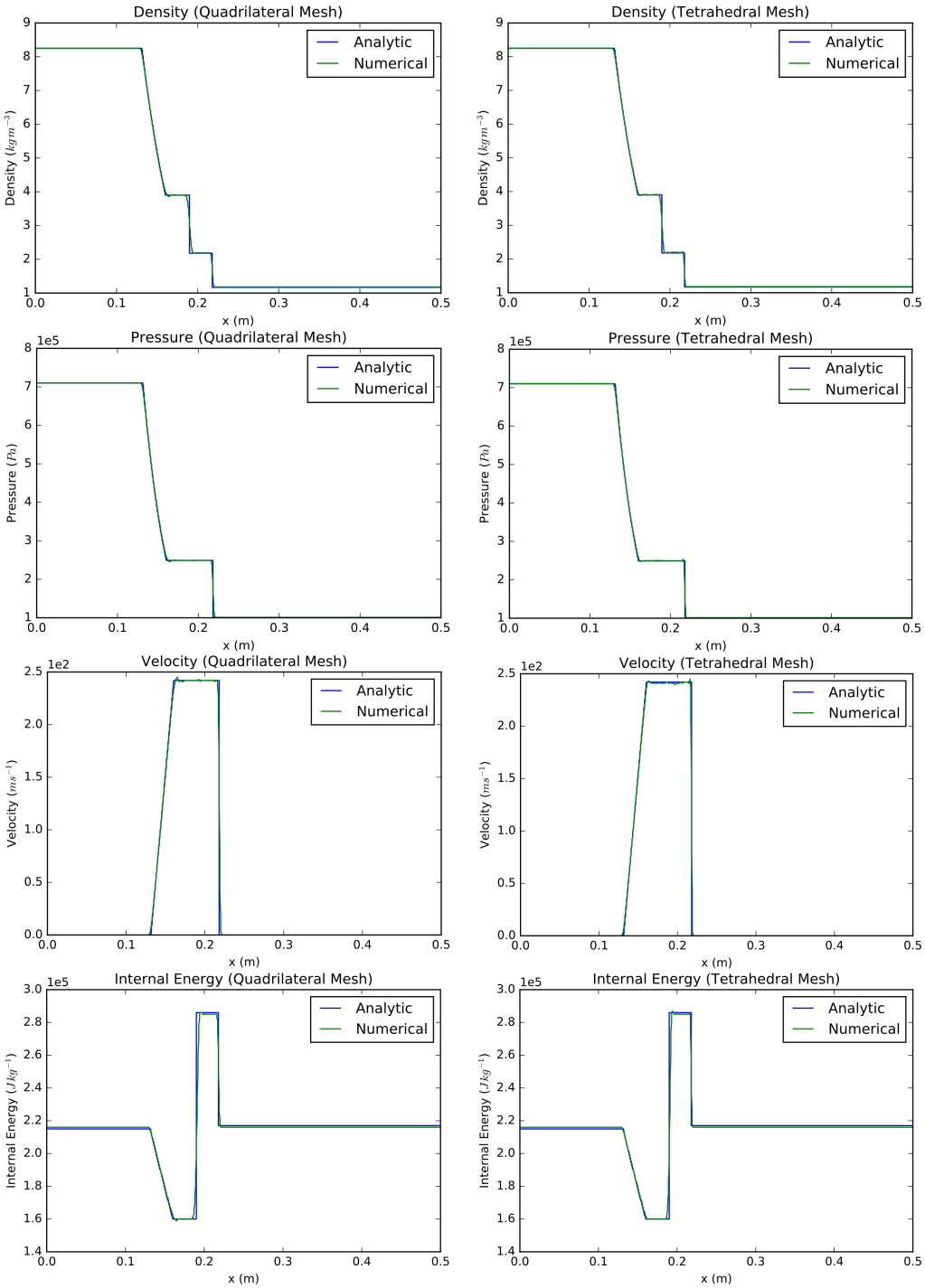

Figure 3.7: 1-dimensional $x-axis$ distributions of density, pressure, velocity and energy across the numerical simulation of the quadrilaterally and tetrahedrally meshed shock-tubes at 100 $\mu\, s$, with comparison to the analytic case.

Results

The development of the flow and the distribution of the values of pressure, density, velocity and internal energy at $t = 100\mu\, s$ is shown in Figure 3.6. The corresponding 1-dimensional x-axis distributions of p, ρ, u, E_{int} are shown for the quadrilaterally and tetrahedrally meshed shock-tubes in Figure 3.7, alongside comparison to the analytic solution. The data used to generate the plot-line for the analytic solution was generated from a 1-dimensional analytic shock-tube solver transcribed into Python by [111] and is based on an earlier FORTRAN solver written by Bruce Fryxell [112]. The source code is presented in Appendix B.

The numerical results for both the quadrilaterally and tetrahedrally meshed shock-tubes show excellent agreement with both the analytical result and with each other. The tetrahedral mesh demonstrates slightly superior performance in the presence of discontinuities, where a sharper gradient in the rise can be seen. This is attributed to the higher element count for the tetrahedral mesh yielding improved spatial resolution of these features. Minor over and undershoot are produced at discontinuities for both mesh types. These results indicate that the selected flux transport and time-stepping schemes are capable of providing accurate numerical approximations to a shock-tube on both regular and unstructured grids.

3.2 The inlet boundary condition approach

Section 3.1 establishes the performance of the MUSCL/AUSM flux transport approach for the simulation of shocks. However, the use of a cell-patched driver section requires that the computational domain be extended to incorporate the driver section. This requirement carries a cost as additional cells are used to model this feature, which in turn increases both the quantity of computer memory needed to hold cell variables and the number of calculations that must be performed in a time-step. While the simple 2-dimensional simulations performed so far will not tax the resources of a modern desktop computer, the incorporation of turbulence models and expansion of the problem to 3 dimensions will introduce significant penalties to the required memory and processor operations for a simulation. These penalties are sufficiently great that removing the driver section is desirable. In this Section, an inlet boundary-condition approach to the

generation of shocks is introduced and evaluated as an alternative methodology.

3.2.1 Simulation setup

In this simulation, a pressure-inlet boundary condition is applied to the problem of generating a shock of arbitrary Mach number in a shock-tube like environment. A similar approach applied in the MSC.Dytran solver can be seen in the work of Berger et al [73], although specific details regarding the generation of the shock are not given.

In generating a shock-front from an inlet boundary condition, a pressure condition at the inlet must be established. While the Friedlander model discussed in Chapter 1 is standard in blast defence, the model is based on the presumption that the detonation is occurring in free space. A pressure profile capable of generating a shock with equivalent structure to that of a shock driven by a driver-section must be found. It can be seen in Figure 3.7 that the pressure across the shock-front describes a step function. The aim is to generate a square pressure wave, which is accomplished by setting the inlet pressure to a constant value. However, in doing so, the dynamics of a driver section are lost; the position of the upstream high-pressure region is now spatially fixed at the inlet, and the structure of the flow will no longer be given by the conventional solution to the Riemann problem. To test the inlet-based approach, the 2-dimensional shock-tube environment used for validating the flux and time-stepping schemes is applied. The leftmost wall is now designated as an inlet, to which a short user-defined function (UDF) is applied. The user-defined function specifies the pressure condition at the inlet boundary. The pressure can be applied either as an absolute value or relative to the operating pressure. To establish the dependency of the generated Mach number on the inlet conditions, pressures of between 400 and 900 kPa (at intervals of 50 kPa) are applied for a duration of 100 μs. The pressure wave is ended by returning the pressure condition at the inlet to the pressure of the unshocked gas. As the pressure condition is defined as an absolute value, then past 100 μs, the pressure is set to immediately fall to 101,325 Pa. The applied UDF is defined below:

```
#include "udf.h"

DEFINE_PROFILE(inlet_pressure, t, i)
{
  face_t f;
```

```
  real time = CURRENT_TIME;

  begin_f_loop(f,t)
    {
      if (time <= 0.0001)
        F_PROFILE(f, t, i) = 520902.0;
      else if (time > 0.0001)
        F_PROFILE(f, t, i) = 101325.0;
    }
  end_f_loop(f,t)
}
```

Simulations with identical mesh sizing and solver methods to the case outlined in Section 3.1 are executed for the inlet boundary conditions described above.

3.2.2 Results

Figure 3.8 shows the downstream Mach number as a function of the inlet pressure. A non-linear dependency on the inlet pressure condition can be seen. The distribution is best fit to a logarithmic function[1]

$$M = 0.1602ln(p) - 0.474,\ R^2 = 0.998 \tag{3.4}$$

where M is the generated Mach number and p is the inlet pressure condition. A comparison is given to the Mach number that would be generated by a driver section of equivalent pressure. It can be seen that neither distribution is linear, although no attempt is made to explain the physical origin of the inlet boundary dependency. An example of the square pressure pulse generated by the inlet condition is shown in Figure 3.9, moving from left to right.

In performing later simulations, a constant shock value is selected. Britan et al apply shocks of $M = 1.46$ and 1.58 in their shock-tube studies [68], and indicate that there is no particular relationship between the strength of the incident shock and the relative downstream mitigation. While real detonations produce stronger shocks, for the purposes of comparison to experimental data a value that remains close to those

[1] Although it is not concluded that the analytic solution is a logarithmic function

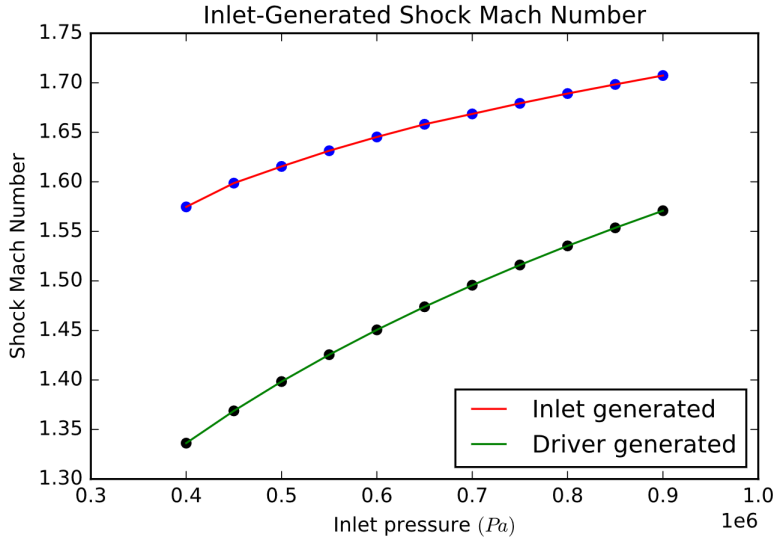

Figure 3.8: The variation in shock Mach number generated by varying the inlet pressure. The red line corresponds to the shock Mach number generated by the inlet condition, the green line to the Mach number generated by a driver section.

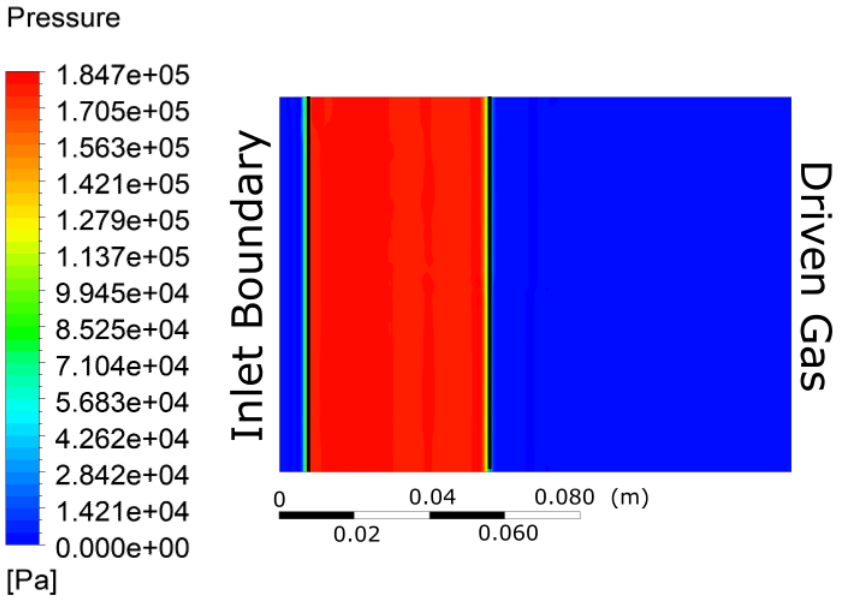

Figure 3.9: The pressure pulse generated by an applied inlet condition of at $t = 120\mu\, s$. The shock is followed by a square pressure pulse moving from left to right.

applied by Britan et al is sought. $M = 1.63$ is selected as the applied Mach number, a value 0.05 higher than applied by Britan. Applying the fit line in Equation 3.4 yields an inlet pressure of 520,902 Pa, which is applied in all future inlet-generated shock-tube studies.

3.3 Turbulence model selection

Methodologies for the generation and propagation of shock-waves moving within a shock-tube environment have been established in Sections 3.1 and 3.2. However, the simulations so far have been deliberately simplified with respect to fluid behaviour and geometric complexity. In this Section, the issues of turbulence modelling and mesh dependence are addressed. The standard and realisable $k-\varepsilon$ models and the standard and shear-stress transport $k-\omega$ models described in Chapter 2 are assessed for stability and mesh-sensitivity in the context of a partially-obstructed 2-dimensional shock-tube.

Flow environment

To ensure consistency, an identical geometry is applied for each simulation. The domain is $64mm$ in length, and 32 mm in height. These dimensions are selected on the basis of the work previously performed by Britan et al, who performed their work in shock-tubes of 32mm by 32mm cross-section [68]. A narrow obstruction of length $4mm$ and height $19.2mm$ is introduced 20 mm downstream from a pressure inlet as defined in the previous section. An annotated display of the domain is shown in Figure 3.10.

The pressure inlet condition is set at the leftmost limit of the domain; a pressure outlet is defined at the rightmost limit. This permits the flow to exit the domain, allowing the shedding of vortices and development of an expected jet-type flow through the gap without interference from the reflected shock.

Meshing

These simulations examine several RANS models with regards to mesh sensitivity. For each RANS model, 3 cell sizes are applied: $1mm$, $0.5mm$ and $0.25mm$. Each reduction in cell scale yields a fourfold increase in spatial resolution in a quadrahedral mesh. The

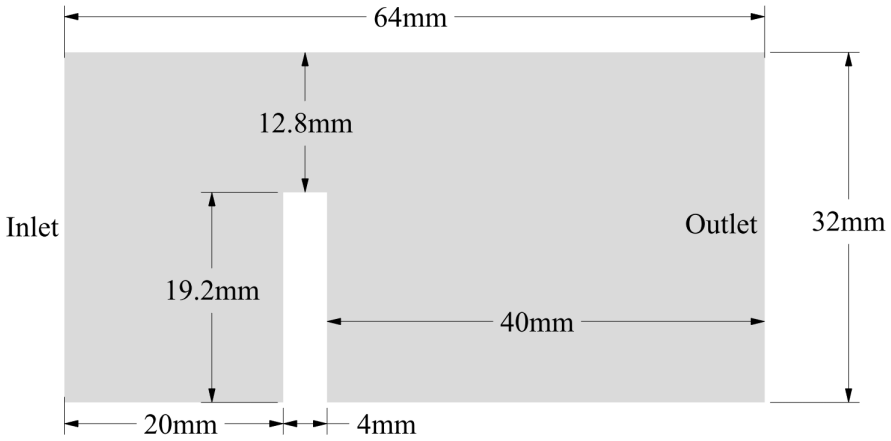

Figure 3.10: Geometry of the domain applied in the examination of turbulence models

introduction of fluid viscosity requires that turbulence and boundary effects be taken into account. For both the $k-\varepsilon$ and $k-\omega$ models, the respective enhanced wall treatment functions as described in Chapter 2 are activated. As per the recommendation of the FLUENT manual [93], an inflation layer of first-layer thickness $1.5 \times 10^{-5} m$ is applied at the walls, growing in thickness at a rate of 1.2 over 10 cell layers. This is derived from Equations 2.24, 2.25 and 2.26 for a $y^+_{max} = 30$ for air at a maximum free-stream velocity of $600 ms^{-1}$ (as determined from initial testing) with density $1.21 kg\, m^{-3}$ and dynamic viscosity $1.81e^{-5} kg\, ms^{-1}$.

3.3.1 Additional solver settings

The inclusion of a turbulence model requires that the viscosity of the fluid be included in the calculation. For an ideal gas, the viscosity is calculated in FLUENT using the kinetic theory model [93]

$$\mu = 2.67 \cdot 10^{-6} \frac{\sqrt{M_w T}}{\sigma^2 \Omega_\mu} \tag{3.5}$$

where μ is the viscosity, M_w is the product of the molar mass of the gas M and the gas constant R, T is the temperature in Kelvin, σ is the cross-sectional collision radius of the spherical gas molecule and Ω_μ is a function of T^* where

$$T^* = \frac{T}{\epsilon / k_B} \tag{3.6}$$

where k_B is the Boltzmann constant and ϵ is the depth of the Lennard-Jones potential well that governs inter-particle interaction in the gas. σ and ϵ/k_B are collectively defined in FLUENT as the Lennard-Jones parameters and are supplied for a given fluid by the FLUENT material library.

3.3.2 Measurement

To investigate the effects of mesh sensitivity, convergence[1] of the pressure downstream of the barrier is sought. A pressure monitor is established downstream of the barrier at 44mm, in the form of a line which reports the average pressure acting over it. The purpose of this approach is made clear in Figure 3.11, in which a curved shock-front can be seen as it emerges from the aperture. If the shape or pressure of this shock-front is affected by the turbulence model or the mesh, this will be reflected in the variation in average downstream pressure.

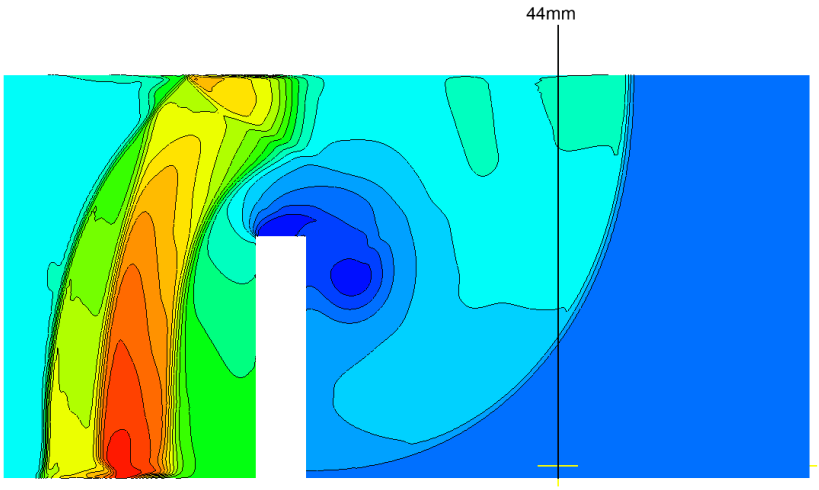

Figure 3.11: Location of the downstream pressure monitor and the curved shock-front that passes through the aperture.

As the flow is now anticipated to vary in velocity throughout the simulation, program-controlled time-stepping is applied to yield the highest possible Δt for any given time-step. The Courant number is limited to a safety factor of 0.9; FLUENT then calculates a global time-step that does not breach this condition. The variable

[1] In which the measured value does not change past a certain mesh scale

time-step also allows assessment of the computational efficiency of each model; a more efficient model will reach a later flow-time in a fixed number of time-steps. To maintain equivalence, the different turbulence models are run on identical meshes. The state of the flow is saved at intervals of 100 time-steps; the total time that the flow has progressed in 15000 time-steps is then used to compare the speed and efficiency of the models.

3.3.3 Results

As the time-step is program-controlled, output files are saved at slightly varying times across models. The state of the flow across the models at approximately 86 μs is displayed in Figure 3.12. The section of the shockfront that strikes the obstacle has reflected, and is visible as a high-pressure region to the left of the barrier. The section of the shock which encounters no impediment has transmitted through the gap and expanded into a curved shock-front. A low density region at the lip of the aperture is visible in all cases. The plots of vorticity in Figure 3.12 indicate that these low density regions correspond to a shed vortex from the aperture lip.

The transmitted shock produced by the standard $k-\omega$ model is highly deformed in comparison to those of the other models, although the structure of the reflected shock is consonant with the predictions of the other models. A delayed separation of the flow from the barrier can be seen in the vorticity plot wherein the detachment of the vortex occurs towards the rear of the aperture lip. These observations, taken in the context of the known weakness of the standard $k-\omega$ model in resolving turbulence in the free-stream, indicate that the structure of the transmitted shock is strongly influenced by the turbulence of the upstream flow. In particular, the retardation of the progress of the shock-front in the region directly behind the barrier is a consequence of the manner in which the shed vortex is pulled closer to the rear of the barrier. By contrast, the standard and realisable $k-\varepsilon$ and $k-\omega$ SST models predict flow separation near to the front of the barrier and display comparable transmitted shock-front structures. The density and vorticity plots of the realisable $k-\varepsilon$ and $k-\omega$ SST models are highly similar with respect both to the downstream structure of the shock and the vortex

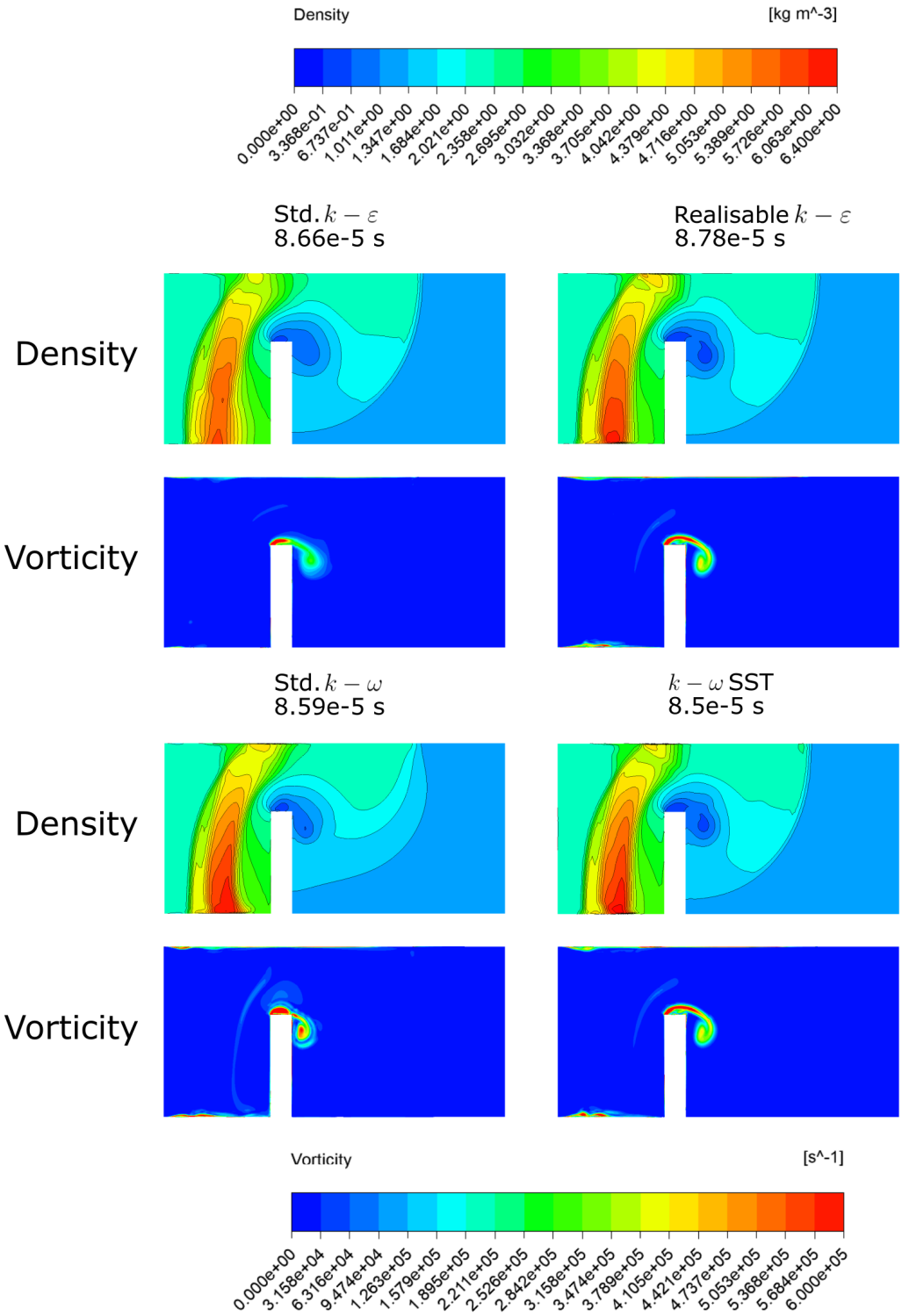

Figure 3.12: Plots of density and vorticity across the turbulence models. Across all images, the scale of density and vorticity is constant, and corresponds to the legends.

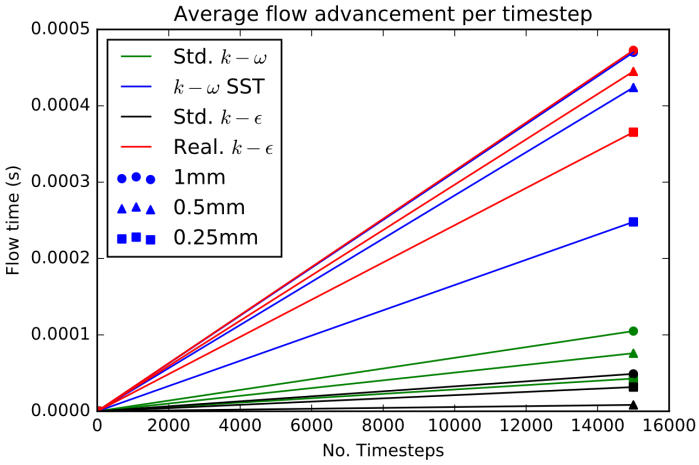

Figure 3.13: Maximum flow-time reached over 15000 time-steps per model and mesh sizing. The realisable $k-\varepsilon$ and $k-\omega$ SST models significantly outperform their standard counterparts.

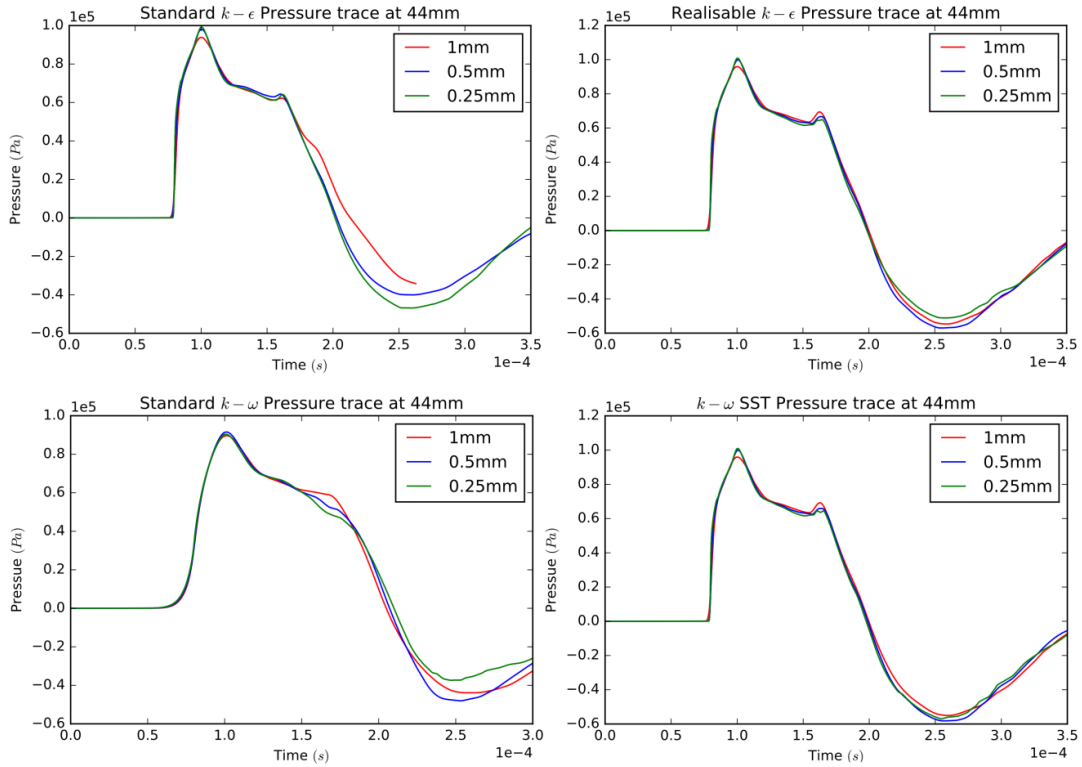

Figure 3.14: Pressure traces for varying turbulence models and mesh resolutions at the monitoring line.

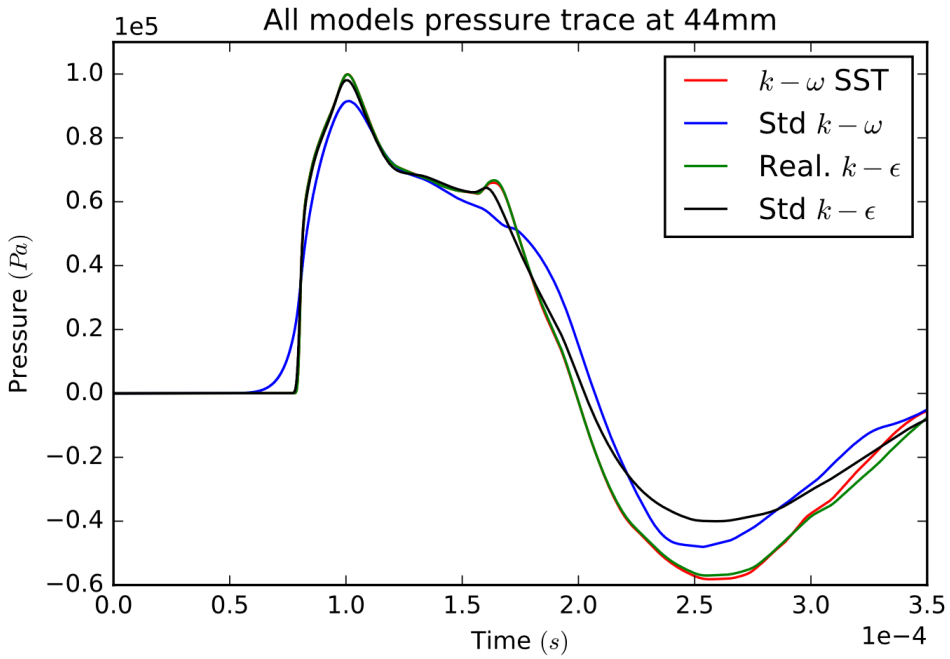

Figure 3.15: Comparison of pressure traces over all models (0.5mm mesh sizing). The traces produced by the realisable $k-\varepsilon$ and $k-\omega$ SST models are indistinguishable until $2.5 \cdot 10^{-4}s$. The standard $k-\omega$ and $k-\varepsilon$ models show greater deviation, and slightly under-predict the peak pressure

formation. A similar vortex can be seen for the standard $k-\varepsilon$ model, although the magnitude of the vorticity and the detail of the structure are significantly attenuated. The realisable $k-\varepsilon$ and standard/SST $k-\omega$ models also indicate the presence of vorticity in the regions at which the reflected shock meets the channel walls. This is attributed to the onset of a flow bifurcation caused by the boundary layer flowing in the opposite direction to the transit of the reflected shock; the pressure behind the reflected shock creates an adverse pressure gradient that separates the boundary layer flow from the surface. This feature is barely discernible in the standard $k-\varepsilon$ prediction.

The relative computational efficiency of each turbulence model is shown in Figure 3.13. Both the realisable $k-\varepsilon$ and $k-\omega$ SST models show clear superiority in computational tractability (even at the highest spatial resolutions) when compared to the original $k-\varepsilon$ and $k-\omega$ models. Interestingly, the standard $k-\varepsilon$ model exhibits greater computational tractability at the 0.25mm mesh scale than at 0.5mm, although it is less efficient than all other models.

The pressure traces across mesh scales are shown for their respective models in Figure 3.14. Convergence of the peak pressure is seen in all models at the 0.5mm mesh, although the prediction of the standard $k-\omega$ model is lower than that of the other models, a consequence of the deformation of the transmitted shock. Full convergence of the whole pressure trace is only seen in the $k-\omega$ SST model. A comparison of the predicted pressure between models for the 0.5mm mesh is shown in Figure 3.15.

The results show that the realisable $k-\varepsilon$ and $k-\omega$ SST models perform extremely well from a computational perspective, and provide near identical predictions of both flow features and pressure measurements. A 0.5mm mesh with wall inflation layer provides full convergence of the $k-\omega$ SST model, and accordingly both are selected for use in later simulations.

3.4 A dual aperture flow-field

In Section 3.3, the flow downstream of a single aperture was examined. Vortex shedding from the lip of a barrier was observed. In this Section, the barrier is now modified to create two apertures. While perforated plates (and certain related values such as D_h) are innately 3-dimensional, an increase in the number of apertures functions as a 2-dimensional corollary to an increasing hydraulic ratio. However, distinctions cannot be made between different aperture shapes, such as circles and rectangles. Only a brief study of the 2-dimensional case is made, to examine the structure of the downstream flow close to the barrier. The $k-\omega$ SST turbulence model and shock generation techniques used in the previous sections are now applied on a triagonal mesh of side-length $5\times10^{-4}m$ to the case of a dual aperture of total porosity $\varepsilon=0.4$.

3.4.1 Results

The flow through the apertures is shown in Figures 3.16 and 3.17 in the form of velocity vectors. To demonstrate the turbulence present in the shed vortices, the turbulent intensity of the flow is shown in the same images as a contour plot. The turbulent intensity is a measure of the ratio of turbulent velocity fluctuations $u^{'}$ to the mean flow velocity u_{avg}, or

$$I = \frac{u^{'}}{u_{avg}}. \tag{3.7}$$

where I is the turbulent intensity. A value of I above 10% is considered to be high [80]; the peak turbulence intensity shown in Figure 3.16 is approximately 50%, and 60% in Figure 3.17. The regions of peak turbulence intensity correspond to the shed vortices.

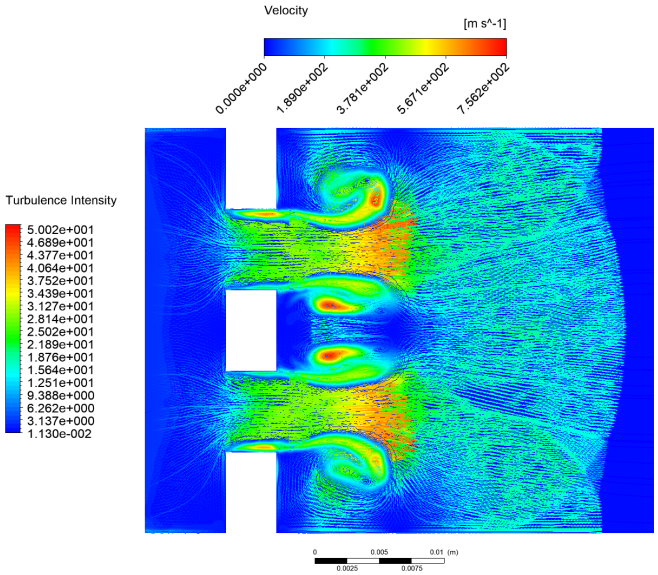

Figure 3.16: The flow-field through a dual aperture configuration at $t = 9.16 \cdot 10^{-5}s$ after flow initiation. The domain is truncated to show the flow-field at the apertures in greater detail. Velocity vectors are overlaid over a contour plot of the turbulent intensity I as defined in Equation 3.7.

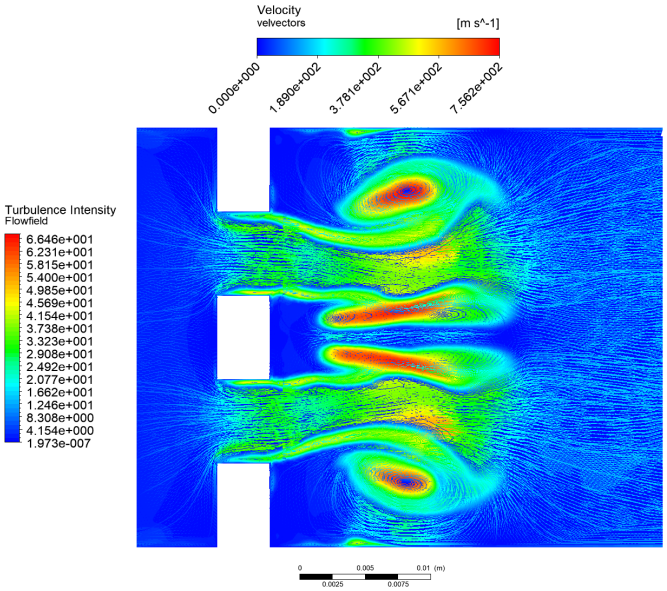

Figure 3.17: The flow-field through a dual aperture configuration at $t = 1.48 \cdot 10^{-4} s$ after flow initiation. Elongation of the central vortices can be clearly seen. The jet flow is curved by the vortex interactions.

In Figures 3.16 and 3.17, an increase in the 2-dimensional approximation to the hydraulic ratio is demonstrated to produce additional vortices. The jet stream from the barrier is constrained by these vortices and pinched, causing the jet flow to accelerate. The complex interaction between vortex and jet flow also causes the path of the jets to diverge from one another. The results confirm that the flow-field downstream of the barrier is highly turbulent.

3.5 Concluding remarks

In this Chapter, a methodology for the generation of shocks in a shock-tube environment has been demonstrated. A combination of the MUSCL and AUSM schemes as outlined in Chapter 2 yields good agreement with an exact solution to the Sod shock-tube problem on 2-dimensional meshes of both quadrilateral and triagonal elements. A pressure-inlet method of generating a shockfront and the associated dependence of the shock Mach number on the inlet pressure has been presented. Several two-equation

turbulence models are compared to determine the optimal model for the simulation of a shock striking a partial obstruction in an enclosed channel. The $k-\omega$ SST model with a y^+ insensitive boundary treatment is selected on the basis of superior mesh convergence, near-wall treatment and computation time. Mesh sensitivity for a flow with the dimensions of future work has been investigated. A grid sizing of $0.5mm$ with a 10 layer thick inflation layer of first layer thickness $1.5 \cdot 10^{-5}m$ produces full convergence of the flow pressure and consistent results across turbulence models. A brief study is made of the effects of increasing the number of apertures in a barrier of fixed porosity. Increased shedding of turbulent vortices and consequences for the downstream flow structure as a factor of vortex interaction are observed.

Chapter 4

3D Modelling of Perforated Plate Shock Interaction

This Chapter presents the numerical simulations performed in FLUENT for 3-dimensional perforated barriers in which the effects of barrier flexibility are removed. The simulation methodology is explored and developed in Chapter 3. Two distinct simulation groups are presented:

- In the first, the "long-separation" case, the rear-wall of the shock-tube is placed at a distance greater than $x/D_h = 10$. A perforated plate in a defensive role is intended in part to minimise the pressure acting on the surface it protects. The mitigation of the peak measured overpressure downstream of the barrier, and the reduction in peak pressure acting on the rear-wall of the tube are taken as measures of protection.
- In the second, the "short-separation" case, the separation between the perforated plate which provides the greatest shock mitigation and the rear-wall is reduced significantly. The intent is to place the rear-wall in the region close to the barrier in which the jet-flow is dominant. A novel flow-divertor concept designed with the intention of preventing flow stagnation and peak shock reflection pressure is compared to the case of a flat rear-wall.

The findings of this research were presented at a meeting with members of the crew survivability and simulation teams at BAE Systems, and are currently under publication embargo. The draft paper presented at this meeting was co-authored with Dr Julian Pittard of The University of Leeds.

4.1 Simulation Set-up

3-dimensional models were developed in ANSYS SCDM for solution in FLUENT. 5 plate designs are selected to cover a range of hydraulic ratios and aperture shapes. These are presented in Figure 4.1. A summary of the apertures is given in Table 4.1. The geometry is constructed in Spaceclaim Direct Modeller, meshed in ANSYS Meshing and preprocessed using the FLUENT preprocessor GUI. The user-defined function approach developed in Chapter 3 is applied to generate an initial shock of strength $M = 1.63$. Solutions apply the $k-\omega$ SST model with enhanced wall treatment for the calculation of turbulence and the MUSCL/AUSM scheme for flux transport. Automatic RK4 time-stepping is applied to ensure the Courant stability criterion is not breached while allowing the simulation to proceed at the highest possible speed.

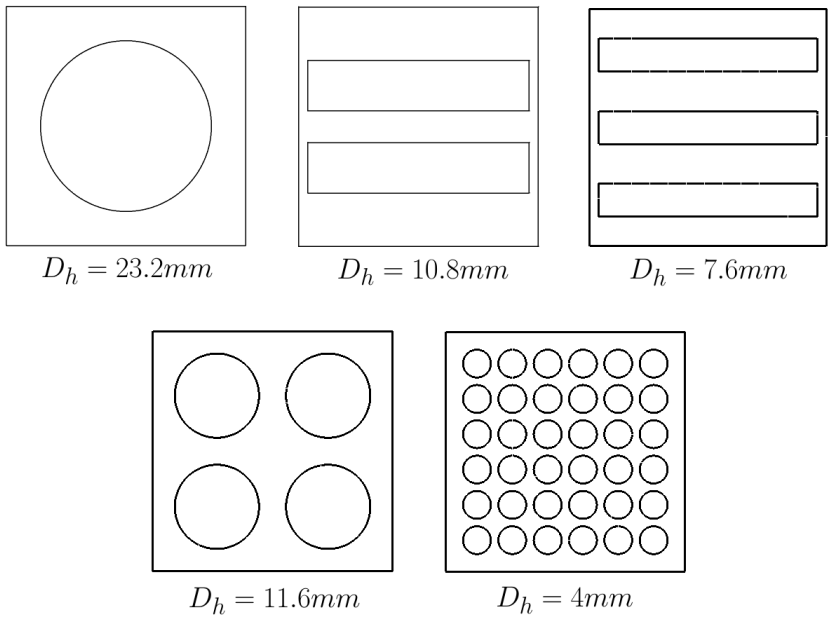

Figure 4.1: End-on view of the barrier designs and their respective hydraulic ratios

Table 4.1: A summary of aperture structure, hydraulic ratio and porosity for the plate designs used in the simulations

No. Apertures	Type	D_h (mm)	Porosity ε
1	Circular	23.2	0.4
2	Rectangular	10.8	0.4
3	Rectangular	7.6	0.4
4	Circular	11.6	0.4
36	Circular	4	0.4

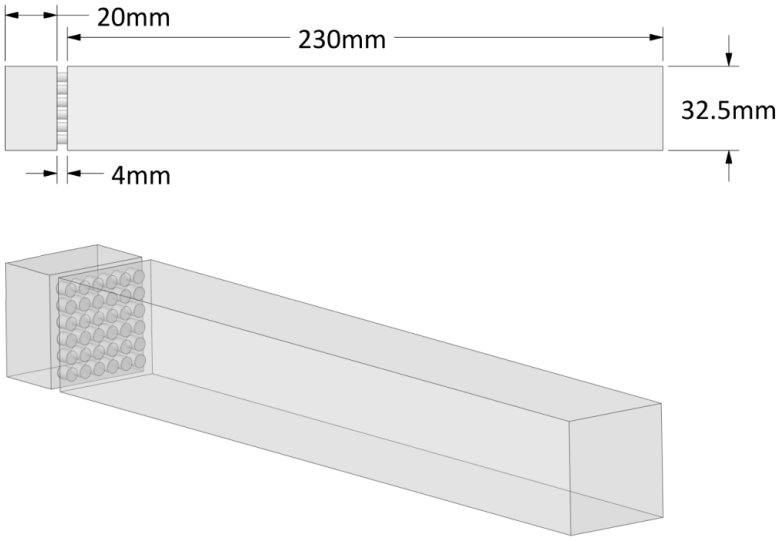

Figure 4.2: Dimensions of the long-separation simulation, and an isometric view of the 36 circular aperture shocktube

4.2 Long-Separation Case

In the long-separation case, the length of the geometry of the shock-tube downstream of the barrier is 231 mm long. This ensures that, for the plates with the highest hydraulic ratios, a downstream value of $\frac{x}{D_h} = 10$ can still be achieved in order to examine the anticipated drop-off in additional mitigation after $\frac{x}{D_h} > 7$ observed in the work of Britan et al [113]. The height and width of the shock-tube is 32.5mm. The design of the domain is shown in Figure 4.2.

As per the mesh sensitivity investigated in Chapter 3, the domain is meshed using an unstructured tetrahedral mesh limited to a maximum cell side length of $5 \cdot 10^{-4}m$ with an inflation layer applied to the walls of first-layer thickness $1.5 \cdot 10^{-5}$, growing in thickness at a rate of 1.2 times the previous layer thickness for a total of 10 layers. Each simulation contains approximately 4.1 million control volumes. This inflation layer is applied to each interior surface, including the interior of the apertures. Pressure measurements are taken as area-averages over planes that transect the computational domain orthogonal to the direction of the flow. These planes are placed at both numerical intervals of $\frac{x}{D_h}$ (which vary in their spatial separation depending on

the hydraulic ratio of the plate) and at fixed intervals of 20 mm. This planar approach to the measurement of downstream pressure, as opposed to the use of point sensors is especially helpful in capturing the bulk pressure behaviour of the flow in the immediate vicinity of the rear of the barrier, where the flow structure is highly irregular.

4.2.1 Simulation execution

On completion of pre-processing, simulations are uploaded to the ARC2 HPC cluster. Output files are saved every 1000 time-steps for future postprocessing and examination of the changing state of the flow. Simulations are advanced for 2ms of flow time, corresponding to the typical loading time over which a real plate subjected to a buried charge detonation will reach maximum velocity, as indicated by Bouamoul et al [22]. Between 100,000-120,000 time-steps are required in total. Each simulation takes approximately 2 weeks to run to completion on 16 computational cores.

4.2.2 Results

Flow Structure

The density of the transient flow for the $D_h = 10.8mm$ (dual-rectangle) aperture case is presented in Figure 4.3 for the period shortly after the emergence of the shock-front from the barrier through to the return of the reflected shock-front. In the initial time-frame shown at $145\mu s$, the shock has recently emerged from the barrier and is beginning to travel down the length of the shock-tube. The jet flow from the barrier is maintained throughout the full transit of the shock. The reflected shock encounters the jet flow and the structure of the discontinuity is disrupted. The same behaviour can be seen in Figure 4.4, although the particular flow features differ. The progression of the flow is similar to that observed in 4.3; a jet flow from the barrier apertures is formed, although the structure of the flow is considerably different, and reaches homogeneity over a shorter distance than in Figure 4.3. In Figure 4.4, the reflected primary shock from the rear wall encounters the high density region arising from the jet flow from $767\mu s$ onwards.

The development of the high speed jet close to the barrier into a homogeneous high speed flow can be seen in Figure 4.5.

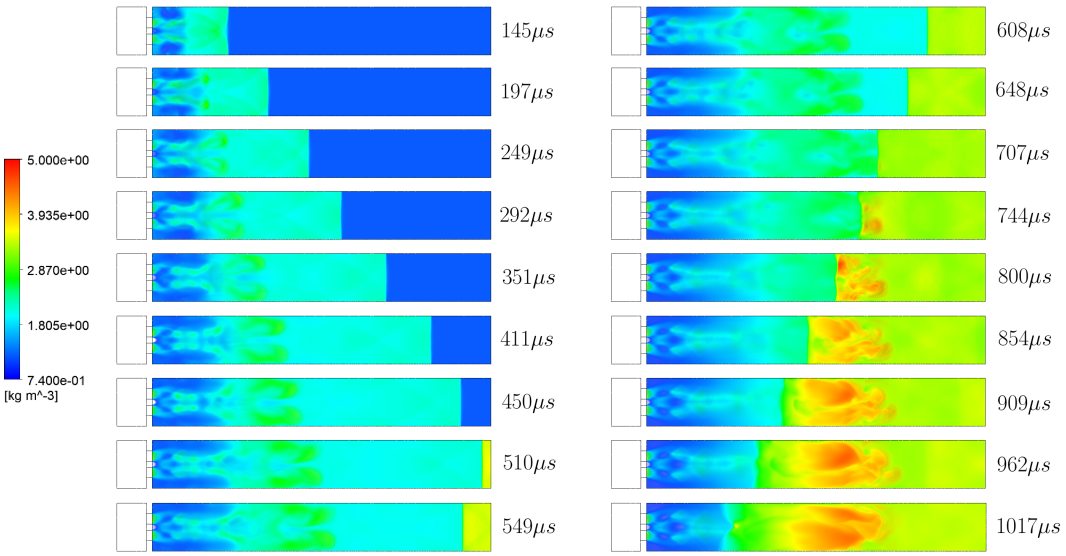

Figure 4.3: Side view of the mid-plane flow density downstream of the barrier for the $D_h = 10.8mm$ dual aperture simulation. The colour scale is fixed across each time period and is scaled to show the major details of the flow. The region in the pre-barrier domain is excluded from the visualisation to allow for this scaling. The jet stream emerging from the barrier can be seen at all times. The initial jet abruptly transitions into a high density region that spans the entire tube; as the shock-front moves downstream, the length of the primary jet can be seen to increase. As the shock reflects and returns towards the barrier, it encounters the jet flow from the aperture, which can be seen from 806 μs onwards to disrupt the planar front and create an irregular flow in the post-shock region. While initially difficult to discern in the higher-density region, this encounter indicates that the irregular flow due to the jet continues for a considerable downstream distance.

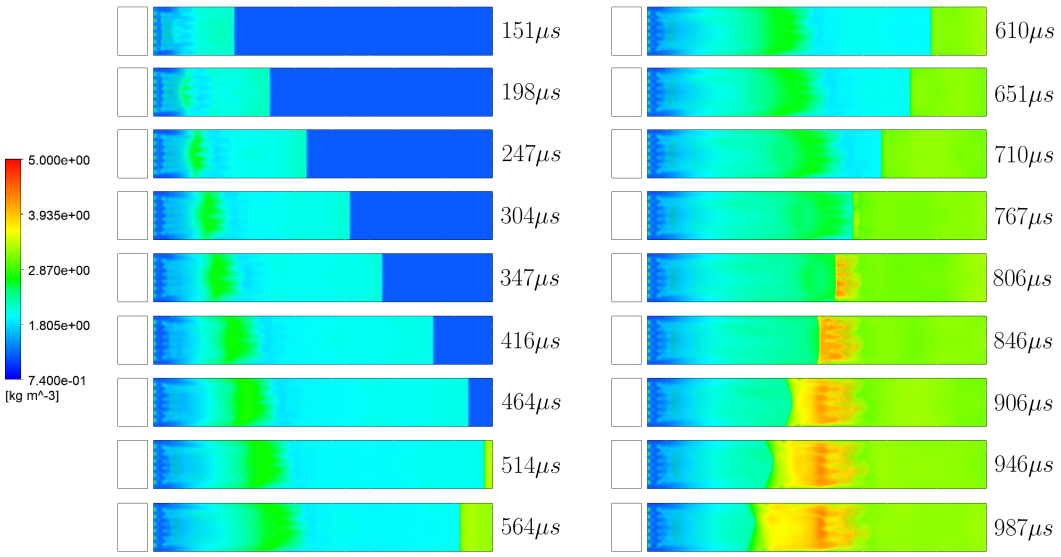

Figure 4.4: Side view of the mid-plane flow density downstream of the barrier for the $D_h = 4mm$ (36 circular) aperture simulation. As in Figure 4.3, a jet-flow can be seen emerging from the perforations. The structure of the jet flow is considerably different; the presence of multiple smaller jets in close proximity acts to keep the flow through the central apertures on a consistent trajectory, and the flow reaches the transition to the higher density region over a shorter distance than in Figure 4.3. As in Figure 4.3, the encounter between the reflected shock and the jet-flow from 806 $\mu\, s$ onwards shows that the downstream flow retains an irregular structure for a considerable distance downstream, although the later time of this encounter demonstrates that the irregular flow-field does not extend as far. The shock is disrupted by this flow and the initially sharp discontinuity becomes smeared

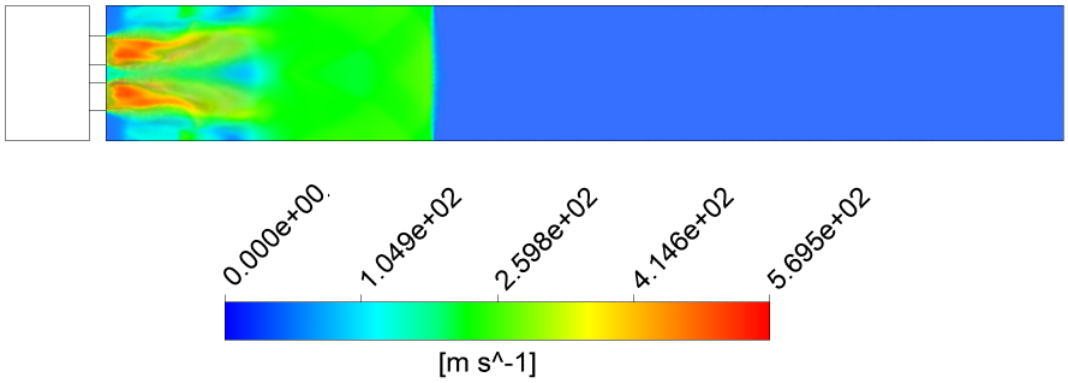

Figure 4.5: Side view of the velocity magnitude downstream of the barrier for the dual-aperture case at 249 μs. The jet flow from the barrier can be seen to bifurcate in the same manner as the 2-dimensional case explored in Chapter 3.

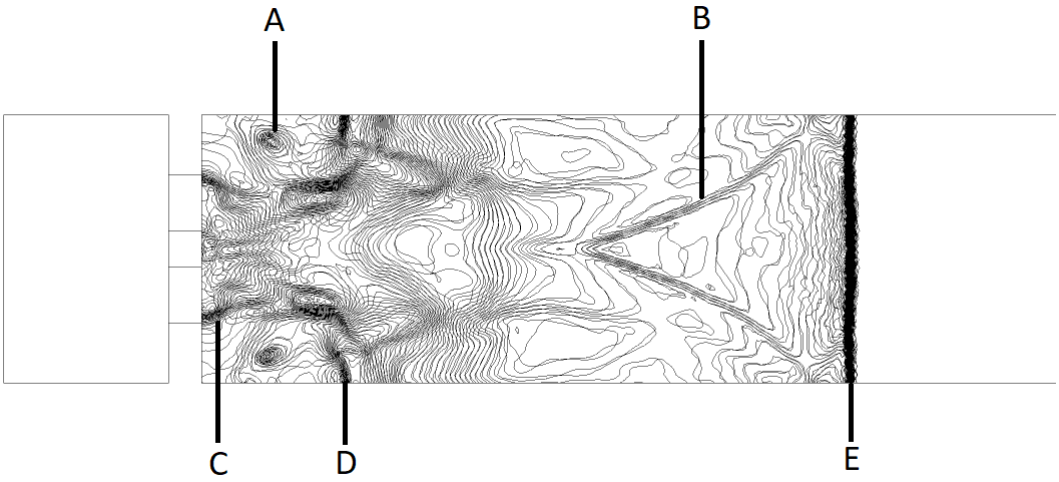

Figure 4.6: Black and white contours of density for the post-barrier flow at the shock-tube external wall at 197μs. A is one of two symmetrical vortices formed in the region next to the jet flow at the aperture. B is a secondary shock reflected from the wall as the incident shock expanded on passing through the aperture, and describes a Mach stem. C marks the separation of the flow from the barrier and defines the initial edge of the jet-stream. D is a secondary shock travelling backwards towards the barrier, and E is the main planar shock-front. The shock-front is visibly smeared over several cells.

Figure 4.6 shows the flow density in this region in isopycnic form, which better displays the structure of the shock past the barrier. The flow displayed in Figure 4.6 is the flow at the wall of the shock-tube, propagating left to right. The reflection of the vertical components of the transmitted shock can be seen, alongside the complex structure of the jet flow.

Shock mitigation

The attenuation of the shock downstream of the barrier is defined as

$$k = \frac{\Delta p}{\Delta p_i} \tag{4.1}$$

where Δp is the initial pressure jump measured downstream of the barrier and Δp_i is the pressure jump across the incident shockwave prior to the barrier. k for the full range of plates studied in this work is shown as a function of dimensionless x/D_h in Figure 4.7, and downstream distance in Figure 4.8. It is shown in these Figures that the peak overpressure is sharply attenuated in the immediate post-barrier region, but rapidly climbs further downstream. This is followed by a steady decline in shock intensity, reaching a minimum for all designs at the greatest downstream distance. There is extensive variation in the mitigation as a factor of barrier design, with the $D_h = 4mm$ (36 circular aperture) structure significantly outperforming the other designs in terms of overall mitigation over the full distance of the post-barrier domain.

In comparison to the experimental results displayed in Figure 1.21, both show an initial rise in shock intensity in the immediate post-barrier region, although the shock intensity predictions of the numerical results are considerably greater. When examining the mitigation over downstream distance, all designs show a similar mitigation behaviour; an initial reduction in the pressure is followed by a rapid increase to a maximum pressure, reaching a plateau of this value and then decreasing with further downstream distance. While the progress of the pressure reduction over distance is seen to be initially disordered with regards to plate design, at the maximum downstream distance the mitigation of the shock broadly corresponds to a decreasing hydraulic ratio of the plate. However, if the particular aperture designs (circular or rectangular) are considered, the mitigation at the maximum distance is fully ordered on the basis of hydraulic ratio.

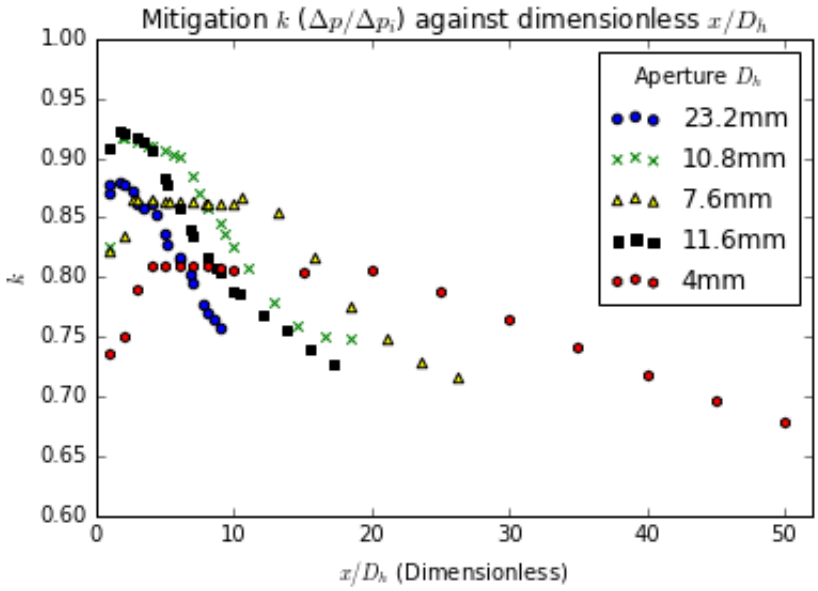

Figure 4.7: Plot of k against dimensionless $\frac{x}{D_h}$ for the various apertures considered.

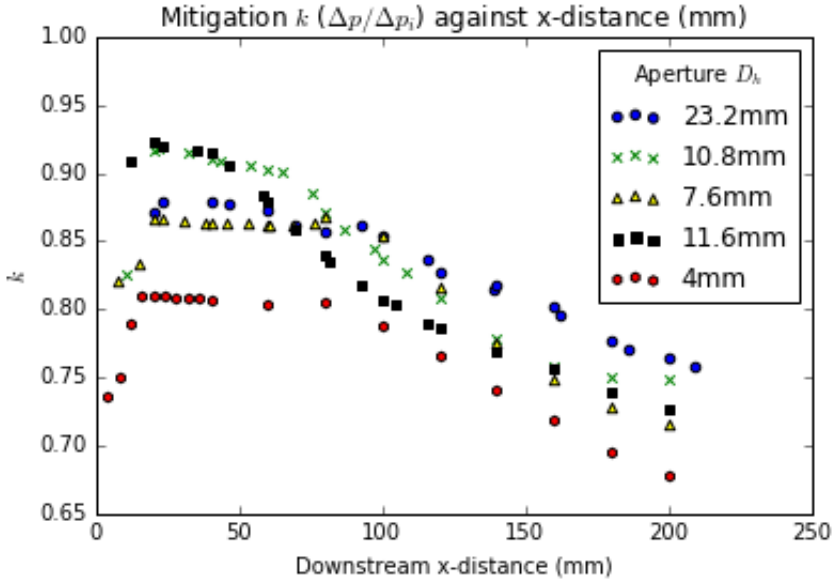

Figure 4.8: Plot of k against downstream distance (mm) for the various apertures considered.

The rectangular aperture with a higher hydraulic ratio provides less mitigation than the rectangular apertures with a smaller mitigation. The same is true for the circular apertures. In Figure 1.21, after reaching a peak k, the majority of plate designs also display a subsequent drop in pressure (and corresponding decrease in k) with increasing x/D_h, although this drop is less visibly pronounced when compared to Figures 4.7 and 4.8.

The origins of this behaviour are seen explicitly on the plots of flow overpressure presented on the left hand side of Figure 4.9, in which the overpressure representing the shock-front and associated shocked region are presented as a time series for the 36 aperture barrier. The attenuation shown for this barrier in Figure 4.7 has a plateau between $x/D_h = 4$ and $x/D_h = 20$, and these regions are marked in Figure 4.9 for the values of downstream x that correspond to $x/D_h = 4$ (the region over which k increases), the plateau region extending to $x/D_h = 20$, and the region between this and $x/D_h = 30$ over which the initial decrease in k is seen. In the $x/D_h < 4$ volume at $76\mu s$, the flow is highly irregular, a condition which continues within the region for all later times but from $164\mu s$ - $198\mu s$, the flow downstream of this point between $x/_{Dh} = 4$ until 20 can be seen to abruptly transition, becoming consistent in velocity and representing a highly pressurised region which follows the shock and is sustained by the jet stream from the barrier. However, at $198\mu s$, it is possible, on the right hand side of Figure 4.9, to see the high velocity volume of gas in the wake of the shock-front begin to detatch from the jet flow. By $246\mu s$, where the shock-front is now past the plateau observed in Figure 4.7, this separation has become more pronounced with a corresponding drop in the post-shockfront pressure, a situation that continues throughout the remaining time-steps, with both the post-shock pressure and the velocity of the gas volume driving the front declining.

The fractional reduction in pressure (compared to an unprotected surface) acting on the rear wall of the shocktube is shown for the blue line in Figure 4.10, wherein the peak overpressure for lower hydraulic ratio designs is 8% lower than for the design with the highest hydraulic ratio. The peak rear-wall over-pressure for an unobstructed shock-tube with identical inlet, boundary and calculation methods is 612,855 Pa, while the peak over-pressure for the protected cases ranges between 362,017 and 413,973 Pa,

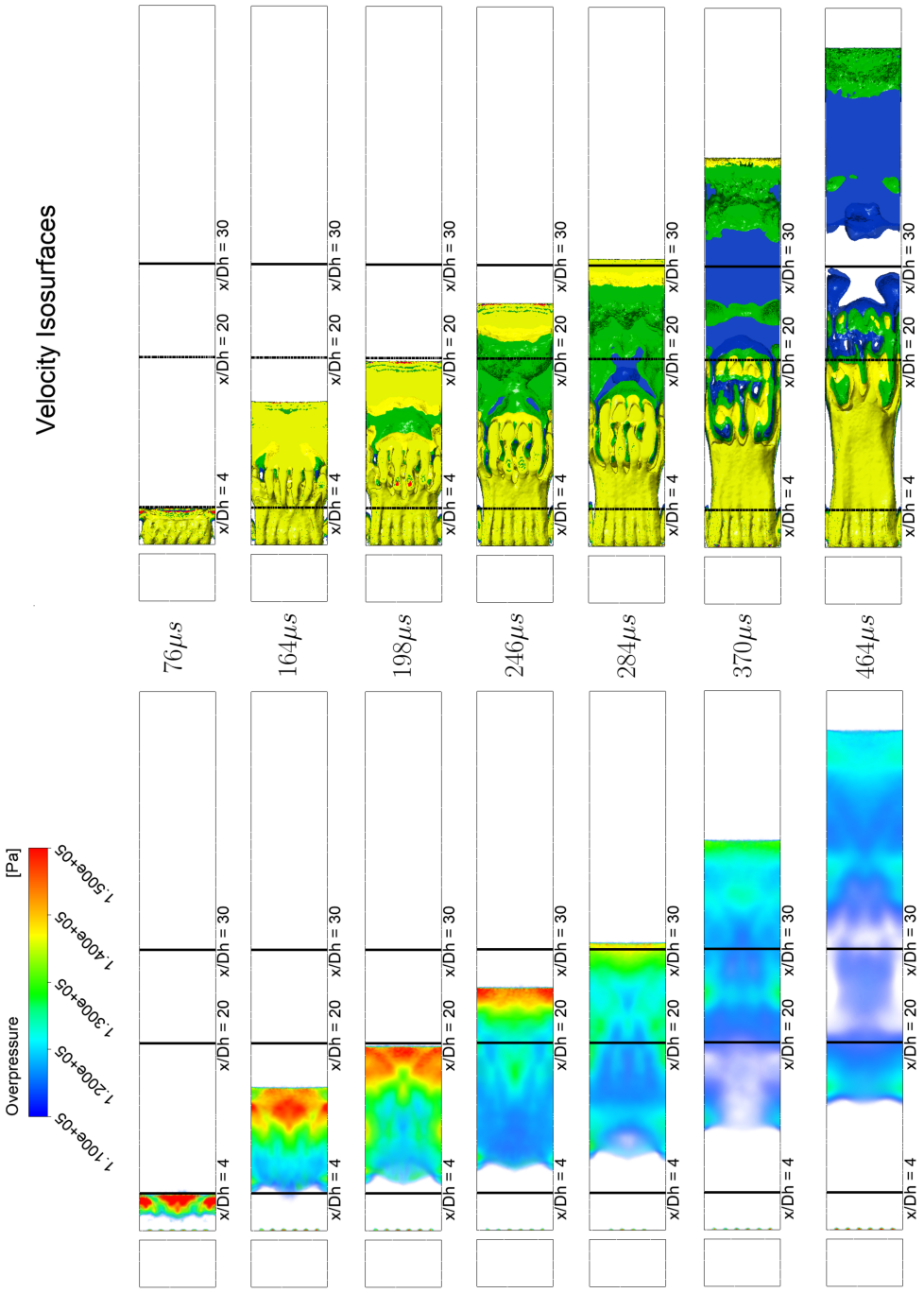

Figure 4.9: Volumetric render of overpressure (relative to pressure of unshocked gas) development over time downstream of the $D_h = 4mm$ 36-aperture barrier, with associated isosurfaces of velocity corresponding to 200 (blue), 210 (green), 220 (yellow) and 230 (red) meters per second.

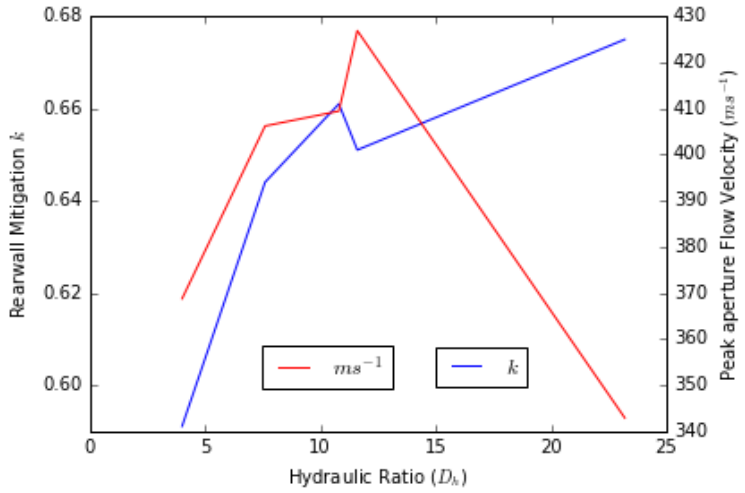

Figure 4.10: Plot of rear-wall pressure mitigation and related peak aperture flow velocity against hydraulic ratio.

with the best-performing design being the 36 circular aperture ($D_h = 4mm$) plate, which provides a 41% reduction in peak pressure. Given the fixed plate porosity of $\varepsilon = 0.4$, the perfect rigidity of the plate, and the identical conditions and methodology applied in all simulation cases, this significant variation in peak overpressure can only be due to factors introduced by the variation in plate design. The peak velocity at the center-rear of each aperture is also presented as the red line in Figure 4.10. When compared to the reduction in rear-wall pressure, for plates with hydraulic ratios between $D_h = 4mm$ and $D_h = 10.8mm$, the mitigation of the shock can initially be seen to decrease with increasing flow velocity through the aperture. A slight divergence in this trend occurs between the plates with $D_h = 10.8$ and 11.6, which is attributed to the different aperture types; the $D_h = 10.8$ barrier apertures are rectangular, while the $D_h = 11.6$ apertures are circular. This relationship between peak flow velocity and rear-wall mitigation then diverges significantly for the single aperture plate. The velocity drops markedly, while the shock strength at the rear-wall continues to climb. While suggestive of a state of choked flow, wherein reducing the width of individual apertures eventually results in diminishing flow velocity with an associated increase in pressure duration, examination of the over-pressure $2mm$ from the barrier surface in the pre-barrier region indicates that there is little variation between plates. Diminishing individual aperture sizes therefore has no adverse consequences in terms of additional

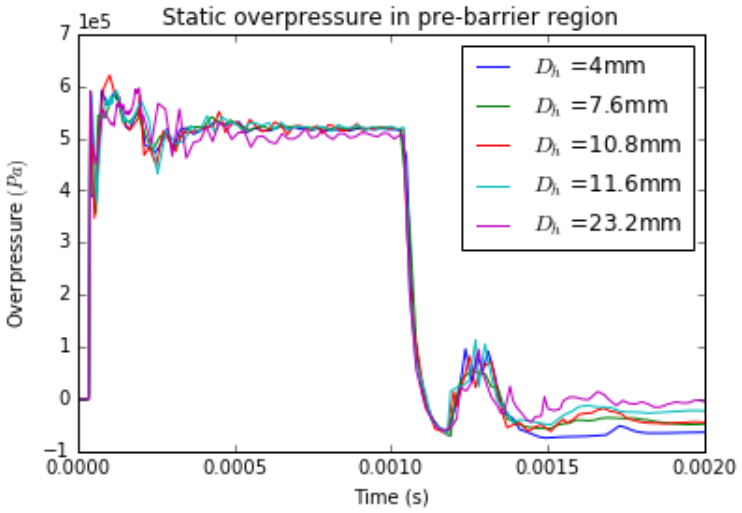

Figure 4.11: A plot of the static pressure $2mm$ from the face of each barrier. Initial peaks of identical magnitude corresponding to the initial shock can be seen, followed by pressure oscillations of comparable magnitude. The pressure then reaches a consistent step distribution as per the applied UDF, although the average pressure is slightly lower for the large circular aperture. Following the sharp drop-off of the pressure corresponding to the end of the applied pressure condition, a brief period of suction can be seen, followed by a small complex of peaks due to the partial transmission of the reflected shock through the barrier.

pressure exerted on the barrier itself for barriers with equivalent ε. The static overpressure as measured $2mm$ from the surface of each barrier is presented in Figure 4.11.

An alternative cause for the divergence of the trend is suggested. When viewed alongside the previous observation that, within aperture shape categories, the downstream mitigation provided by the plates eventually becomes fully ordered on the basis of hydraulic ratio, the absence of additional jet-streams in the flow-field downstream of the barrier is a contributing factor. While the peak velocity of the flow through the single aperture is the lowest of the group, there are no competing jets which may constrict or otherwise deviate the jet flow over time as seen in Figures 4.4 and 4.3, and in the 2-dimensional dual-aperture study in Chapter 3.

4.3 Short Separation Case

Based on the results presented in Figures 4.7 and 4.8, a second set of simulations was performed wherein the separation distance between the rear-wall and the barrier was reduced to 8mm, which places the rear-wall of the post-barrier section within the highly chaotic flow envrionment in the immediate post-barrier region. The impetus for this decision was to observe if the pressure reduction observed in the very near post barrier region as seen in 4.8 could be parleyed into a defensive scheme with similar performance to the long-separation case, albeit one which occupies significantly less space under the vehicle. By placing the rear-wall in the region occupied by the high-speed jets exiting the barrier, the potential for further re-directing the jet flow (and subsequently reducing flow stagnation and the associated pressure) through the use of a post-barrier flow divertor scheme was investigated. With regards to shock mitigation, the most efficient of the designs explored in the earlier section is the design with the lowest hydraulic ratio, that of the 36-aperture plate, and it is this design which is employed in the exploration of the short-separation case. The flow-divertor structure is shown in Figures 4.12. The particular dimensions of the divertors at the rear wall are shown in Figure 4.13.

4.3.1 Flat rear-wall

The state of the local pressure and velocity stream function at the flat rear-wall shortly after the arrival of the shock is presented in Figure 4.14. The shock-front has impacted upon the back wall of the tube and reflected, and is now travelling downwards (relative to the orientation of the Figure) towards the barrier. The flow from the barrier apertures can be seen to slow and stagnate as it enters this returning shock-front. Upon encountering the rear-wall, the jet stream from the barrier can be seen to bifurcate and splay out to the sides, encounter flow from other apertures, and begin to circulate. This region of circulating flow serves to constrict the jet stream, resulting in a compressed region which can be identified from the red colouration of the pressure contour (fig. 4.15). Downstream of this compressed region, the flow expands, further driving the rotation of the flow.

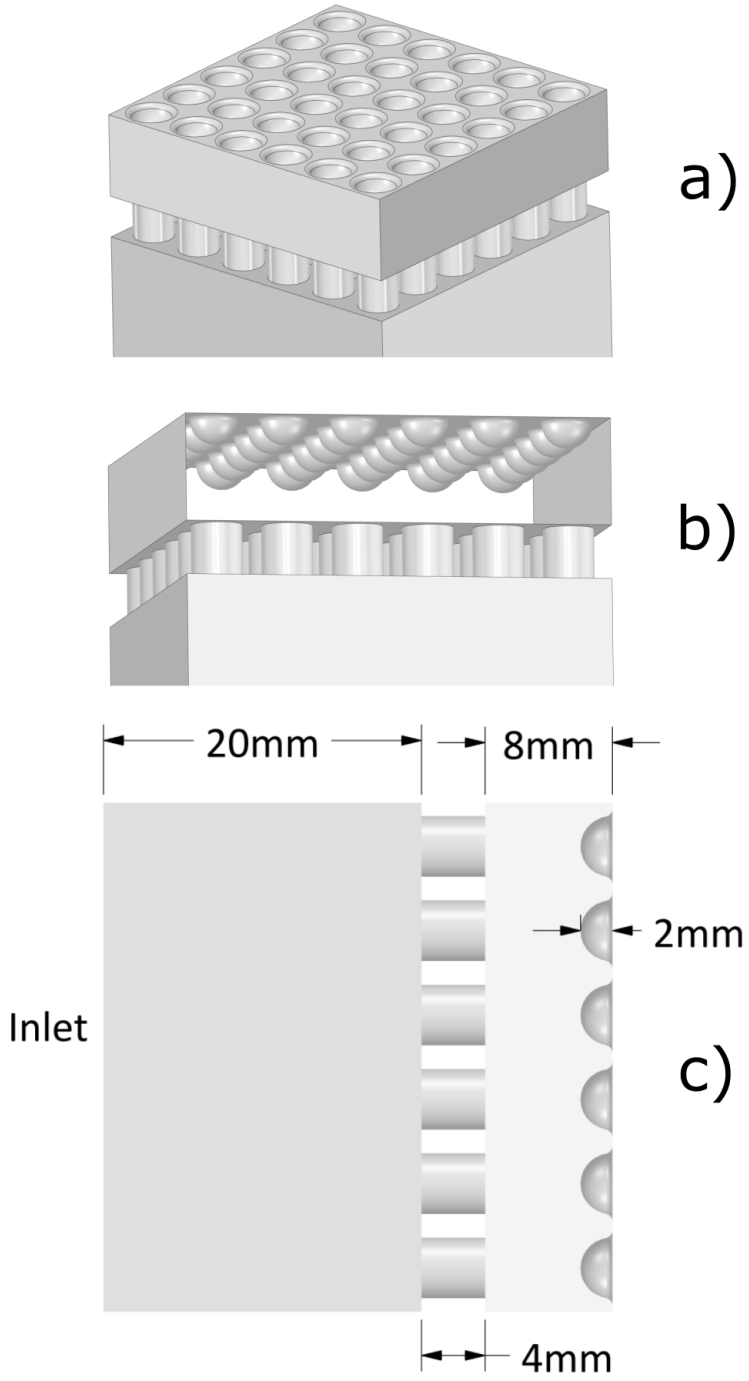

Figure 4.12: a) Isometric view of the 36-aperture plate and the indentations made at the rear-wall to form the flow divertors, b) side cutaway view of the post-barrier region showing the divertor arrangement and structure c) the dimensions of the domain

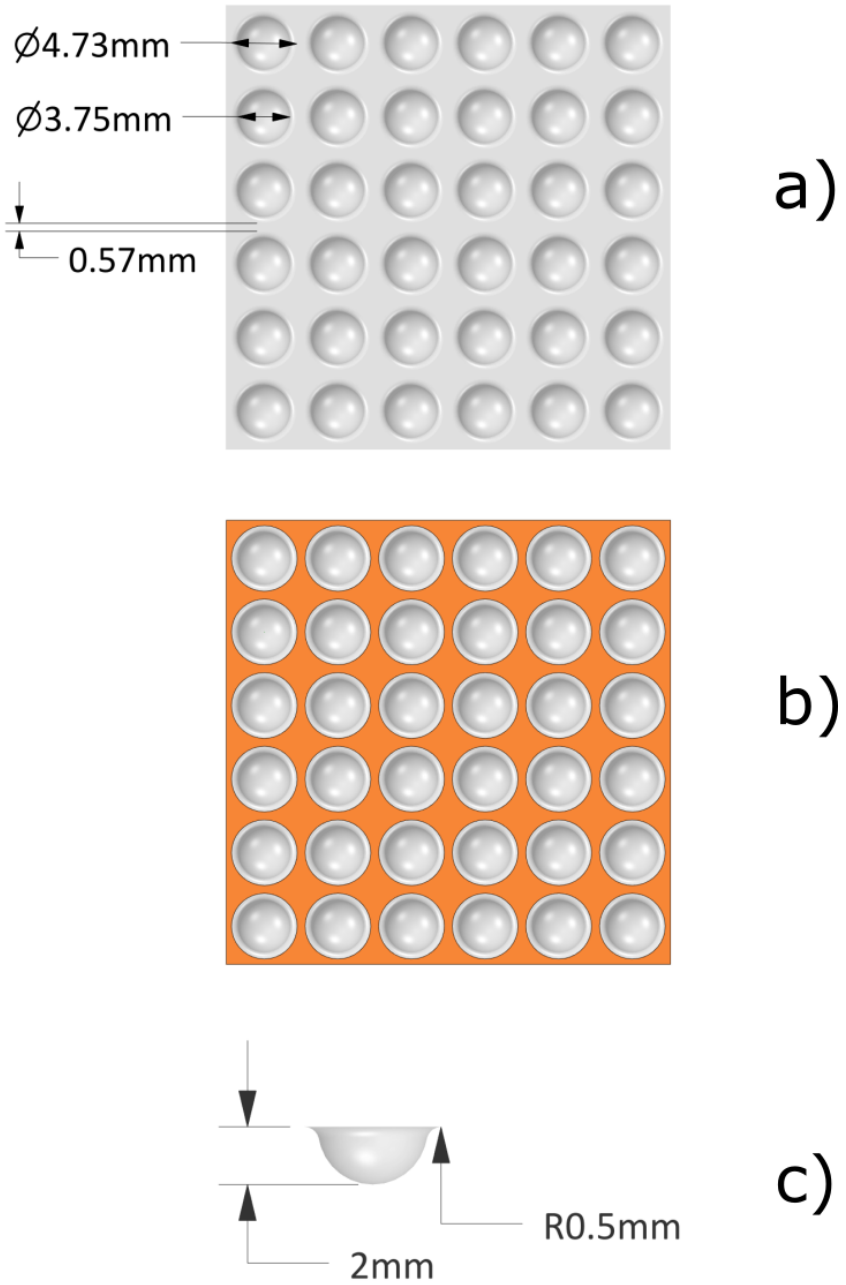

Figure 4.13: a) The dimensions of the divertor indentions as viewed from above, b) the flat region of the rear-wall at which averaged pressure measurements are made, c) the dimensions of an individual divertor and the radius of the fillet at the base, viewed side-on.

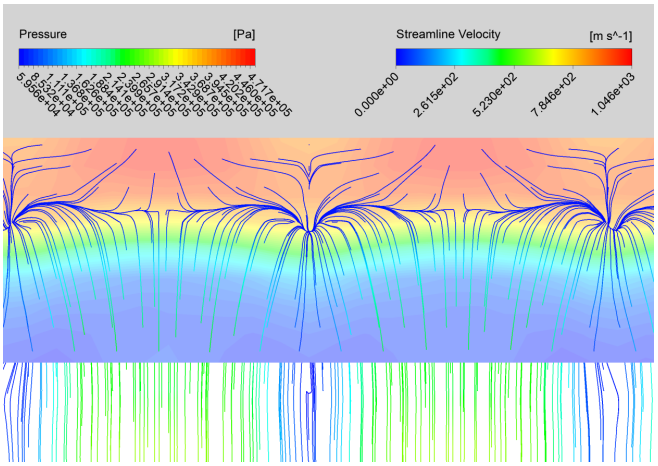

Figure 4.14: Pressure contours in immediate rearwall vicinity with overlaid forward-only streamlines of velocity at $65\mu s$. The jet flow is visible; a reduction in the velocity corresponds to the high pressure region as the flow stagnates.

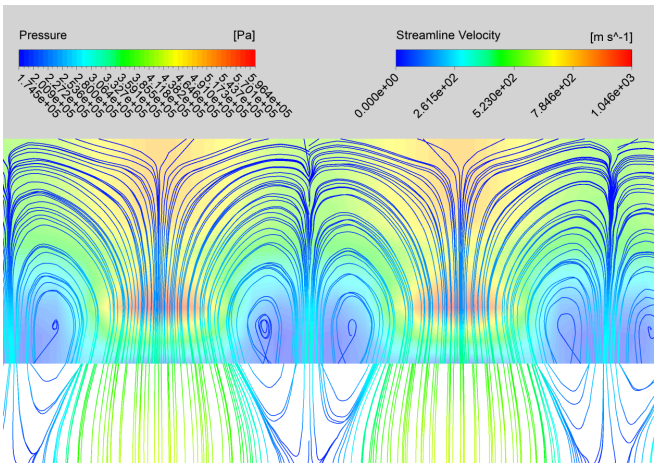

Figure 4.15: Forward and backward streamlines of velocity and pressure contours at $73\mu s$ at the rear wall. The high pressure region at the tip of the flow causes the flow to splay. The splayed flows encounter each other and reverse direction, back towards the barrier. This reversed flow feeds the vortices which creates further deviation of the flow. It can be seen that the bounding of the jet stream by vortices maintains the position of each jet.

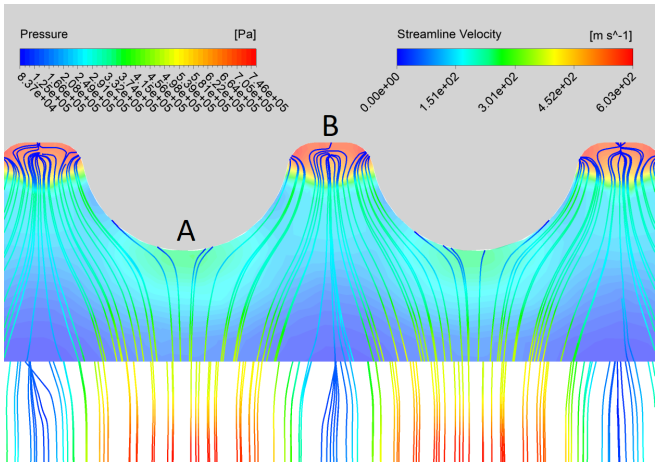

Figure 4.16: 2D forwards-and-backwards streamlines of velocity and associated local pressure contours at $62\mu s$ in the region immediately surrounding the flow divertor design. A high pressure region can be seen at the tip of each deflector dimple at point A. The flow follows the dimple and encounters the rear wall at point B. It can be seen that the flow is halted, forming a high pressure region.

4.3.2 The post-barrier flow disruption design

The case in which the end-wall of the tube features a system of raised dimples positioned directly behind each aperture orifice in the plate is now considered. The intention of these dimples is to present a curved, oblique surface to the flow with the intention of preventing the flow stagnation and sustained pressure condition at the rear-wall as seen in the flat-wall case. This approach incorporates conceptual elements of the V-hull principle. In this case, the use of multiple smaller deflectors requires considerably less vertical height than a single large V-hull. The perforated plate is central to the model, as it enables the position of each jet flow to be known ahead of time. Given the manner in which jet structure is influenced by the surrounding vortices (as seen in the dual aperture structure in Chapter 3 and in Figures 4.16 and 4.17), the flow strikes the deflectors head-on. The streamlines of the flow and the associated pressure condition in the region surrounding the flow divertors shortly after the arrival of the shock-front are depicted in Figure 4.16. A grey background is applied to highlight the divertor structure. It can be seen from this image that the high-speed flow from the barrier apertures (not shown) encounters the divertors and is partially deflected.

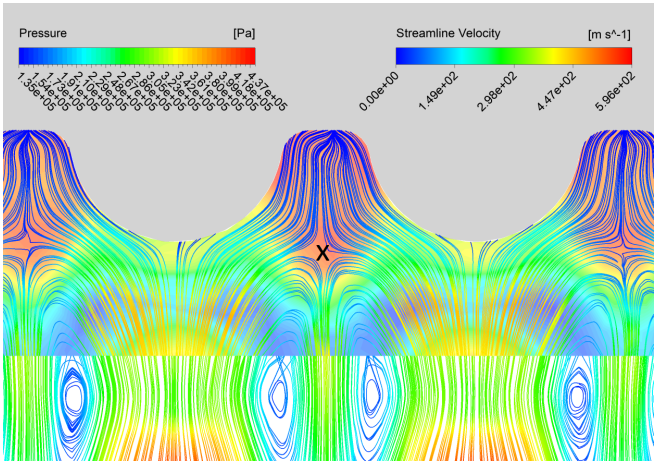

Figure 4.17: Streamlines of velocity and local pressure contours at 77μs in the divertor region. While it can be seen that the divertors do force the flow to deviate, the presence of multiple diverted flows and the proximity of multiple divertors forces the deflected flows to encounter each other head on as seen at the position labelled with an X. The diverted flow splits; part of the flow is fed into The same compressed vortex structure seen in Chapter 3 can be seen in the streamlines. Unlike the dual-aperture flow in Chapter 3, the increased jet density forces the flow structure to strike the divertor head on

The high pressure region at the tip of the divertor structure (identifiable as point A in fig. 4.16) corresponds to the stagnation of the flow visible from the colouration and direction of the streamlines in this region, with the remainder of the flow being deflected to the sides of the divertor structure where it stagnates at the flat surface of the rear-wall (point B in fig. 4.16). It is shown in 4.16 that while this hemispherical divertor design manages to achieve a degree of flow redirection, the resulting flow path still leads to significant stagnation at the rear-wall surface of the shock-tube.

The later development of the flow is shown in Figure 4.17, in which the streamline density is increased in order to better demonstrate the flow structure. The stagnant region in proximity to the flat section of the rear wall has grown, with the jet flows impinging upon the divertor structures now encountering each other head on, with the

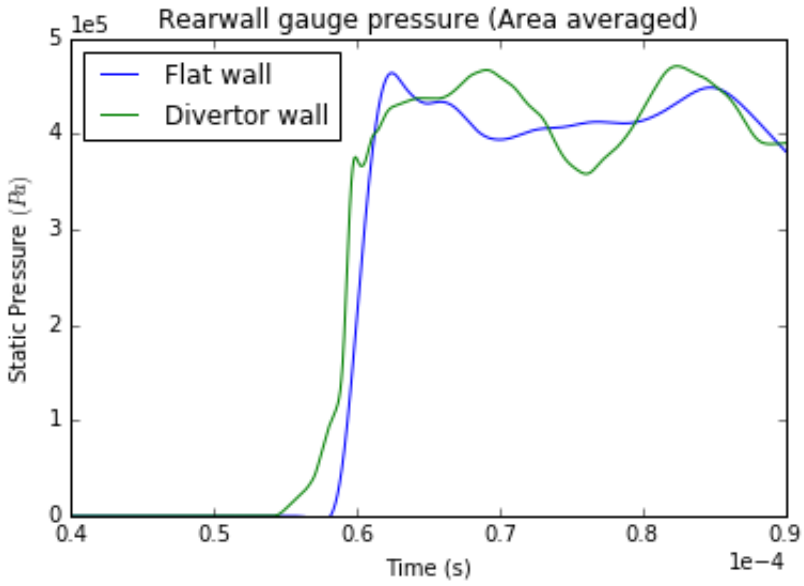

Figure 4.18: Gauge pressure history for the flat and divertor-based rear walls in the 8mm separation case. While both traces reach the same pressure, the rise time to maximum pressure is longer for the divertor wall case. The retardation of the rise time at the flat wall is caused by the irregular arrival time of the transmitted shock in the complex near-barrier region.

center of the horizontal flow marked in 4.17 at the point marked with a black X. By comparison to the flat wall case described previously, it is apparent that the principal effect of the divertor structures employed in this simulation is to move the point of jet flow redirection and collision away from the vicinity of the rear wall. This collision point forces the flow into the structures visible in the streamlines in 4.17, wherein some flow continues to be redirected into the stagnant region at the rear wall, and the remainder redirected back towards the barrier, causing a region of recirculating flow that serves to constrict the incoming jet stream in the same manner as the flat-walled case.

Figure 4.18 displays the area-averaged pressure history for the flat region of the rear-wall in the baffle case. The usual structure for the arrival of a shock is a sharp initial climb in pressure; the slight retardation in the pressure rise is due to the irregular structure of the arriving shock-front in the near-barrier region impinging on the surface.

The variation between the peak pressure at the rear-wall between the flat case and

the case with the divertor pattern is 1.6%, with the peak pressure at the flat rearwall at 463994 Pa and the peak at the baffle rearwall at 471104 Pa, respectively providing a 24% and 23% reduction in peak over-pressure at the rear-wall in comparison to the unprotected case. It is apparent that the additional flow divertor structure as implemented does little to ameliorate the over-pressure at the target wall, although the principle of redirecting the complex post barrier flow has been shown to be plausible. Both short-separation cases provide a degraded mitigation capability in comparison to the long-separation cases with an identical barrier.

4.4 Discussion

4.4.1 The long separation case

While the mitigation of the shock in the post-barrier region is similar to that of Britan et al [113], the overall mitigation is shown to vary significantly with the plate design and corresponds to both the hydraulic ratio and the particular shape of the barrier. Smaller apertures and hydraulic ratios produce greater mitigation. This stands in contrast to the experimental observation that the particular aperture shape is of little consequence to the downstream mitigation at sufficient distance. The magnitude of the mitigation is also underestimated compared to the experimental work. However, the absence of point measurements of the pressure[1] prevents full comparison between the experimental work of [113] and these numerical simulations. In particular, the pressure transducers in the experimental work must be placed at the wall whereas the measurement planes applied in this work report an area average, a practice which may act to limit the effect of pressure fluctuations such as reflected shocks on the measurements while yielding a generally higher overall pressure.

As can be discerned from Figure 4.11, the sustained pressure condition in the short driver section feeds the jet-flow throughout the time-frame for the initial transmission and full reflection of the shock, and it is therefore not the case that the separation of the high-pressure post-shock region from the jet flow as seen in Figure 4.9 is due to a loss of upstream pressure. In light of the relationship between hydraulic ratio, aperture design

[1] In the style of experimental pressure transducers

and mitigation, the separation (and related consequences for the mitigation structure in Figures 4.7 and 4.8) is attributed to the following:

- A decreasing hydraulic ratio increases the turbulence of the downstream flow through enhanced vortex shedding, which serves to extract momentum through the effects of turbulent mixing as identified by Berger et al [73]
- The interaction between jets. It is seen in Figure 4.4 that the presence of multiple jets in close proximity has consequences for the structure of the downstream flow, and produces a flow field considerably different to that of the dual-aperture case in Figure 4.3. The flow reaches a homogenised distribution over significantly less distance, and indicates a greater degree of flow mixing as a consequence.

4.4.2 The short separation case

The placement of the rear-wall of the shock-tube in the jet-flow dominated region behind the barrier adversely affects the mitigation. The flow effects which contribute to the downstream mitigation in the long-separation case do not have sufficient distance over which to act on the flow before the transmitted shock and the jet flow strike the wall and reflect. In both the case of the flat rear wall and the divertor scheme, the jet flows are seen to encounter the target surface and stagnate, spreading outwards parallel to the wall from the initial point of impact, meeting one another and recirculating into the vortex structures seen in Figures 4.14 - 4.17. While shown to be capable of re-directing the flow, the current divertor design contributes to this outcome.

4.4.3 Collaboration

The work in this Chapter was produced in part through a collaboration with Dr Julian Pittard of The University of Leeds, the co-author of a currently embargoed paper from which this Chapter is drawn.

Chapter 5

Initial Blast Modelling

In this Chapter, a methodology for the interaction of a buried charge detonation with a perforated plate is investigated. A simulated buried charge blast is examined with respect to the features expected from Chapter 1:

- The initial detonation of the charge
- Cavitation and plastic compression of the surrounding sand
- Ejection of a sand-slug
- The venting of gaseous detonation products

The sensitivity of the detonation process to the mesh sizing is tested. The model is then expanded to examine the impact of the blast on a flat metal witness plate and the mechanical response with regards to both Eulerian and Lagrangian mesh scales. These examinations provide a basis for the later work in Chapter 6, in which the model is expanded to incorporate a perforated plate as a defensive adaptation.

5.1 Methodology

STANAG 4569 qualification of the blast resistance of a vehicle is based on three discrete phases of testing, two of which require a production vehicle. In this work, the phase A testing criteria for engineered parts exposed to mine blast is adopted as a guideline.

The layout for a phase A component test is displayed in Figure 5.1. The testing arrangement consists of a rigid structure which permits the component to be mounted above the sample charge. The mass of the vehicle is represented by a weight, which allows assessment of the predicted impulse transfer to a hypothetical “real” vehicle. The additional factors of a real vehicle such as wheels, running-gear, engine, armour and occupants are all absent. There are numerous techniques in the literature that can be applied to the simulation of buried charge detonation. These include:

- Simulation of the plate and sand materials using a Lagrangian mesh, with simulation of the air and explosive charge using the Euler-FCT method as found in Grujicic [114]
- Simulation of the sand, charge and air using the multi-material Euler technique found in Fišerová [8] and Grujicic [115]

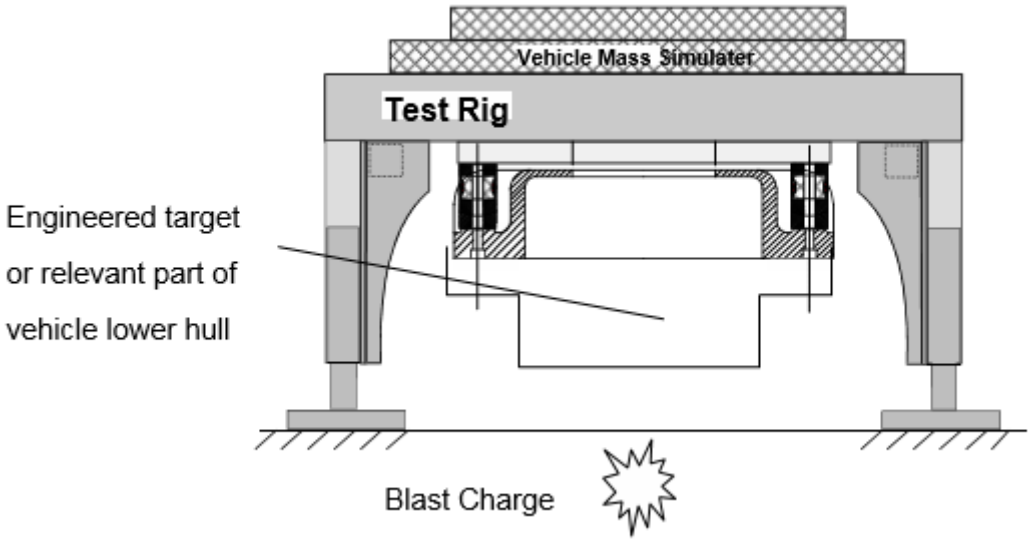

Figure 5.1: The example test rig for phase A tests [3]

- Smooth particle hydrodynamics as found in Trajkovski [116]
- Arbitrary Lagrange-Euler modelling, as found in Boumaoul and Toussaint [117].

The ultimate goal of these simulations is to examine the intrusion of sand and blast materials through the apertures of a perforated plate, and assess the structural response. Complex separation and deformation of the sand-slug in the post-barrier region is expected. To avoid the tangling of Lagrangian mesh elements, an Eulerian approach to the modelling of the sand is determined to be most suitable. However, under the multi-material Euler scheme, this approach precludes the use of re-meshing from finer to coarser meshes, and so the mesh scale must be continuous throughout the simulation.

5.2 Initial Buried Charge Simulations

In this section, a simulation geometry and material models are selected for the simulation of the detonation of a charge buried in sand. The pressure history in the region above the charge and the sand response are investigated with respect to mesh sensitivity.

5.2.1 Material selection

The sand model

AUTODYN contains a model for sand based on the work of Laine and Sandvik [21], with further experimental validation found in Fišerová [8]. Sand and soil are highly complex materials in which three discrete phases (solid, liquid and gas) are present to various degrees, depending on the compaction and water saturation of the material. Derivation of the material properties of sand is highly dependent upon these factors; a detailed summary of the specific mechanics of soil properties and the methodology by which the mechanical properties are derived is given in [8]. The Laine and Sandvik model is derived for a dry sand of medium to coarse grain size with a water content of 6.57% and initial in-situ density $1574 kg\, m^{-3}$. The model is implemented in the AUTODYN materials library as a modification to the MO-granular material model. While recognised [118] as performing reasonably well in simulating the typical features of mine-blast, the model deviates from the STANAG 4569 experimental standard of water-saturated sandy gravel. This selection is ultimately made on the basis of sand cohesion (the degree to which sand holds together under loading); it is demonstrated in Fišerová that a more cohesive sand (modelled through alterations to the yield surface) delivers lower impulse loading [8]. Furthermore, the intention is to study the intrusion of sand through the apertures of a perforated plate. A model for dryer sand is therefore actively desirable, both from the perspective of an increased slug impulse and to allow smaller apertures to be modelled without the potential for blockage.

Sand compacts under loading, and requires an equation of state that reflects the transition from loose, uncompacted sand to fully-compacted sand. On being shocked, sand compacts; once the shock has passed, if the sand is not fully compacted, then it also "unloads" and returns to a less-dense configuration. This behaviour is represented in AUTODYN by a density-dependent bulk soundspeed

$$p = c^2(\rho)\rho \tag{5.1}$$

where c is the wave-speed, p is pressure and ρ is density. In AUTODYN, the compaction and unloading behaviours are given as 10-point piecewise-linear curves. The second consideration of the model of Laine and Sandvik is that the compaction of the sand

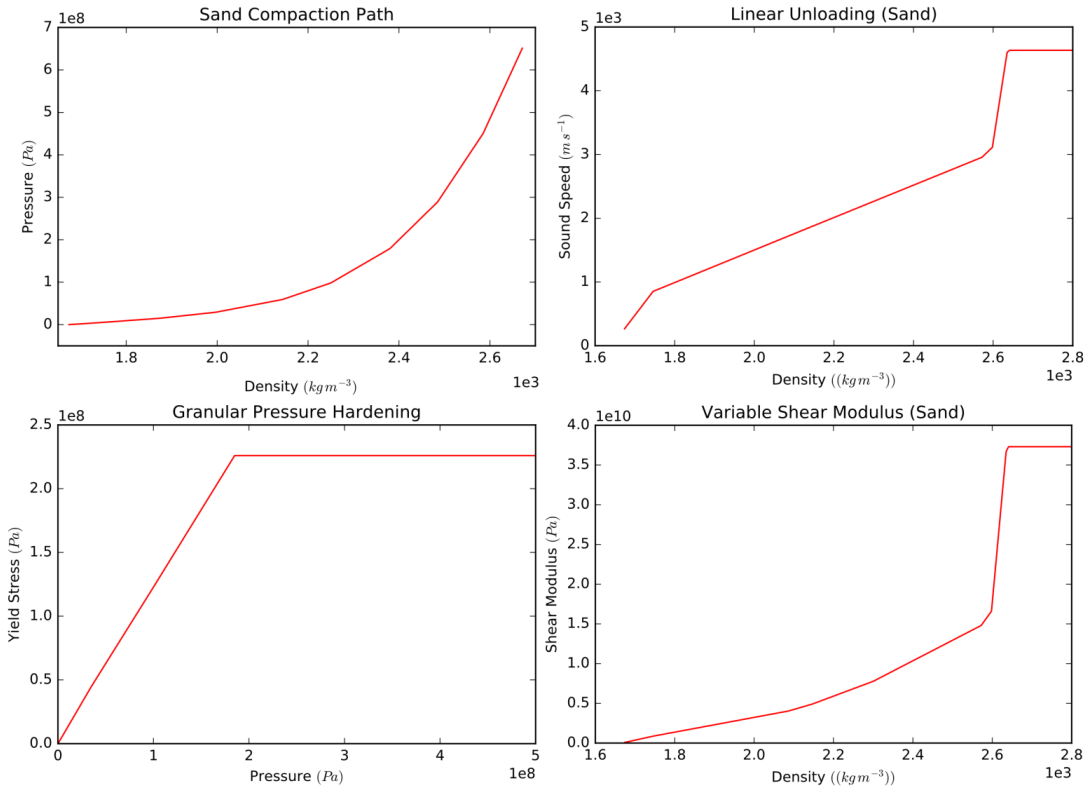

Figure 5.2: The piecewise curves used to define the sand EOS in AUTODYN. ([21]/AUTODYN materials library)

alters the shear modulus; the yield surface is therefore highly density and pressure dependent, and is given as

$$Y = f_1(p) + f_2(\rho) \tag{5.2}$$

with the dependent functions f_1 and f_2 given by piecewise-linear curves that relate p to Y and ρ to Y, which also relates the density to the shear modulus G. The compaction, unloading, granular hardening and shear modulus paths are displayed in Figure 5.2.

In an uncompacted state, sand grains are loose and the sand has no bulk cohesion. This is reflected in Figure 5.2, where the shear modulus for uncompacted sand is 0 at a density of $1.6 \cdot 10^{-3}\, kg\, m^{-3}$. Consequently, the tensile strength of overburden sand is extremely low and cannot sustain significant negative pressure. Negative pressure in the form of the tensile wave is responsible for the ejection of the sand-slug. In

AUTODYN, this tendency of the material to separate under tensile stress and the associated negative pressure would pose a problem in the calculation of internal energy in the cell. This is addressed by the introduction of a tensile failure criteria in which, upon reaching a minimum pressure $P_{fail} = 1 \cdot 10^{-3} Pa$, the pressure in the cell is re-set to 0 and the internal energy re-calculated. The material does not undergo separation due to failure during this time. This process allows the cell to sustain negative pressure over multiple time-steps without causing numerical failure of the model. However, it is indicated [119] that due to the simplicity of the model, conclusions should not be drawn from specific details of cavitation. Fišerová indicates that variations in the failure limit do not affect the blast loading, and so the default tensile failure model is applied in this work [8].

The explosive charge material

STANAG 4569 defines the standard explosive for mine-blast testing as Trinitrotoluene (TNT), and states the charge sizes that correspond to increasing threat levels. As noted in Chapter 1, the progression of a buried charge includes two distinct periods; during the first period, the detonation products have not yet breached the surface of the soil. During the second, the soil cap is fractured and the detonation products are exposed to the surrounding air. In the first period, the supply of oxygen to the detonation products is restricted. If the explosive material is oxygen-deficient, then complete reaction of the detonation products only occurs in the second period in which the detonation products are exposed to the oxygen-bearing air, leading to the "afterburning" effect. Fišerová [8] indicates that the TNT model in AUTODYN overpredicts the loading of a buried charge by approximately 40% when compared to experimental results, and attributes this to the absence of afterburning in the simulated detonation products. AUTODYN models the detonation of explosive materials through the JWL equation of state, and does not account for the specific reaction chemistry. While the JWL-EOS implementation in AUTODYN does allow for modifications to the explosive energy release over time, in the absence of appropriate modelling data a different explosive material with an oxygen balance closer to neutral is sought to minimise the influence of afterburn. TNT has the chemical composition $C_7H_5N_3O_6$. The oxygen balance calculation of Lothrop and Handrick [120] is

Table 5.1: Atomic masses [121]

Element	Atomic mass (u)
Oxygen (O)	15.9994
Hydrogen (H)	1.00794
Carbon (C)	12.011
Nitrogen (N)	14.00674

Table 5.2: C4 chemical composition [110].

Component	Composition
RDX (91%)	$C_3H_6N_6O_6$
Di(2-ethylhexyl) sebacate (5.3%)	$(CH_2)_8(COOC_8H_{17})_2$
Polyisobutylene (2.1%)	$(C_4H_8)_n$
Motor oil (1.6%)	Various
C4 Composite	$C_{1.82}H_{3.54}N_{2.46}O_{2.51}$

$$OB(\%) = \Big[-1600\Big(2C + \frac{H}{2} - O\Big)\Big]/m \tag{5.3}$$

where C, H and O are the number of moles of carbon, hydrogen and oxygen respectively present in a balanced reaction, and m is the total molecular weight determined by atomic mass. Applying Equation 5.3 and the atomic masses shown in Table 5.1, it can be shown that TNT has an oxygen balance of -74%, and is significantly oxygen deficient. STANAG 4569 permits the use of two surrogate explosive materials: Composition-4 (C4), and PETN. C4 is, per the name, a composite plastic explosive. The specific chemical composition of C4 is given in Table 5.2.

PETN (Pentaerythritol Tetranitrate) is a multi-purpose explosive of chemical composition $C_5H_8N_4O_{12}$. PETN is frequently mixed with varying quantities of wax, depending on intended application, and may vary with respect to density. STANAG 4569 mandates the use of PETN with a density of $1.54g\,cm^{-3}$ ($1540kg\,m^{-3}$). The closest available JWL parameters in the literature for PETN of this density are those given in the Lawrence Livermore National Laboratory explosives handbook [110] for PETN 1.5, which has a density of $1500kg\,m^{-3}$. The same source also provides JWL parameters for C4. Application of Equation 5.3 to PETN and the values specified in Table 5.2

for C4 yields an oxygen deficiency of -46.4% for C4 and -10.1% for PETN. PETN is much closer to a neutral oxygen balance than either TNT or C4, and is selected as the appropriate charge material. The JWL parameters for PETN 1.5 are given in Table 5.3.

Table 5.3: Jones-Wilkins-Lee and other detonation parameters for PETN 1.5 [110]. These values are also incorporated into the ANSYS materials library as a standard part of the distribution.

JWL Parameters	
Parameter	Value
A	$6.253 \cdot 10^{11} Pa$
B	$2.329 \cdot 10^{10} Pa$
R_1	5.25
R_2	1.6
ω	0.28
Chapman-Jouget Values	
Parameter	Value
Detonation Velocity	$7450 ms^{-1}$
Energy/Unit Mass	$5.707 \cdot 10^{6} J\, kg^{-1}$
Pressure	$2.2 \cdot 10^{10} Pa$
Initial Density	$1500 kg\, m^{-3}$

STANAG 4569 indicates the TNT equivalent mass of a PETN charge and defines a cylindrical width. The geometry and masses of the STANAG charges are presented in Table 5.4. STANAG 4569 also stipulates that detonation of the charge must be initiated from no greater than one third of the total height of the charge as measured from the base. The locations of the detonation initiation points (relative to the charge geometry) are also given in Table 5.4.

Throughout the majority of this simulation work, the charge is a cylinder of PETN of width 235mm and 102mm in height, which weighs 6.34 kg (corresponding to 7.23 kg TNT). While this is not a standard charge size under STANAG requirements, a deeper yet narrower charge is used with the intention of generating greater slug loading. The rationale for this decision is twofold: The first is the selection of slightly lower density

Table 5.4: TNT equivalent charge scaling for PETN-B. Reproduced from [3] with additional charge and detonation initiation height dimensions

Threat Level	Charge:			
	Diameter (mm)	Mass (kg)	Height (mm)	Det. height (mm)
2b (6kg TNT)	230	5.04	81	24
3b (8kg TNT)	245	6.72	95	28
4b (10kg TNT)	265	8.40	102	30

of the modelled PETN charge, which requires an explosive mass slightly greater than that of the 2b charge. The second is that the slug threat is of particular interest; the deep burial of a taller charge is intended to further enhance this. In Chapter 6, a comparison is also made to a maximum-scale 4b charge detonation.

The air model

In AUTODYN, air is modelled with the ideal gas equation of state

$$p = (\gamma - 1)\rho e \tag{5.4}$$

where γ is the adiabatic exponent and e is the internal energy of the air. Parameters for the air model are presented in Table 5.5

Table 5.5: Ideal gas modelling parameters

Parameter	Value
Density (ρ)	$1.225\,kg\,m^{-3}$
Specific Heat (C_0)	$717.6\,J\,kg^{-1}\,C^{-1}$
γ	1.4
Initial temperature (T)	$292\,K$
Specific internal energy (e)	$2.096 \cdot 10^5\,J\,kg^{-1}$

5.2.2 Domain Geometry

The domain is constructed following the reference diagram for a STANAG 4569-compliant phase A test as shown in Figure 5.3.

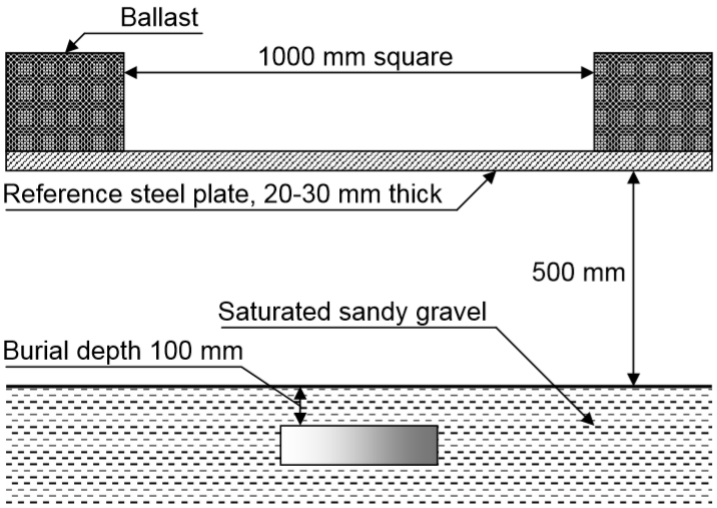

Figure 5.3: The arrangement for a phase A buried charge test. Taken from [3]

The dimensions of the testing environment and burial depth are reproduced corresponding to these requirements. To prevent the outflow of material from the sides of the simulation that lie below the initial surface of the sand, a thin containing wall is

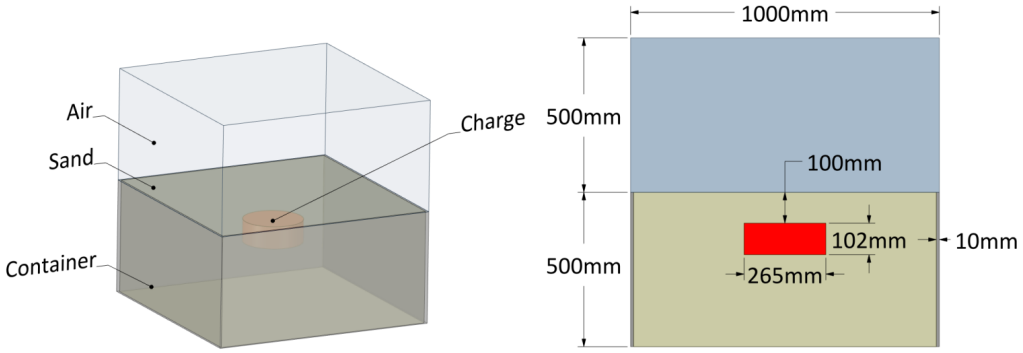

Figure 5.4: The geometry for the initial sand blast test

constructed around the side of the sand domain. The initial geometry of the problem is shown in Figure 5.4. This geometry has two planes of symmetry; to reduce the computational load, the domain can be reduced to a quarter of the total size along the symmetry lines. The final state of the domain is shown in Figure 5.5. To apply the

symmetry condition at the pre-processing stage, the edges of the domain that connect at the interior must lie exactly along the global symmetry of the CAD model.

5.2.3 Set-up process

The quarter geometry defined in Figure 5.5 is imported into ANSYS Explicit Dynamics, the main pre-processor for the AUTODYN simulations in this work. Standard Earth gravity of $9.807ms^{-2}$ is applied to the model. The gravity vector is downwards, in the -y direction.

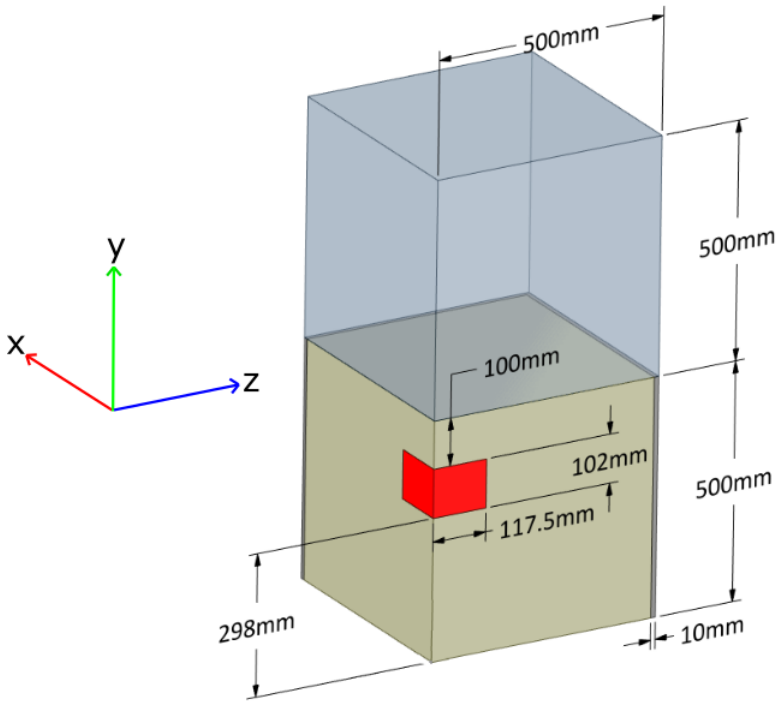

Figure 5.5: The quarter geometry over which calculations are performed. The x,y,z axes shown are universal across all future simulations.

Material assignment

The bodies that make up the geometry must be assigned a material model and solver. The containment wall is "scoped" (assigned) to the Lagrangian domain and defined as fully rigid, and so the choice of material model for this body is moot; the ANSYS Mechanical Structural Steel material model is applied by default. The remaining en-

tities, the sand, charge and air volumes, are assigned the respective material models defined previously and scoped to the Eulerian domain.

Detonation point

An initial point in the charge material must be specified as the locus of detonation. The detonation wave expands radially from this point, initiating the burn-over-time of explosive material. The transit of the detonation wave can either account for variations in the structure of the charge (indirect detonation), or simply expand radially (direct detonation). The indirect model is applied by default, although the distinction in this case is minimal. As the center of the charge lies directly on the corner of the interior of the quarter domain (which in turn lies at the origin of global symmetry along the x and z axes), only the height of the detonation point needs specification, with the x and z co-ordinates left at 0. The base of the charge begins at a global height of 298mm. The detonation point is placed 30mm above this point, at a height of 328mm; this location is shown in Figure 5.6.

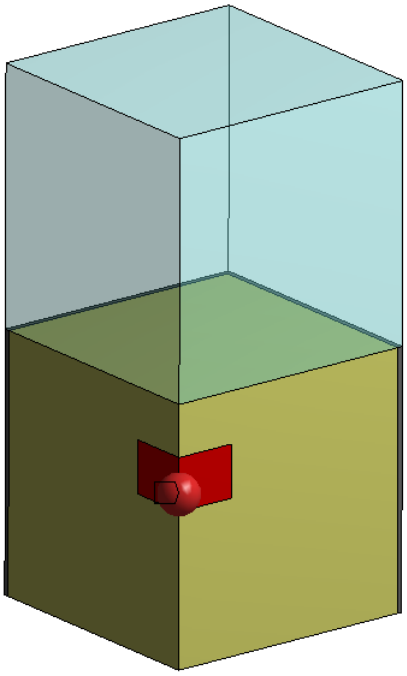

Figure 5.6: The placement of the detonation point (red ball point) in the Explicit Dynamics model

Fixed supports

For Lagrangian bodies, it is possible to define a particular face or body as being locked or clamped in place, which is represented in AUTODYN is the imposition of $v = 0$ as a constant velocity condition for the relevant nodes. This condition is applied to all nodes within the rigid containment wall body, locking it in place around the sand volume.

Euler domain properties

Adjustment of the Euler domain is performed in the analysis settings. AUTODYN requires the Euler domain be described with a structured mesh. During pre-processing, all components imported into Explicit Dynamics are initially discretised using an unstructured mesh. Components which are scoped to the Euler domain are subsequently re-meshed to a regular structured mesh when imported into AUTODYN. The Euler domain itself is defined in terms of the cardinal x, y, z dimensions and is rectangular. For these simulations, the limits of the Euler domain correspond to the initial dimensions of the geometry. The initial unstructured mesh and the structured Euler mesh are shown in Figure 5.7. The mesh size is defined in terms of cell edge length in the analysis settings. The behaviour of the flow at the limits of the Euler domain can be adjusted at this stage. The limits of the domain lying along the internal symmetry faces and at the lower y-face are defined as rigid; material encountering these interfaces is not permitted to pass through; this describes an Eulerian symmetry condition. The remaining walls corresponding to the external limits of the simulation are set as outflow conditions, which allow the free exit of material.

Multiple element scales are applied to investigate the sensitivity of the simulation to the applied mesh. The mesh sizes are given in Table 5.6, where it can be seen that the cell count for the Euler domain climbs rapidly with increasing resolution. This introduces a non-trivial computational expense, and determining a mesh scale that produces consistent results with a minimum of excess computation is desirable. For these simulations, there are no Lagrangian bodies for which the mesh resolution is of importance. The containment wall is Lagrangian but fully rigid, and so the coarse unstructured mesh generated by the Explicit Dynamics mesh generator is retained for this body.

Table 5.6: Mesh sizes for the Lagrangian and Eulerian domains, and associated cell counts

	Simulation			
	1	2	3	4
Euler element size (mm):	10	6.6	5	4
Euler element count:	250,000	869,577	2,000,000	3,906,250

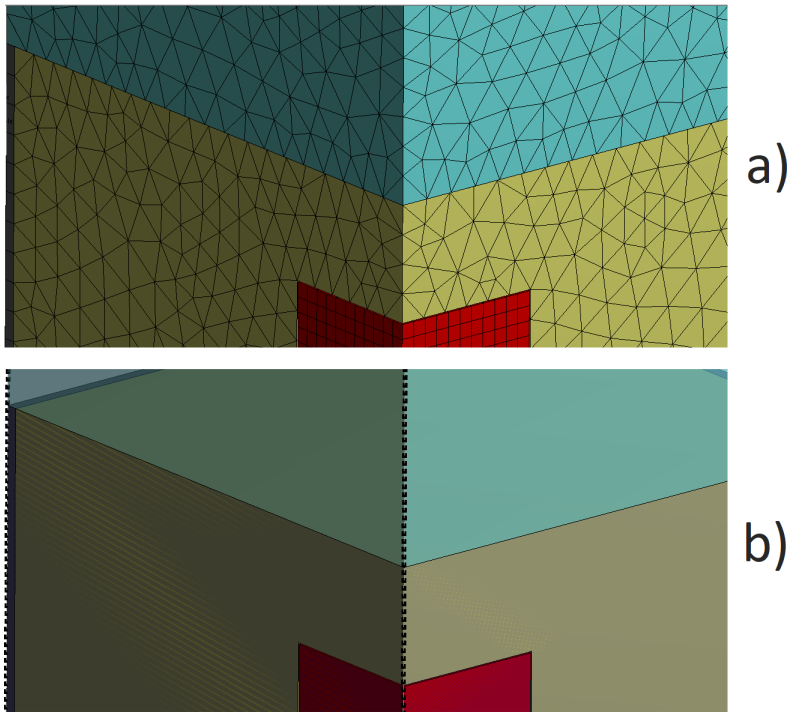

Figure 5.7: a) The initial coarse, unstructed mesh generated in Explicit Dynamics and b) the edge points corresponding to the Euler grid which replaces the mesh on components scoped to the Euler domain. In this image, the Euler mesh resolution corresponds to a total of 869,577 control volumes, approximately 6.6mm per side. Components scoped to the Lagrangian domain retain the unstructured mesh generated in Explicit dynamics.

5.2.4 Import into AUTODYN and Solver Settings

The simulation is now imported from Explicit Dynamics into AUTODYN, where measurement gauges can be inserted and simulation techniques adjusted. It was noted during early simulation attempts that the default total energy transport method applied by AUTODYN is unsuitable; during the detonation process (especially during the early stages of the detonation), large quantities of material are transported between Euler cells in each time-step , resulting in an "over-emptying" of individual cells. AUTODYN warns the user that the stability and accuracy of the simulation will be impaired. The energy transport method is as a result set to "internal".

Gauges

AUTODYN permits the extraction of information regarding time-varying conditions at specific points in the computational domain through the placement of measurement gauges. An initial set of gauges are placed in a direct line above the charge at intervals of 50mm in order to establish the pressure conditions directly above the charge as the detonation progresses. To examine the pressure condition towards the outermost limits of the domain, an additional set of gauges is placed at a 45-degree diagonal starting from the same initial position as the vertical array, with the same y-spacing. Gauge 1, placed at a height of 550 mm relative to the base of the enclosure, is the starting point for both gauge arrays. The configuration of the gauges can be seen in Figure 5.8.

5.2.5 Simulation execution

Simulations are solved on the ARC3 HPC cluster at the University of Leeds[1]. On the basis of the observed pressure behaviour, simulations are run for 5ms, by which time the pressure has returned to nil. This is consistent with the observation of Bouamoul et al [22] that the local deformation dynamics of a buried landmine detonation occur over this time-frame. Visual results are drawn from solution files saved every 0.2 ms, while data is saved for gauge measurements on every time-step. There is significant variation in the run-time and computational resources required for each simulation; the coarsest simulation will run to full completion on a modern desk-top computer over

[1]Parallel processing capabilities were retroactively added to AUTODYN by ANSYS Inc. Running AUTODYN in parallel on a modern Linux HPC cluster where compute nodes are dynamically assigned at runtime presents certain difficulties. A solution is presented in Appendix C.

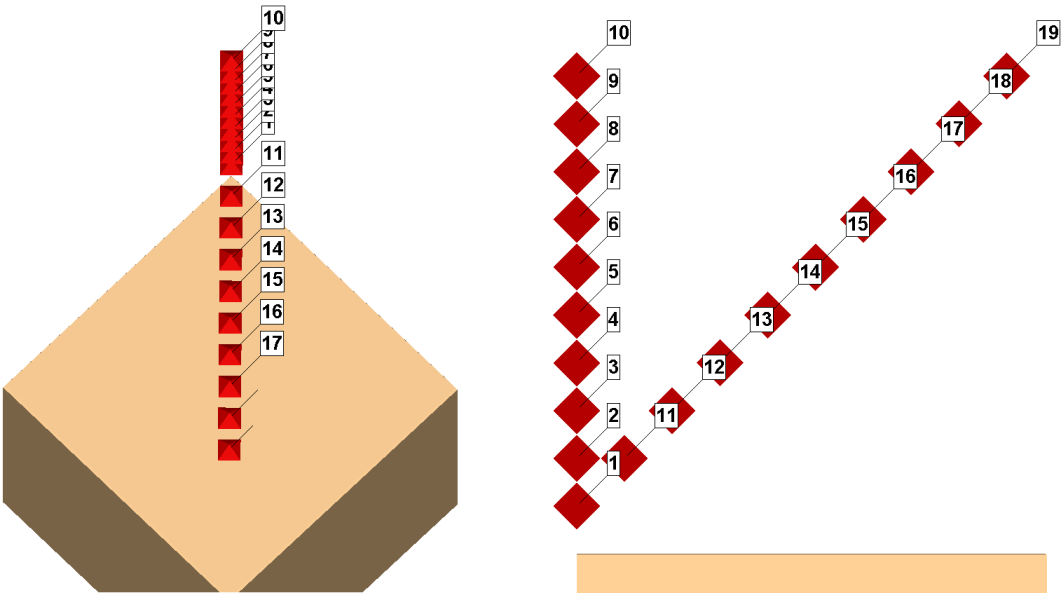

Figure 5.8: The gauge array as shown over the quarter-symmetry of the domain from top-down and side-on viewpoints.

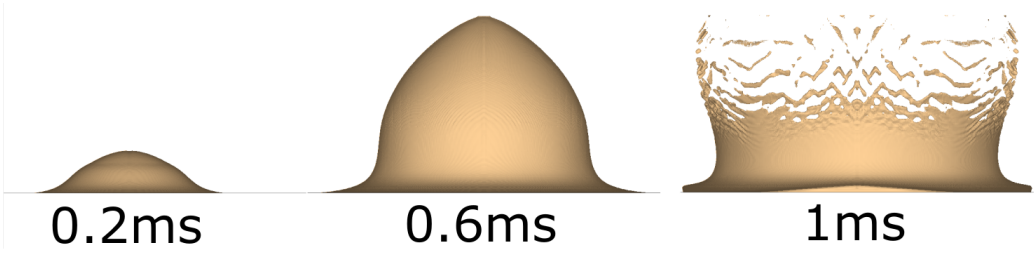

Figure 5.9: Sand-slug formation. At $t = 0.2ms$, an initial rising bulge in the soil can be seen; by $0.6ms$, the bulge has risen considerably, to nearly 500mm. By $1ms$, the bulge has fully erupted, with material from the edge of the cavity continuing to be launched upwards by the continued egress of gas.

several hours, while the finest resolution is intractable without HPC capabilities, and takes approximately 2 days to run to completion over 16 computational cores.

5.3 Results for the initial blast model

The initial detonation progression is shown in Figure 5.9. The surrounding air and detonation products are hidden to show the development of the slug and associated ejecta. The features of a typical buried charge detonation are seen, including the initial displacement in the soil surface followed by a rising sand-slug. The ejection and separation of the sand-slug is followed by the continued ejection of material from the edge of the crater as the detonation gases continue to vent.

The mechanics of the process are shown in Figure 5.10, in which the sand is coloured by material state. The cavitation of the sand surrounding the charge can be seen. Beyond this cavity, the soil is plastically compressed. The enclosure that constrains the sand is small, and so the full inventory of sand is eventually plastically compressed by the detonation. The ejection of the sand-slug due to the tensile condition created at the air-sand interface forces can be seen in the material which has undergone bulk failure.

The pressures in the vertical and diagonal gauge arrays are shown in Figures 5.13 and 5.15. By 2ms the blast pressure has largely decayed, and the time axis is truncated to show the traces in detail.

Similar pressure structures are seen for both gauge configurations. However, the gauges in the diagonal array from 750mm onwards do not display the dual-peak structure present in the vertical array, and instead obey a structure much closer to that of a conventional air-burst. Examination of the state of the domain over time indicates the cause; the main sand-slug does not pass through the more distant gauges. As both sand and gas products are transported within the same control volumes, AUTODYN cannot distinguish between the two materials with regards to pressure. Further comparison between the pressure structure at a gauge position of 550mm indicates that the magnitude of the secondary peak is the same across both mesh sizes. The cause of the peak splitting in Figures 5.13 and 5.15

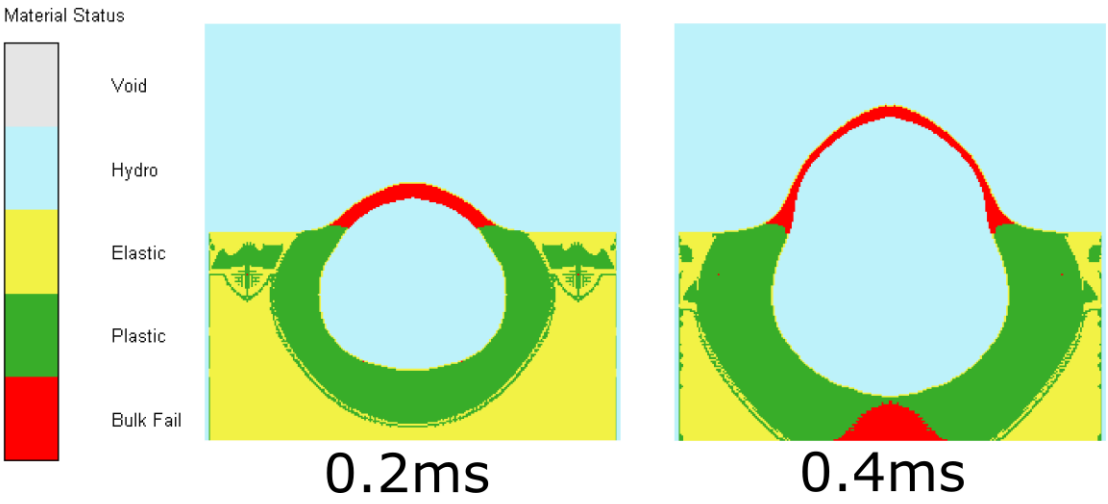

Figure 5.10: The changing material status in the sand during the early stages of the detonation at 0.2 and 0.4 ms. At $t = 0.2ms$, cavitation of the sand in the region proximate to the charge is observed, with a compression wave plastically deforming the surrounding material. At the air-sand interface, failure of the sand due to the reflection of the initial shock (the passage of which can be seen in the structures to the left and right of the main plastic region surrounding the charge) and the associated tensile forces can be observed in the formation of the nascent sand-slug. At $t = 0.4ms$, the compression wave within the sand has encountered the bottom of the container and reflected.

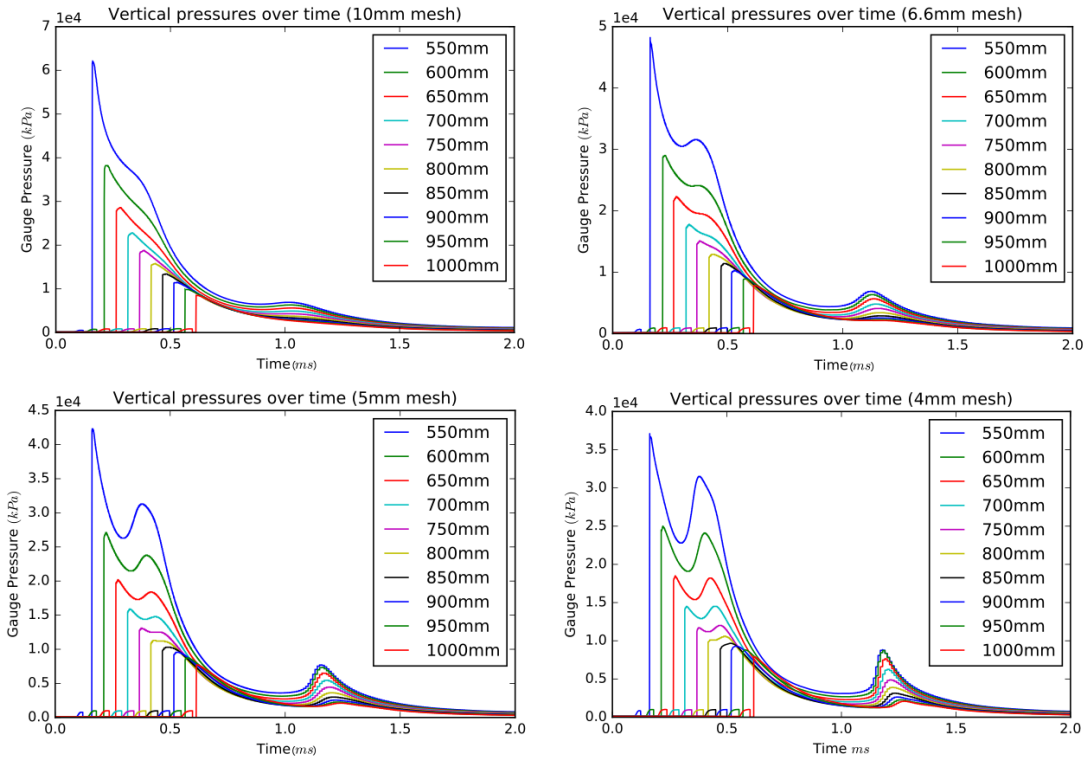

Figure 5.11: Pressure traces over the vertical gauge array. An initial sharp Friedlander-type peak is followed by a secondary peak corresponding to the internal pressure in the ejected sand-slug. The tertiary peak is the reflected wave from the bottom of the enclosure.

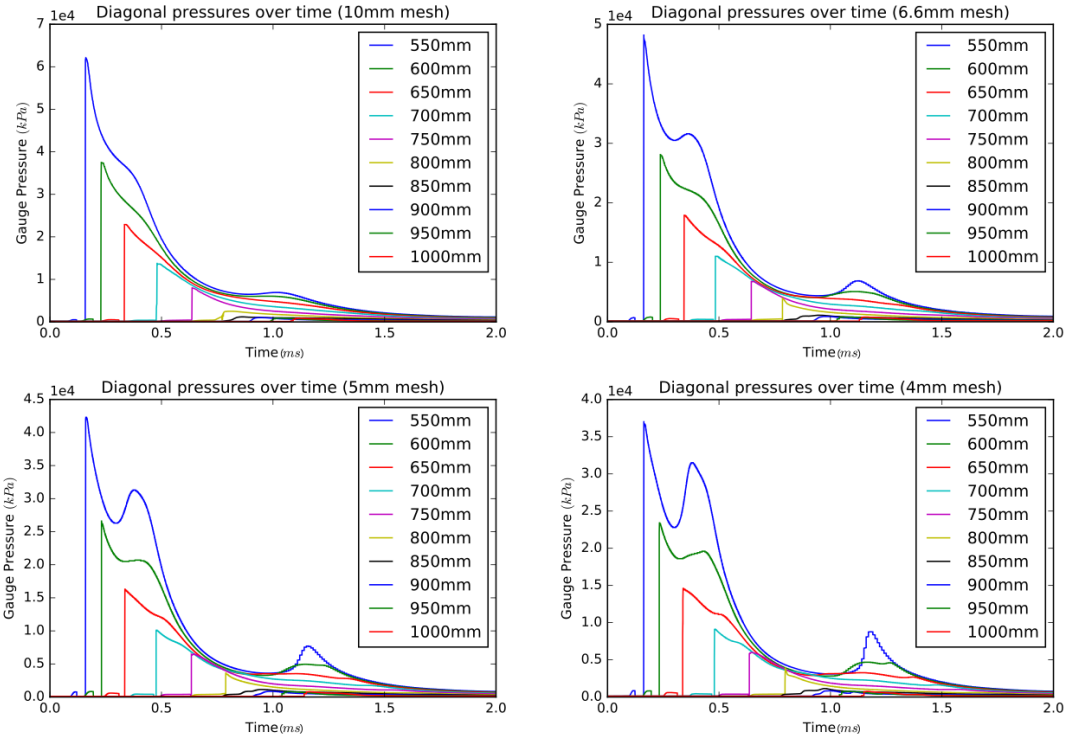

Figure 5.12: Peak pressures achieved over the diagonal gauge array. The secondary peaks visible in Figure 5.13 are mostly absent in the measurements from the 700mm gauge onwards.

is attributed to the passage of the sand-slug through the gauge points. The inability to distinguish between the pressure exerted by different materials when using the multi-material solver represents a weakness with respect to the analysis method, and presents a difficulty when attempting to determine the relative contribution of the detonation products and sand-slug to the loading. A further tertiary peak is visible in the trace, most notably in the 550mm gauge; this is attributed to the reflected wave from the base of the enclosure. The reflected wave is small, and is negligible at higher gauge points.

Figure 5.14 establishes that the secondary peaks of the pressure traces are consistent across mesh scales. The magnitude of the peak pressure traces is therefore taken as a measure of convergence. The peak pressures observed at the vertical and diagonal

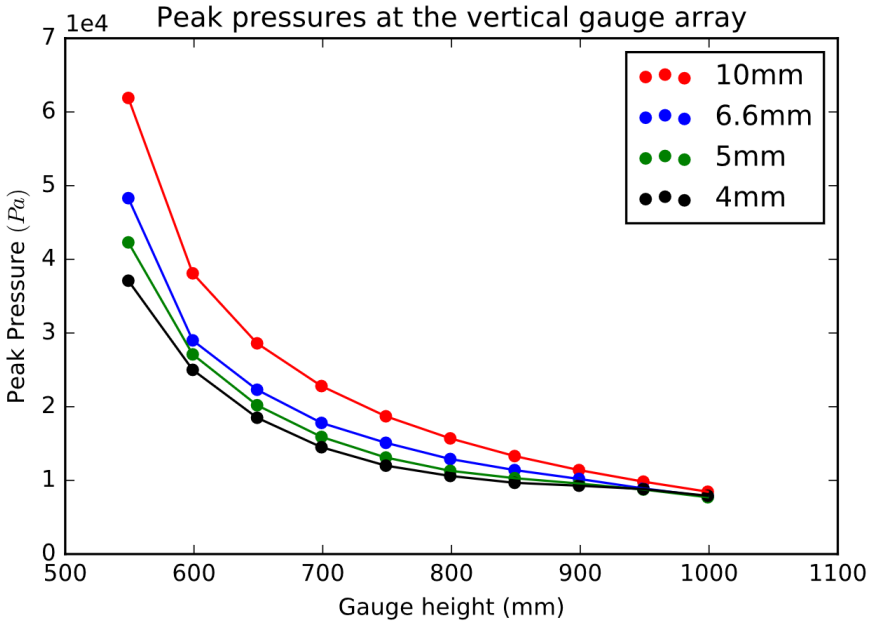

Figure 5.13: Peak pressures achieved over the vertical gauge array for mesh sizes ranging from 10-4mm

gauges are shown in Figures 5.13 and 5.15.

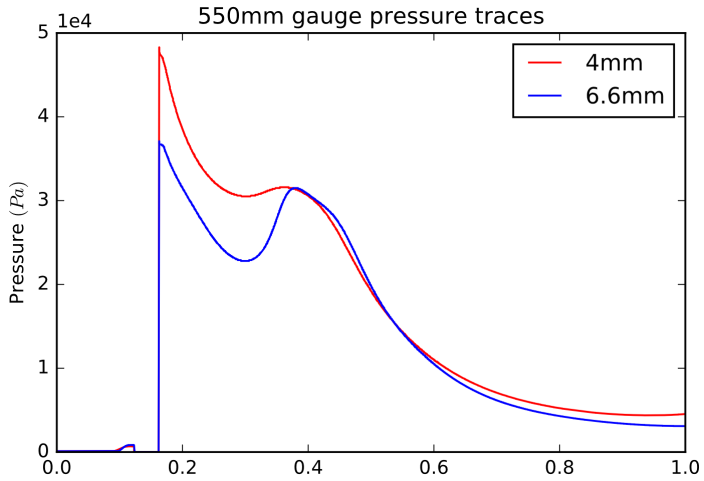

Figure 5.14: A comparison between the pressure traces observed at the lowest gauge point for meshes of 4mm and 6.6mm; the secondary peak reaches an identical magnitude, while the initial Friedlander-type pressure peaks differ.

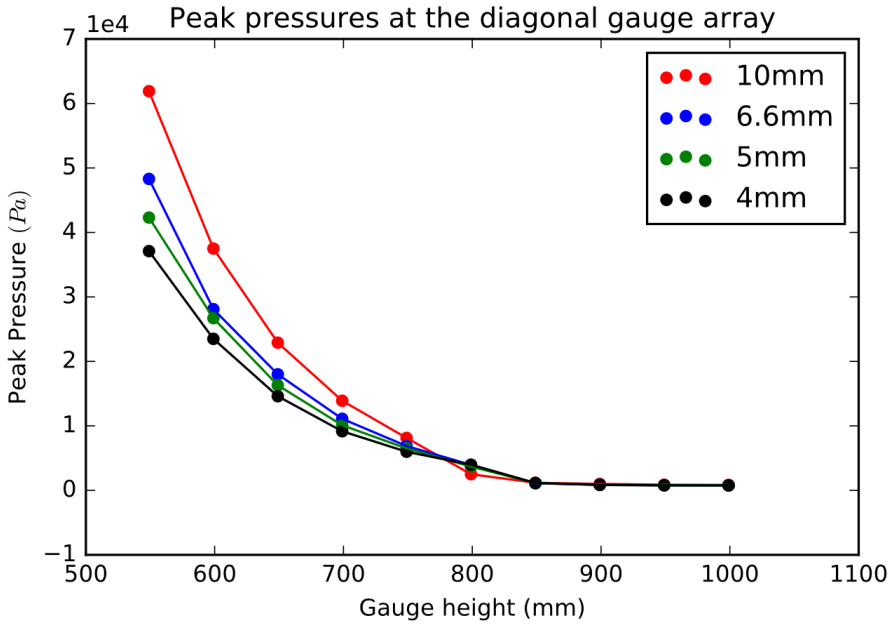

Figure 5.15: Peak pressures achieved over the diagonal gauge array for mesh sizes ranging from 10-4mm

Significant variation in the pressure condition at the 550mm gauge with respect to mesh size is seen in Figure 5.13. This difference in pressure is not consistent over the array, and the pressure across all 4 mesh scales is converged at the 1000mm gauge. While full convergence does not occur for any mesh scale, the greatest variation in measurement occurs at the lowest gauge point. Similar results are seen in the diagonal array; while the pressure closest to the charge varies significantly, the difference in pressure between mesh sizes reduces with distance until 850mm, at which point the peak pressures become comparable. Beyond this distance, the pressure is significantly reduced. It is noted that the simulation with the coarsest (10mm) mesh terminates on the basis of excessive energy error if the default limits are applied. A sharp variation in the calculated energy error plot is observed corresponding to the time-frame of the initial charge detonation. The pressure at very close range is therefore attributed to major variations in the accuracy of the detonation process across meshes. While AUTODYN cannot distinguish between materials on a local gauge level, bulk properties for materials in the multi-material Euler solver can be examined. The effect of the variation in detonation on the total kinetic energy transferred to the sand is examined

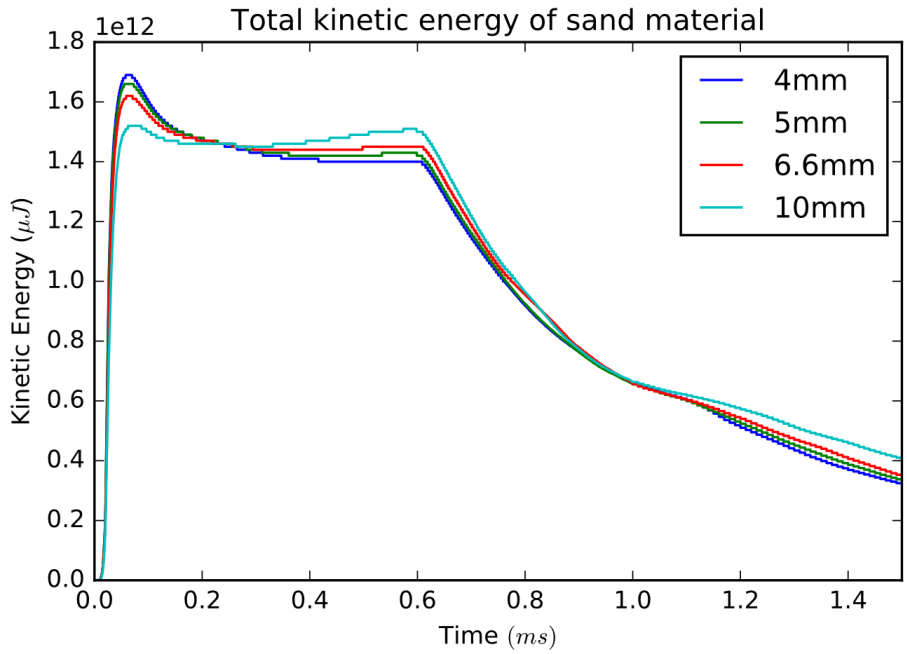

Figure 5.16: Total kinetic energy of the sand material over time with respect to individual mesh element size

Table 5.7: Relative difference in kinetic energy at 0.6 ms

	Mesh size (mm)			
	10	6.6	5	4
% Difference E_k :	6.62	2.76	1.4	N/A

in Figure 5.16. An initial rapid transfer of kinetic energy is followed by a steady decline, with an inflection point shortly after $0.6ms$ corresponding to the time at which the slug encounters the outflow condition. On examination of the simulation domain, it is assumed that the majority of the kinetic energy belongs to the material ejected vertically. With respect to the mesh, the kinetic energy traces represent an apparent paradox which is most apparent for the 10mm mesh; despite the considerably higher gas pressures across the vertical gauge points, the initial total kinetic energy transfer to the sand on a coarse mesh is the lowest, while rising to the largest value by the time the slug begins to exit. The inverse is true for the remaining mesh scales, and is ordered accordingly. The relative difference in kinetic energy from the coarsest to finest mesh at 0.6 ms is given in Table 5.7.

5.4 Plate - Blast Interaction

The response of a quadrangular plate affixed above the blast is now examined using the geometry of Section 5.1. The plate is $1000mm$ per side (500mm per symmetry quarter), with a thickness of 25mm as per STANAG 4569. The underside of the plate is 500mm above the soil, a stand-off distance of 600mm from the charge. To allow the deformation of the domain, the Euler mesh extends into the region above the plate to a total y-axis height of 1200mm.

Plate model

The selection of a deformable metal model is informed by the need for a material with both ductility (to reflect the variation in loading) and high toughness (to withstand significant deformation without rupture). During initial simulation tests, two steel models were examined for use as a witness plate: RHA (Rolled Homogeneous Armour, a military-grade steel), and Steel 4340 (a high-toughness high-strength nickel-chromium-molybdenum alloy). A desirable characteristic for a witness plate material is an ability to achieve a high range of deformation under variable loading (the better for establishing load variation) while exhibiting relatively little excess elastic motion. Steel 4340 was found to deform predictably and smoothly under blast loading. By contrast, while highly resilient to blast loading, RHA exhibited a significantly higher degree of elastic motion. Steel 4340 is selected as the material for both the witness and perforated plates.

In AUTODYN, steel 4340 is modelled with the Johnson-Cook strength model. The Johnson-Cook yield stress is defined as

$$\sigma_y = [A + B\epsilon_p^n][1 + C\, ln\epsilon_p^*][1 - T_H^m] \tag{5.5}$$

where the 5 parameters A, B, C, n and m are model constants, ϵ_p is the effective plastic strain, ϵ_p^* is the normalised effective plastic strain rate and T_H is the homologous temperature defined as

$$\frac{T - T_{room}}{T_{melt} - T_{room}} \tag{5.6}$$

which has a value of 0 when the material is at the reference temperature. The model parameters are given in Table 5.8.

Table 5.8: Steel 4340 modelling parameters

Parameter	Value
Density (ρ)	$7830\,kg\,m^{-3}$
Shear Modulus	$8.28 \cdot 10^{10}\,Pa$
Bulk Modulus	$1.59 \cdot 10^{11}\,Pa$
Specific Heat Capacity	$477 J\,kg^{-1}\,C^{-1}$
Initial temperature	$285.16\,K$
Johnson-Cook Parameters	
Initial Yield Stress (A)	$7.92 \cdot 10^{8}\,Pa$
Hardening Constant (B)	$5.1 \cdot 10^{8}\,Pa$
Hardening Exponent (n)	0.26
Strain Rate Constant (C)	0.014
Thermal Softening Exponent (m)	1.03
Melting temperature (T_{melt})	$1793.06\,K$

5.4.1 Solver settings and meshing

The Euler domain settings and total simulation time of 5 ms are the same as in Section 5.1. As a Lagrangian body is now present, the Euler-Lagrange coupling method described in Chapter 2 is applied to model the fluid-structure interaction. The witness plate is modelled using a hexahedral mesh with full nodal integration. Multiple element scales are investigated. The mesh sizes and simulation identifiers are given in Table 5.9; as the Euler domain is now expanded to allow the deformation of the plate to be captured, the Euler cell counts are higher than in the preceding simulations.

Table 5.9: Mesh sizes for the Lagrangian and Eulerian domains, and associated cell counts.

	Simulation			
	S1	S2	S3	S4
Euler mesh (mm):	10	6.6	5	4
Lagrangian mesh (mm):	12.5	6.25	6.25	5
Euler element count:	300,000	1,043,493	2,400,000	4,687,500
Lagrangian element count (mm):	3,200	50,000	50,000	97,656

5.4.2 Results

The detonation of the charge and the formation of the sand-slug is identical to that of Section 5.3. The introduction of a flexible Lagrangian body significantly alters the computation time; for the highest resolution simulation (S4), 5-6 days of run-time across 16 cores are now required to progress the simulation to 5 ms. The simulation is also significantly less stable at this resolution. Under the default AUTODYN settings, simulations S3 and S4 initially terminated early as the dynamic time-step reached a default minimum limit. Alteration of the Euler cover fraction (the volume criteria by which Euler cells are merged with neighbours when intruded upon by a Lagrangian mesh) to 0.4 allowed the simulation to run to completion; the time-step instability is thus attributed to the rapid deflection of the plate into the fine Euler volumes. In addition to the numerical instabilities, memory leaks repeatedly caused simulations S3 and S4 to be halted by the Linux operating system on ARC3, requiring brief but frequent local solution of the model. The memory leak behaviour was not replicated on the Windows operating system of the local machine. The interaction of the slug and blast with the witness plate is shown in Figure 5.17, from the initial slug contact through to the peak deformation of the plate.

- 0.6ms: The tip of the sand-slug has just begun to make contact with the plate. Full separation of the slug from the surface has not yet occurred. A large volume of detonation products lies within the cavity behind the slug.

- 0.8ms: The sand-slug has begun to separate and tear away from the surface material and has made partial contact with the plate, although the edges of the initial slug are still visible. Initial venting of the detonation products through the tearing of the sand can be seen. The deformation of the plate has begun, with a sharp deflection in the local region impacted upon by the slug.

- 1.0ms: The initial slug has now made full contact. The launching of additional material from the edge of the crater is seen. The irregular venting of detonation products has become more pronounced, and is beginning to encounter the flow-out condition at the limits of the domain. The deformation of the plate is still limited to the regions struck by the sand-slug, but continues to grow.

- 1.2ms: The detonation products and sand-slug are now fully engaged with the

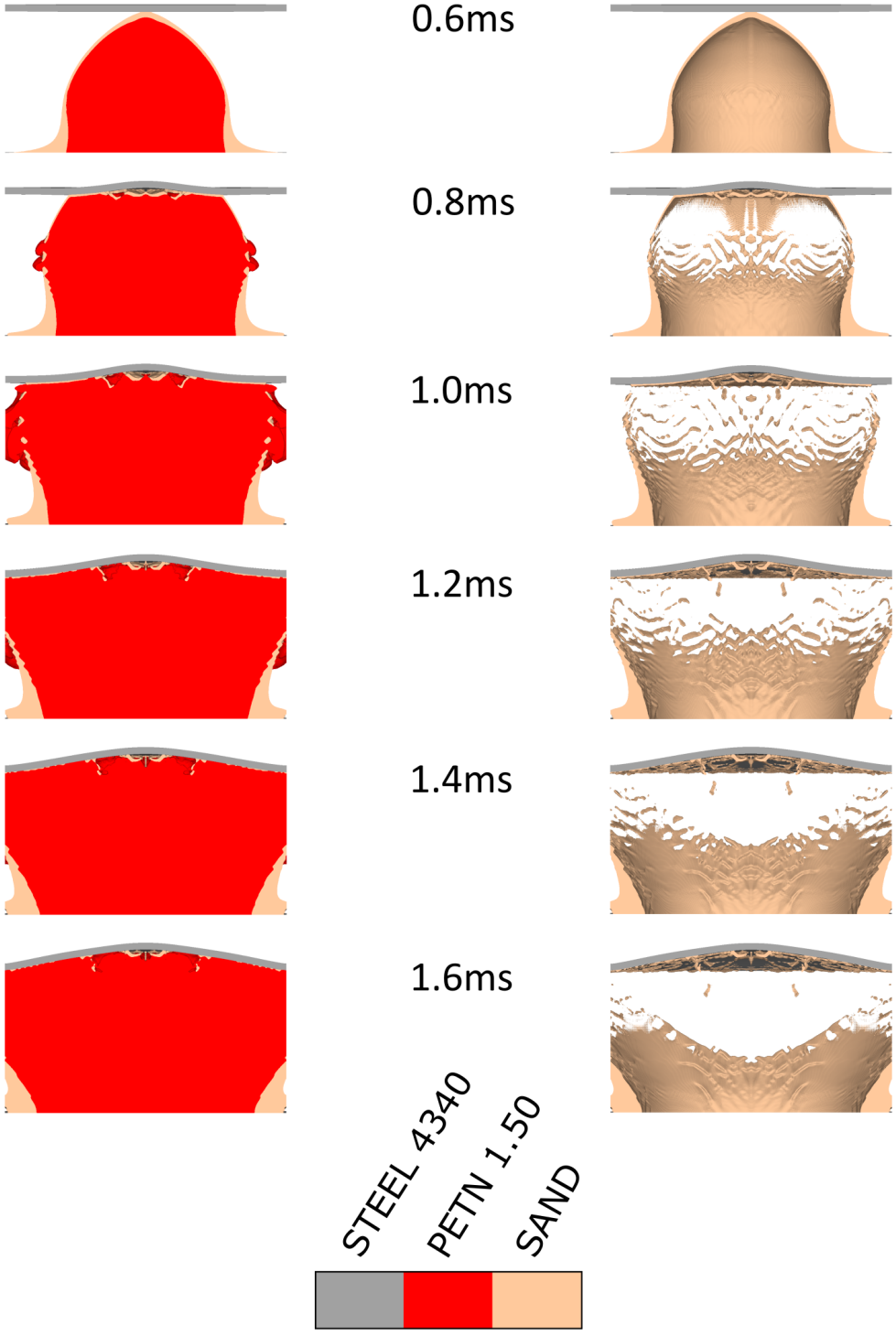

Figure 5.17: The deformation over time of a solid, unprotected witness plate exposed to a simulated mine blast. Blast products are shown in red in the left set of images. Venting of the blast products at the separating base of the sand-slug can be seen. The sand component of the blast is shown in the right image set.

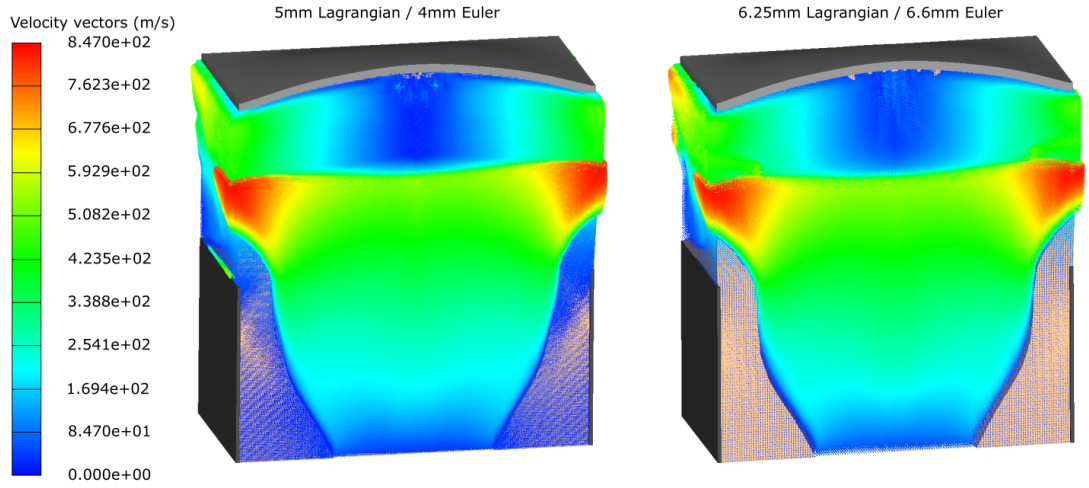

Figure 5.18: The state of the detonation and plate response for simulations S2 (right) and S4 (left) at 2ms. A slightly smoother crater can be seen in S4. The magnitude of the gas velocity is the same, and given by the inset legend.

plate. The initial sharp, local deformation of the center of the plate is becoming less pronounced as the entire plate is now beginning to bend and deform upwards through a combination of gas pressure and solid material impact.

- 1.4ms: The plate continues to deform. The impact of the initial sand-slug is now secondary to the continued deformation of the plate by the pressure

- 1.6ms: The plate has now reached the first deflection peak. The initial slug-driven local deformation peak is still present, and the deformed plate has a discernable two-tiered deformation, in which the central region has a slightly greater deformation than the material towards the edges.

An overview of the domain including the velocity of the gas products is shown in Figure 5.18 for simulations S2 and S4. The slug has impacted and the initial shock is reflected from the plate, driving the continuing gas flow outwards and to the side.

The centre-point deflection of the plates over time is shown in Figure 5.19. Beyond 1.6ms, a consistent behaviour can be seen in which the plate deforms vertically to a

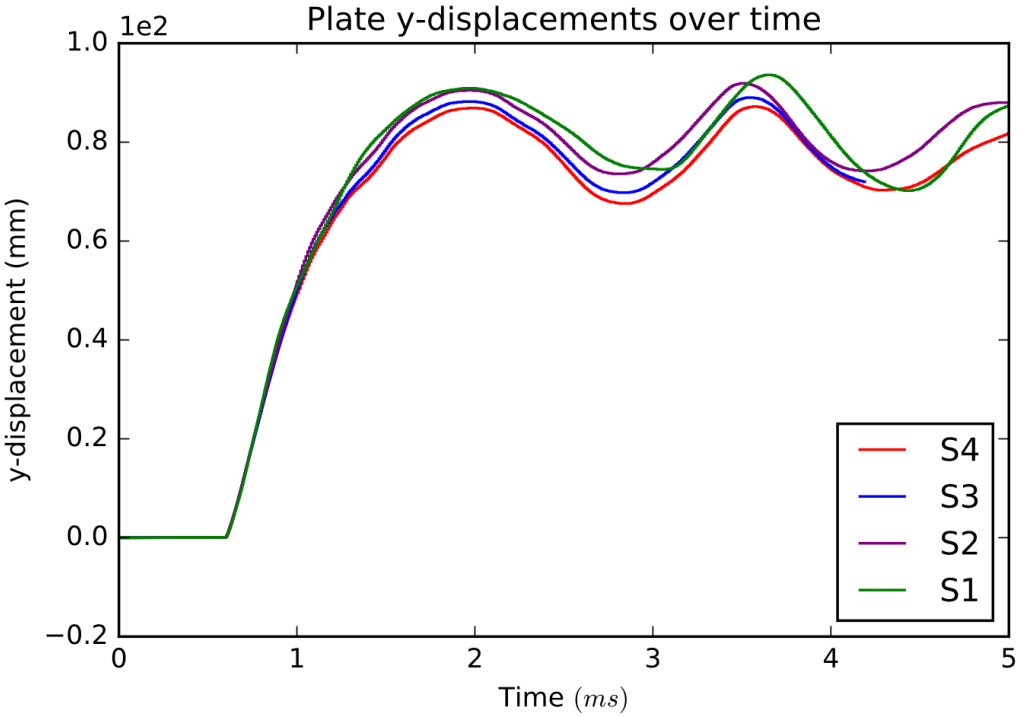

Figure 5.19: Deformation of the witness center-point over time across varying mesh scales.

Table 5.10: Peak plate deflections by simulation

Simulation	S1	S2	S3	S4
Peak Deflection (mm)	90.92	90.45	89.03	86.89
% difference from finest mesh	6.94	3.9	2.41	N/A

point of maximum deflection, before oscillating around a new average position. However, the magnitude of the displacement varies across mesh scales. The variation in the peak deflection is summarised in Table 5.10.

In Figure 5.19 and Table 5.10, it can be seen that the peak deflection declines with an increase in simulation resolution. The reduction in peak deflection with increasing mesh resolution reflects the lower measured air pressures and slug kinetic energies as examined in Section 5.3. The deflection values are derived from the motion of a single gauge placed directly above the charge in the region in which the loading is anticipated to be highest. To compare the deflection in a broader sense, the deformation of the

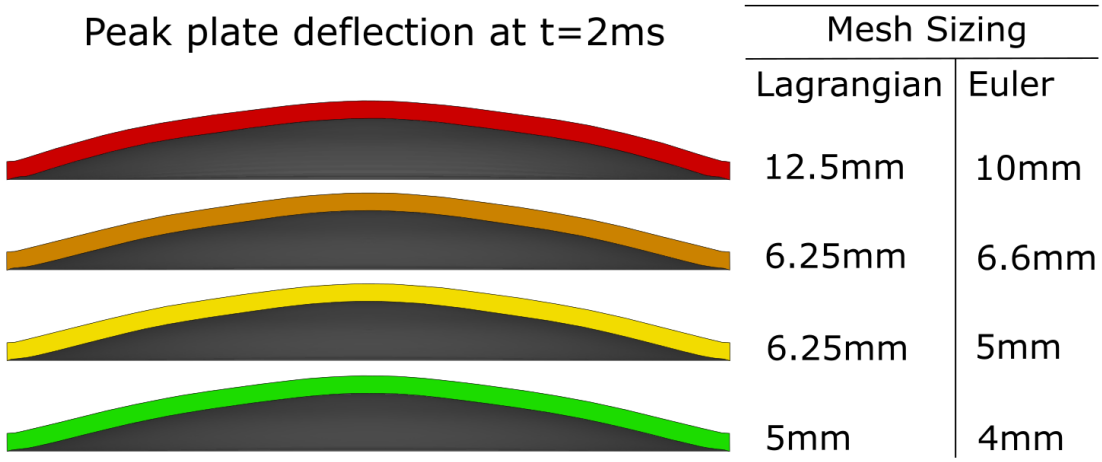

Figure 5.20: Deformation of the single solid plates at $t = 2ms$, the instant of peak deflection across all plates.

plate across the midsection is shown in Figures 5.20 and 5.21, allowing for comparison of the state of the plate close to the moment of greatest deflection. In Figure 5.21, the variation in deflection across the full cross-section of the plate can be seen to be consistent, with the greatest deviations occurring for the simulation with the coarsest mesh. A slight narrowing of the material adjacent to the fixed edge of the plate consistent is visible, consistent with the shear thinning of edge-clamped plates observed by Langdon et al.

5.5 Discussion

This Chapter presents the results of 3-dimensional buried charge detonations. A 6.34kg PETN-B charge is buried at a depth of 100mm under a dry, coarse-grained sand with a moisture content of 6.57%. Pressure measurements in the region above the charge were taken. A 25mm thick edge-clamped steel witness plate model was examined with respect to the deflection imparted by the blast. Significant attention is given to the effects of mesh sizing.

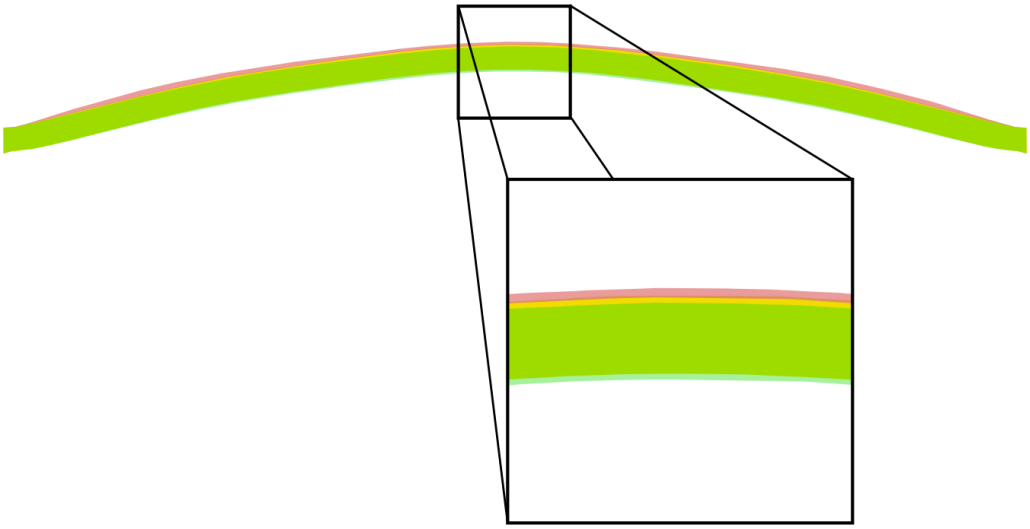

Figure 5.21: Overlaid plate profiles and inset magnification at the time of greatest deflection; colouration as in Figure 5.20. A consistent variation in deflection across the plates can be seen

5.5.1 Initial buried charge simulation

Both sand and charge are modelled using a multi-material Euler approach. While in response to the need to model the extreme deformation of the sand-slug as it passes through an aperture, this approach imposes certain limitations:

- For this solver the mesh cannot be refined, and must remain at a fixed and consistent scale throughout the simulation. In addition to posing practical limitations on the size of the computational mesh, there is significant variation in the pressure close to the slug. A progressive reduction in the variation with distance is observed. Convergence of the pressure at very close range could not be achieved with a practical mesh sizing.
- The multi-material solver is incapable of distinguishing between loads exerted by different materials, as reflected in the convolution of the pressure trace with the passage of the sand-slug. This prevents assessment of the relative contribution of the slug to the loading.

Similar results for the multi-material scheme and Laine-Sandvik sand model as applied in this Chapter are seen in the work of Fišerová. In that work, only rough agree-

ment with empirical CONWEP measurements at close range could be achieved with 2-dimensional mesh sizes of less than 0.1mm, a scale impractical for a 3D simulation with the dimensions applied here. Despite the identified limitations of the multi-material approach, the predictions of the initial buried charge simulations are consonant with the detonation of a buried charge. The expected features of a mine-blast detonation including the formation and ejection of a sand-slug, venting of detonation products and the cavitation and compression of the surrounding sand are present. The sand at the interface between ground and air undergoes the expected tensile failure, and it is further noted that the internal angle of the ejected slug is approximately 60° (depending on measurement location), although caution is applied to a feature which is dependent in part on the hydro-tensile failure condition.

5.5.2 Witness plate interaction

Exposure of a 25mm thick witness plate to the detonations simulated in this Chapter produces deformations broadly (allowing for differences in experimental configuration, including witness plate separation and charge composition) comparable to those observed by Bouamoul et al [22]. Despite the range of pressures observed close to the charge, the variation in the deformation of the witness plate across mesh scales is considerably smaller, and comparable to the variation in slug kinetic energy. On the basis of the observed deformation history as shown in Figure 5.19, it can be seen that the variation between progressively higher resolution simulations is decreasing, to the degree that simulation S4 can be considered to be fully converged. However, the element count and associated computational expense is significantly greater for a mesh of this scale. The trend is also for higher resolutions to produce lower pressures and peak deflections. In the interests of ensuring both a conservative estimate and computational tractability, a Lagrangian mesh size of 6.25mm and an Eulerian mesh size of 6.6mm are selected for use in the following Chapter, in which a perforated plate defensive scheme is inserted between the charge and witness plate.

Chapter 6

Perforated Plate Mine Blast Simulations in AUTODYN

6. PERFORATED PLATE MINE BLAST SIMULATIONS IN AUTODYN

In this Chapter, the techniques and models previously established for the simulation of a buried charge blast based on STANAG 4569 testing conditions are applied to the case of a flat witness plate protected by a range of perforated plate designs. As previously noted in Chapter 1, while perforated plates have been suggested as a form of land-mine defence, no investigation has been performed into their performance in a mine blast scenario that incorporates threat elements such as non-planar shocks and gas flow, the dynamics of soil ejecta, and charges of a size representative of a typical mine or IED. This work is the first investigation of perforated plates as a form of mine or IED protection in which mine-blast specific features are considered. As the primary intent is to provide protection (as opposed to the flow investigations of Chapter 4), the porosity of these plates is reduced to $\varepsilon = 0.2$. The scenario of interest is shown in Figure 6.1.

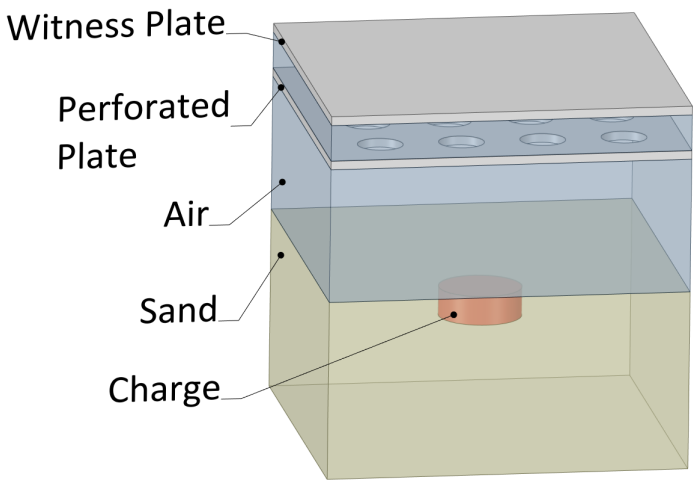

Figure 6.1: Isometric view of the perforated plate test environment. The containing wall around the sand is not shown.

The blast-facing side of the witness plate begins 500mm above the surface of the sand, a distance of 600mm from the charge. As in Chapter 5, the witness plate is constrained at the edges. This represents a deviation from the free-flying plate scenario of the STANAG 4569 methodology. The reason for this decision is that determining the particular method by which the perforated plate may be affixed to the underside of a vehicle is not trivial, and establishing the optimal method of doing

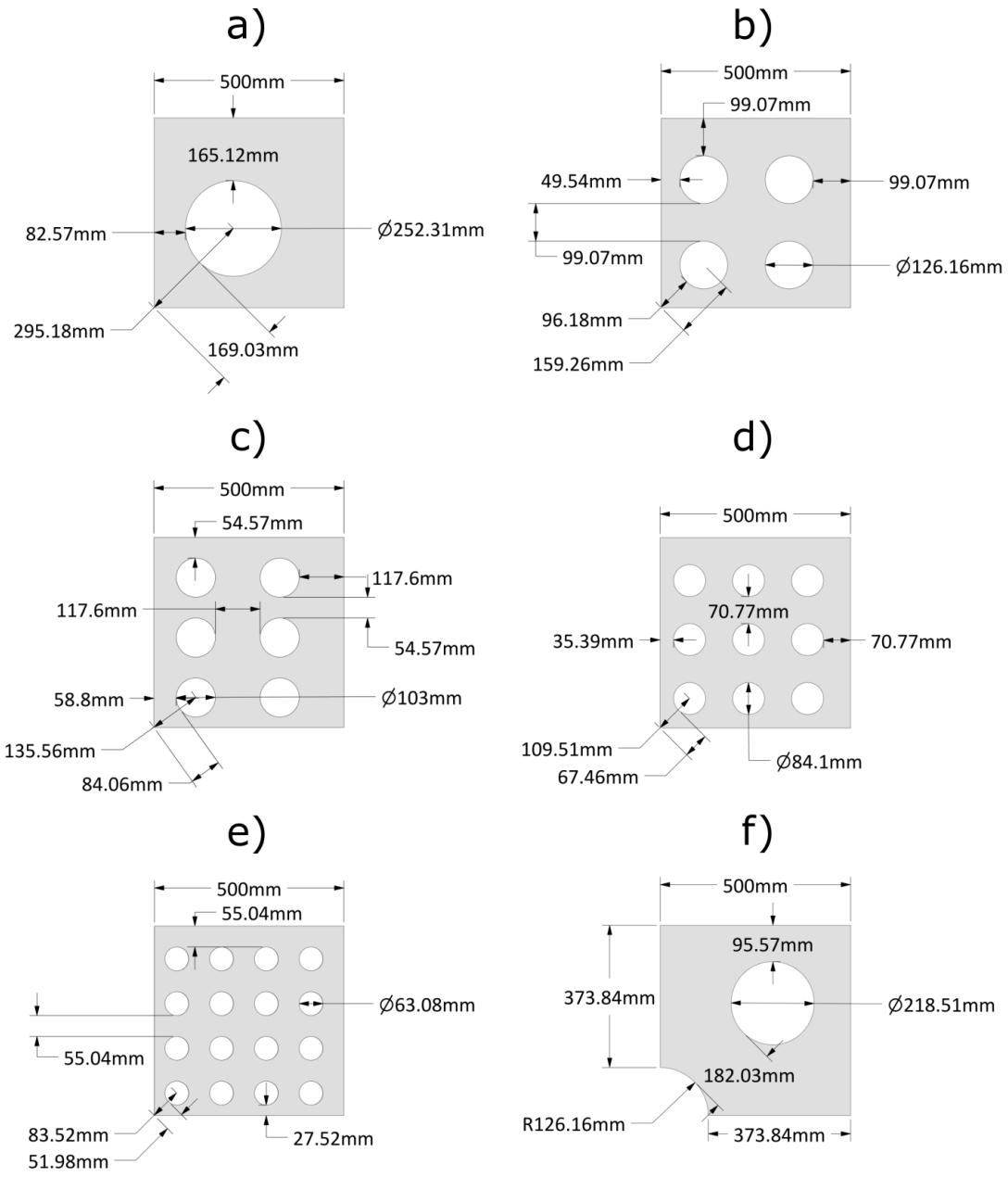

Figure 6.2: Plate designs and dimensions over the quarter symmetry for a) 4 b) 16 c) 24 d) 36 e) 64-hole plates. f) is a plate with a central aperture corresponding to the dimensions of the hole in a). The central origin of symmetry for each plate is located at the bottom left corner of each plate quarter.

.

so is beyond the scope of this current investigation. The rear-side of the perforated plate is placed at a 100mm separation distance from the face of the witness. The blast-facing side of the perforated plate is 375mm above the surface of the sand, translating to a 475mm stand-off distance from the surface of the charge itself. The perforated plates examined in these tests have varying numbers of circular apertures: 4, 16, 24, 36 and 64-hole configurations are examined. The dimensions of these plates are shown

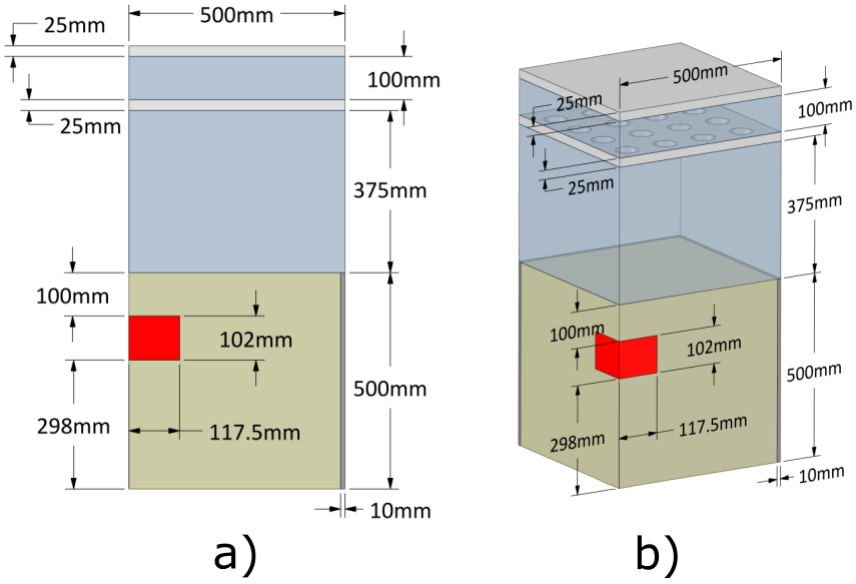

Figure 6.3: Standard dimensions of a perforated plate simulation domain in a) side-on view and b) isometric. The perforated plate shown is for the 64-hole design (16 holes per symmetry quarter)

.

in Figure 6.2. The perforations are evenly spaced across the plate; this places the apertures for the 4-hole plate ((a) in Figure 6.2) at a significant distance from the center of the blast. As the assumption cannot be made that detonation will always occur in an optimal position, an additional plate ((f) in Figure 6.2) with a central aperture of equivalent diameter to the perforation in a) is also considered. The total porosity of the (f) plate is maintained as $\varepsilon = 0.2$ through the use of an additional smaller aperture. The dimensions of the simulation domain are shown in Figure 6.3. Evaluation of the defensive properties is made on the basis of the deformation of the witness plate. This plate serves as a stand-in for a notional vehicle hull, and as described in Chapter

1 the deflection or rupture of this surface is a major risk factor for vehicle occupants. The perforated plate scheme is compared with two alternative designs. These designs are shown in Figure 6.4.

- Comparison 1 (C1): No protective plate is applied. Instead, the witness and perforated plates are combined into a single solid plate of equivalent combined mass. This plate is 45mm thick, and is placed at the same stand-off location as the witness plate.
- Comparison 2 (C2): A solid plate of equivalent mass to the perforated plate. This plate is 20mm thick, and is placed at the same separation as the perforated plates, 100mm from the standard witness plate. The structure of the C2 plate array is an approximation to a defensive adaptation used in modern armoured vehicles, in which the internal vehicle floor is isolated from the exterior hull. This prevents the direct transmission of blast shock to the crew compartment [57].

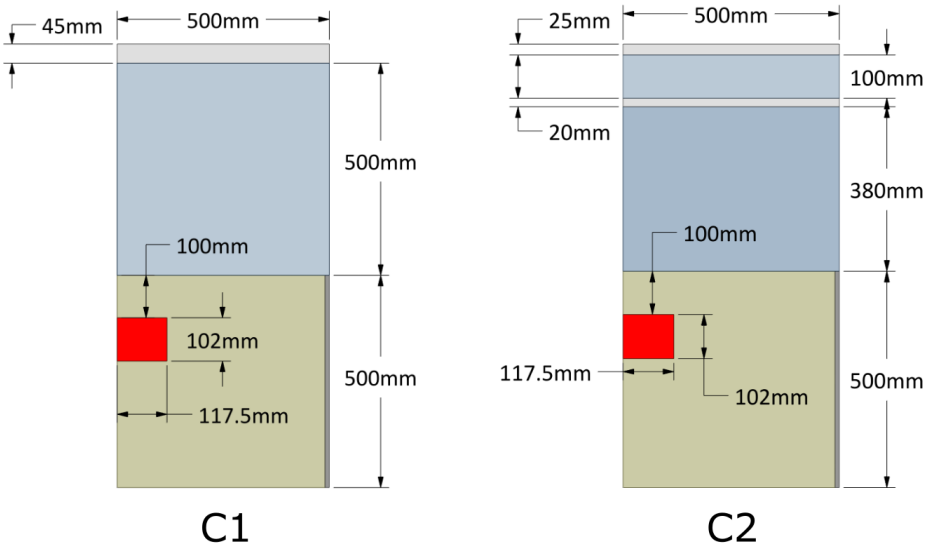

Figure 6.4: Dimensions of the C1 and C2 plate test environments as seen from the side. All plates shown are solid.

To determine the relative contribution of slug loading and gas pressure to the deformation of both the witness and perforated plate, and to compare the dynamics to those of the comparison plates, an additional set of simulations is performed for surface

flush charges at stand-off distances of 500 and 600mm from the witness plate. Only the 64-aperture plate is considered in the surface-flush tests. The dimensions of the simulation domain are shown in Figure 6.5.

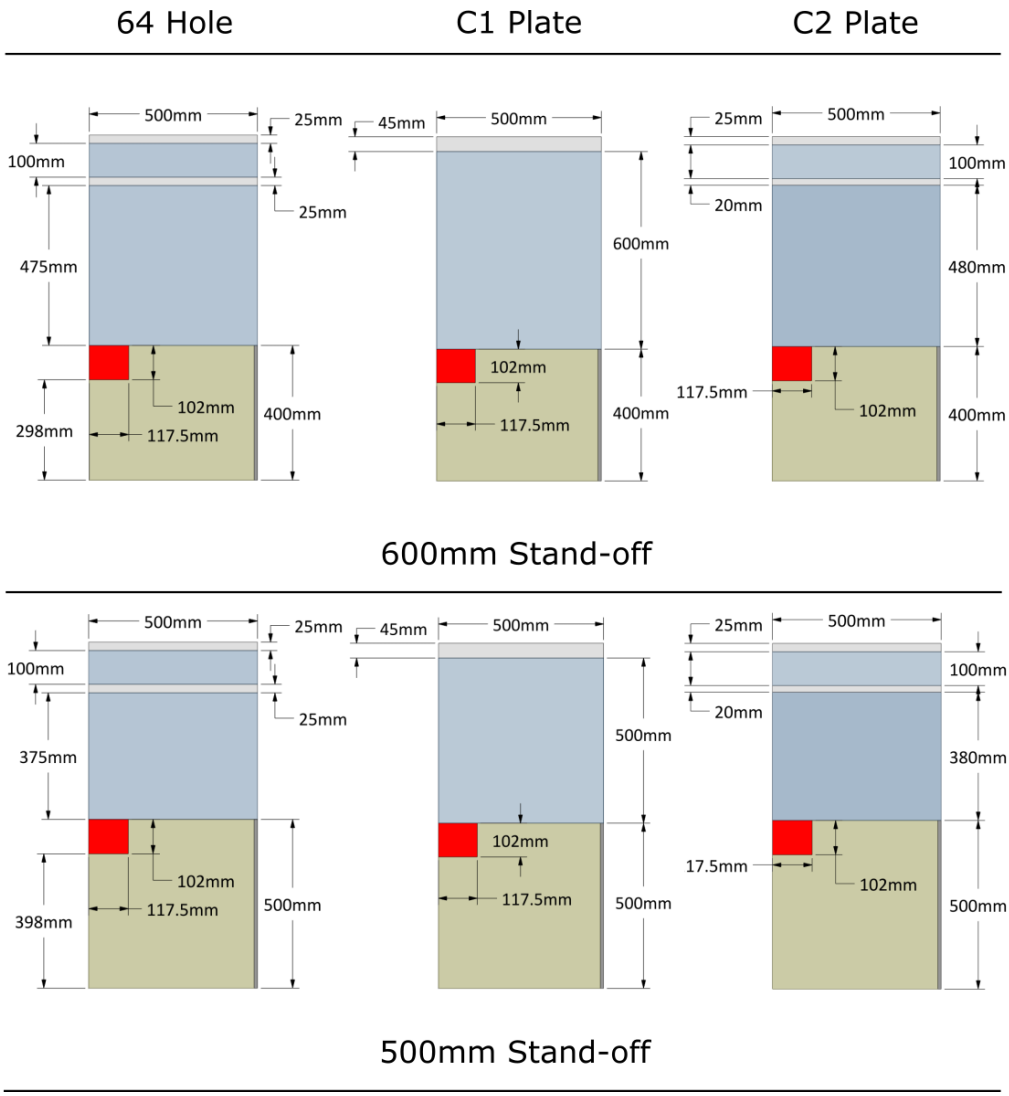

Figure 6.5: Dimensions of the surface flush comparison cases.

In all cases, the mesh sizes identified in the preceding Chapter as an optimum balance between accuracy and computational efficiency are applied.

6.0.1 Measurements

From the centre of the rear of the innermost aperture, Euler gauges with spacings of 20mm are placed from 900mm to 980mm. A Lagrangian gauge is embedded in the center of both the witness plate and perforated plate, to assess the relative y-deflection of each. The arrangement of both Euler and Lagrangian gauges is shown in Figure 6.6.

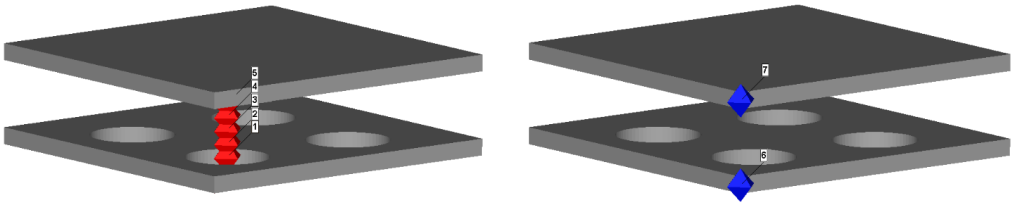

Figure 6.6: Gauge placement for the perforated plate mine-blast simulation. Red corresponds to fixed gauges in the Eulerian mesh, while blue corresponds to moveable gauges embedded in the Lagrangian mesh.

6.0.2 Solver configuration

The techniques and models described in Chapter 5 for the detonation, Euler material transport, simulation gravity and Lagrange-Euler interaction are applied. There is now the potential for collision between two distinct Lagrangian bodies; the penalty-contact method of Lagrange-Lagrange coupling described in Chapter 2 is used to capture the impact. As for the initial single-plate studies, simulations are run with a termination time of 5ms.

6.1 Results

6.1.1 Perforated Plates

The general progression of the detonation and its interaction with both the perforated plate and the witness plate are described as follows:

1. The detonation of the charge propels both sand and gas towards the plate arrangement.

2. The impact of the sand-slug begins to deform the perforated plate. At the same time, the sand-slug breaks apart, with sand passing through the apertures. This material strikes the witness plate; if the perforated plate apertures are small, this produces small dimples on the witness. If the apertures are large, more significant deformation can occur, depending on aperture position. This process is shown in Figure 6.7.

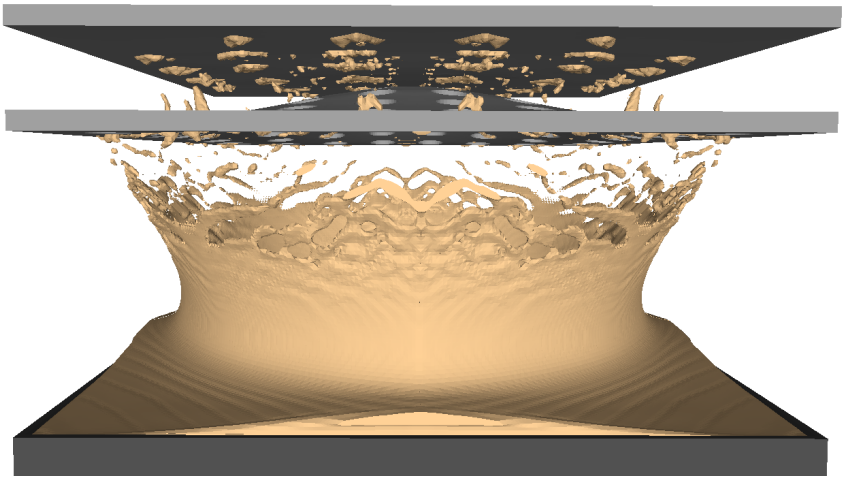

Figure 6.7: Visualisation of the sand intrusion through a 64-hole perforated plate. The initial sand-slug impact has deformed the perforated plate and partially disintegrated, with sand passing through the apertures. This sand strikes the witness plate. The continued ejection of sand from the lip of the crater propels sand through the majority of the perforations.

3. Following the sand-slug is the flow of gaseous detonation products. Unlike a planar shock-wave, the gas products from the detonation are initially in a roughly dome-like configuration, and the arrival of these products at the surface of the perforated plate is not simultaneous. On encountering an aperture, the gas products enter the hole. On the other side of the aperture, the flow develops into the jet-like structures as seen in Chapters 3 and 4.

4. As a jet encounters the witness plate, the flow is abruptly halted and stagnates and spreads out sideways, with a corresponding increase in pressure. If not initially impacted by the sand-slug, the witness plate begins to deform under this loading.

5. The staggered arrival of the detonation products over the perforated plate surface has consequences for the flow field behind the perforated plate, most noticeably for plates with smaller, more numerous apertures. The gas flow developing through holes further from the central axis of the simulation domain (where the flow arrives later) is deflected away from the witness plate by the sideways spreading of the developed jet streams from the central holes. This can be seen in Figure 6.8

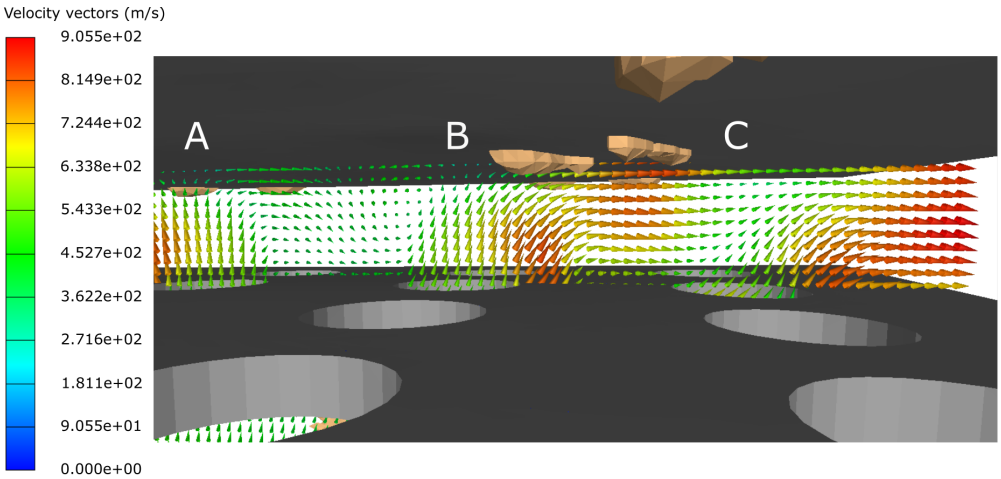

Figure 6.8: View of the flow-field from within the spacing between a 64-hole perforated plate and the witness. The aperture at position A is closer to the center of the detonation, and the jet flow through this aperture develops before the flow through B and C. The stagnation and spreading of the flow at the witness surface can be seen from the direction of the velocity vectors. At B, the flow is partially deviated by the spreading flow from A; a region of circulating flow can be seen where the two flows interact. At C, the velocity vectors are fully parallel to the surface of the witness, indicating that the flow through C is wholly deflected.

6. Both perforated plate and witness deform continuously until a peak deformation is reached, typically at around 2ms after detonation. Contact between the perforated plate and witness is observed for the 4 hole case. After this point, the perforated plate continues to oscillate in the y-axis around a new peak deflection. Similar behaviour is seen in the witness plate, although the magnitude and frequency of the oscillation is significantly less than that of the perforated plate.

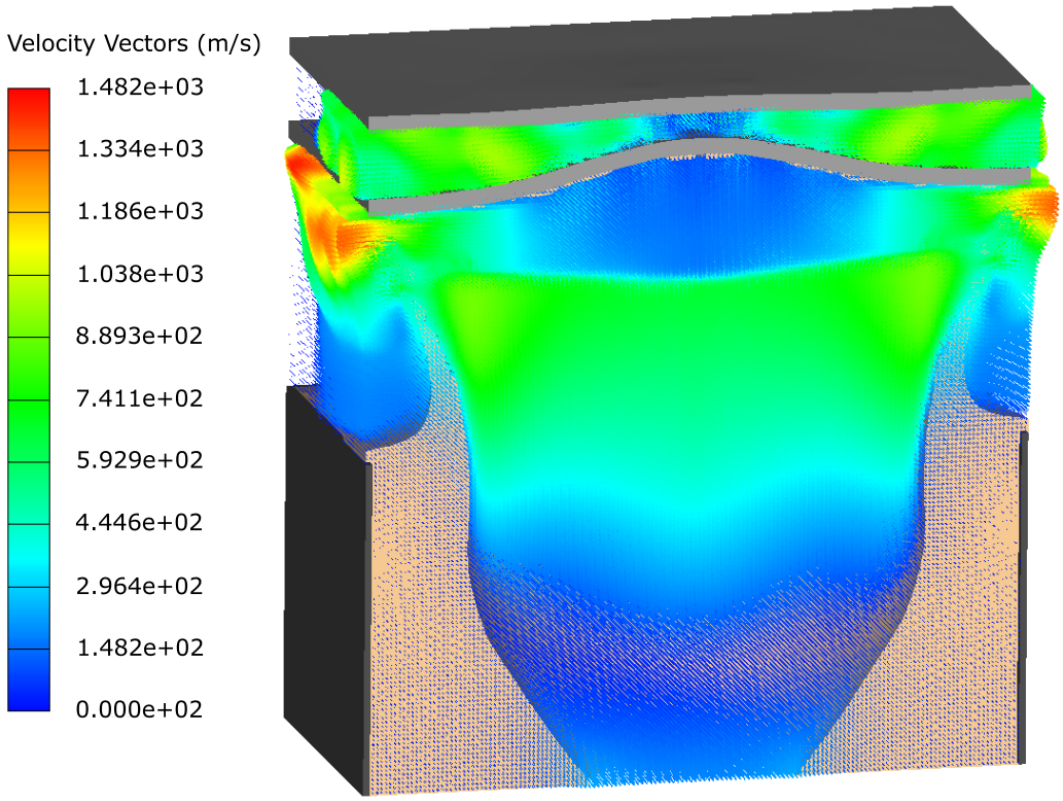

Figure 6.9: Cutaway visualisation of the blast impacting upon a 64-hole perforated plate $1ms$ after charge detonation. Velocity vectors are used to illustrate the gaseous flow-field. The flow of gas through the perforations can be clearly seen. The sand-slug has made contact with the perforated plate, locally deforming it in the impact region. It can be seen that the deformation of the perforated plate has consequences for the flow through the aperture; as the plate deforms, the direction of the gas flow through the apertures is altered, and spreads outwards. Sand has intruded through the perforations, striking the witness and forming small dimples which may be faintly seen on the top of the witness plate. The reflected shock from the perforated plate can be observed from the sharp delineation in the flow velocity in the region below the perforated plate. The charge cavity and continued ejection of material from the cavity lip can also be seen.

The general state of the simulation shortly after the arrival of the blast is shown in Figure 6.9, alongside commentary on the visible features. The displacement of both the

perforated and witness plates over time is shown in Figure 6.10. The peak deflections of the plates are summarised in Table 6.1.1, alongside a summary of the hydraulic ratio of individual apertures, the maximum downstream x/D_h and the peak pressure measured closest to the witness plate.

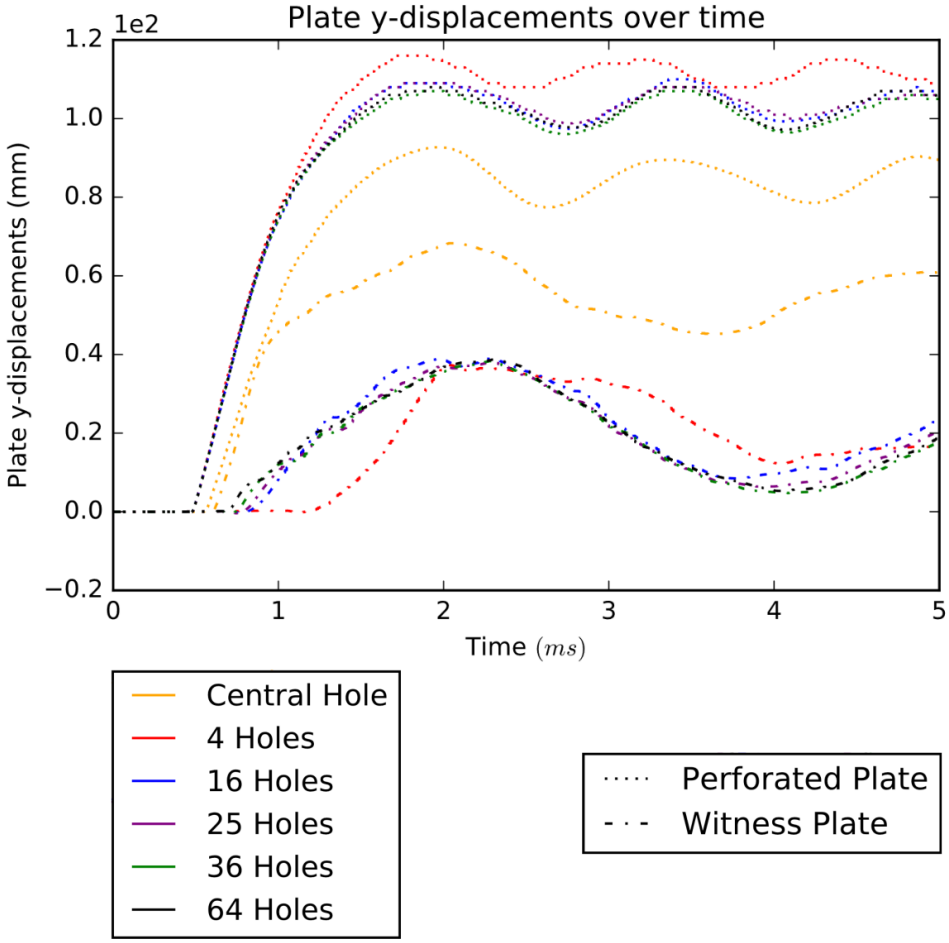

Figure 6.10: Vertical displacement over time for the perforated and witness plates. The dotted lines represent the perforated plates, while the dashed lines represent the witness plates.

In all cases the shock does not return to a planar configuration. The space between the perforated plate and the witness is dominated by jet-flow through the aperture. The pressure traces of the through-aperture gauges are shown in Figure 6.11.

Table 6.1: Peak deflections of the witness and perforated plates

	No. holes				
	4	16	24	36	64
Hydraulic Ratio	63.1	31.5	25.75	21	15.7
Peak gauge pressure (MPa)	14.2	19.9	21.4	25.3	20.4
Witness Deflection (mm)	37.28	38.92	37.82	38.29	38.72
Perforated Plate Deflection (mm)	115.97	109.95	109.47	107.26	108.38

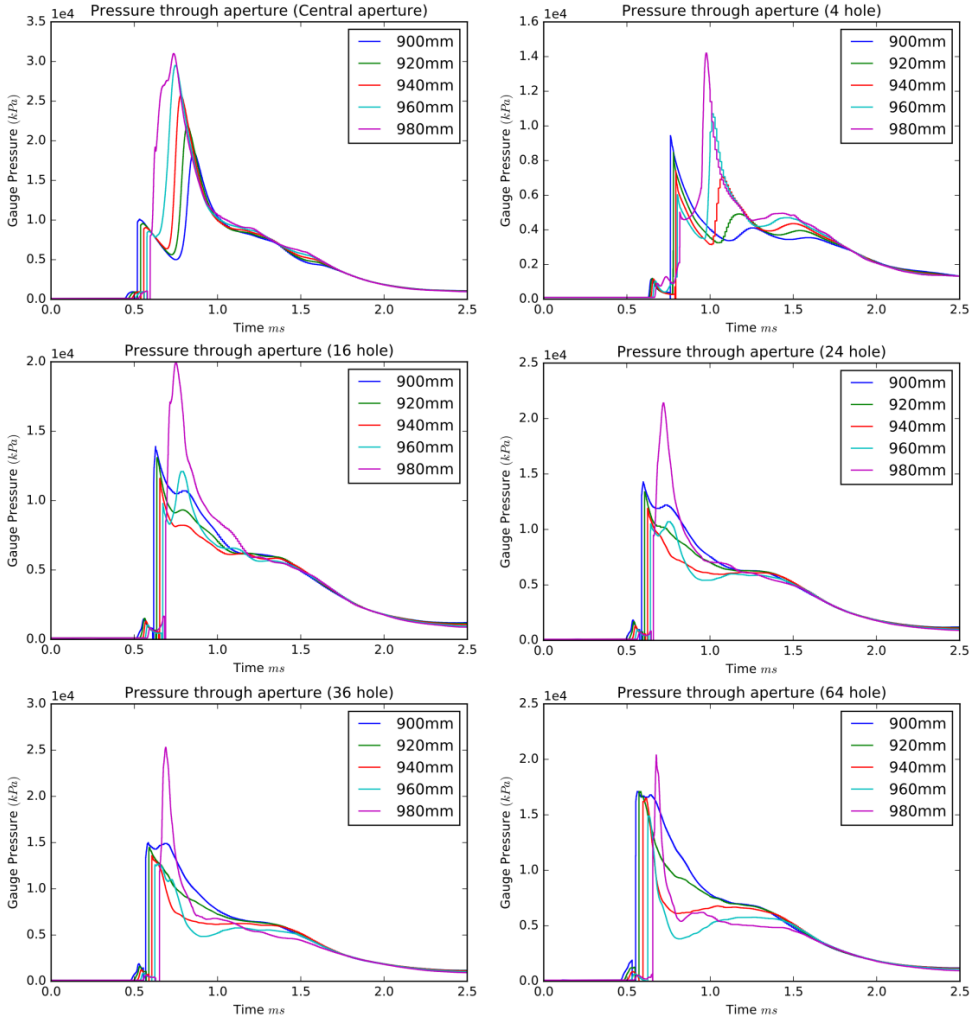

Figure 6.11: Pressure traces through the aperture closest to the center of detonation. An initial complex of small pressure peaks corresponding to the initial air-shock can be seen; this is followed by the flow of detonation products and the subsequent increase in pressure as the flow is arrested by the witness plate.

Across all cases, the initial flow pressure peaks decline with distance. On striking the rear wall, the flow is arrested resulting in a significant overpressure. This is reflected in the measured pressure at the 980mm gauge (closest to the witness plate) in Figure 6.11. The time-position of the pressure peak at the 980mm gauge is seen to be dependent on the number of apertures; in the 4-hole case, the peak occurs at 1ms, and occurs progressively sooner in plates with apertures closer to the center of detonation. Comparison between the pressures shown in Figure 6.11 and the displacement histories in Figure 6.10 shows that the plate begins to deform shortly after the 980mm gauge records a peak value. This indicates that in all cases the gauge is in close proximity to the witness plate at the time of peak pressure loading, allowing comparison of the peak magnitudes as a measure of mitigation.

Central aperture

The majority of the loading occurs directly above the detonating charge. It is not plausible to place the evenly-spaced apertures at equivalent distances from the center of the detonation, so the effects of aperture location are investigated through the use of a centrally-placed aperture of equivalent diameter to an aperture from the 4-hole plate. The central aperture case produces the highest witness deflection of 68.32 mm, a deflection 1.8 times greater than the original 4-hole plate. The deformation of the perforated plate reaches a maximum deflection at the aperture edge of 92.73mm. The peak pressure at the 980mm gauge is 31 MPa. Figure 6.12 shows the penetration of the aperture by the central peak of the sand-slug, which strikes the witness plate largely intact.

The plate configurations are edge-clamped, so studies cannot be made of the global vertical displacement of the array. Instead, Figure 6.13 presents the total momentum transferred to both plates over time in the y-axis as a sum of the momentum of each plate at a given time-step. The momentum across plate designs follows a similar behaviour over time, although there is a 9% total variation in the peak vertical momentum.

Perforated plate structural response

In Chapter 1, undesirable blast enhancement was observed in studies on the use of foams as a blast mitigation [36, 49, 52–54]. In developing a novel scheme, the possibil-

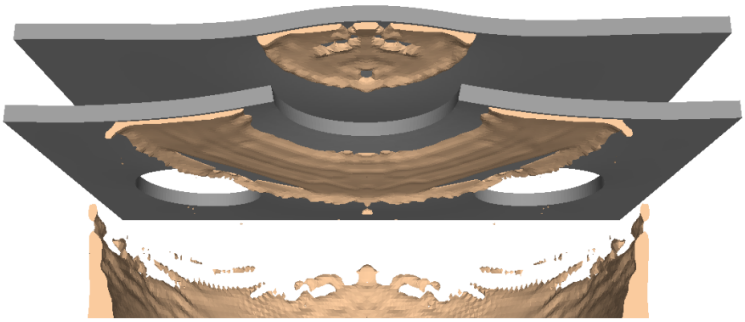

Figure 6.12: Passage of the sand-slug through a large central aperture directly above the locus of the blast.

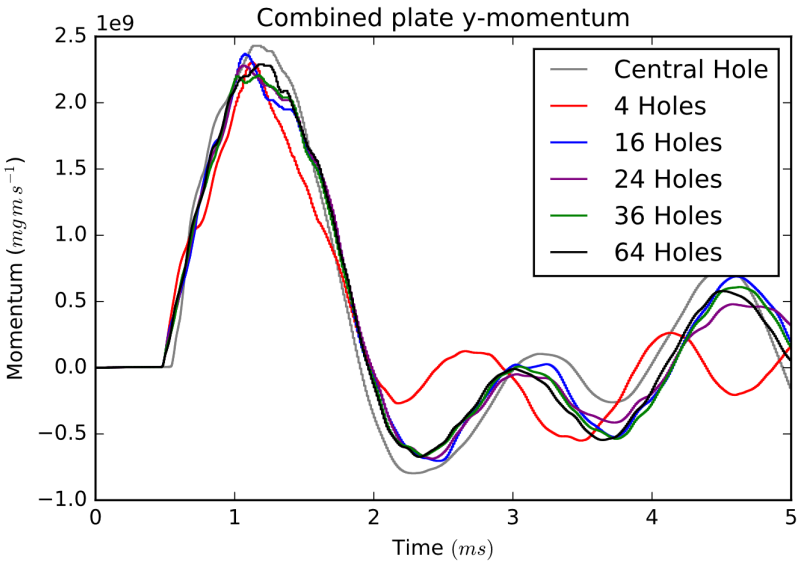

Figure 6.13: Total momentum of the plate array as a sum of the momentum of both plates over time. The total momentum is shown to be highly similar across plate designs.

ity of the scheme failing and actively enhancing the threat must be examined. Landgon [69] observed a "petalling" failure in perforated plates exposed to detonation, in which the failure of the plate occurred along the narrowest spacing between apertures. The effective strain and Von Mises stress present in the perforated plate at the moment of greatest deflection are presented for the 36 and 64 hole perforated plates in Figure 6.14.

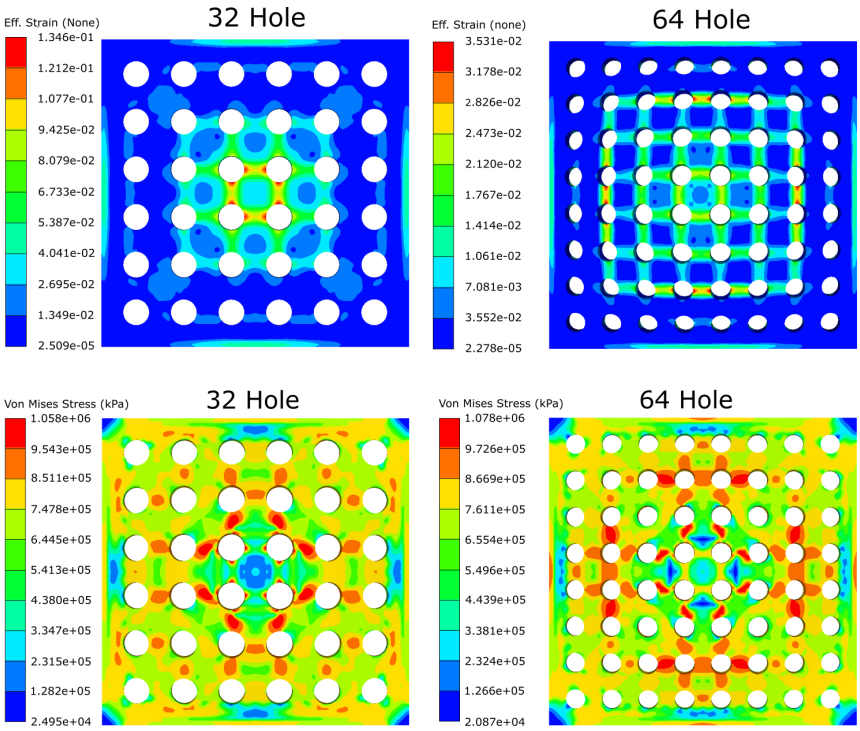

Figure 6.14: Von Mises stress and effective strain in the 36 and 64-hole perforated plates at the time of maximum deflection. The effective strain highlights the regions undergoing active deformation, indicating that the material has reached the Johnson-Cook yield stress. The Von Mises stress plot indicates the regions of the plate exceeding the tensile limit of the material. The strain in the 64-hole plate is highly localised and produces a grid pattern, with the regions of greatest strain lying along the shortest path between apertures. The strain is less localised in the 32-hole plate.

It can be seen in Figure 6.14 seen that the greatest stresses and strains are directed along the shortest distance between individual apertures. Thinning of the material

along these connections can be seen for the 64 hole plate in Figure 6.15.

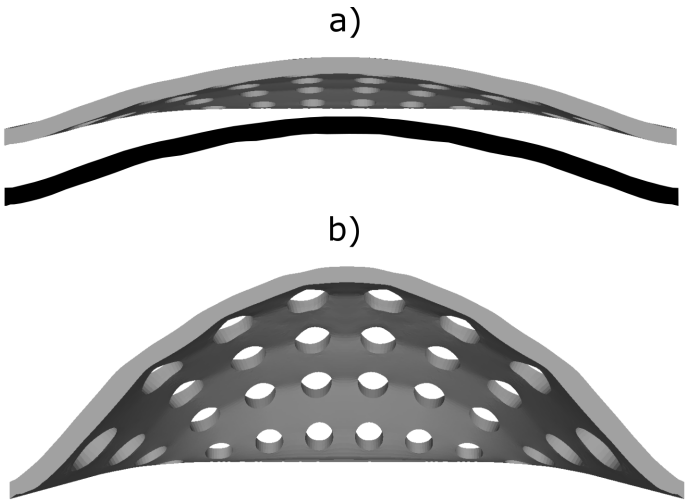

Figure 6.15: Thinning of the material between apertures. In a), the cross-section of the perforated plate at the time of maximum deflection (1.8ms) is seen alongside a silhouette of the cross-sectional face. In b), the deformation is amplified by a factor of 3 to enhance the visible thinning and expose the characteristically "ribbed" structure to the plate, a consequence of the thinning of material between apertures. This thinning corresponds to the regions of greatest strain seen in Figure 6.14.

6.1.2 Comparison Plates

The deflections for the comparison plates and their relative performance in reducing the peak deflection are shown in Table 6.17.

The C1 plate is a thicker version of the witness plate applied in Chapter 5 and behaves as such, although the displacement is considerably reduced. The solid protective plate in C2 is deflected upwards by the blast, and makes contact with the witness plate. It can be seen in the C2 y-displacement graph in Figure 6.17 that the start of the deformation of the witness plate coincides with the deflection of the protective plate to 100mm, indicating that the witness deformation is driven entirely by this contact. The total vertical momentum of the C2 plate array is dominated by the movement of the protective plate. The simulations at peak deflection are shown in Figure 6.17.

Table 6.2: Peak plate deflections by total number of perforations

	C1		C2		
Witness Deflection (mm)	53.13		12.2		
Protective Plate Deflection	N/A		112.3		
	No. holes				
	4	16	24	36	64
Witness Deflection (mm)	37.28	38.92	37.82	38.29	38.72
Comparison to C1 (% Reduction)	29.8	26.75	28.8	27.9	27.1
Comparison to C2 (% Reduction)	-67.3	-74.1	-67.7	-68.1	-68.5

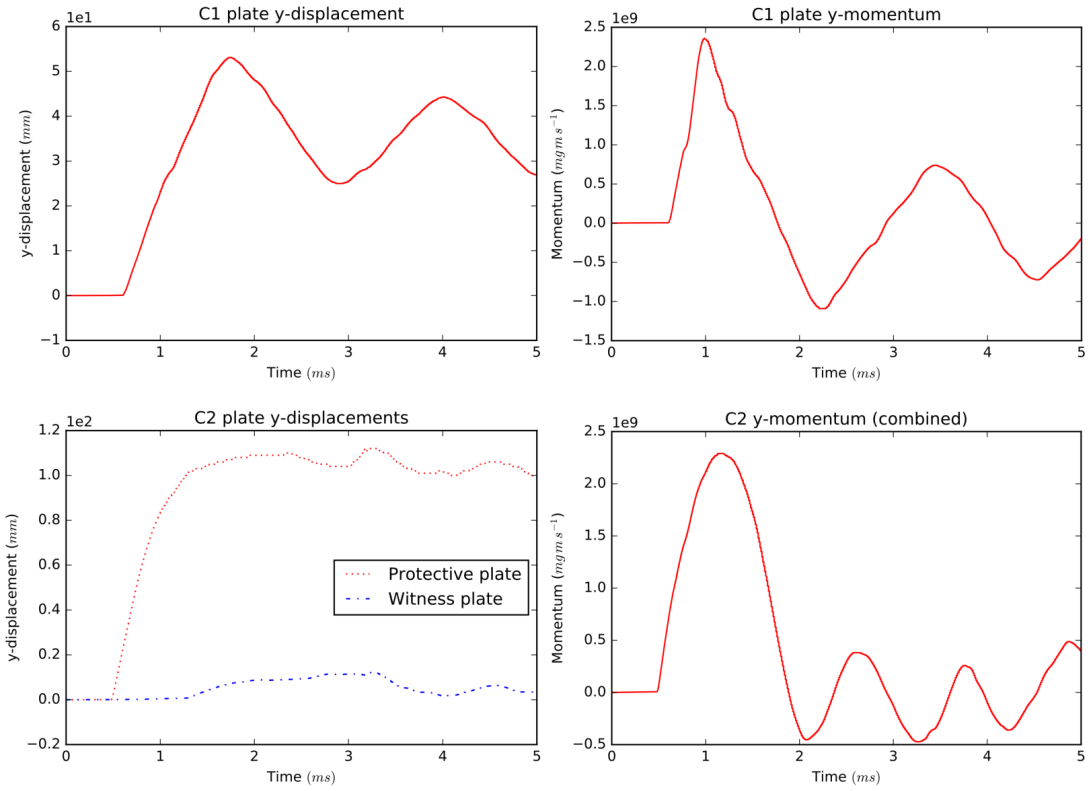

Figure 6.16: y-axis deflection and total momentum plots for the C1 and C2 comparison cases.

In comparison to C1, a perforated plate reduces the maximum deflection by an

average of 28.1%. In comparison to C2, a perforated plate scheme under-performs by an average of 69.1%

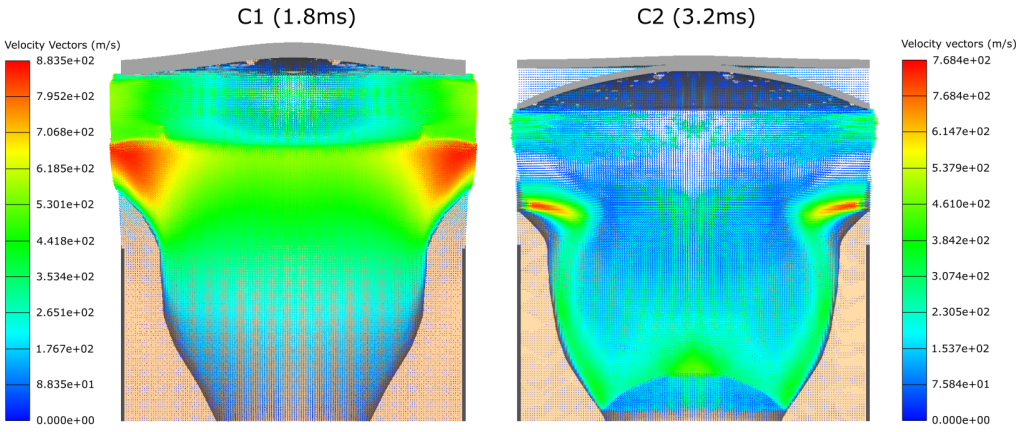

Figure 6.17: The C1 and C2 plates at the time of maximum deflection. C2 has made contact with the witness plate, deforming it.

6.1.3 Surface-flush charges

In light of the apparent insensitivity of the 64-aperture plate to the slug loading, it was decided that only this plate would be examined against C1 and C2. The detonation of the surface-flush charge produces a conical crater with shallow sides. No slug is ejected. A comparison of the detonation of a surface-flush and buried charge is shown in Figure 6.18.

The displacement histories of the perforated and witness plates in the surface-flush simulations are shown in Figure 6.19. The corresponding pressure histories behind the centre-most aperture are shown in Figure 6.20. The surface flush charges produce significantly higher peak pressures. However, by comparison to the buried charge pressures shown in Figure 6.11, the pressure also drops significantly faster when the charge is placed surface-flush and is negligible by 1.4ms. The post-barrier pressure in the buried case is similarly decayed at the later time of 2.5ms. The pressure at the lowest (900mm) gauge is now dominant, reaching 37.9 MPa at the 600mm stand-off, and 45.73 MPa at 500mm. The peak pressure at the 980mm gauge is reduced significantly, to 17.13 MPa

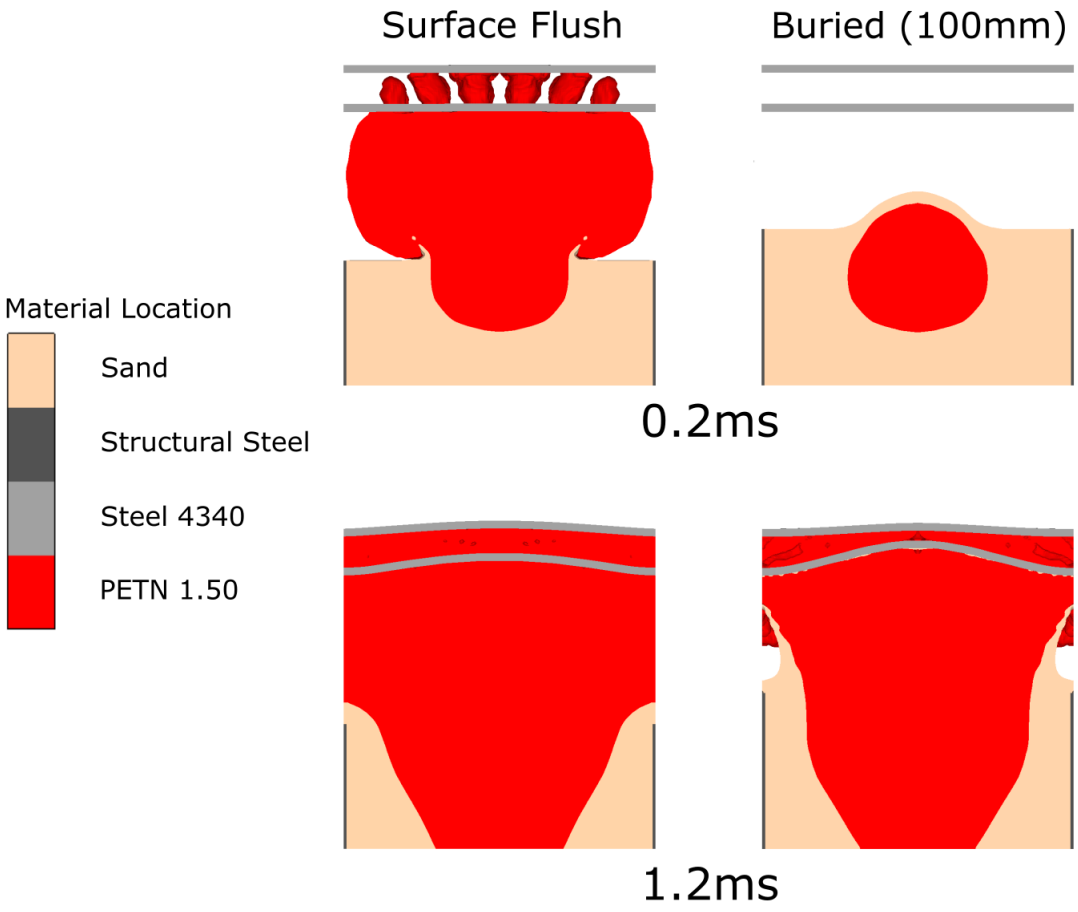

Figure 6.18: Cut-through of the detonation of a surface-flush and buried charge at 0.2ms and 1.2ms. At 0.2ms, the detonation products of the surface-flush charge have expanded and entered the perforations. The staggered arrival of the detonation products through the apertures can be seen. At the same time in the buried charge simulation the detonation products are fully enclosed by the sand. At 1.2ms, both charges have excavated conical craters, although the sides of the buried charge crater are considerably steeper. The deeper, narrower crater and the lip of ejected material are seen to direct the venting of detonation products towards the plate. In the surface-flush case, the detonation products have expanded to occupy the entire region beneath the perforated plate. The deformation of the perforated plate is visibly less pronounced in the surface-flush case.

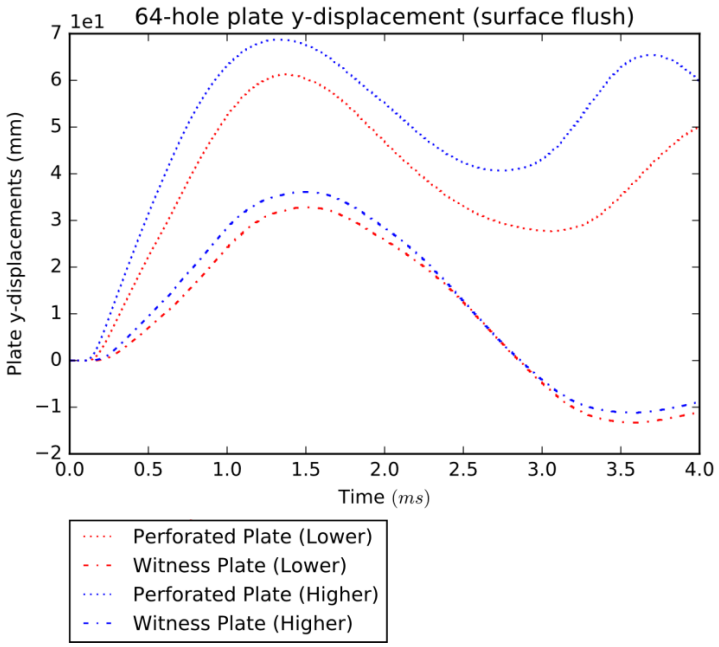

Figure 6.19: Displacement over time for the witness and perforated plates in the surface-flush charge simulations

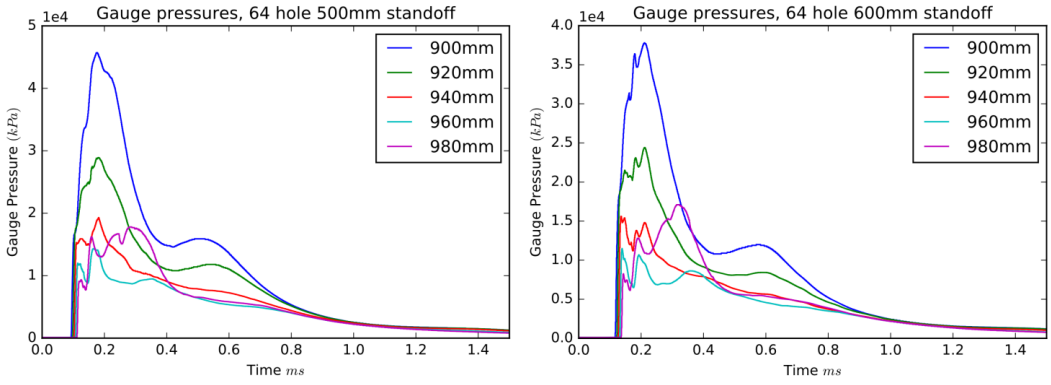

Figure 6.20: Pressure histories for the post-aperture gauges in the 64-hole surface flush simulations

and 17.79 MPa at 500 and 600mm stand-offs respectively. These peaks are lower than the maximum pressure measured at the witness in the buried charge case.

Table 6.3: Surface flush charge results

	Plate type		
Peak deflections (mm)	C1	C2	Perforated (64 hole)
Witness stand-off: 600mm			
Witness deflection	25.07	1.46	32.84
Protective plate deflection	N/A	84.88	61.27
Witness stand-off: 500mm			
Witness deflection	30.98	1.64	36.14
Protective plate deflection	N/A	97.07	68.75

The surface-flush charges show considerably different results for the comparison plates. These are summarised in Table 6.1.3. Where previously the perforated plate provided a 27.1% reduction in witness deformation compared to C1, the C1 plate witness deformation is now lower than that of the perforated plate model by 23.7%. The performance of the C2 plate is also enhanced, with the witness deflection reduced to $<2mm$. In C2, the protective and witness plates do not make contact; the minor deflection of the witness plate is attributed to the pressure loading arising from the rapid deflection of the protective plate.

6.1.4 Expansion to a 4b charge

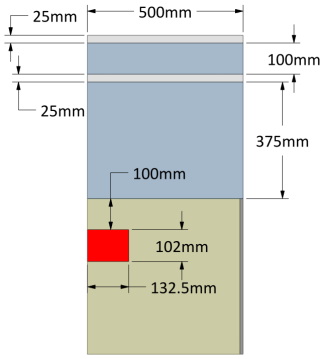

Figure 6.21: Dimensions of the 4b charge simulation. The radius of the charge is expanded to 135.5mm; the total weight of the charge is 8.4 kg of PETN-B.

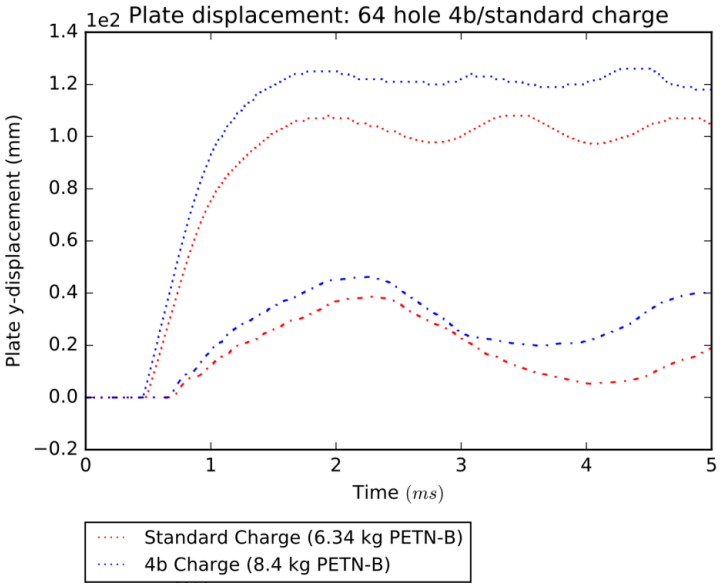

Figure 6.22: Displacement history for the 64-hole perforated and witness plates

The charge mass and dimensions are now expanded to those of a 4b threat under STANAG 4569 classification. The dimensions of the simulation are shown in Figure 6.21. Only the 64-hole perforated plate is examined, on the basis of insensitivity to charge location. The detonation cavity is significantly enlarged. By 5ms, the majority of the sand has been ejected from the container, leaving a significant crater. The sand-slug strikes the perforated plate and disintegrates, with both slug material and PETN detonation products passing through the apertures. The dimples produced on the witness plate by the impacting sand fragments are deeper. Peak deflection of the witness plate is 46.23mm, and occurs at a similar time (2.26ms) to the case of the smaller charge. The peak deflection of the perforated plate is 126.36mm. A history of the deflection alongside a comparison to the original simulation with the smaller charge is shown in Figure 6.22.

Despite the significant deflection of the perforated plate, no contact occurs between this plate and the witness throughout the simulation. The center of the witness is continuously displaced beyond the maximum deflection of the perforated plate. The pressure behind the aperture is presented in Figure 6.23.

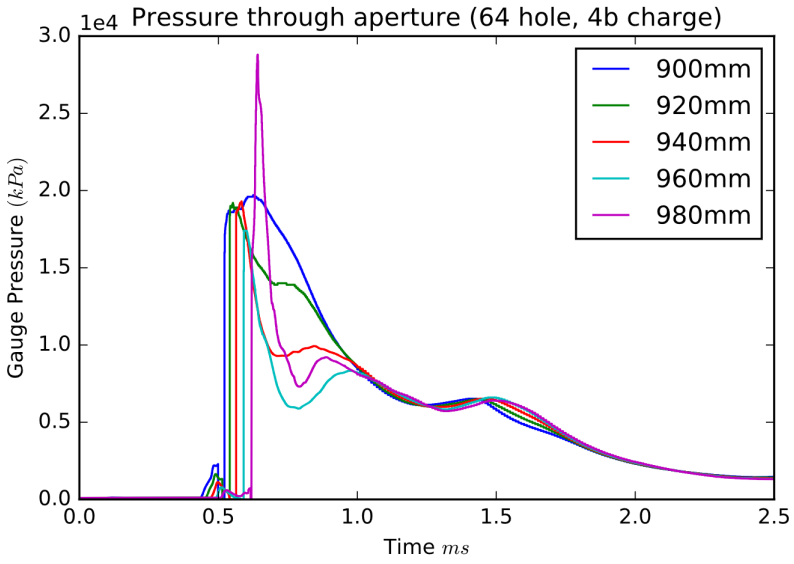

Figure 6.23: Pressure in the post-barrier region for the 4b charge simulation

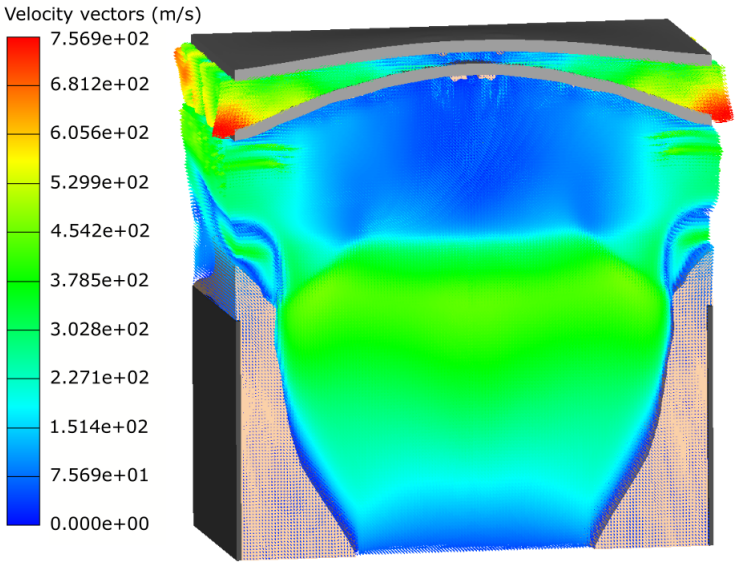

Figure 6.24: The state of the 4b charge simulation at the time of peak deflection (2.2ms). The deflection of both perforated plate and witness plate is enhanced; no contact is made between the two throughout the simulation.

The state of the simulation at peak deflection is shown in Figure 6.24.

6.2 Discussion

6.2.1 Perforated Plates

The perforated plate designs consistently provide additional mitigation. Even in the worst-case scenario in which the charge is placed directly below the largest aperture, the deflection of the witness is 23.5% lower than the average deflection of the unprotected witness plates in Chapter 5. The perforated plates survive the detonation process across all charge scales and positions. While the plates in this study are sufficiently thick that they withstand rupture, the predicted failure mode of a perforated plate is the partial failure or full detachment of a section of the plate along the lines of greatest stress and strain between apertures.

Aperture position and sources of loading

The position of the aperture relative to the detonation is shown to be significant when apertures are large and of comparable width to the slug. As the apertures decrease in size and their distribution across the plate becomes more consistent, the loading on the witness becomes less sensitive to the position of the charge under the plate. Figure 6.25 is an illustration of the effect of increasing aperture distribution on the porosity of the region struck by the slug.

In all buried charge simulations, sand from the disintegration of the slug passes through the apertures. The dimples visible on the witness plate confirm that these fragments exert loading. The use of the multi-material Euler solver for the sand transport prevents analysis of individual fragments. The formation of dimples suggests that the effects of the slug on the witness are limited to producing localised deformations when the plate apertures are small. This is a consequence of the ductility of the steel used in the plate model, and is an observation specific to this analysis.

The higher peak deflection of the 4-hole perforated plate as seen in Figure 6.10 indicates that the plate absorbs a greater fraction of the slug loading in comparison to the other perforated plates, which display similar deflections to each other. The deformation of the witness plate behind the 4-hole perforated plate occurs later than the other witnesses due to the later arrival of the gaseous detonation products, but

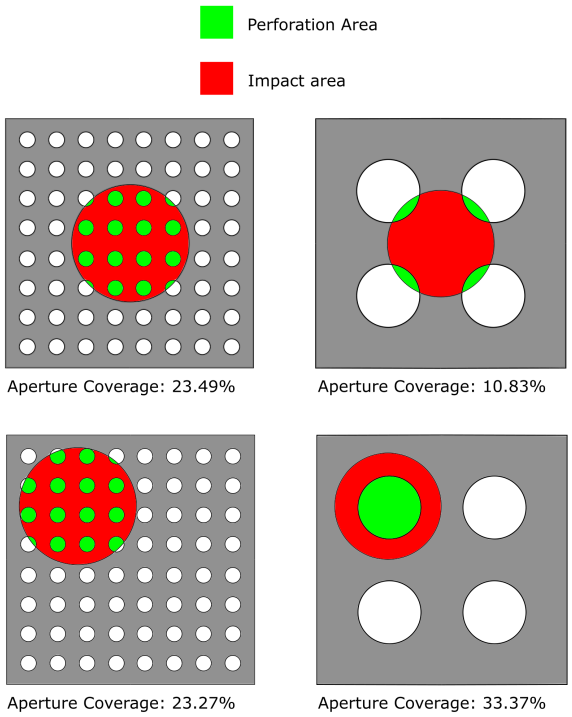

Figure 6.25: Illustration of the ratio of porous area to primary slug impact region for the 64 and 4 hole plate cases. Varying the slug impact region can be seen to significantly influence the ratio of open space for plates with fewer, larger apertures, while minimally affecting the ratio for smaller apertures.

the peak deflection remains comparable with other designs. This indicates that the deformation of the witness plates is governed by the gas pressure loading.

In the surface-flush simulations, the 64-hole perforated plate experiences a 43.5-36.6% reduction in deformation compared to the buried charge case. The deformation of the witness plate is reduced by only 15.2-6.7%. The absence of the slug is shown to reduce deflection of the perforated plate moreso than the witness. While the peak pressures due to the detonation of the surface flush charge are initially higher than the buried case, the peak pressure measured closest to the witness is reduced by 17.1-12.8%. The reduction in witness deformation correlates with the reduced peak gas pressure when the slug is absent.

The effect of perforated plates on the gas flow

The flow field behind the perforated plates is dominated by the jet flow of gas through the apertures. The cloud of detonation products is not planar, and the flow entering through apertures further from the center of the detonation encounters the witness plate at an oblique angle. This can be seen during the early stages of the penetration of the perforated plate by the detonation products of a surface-flush charge in Figure 6.18, in which the flow through apertures further from the apex of the detonation is visibly angled away from the plate. Further deflection of the flow through distant apertures by the spreading of the central jets is shown in Figure 6.8.

The deformation of the perforated plate is significant and influences the development of the flow field. As the perforated plate deflects into a dome, the spacing between the perforated plate and the witness in the region directly above the charge is reduced. The effect on the jet flow through the central apertures can be seen in Figure 6.9. The deformation of the plate is favourable towards the redirection of the flow towards the outflow between the perforated and witness plates. This can be considered an inversion of the V-hull concept; rather than the deflection of the flow by a convex geometry, the deformation of the perforated plate into a concave shape now assists in driving the deflection of the jet-streams. However, the plates in these studies are fully separated, with no consideration given to structures which may impede the free outflow of the gas at the limits of the domain. In practice, a perforated plate scheme mounted beneath a vehicle is unlikely to feature a free outflow condition in all directions.

Comparison of the pressure measurements for the buried (Figure 6.11) and surface-flush (Figure 6.20) charges show that the pressure in the post-aperture region is sustained for longer when the charge is buried. This is a consequence of the directional venting of detonation products from the detonation cavity of the buried charge as shown in Figure 6.18. When the flow is sustained, the peak pressure of the flow entering the aperture is lower but the peak pressures acting on the witness plate are greater. The inverse is true in the case of the surface-laid charge. The perforated plate scheme is shown to reduce the peak pressure load of a surface-flush charge significantly, by 55% at

the 600mm stand-off and by 61% at the 500mm stand-off. The % mitigation attributed to the perforated plate is shown to actively increase as the distance to the charge is reduced.

6.2.2 Comparison to other designs

It is shown that a perforated plate outperforms the C1 plate in defending against a buried charge, with an average reduction in deflection of 28.07 %. Even at the larger 4b charge scale, the deflection of the witness behind the 64-hole plate is 17.6% lower than the deflection of the C1 plate by the standard charge. However, in the surface-flush tests, C1 outperforms the perforated plate. In the surface-laid case the deflection of C1 is reduced by approximately 53%, a result in good agreement with the observation of Taylor [23] that the slug accounts for half of the total loading at deeper burial depths. The benefit of the perforated plates is that the witness deflection is consistent to a greater degree across charge scales and deployment methods. Slug protection is enhanced at the cost of permitting the gas flow to penetrate.

In comparison to C2, the perforated plate scheme is outperformed across all simulations. The deflection of the C2 protective plate is consistently arrested by contact with the witness. The deformation of the C2 witness is almost entirely driven by contact with the solid protective plate. The separation between the defensive plates and the witness prevents assessment as to which scheme is likely to fail first. The solid plate is thinner than the perforated plate and experiences generally greater deflection. Perforated plates allow material to partially pass through them and experience lower deflections, but the limiting factor is the concentration of strain in the mechanically weaker regions between apertures.

Chapter 7

Discussion and Future Direction

In this Chapter, the findings of the work performed in the last several Chapters are combined to provide an overview of the defensive qualities of perforated plates. The two research goals investigated in support of the answer are

- To establish the role of perforated plate structure in mitigating a shockwave.
- To model perforated plates defending a target against a buried charge detonation.

7.1 Fully rigid plates

In Chapter 3, the methodology for simulating a shock-tube environment was developed in ANSYS FLUENT. Models for flow transport and turbulence were investigated. The sensitivity of the models to the mesh type and resolution was established. An initial 2-dimensional study is performed on a dual-aperture obstruction.

In Chapter 4, the interaction of shocks with fully rigid perforated plates of constant porosity $\varepsilon = 0.4$ and varying hydraulic ratio was investigated in shock-tube environments. The incident shock has a strength of Mach number 1.63. Attenuation of the over-pressure of the incident shock downstream of the barrier and at the rear wall of the shock-tube is taken as a measure of protection. The rear wall of the shock-tube is placed at both a long separation from the barrier and a short separation. For the long-separation case, comparison is made to existing experimental data available in the work of Britan [113]. A flow divertor concept unique to this work is presented in the short separation case.

It is demonstrated by the CFD simulations in this work that the mitigation of shocks by perforated plates is not a simple factor of their porosity. The reduction in peak pressure acting on the target surface (compared to the unprotected case) varied by 41-32% depending on the aperture design. The greatest reduction in pressure is provided by a plate containing 36 small apertures. An increase in the number of apertures at fixed porosity provides enhanced reduction in peak pressure, and corresponds to a decreasing hydraulic ratio. The progress of the shock mitigation downstream of the barrier is shown to be similar to existing experimental work [113], but the numerical simulation under-predicts the magnitude of the mitigation. Contrary to the experimental work is the observation that the mitigation is fully ordered by hydraulic

ratio when barrier shape is accounted for. The turbulence arising as a consequence of vortex shedding from the barrier and the complex downstream flow interaction acts to extract momentum from the flow. As the shock-front moves downstream, the loss of momentum in the upstream acts to separate the post-shock region from the jet flow.

The mitigation is reduced to 23% when the target wall is placed close to the rear of the barrier. If the wall is in the jet-flow region there is insufficient downstream distance over which the previously identified flow effects can act. The novel divertor scheme applied in this work increases the rise-time of the pressure loading on the surface but provides a similar peak pressure to the flat-walled case, as the design inadvertently re-directs the flow back towards the target.

By holding the plates fully rigid, this assessment also addresses the observation of Langdon et al [69] that difficulty lies in distinguishing between the mitigation contributed by flow effects due to the perforations and the effects of deformation. The flow effects are not negligible, and significant variation in mitigation is seen when the relevant parameters are altered.

7.2 Perforated plates as buried charge defence

In Chapter 5, a methodology for the simulation of the detonation of a buried charge was developed. The simulation methodology had to incorporate the full range of mine blast phenomena, including the detonation of a 6.64kg PETN charge, the formation of a sand-slug, and the mechanical response of both solid and perforated steel plates. The salient features of a mine-blast were observed in the simulations. Examination was made of the impact of the sand-slug on an edge-clamped steel plate and the effects of mesh resolution on the simulation.

In Chapter 6, the simulation structure developed in Chapter 5 is extended to incorporate a perforated plate defensive scheme. The work in this Chapter is the first investigation of a perforated plate scheme as a form of defence that includes buried charge dynamics. Plates of constant porosity $\varepsilon = 0.2$ and varying numbers of perforations are exposed to the detonation of in both surface-flush and buried 6.64kg PETN charges. The deformation of a witness plate placed directly behind the perforated plate

at a separation of 100mm is taken as a measure of protection. Comparison is made to the defensive performance of two alternative plate designs; a single thick solid plate, and a witness protected by a solid protective plate of equivalent mass to the perforated plate. Limited investigation is made into the performance of a perforated plate exposed to the detonation of a "worst-case" blast charge of a scale corresponding to a level 4b threat under NATO STANAG 4569 guidelines.

The perforated plates mitigate the blasts. A minimum additional protection of 23.5% is afforded to the witness plate compared to the unprotected case even under the worst conditions with respect to aperture position and charge size. The position of the charge is found to be significant only for large apertures. The impact of the sand-slug produces significant deflection of the perforated plate, but contributes little to the witness plate loading when the apertures are small. The pressure of the gaseous detonation products is determined to be the primary source of loading on the witness plates. The variation in witness plate deflection under different charge conditions is seen to vary proportionally with the deflection of the perforated plates, indicating that the perforated plate scheme scales well against different blast scenarios.

The perforated plate schemes outperform a single thick plate against buried charges, but underperform against surface flush charges. A separate solid plate is shown to provide greater witness plate protection in all comparisons, although the solid plate experiences greater deflection. Perforated plates are expected to permit material and gases to pass through and strike the protected surface. The particular benefit of the scheme is not the total prevention of loading on the target but the consistency of the mitigation across charge scales and deployment type as seen in this work. The potential for greater mitigation under specific conditions is therefore sacrificed in favour of reliability. However, a pertinent question remains; "under extreme blast conditions, which will fail first; a perforated plate, or a solid protective plate of equivalent mass?". The true distinction between the two schemes lies at higher blast scales than are applied here. As super-heavy IEDs (some of up to 100kg TNT [122]) have been observed in some theatres, the question is not academic.

7.3 Synthesis

Two main investigative strands with different methodologies are used to provide an answer to the research question. The need for two distinct methodologies is consequence of the current state of solver technology. The specifics of the perforated plate scheme and their suggested use in this thesis have required consideration of a broad array of phenomena in both solid and fluid mechanics. Neither solver employed in this work is capable of encompassing the full spectrum of relevant physics. The findings of both research objectives are combined in this section. This thesis demonstrates several distinct mechanisms of action by which perforated plates mitigate the effects of a blast on a protected surface:

1. Partial reflection of the shock

    - The placement of an obstacle between the incoming shock and the target surface prevents the full transmission of shock loading to the surface and is seen in both the fluid-dynamics and multiphysics simulations.

2. Mitigation through the disruption of the shock and the formation of flow features antagonistic to the maximum overpressure

    - A dependency of the downstream shock mitigation on the aperture structure is seen for the long-separation case in Chapter 4. This is attributed to two causes; the first is increased shedding of vortices arising from an increase in total aperture perimeter. This is demonstrated by the detachment of the post-barrier shock from the aperture jet flow, and the variation in this behaviour with respect to the hydraulic ratio. The second is the interaction of jet-flows in the complex post-barrier flowfield. This is shown in the ordering of downstream shock mitigation. In grouping plates by aperture shape, shock mitigation with decreasing hydraulic ratio ceases to be a general trend, and now directly corresponds to an increase in shock mitigation. This is further reflected in the relationship between peak flow velocity at the aperture and the mitigation of the shock acting on the rear-wall of the shock tube. While a single large aperture has the lowest peak flow velocity through the aperture center, this design produces the lowest mitigation

of the shock acting on the rear-wall. This is attributed to the absence of additional interacting jets in the downstream flow.

- In the inviscid multi-physics simulations in Chapter 6, an increase in the number of apertures produces comparable plate deflections. The pressure loading is shown to be dominant. Accounting for aperture position, the peak reflection pressure is observed to generally decrease with an increase in the number of perforations.
- The tendency of jet-flows to spread outwards as they encounter a surface is seen in Chapter 4. However, in Chapter 6, the blast products do not arrive at the plate at a uniform time, and the presence of a free-outflow at the edge of the post-barrier region allows the flow to egress. These factors combine to produce the observed outwards deflection of later-developing jet flows by the spreading of earlier jets.
- The deformation of the perforated plate has implications for the flow-field. The inward deflection of the plate produces an outward splaying of the jets flowing through the central apertures, which further drives the deflection of jet flows.

3. Partial interception of the sand-slug

- This observation is specific to the mine blast simulations of Chapter 6. The sand-slug is disintegrated on contact with the perforated plate.
- Similar deflections of the witness behind a 64-aperture plate are seen for both the buried and surface flush charge simulations. This indicates that the majority of the witness deflection is driven by the flow of detonation products and not the slug.

In both the pure gas-dynamic and multiphysics simulations, multiple smaller holes are superior to fewer, larger holes. This superiority is not derived from the mitigation of a single threat factor but is established across the range of hazards posed by the detonation of a buried charge including air shocks, the venting of detonation products, and the ejection of the slug.

In Chapter 4, the effects of turbulence are shown to significantly influence the pressure loading. These effects are absent from Chapter 6. It is suggested by Britan et al

[113] (based on earlier work by Igra et al [123, 124]) that, in flows with short durations, the effects of turbulence may be negligible in comparison to the kinetic energy. That suggestion was not borne out in [113], in which the role of fluid viscosity was demonstrated to be significant. In Chapter 6, the duration of the flow through the perforated plate apertures is approximately 1.5ms (in the case of a buried charge), and is comparable with the duration of the flow in Chapter 4, in which turbulent effects are seen to be important. The effects of turbulence would therefore have been anticipated to be a significant factor. However, the separation between the perforated and witness plates in Chapter 6 places the witness in the jet flow region, which is demonstrated in Chapter 4 to negatively impact the turbulent contribution to the mitigation. The absence of turbulence from the multiphysics simulations is therefore not as significant as it may otherwise have been had the separation between plates been greater, or the individual apertures smaller. Despite the absence of turbulence and the comparatively shorter pressure loading period, the surface-flush simulations of Chapter 6 also show excellent mitigation of the air shock.

Chapter 8

Conclusions

This thesis opened with the following question: "Is there a novel methodology by which armoured fighting vehicles may be protected against the detonation of buried explosives". This work applied both dedicated computational fluid dynamics and multi-physics analysis in studying the use of perforated plates as a novel form of blast defence for armoured fighting vehicles.

1. In Chapter 3, a methodology was developed for the study of a fully rigid perforated plate interacting with a shock front. The shocks travel in a narrow channel approximating to that of a shock-tube. Appropriate simulation techniques are developed and tested.

2. In Chapter 4, this methodology is applied to large-scale 3-dimensional simulations of rigid perforated plates. These plates are exposed to planar air shocks of strength Mach 1.63. Mitigation of these shocks is shown to be dependent upon the configuration of the plate apertures. Reasonable agreement with existing experimental data is demonstrated. The flow structure and turbulence are significant contributing factors to the mitigation. A novel flow divertor concept is tested; the feasibility of additional post-barrier structures intended to further mitigate the flow is demonstrated, although the specific flow divertor design examined in this work is ineffective.

3. In Chapter 5, a methodology was developed for the study of deformable perforated plates and the protection they afford against the blast produced by a 6.34 kg PETN-B charge placed both surface-flush and at a burial depth of 100mm. The sand under which the charge is buried is modelled as dry sand to simulate maximum breakup and intrusion of the sand-slug material through the perforations. The detonation process and surrounding sand and air are modelled using a Multi-Material Eulerian scheme, while the structural response of both solid and perforated plates is modelled using a Lagrangian solver. The effects of mesh sizing on the detonation pressure and the deformation of a 25mm thick steel witness plate are investigated.

4. In Chapter 6, perforated steel plates of 25mm thickness containing 4,16,24,36 and 64 circular apertures with a fixed porosity of $\varepsilon = 0.2$ are affixed before a solid 25mm thick steel witness plate. Reduction in the peak deflection of the center

of the witness plate is taken as the primary measure of protection. Comparison is made to two alternatives; a single solid plate of 45mm thickness, and the case in which a witness is protected by a 20mm thick steel plate. This is the first study of perforated plates as protection against the conditions of a buried charge detonation.

The findings of this work indicate that perforated plates are capable of mitigating highly complex blasts containing multiple material phases at close range. The answer to the research question is thus: There is a novel methodology by which vehicles can be protected against the effects of buried explosives, in the form of perforated plates. They provide this protection through a combination of physical shielding and complex post-barrier flow effects. While the perforations do admit the ingress of blast products and other detritus, they have the corresponding benefit of scaling well to varying charge deployment and provide consistent protection against the effects of detonation.

8.1 Future Work

The focus of this thesis has been directed towards establishing the plausibility of a novel defensive scheme. That plausibility has been demonstrated. However, all research produces further questions, sometimes more of them than it answers. In this Section, several of the more pressing or interesting avenues of further investigation are presented as a signpost to future work.

8.1.1 Experimental Work

The work in this thesis is performed entirely in simulation. While efforts have been made where possible to provide conservative estimates and make comparison to existing experimental data, the ultimate test of viability is the exposure of the scheme to real detonations.

The use of physical experiments will also provide opportunity to study smaller individual apertures than could be applied in this work. The use of numerical methods and the corresponding requirement for the aperture to be of sufficient width to accommodate multiple cells places a lower bound on the practical diameter. This factor is entirely absent from experimental studies and smaller apertures may yield further

improvements, both with respect to the slug intrusion and if the spacing between plate and hull is required to be small.

8.1.2 Flow divertors

The flow divertor concept was investigated in Chapter 4. Simple hemispherical protrusions provided no significant additional mitigation of the peak pressure experienced by the flat section of the rear wall, although the rise to peak pressure takes place over a longer time-frame than in the flat-walled case. No investigation of the divertor concept was made in Chapter 6, in which significant deformation of the perforated plates was observed. In one simulation, the perforated plates made contact with the witness plate. Ejected sand is also propelled through the apertures alongside the flow. Aside from improvements to be made to the particular design of the divertor elements with respect to the re-direction of the flow, a divertor scheme intended for use under a vehicle must be designed with these factors in mind.

8.1.3 Further Novelty

In this work, the perforated plates have been modelled as a single material. However, in Chapter 1, the survey of the literature also revealed several other promising avenues of research. While the geometric schemes were the most promising and adopted as the research focus, these other methods could be combined with the scheme described in this work to greater effect. The most promising concepts for such additional modifications are the sandwich construction of impedance-mismatched layers and strain-rate dependent materials. The vertical deflection of the perforated plate into the hull is a possible outcome of a blast, and the use of bonded materials with varying responses to strain is shown to frequently result in the delamination of (the breaking of bonds between) layers, a process shown to reduce the peak deflection of a solid plate constructed in this way [41].

During a meeting with BAE systems, the author also put forth a suggestion loosely informed by the study of Nesterenko seen at the start of Chapter 1. The notion involves lining the rear side of the perforated plate with a highly frangible material which would disintegrate under the rapid deformation of the plate, forming a thick dust. Vermiculite, a soft granular form of silica, was mooted as a plausible starting point as it is

soft and light (thus posing no threat as an additional projectile) and chemically inert. This material would act to further disrupt the flow field, and the narrow enclosure between the protective scheme and the hull is anticipated to retain the majority of the fragments during the pressure loading period.

8.1.4 Perforated plates in broader blast defence

The perforated plate studies in the literature have until now focused on the use of these plates as forms of defence for narrow, enclosed channels. The studies in Chapter 6 also represent the first inclusion of a free outflow boundary in the region behind the perforated plate. Significant out-flow of detonation products is observed at this boundary. The perforated plates are also seen to rapidly mitigate the higher but shorter pressure loading of a surface flush charge. The defence of public spaces against the malicious detonation of explosives is complicated by the tendency of shocks to over-pressurise at solid surfaces. While air-shocks decay as a cubic function of distance (as embodied in the form of the Hopkinson-Crantz blast scaling law [10]), individuals standing near to walls or in enclosed infrastructure such as concourses may be exposed to lethal reflection overpressure. The inclusion of narrow perforated structures in these spaces has the potential to mitigate the initial shock while reducing the reflected overpressure. Free-space studies of perforated plates in this role may yield a new form of defence against terrorist activity.

Appendix A

PRISMA Review Methodology

A. PRISMA REVIEW METHODOLOGY

As part of this work, a structured literature review was executed to determine an optimal avenue of research. The PRISMA (Preferred Reporting Items for Systematic review and Meta-Analysis) methodology [25] was adopted Much of the PRISMA standard checklist is addressed towards the specific requirements of medical systematic review; in the following, only the elements of the checklist relevant to structuring the search strategy are addressed. The items applied in this work and the associated courses of action are presented below:

1. **Introduction**

   - **Describe the rationale for the review in the context of known material**

     The review of the literature is intended to identify methods of blast protection which are not currently in use as anti-IED and landmine defensive schemes, but which may be adapted to this purpose.

   - **Provide a statement regarding the questions addressed by the review, and provide a PICO assessment**

     The review asks the question "Do potentially novel approaches to anti-IED and landmine protection exist within the literature and if they do, which is the most suitable". Given the explicit requirement for novelty, terms related to existing schemes such as the V-hull are not included. The PICO format is initially adjusted for the explicit purpose of acquiring and comparing multiple anti-blast and shock protocols in the form of the TO (Threats and Outcomes) table. The TO table is presented below:

Element	Terms
Threat	"Blast", "Shock", "Detonation", "Shockwave", "Blastwave"
Outcome	"Reduction", "Attenuation", "Mitigation", "Protection", "Defence", "Prevention", "Resistance", "Alleviation", "Interaction", "Inhibition"

2. **Review Method**

- **Specify report inclusion criteria**

  The criteria by which papers are included in the initial search of the literature are outlined below:

  Stage 1 Inclusion Criteria (Initial search)

  (a) The search shall not exclude papers on the basis of the study type

  (b) Only air-shocks and detonations are considered

  (c) The literature must be accessible in its full form

  (d) Shock and blast mitigation must be the object of the study

  Stage 2 Inclusion Criteria

  (a) The shocks can be in constrained environments or open space

  (b) The shocks can be generated by any means (shock tube, explosives etc)

  Stage 2 Exclusion Criteria

  (a) The shocks are atypical of a terrestrial environment (i.e astrophysical shocks, plasma discharges)

  (b) The scheme already exists as an methodology of defending against the threats in question

  Stage 3 Inclusion Criteria

  (a) The mitigation schemes must be plausible for the intended purpose

  (b) The mitigation schemes must be passive, and not require active detection of detonation

- **Identify information sources and literature search engines used to search the literature**

  The web of science (https://wok.mimas.ac.uk/) core literature database was selected as the primary literature searching tool. Searches in other engines such as Google scholar returned only duplicate material.

- **Identify the search strategy applied in each database**

  In the selected database, the Boolean operators OR and AND were used to connect the contents of the TO table. The syntax used is given below:

"(Blast OR Shock OR Detonation OR Shockwave OR Blastwave) AND (Attenuation OR Reduction OR Mitigation OR Protection OR Defence OR Prevention)"

Searches were further refined to the following relevant categories:

- Engineering (Mechanical, Civil, Geological, Aerospace)
- Physical (Applied, Multidisciplinary)
- Materials Science (Multidisciplinary, Composites)
- Chemistry (Applied, Physical)
- Computer Science (Interdisciplinary Application)

with the resulting list of titles being ordered by relevance to the search terms.

- **Outline the process by which studies in the literature are selected for inclusion**

  The first 1000 titles presented were assessed for relevance using the stage 1 inclusion criteria. Papers were initially selected on the basis of titles that matched the criteria outlined in the stage 1 inclusion criteria. Once the initial round of selection was complete, the second stage inclusion/exclusion criteria were applied to paper abstracts, and for the remaining papers the third-stage inclusion criteria were applied to the main text of the literature.

3. **Results**

- **Identify how many studies in total were selected initially, and how many were excluded from the final assessment, along with a statement of the rationale for doing so**

  In total, 73 paper titles were identified as relevant based on the stage 1 inclusion criteria. Of these, 58 met the criteria outlined in stages 2 and 3, with the remainder being dismissed on the grounds that they variously a) did not include a potential defensive scheme (being focused instead on the natural dissipation of shocks in air), b) were structurally specific (structural blast wall designs) or c) were materially unsuitable for the intended purpose (such as the proposed use of foamed concrete as a blast mitigator).

On acquisition of the initial selection of relevant literature, a summary of the state of the field was produced. The key elements of this summary are presented in abridged form in Chapter 1. On the basis of this summary and a consideration of both the practical requirements and the potential benefits and shortcomings identified through the literature, a perforated plate-based approach to blast mitigation was selected as the defensive protocol investigated in this work.

Appendix B

The Analytical Riemann Solver Code

As part of the validation process for a section of the work executed in this thesis, comparison is made to data representing the exact solution to the Riemann problem. The data is generated using the following Python code.

B.1 The solver code

The following code was obtained from Github, and is written and distributed by Jerko Škifić. It is applied under the MIT License conditions.

```
# -*- coding: utf-8 -*-

import numpy as np
import scipy
import scipy.optimize


def solve(left_state=(1, 1, 0), right_state=(0.1, 0.125, 0.), geometry
    =(-0.5, 0.5, 0), t=0.2, **kwargs):
    """
    Solves the Sod shock tube problem (i.e. riemann problem) of
    discontinuity across an interface.

    :rtype : tuple
    :param left_state: tuple (pl, rhol, ul)
    :param right_state: tuple (pr, rhor, ur)
    :param geometry: tuple (xl, xr, xi): xl - left boundary, xr - right
    boundary, xi - initial discontinuity
    :param t: time for which the states have to be calculated
    :param gamma: ideal gas constant, default is air: 1.4
    :param npts: number of points for array of pressure, density and
    velocity
    :param dustFrac: dust to gas fraction, should be >=
    :return: tuple of: dicts of positions,
    constant pressure, density and velocity states in distinct regions,
    arrays of pressure, density and velocity in domain bounded by xl, xr
    """

    if 'npts' in kwargs:
        npts = kwargs['npts']
```

```
27      else:
28          npts = 500
29
30      if 'gamma' in kwargs:
31          gamma = kwargs['gamma']
32      else:
33          gamma = 1.4
34
35      if 'dustFrac' in kwargs:
36          # dustFrac = np.min(np.max(kwargs['dustFrac'], 0), 1)
37          dustFrac = kwargs['dustFrac']
38          if dustFrac<0 or dustFrac >= 1:
39              print('Invalid dust fraction value: {}. Should be >=0 and <1.
    Set to default: 0'.format(dustFrac))
40              dustFrac = 0
41      else:
42          dustFrac = 0
43
44      calculator = Calculator(left_state=left_state, right_state=right_state
    , geometry=geometry, t=t,
45                              gamma=gamma, npts=npts, dustFrac=dustFrac)
46
47      return calculator.solve()
48
49
50  class Calculator:
51      """
52      Class that does the actual work computing the Sod shock tube problem
53      """
54
55      def __init__(self, left_state, right_state, geometry, t, **kwargs):
56          """
57          Ctor
58          :param left_state: tuple (pl, rhol, ul)
59          :param right_state: tuple (pr, rhor, ur)
60          :param geometry: tuple (xl, xr, xi): xl - left boundary, xr -
    right boundary, xi - initial discontinuity
61          :param t: time for which the states have to be calculated
62          :param gamma: ideal gas constant, default is air: 1.4
63          :param npts: number of points for array of pressure, density and
    velocity
```

```
64          :param dustFrac: dust fraction, as defined in Tricco, Price and
    Laibe, 2017,
65          Is the dust-to-gas ratio constant in molecular clouds, Eqs. 5-6
66          :param kwargs:
67          """
68          self.pl, self.rhol, self.ul = left_state
69          self.pr, self.rhor, self.ur = right_state
70          self.xl, self.xr, self.xi = geometry
71          self.t = t
72
73          if 'npts' in kwargs:
74              self.npts = kwargs['npts']
75          else:
76              self.npts = 500
77
78          if 'gamma' in kwargs:
79              self.gamma = kwargs['gamma']
80          else:
81              self.gamma = 1.4
82
83          if 'dustFrac' in kwargs:
84              self.dustFrac = kwargs['dustFrac']
85          else:
86              self.dustFrac = 0
87
88          # basic checking
89          if self.xl >= self.xr:
90              print('xl has to be less than xr!')
91              exit()
92          if self.xi >= self.xr or self.xi <= self.xl:
93              print('xi has to be in between xl and xr!')
94              exit()
95
96          # calculate regions
97          self.region1, self.region3, self.region4, self.region5, self.w = \
98              self.calculate_regions()
99
100     def solve(self):
101         """
102         Actually solves the sod shock tube problem
103         :return:
```

```
104         """
105         regions = self.region_states()
106 
107         # calculate positions
108         x_positions = self.calc_positions()
109 
110         pos_description = ('Head of Rarefaction', 'Foot of Rarefaction',
111                            'Contact Discontinuity', 'Shock')
112         positions = dict(zip(pos_description, x_positions))
113 
114         # create arrays
115         x, p, rho, u = self.create_arrays(x_positions)
116 
117         val_names = ('x', 'p', 'rho', 'u')
118         val_dict = dict(zip(val_names, (x, p, rho, u)))
119 
120         return positions, regions, val_dict
121 
122     def sound_speed(self, p, rho):
123         """
124         Calculate speed of sound according to
125 
126             .. math::
127                 c = \sqrt{\gamma \frac{p}{\rho} (1-\theta)}
128         where :math:`p` is pressure, :math:`\rho` is density, :math:`\
    gamma` is heat capacity ratio
129         and :math:`\theta` is dust fraction, according to Tricco, Price
    and Laibe, 2017
130 
131         :rtype : float
132         :return: returns the speed of sound
133         """
134         return np.sqrt(self.gamma * (1-self.dustFrac) * p / rho)
135 
136     def shock_tube_function(self, p4, p1, p5, rho1, rho5):
137         """
138         Shock tube equation
139         """
140         z = (p4 / p5 - 1.)
141         c1 = self.sound_speed(p1, rho1)
142         c5 = self.sound_speed(p5, rho5)
```

```
143
144         gm1 = self.gamma - 1.
145         gp1 = self.gamma + 1.
146         g2 = 2. * self.gamma
147
148         fact = gm1 / g2 * (c5 / c1) * z / np.sqrt(1. + gp1 / g2 * z)
149         fact = (1. - fact) ** (g2 / gm1)
150
151         return p1 * fact - p4
152
153     def calculate_regions(self):
154         """
155         Compute regions
156         :rtype : tuple
157         :return: returns p, rho and u for regions 1,3,4,5 as well as the
    shock speed
158         """
159         # if pl > pr...
160         rho1 = self.rhol
161         p1 = self.pl
162         u1 = self.ul
163         rho5 = self.rhor
164         p5 = self.pr
165         u5 = self.ur
166
167         # unless...
168         if self.pl < self.pr:
169             rho1 = self.rhor
170             p1 = self.pr
171             u1 = self.ur
172             rho5 = self.rhol
173             p5 = self.pl
174             u5 = self.ul
175
176         # solve for post-shock pressure
177         # just in case the shock_tube_function gets a complex number
178         num_of_guesses = 100
179         for pguess in np.linspace(self.pr, self.pl, num_of_guesses):
180             res = scipy.optimize.fsolve(self.shock_tube_function, pguess,
    args=(p1, p5, rho1, rho5), full_output=True)
181             p4, infodict, ier, mesg = res
```

```
182             if ier == 1:
183                 break
184         if not ier == 1:
185             raise Exception("Analytical Sod solution unsuccessful!")
186 
187         if type(p4) is np.ndarray:
188             p4 = p4[0]
189 
190         # compute post-shock density and velocity
191         z = (p4 / p5 - 1.)
192         c5 = self.sound_speed(p5, rho5)
193 
194         gm1 = self.gamma - 1.
195         gp1 = self.gamma + 1.
196         gmfac1 = 0.5 * gm1 / self.gamma
197         gmfac2 = 0.5 * gp1 / self.gamma
198 
199         fact = np.sqrt(1. + gmfac2 * z)
200 
201         u4 = c5 * z / (self.gamma * fact)
202         rho4 = rho5 * (1. + gmfac2 * z) / (1. + gmfac1 * z)
203 
204         # shock speed
205         w = c5 * fact
206 
207         # compute values at foot of rarefaction
208         p3 = p4
209         u3 = u4
210         rho3 = rho1 * (p3 / p1) ** (1. / self.gamma)
211         return (p1, rho1, u1), (p3, rho3, u3), (p4, rho4, u4), (p5, rho5,
    u5), w
212 
213     def region_states(self):
214         """
215         :return: dictionary (region no.: p, rho, u), except for
    rarefaction region
216         where the value is a string, obviously
217         """
218         if self.pl > self.pr:
219             return {'Region 1': self.region1,
220                     'Region 2': 'RAREFACTION',
```

```
221                     'Region 3': self.region3,
222                     'Region 4': self.region4,
223                     'Region 5': self.region5}
224         else:
225             return {'Region 1': self.region5,
226                     'Region 2': self.region4,
227                     'Region 3': self.region3,
228                     'Region 4': 'RAREFACTION',
229                     'Region 5': self.region1}
230 
231     def calc_positions(self):
232         """
233         :return: tuple of positions in the following order ->
234                 Head of Rarefaction: xhd,  Foot of Rarefaction: xft,
235                 Contact Discontinuity: xcd, Shock: xsh
236         """
237         p1, rho1 = self.region1[:2]  # don't need velocity
238         p3, rho3, u3 = self.region3[:]
239         c1 = self.sound_speed(p1, rho1)
240         c3 = self.sound_speed(p3, rho3)
241         if self.pl > self.pr:
242             xsh = self.xi + self.w * self.t
243             xcd = self.xi + u3 * self.t
244             xft = self.xi + (u3 - c3) * self.t
245             xhd = self.xi - c1 * self.t
246         else:
247             # pr > pl
248             xsh = self.xi - self.w * self.t
249             xcd = self.xi - u3 * self.t
250             xft = self.xi - (u3 - c3) * self.t
251             xhd = self.xi + c1 * self.t
252 
253         return xhd, xft, xcd, xsh
254 
255     def create_arrays(self, positions):
256         """
257         :return: tuple of x, p, rho and u values across the domain of
    interest
258         """
259         xhd, xft, xcd, xsh = positions
260         p1, rho1, u1 = self.region1
```

```
261         p3, rho3, u3 = self.region3
262         p4, rho4, u4 = self.region4
263         p5, rho5, u5 = self.region5
264         gm1 = self.gamma - 1.
265         gp1 = self.gamma + 1.
266 
267         x_arr = np.linspace(self.xl, self.xr, self.npts)
268         rho = np.zeros(self.npts, dtype=float)
269         p = np.zeros(self.npts, dtype=float)
270         u = np.zeros(self.npts, dtype=float)
271         c1 = self.sound_speed(p1, rho1)
272 
273         if self.pl > self.pr:
274             for i, x in enumerate(x_arr):
275                 if x < xhd:
276                     rho[i] = rho1
277                     p[i] = p1
278                     u[i] = u1
279                 elif x < xft:
280                     u[i] = 2. / gp1 * (c1 + (x - self.xi) / self.t)
281                     fact = 1. - 0.5 * gm1 * u[i] / c1
282                     rho[i] = rho1 * fact ** (2. / gm1)
283                     p[i] = p1 * fact ** (2. * self.gamma / gm1)
284                 elif x < xcd:
285                     rho[i] = rho3
286                     p[i] = p3
287                     u[i] = u3
288                 elif x < xsh:
289                     rho[i] = rho4
290                     p[i] = p4
291                     u[i] = u4
292                 else:
293                     rho[i] = rho5
294                     p[i] = p5
295                     u[i] = u5
296         else:
297             for i, x in enumerate(x_arr):
298                 if x < xsh:
299                     rho[i] = rho5
300                     p[i] = p5
301                     u[i] = -u1
```

```
302                 elif x < xcd:
303                     rho[i] = rho4
304                     p[i] = p4
305                     u[i] = -u4
306                 elif x < xft:
307                     rho[i] = rho3
308                     p[i] = p3
309                     u[i] = -u3
310                 elif x < xhd:
311                     u[i] = -2. / gp1 * (c1 + (self.xi - x) / self.t)
312                     fact = 1. + 0.5 * gm1 * u[i] / c1
313                     rho[i] = rho1 * fact ** (2. / gm1)
314                     p[i] = p1 * fact ** (2. * self.gamma / gm1)
315                 else:
316                     rho[i] = rho1
317                     p[i] = p1
318                     u[i] = -u1
319 
320         return x_arr, p, rho, u
```

Appendix C

AUTODYN Job Submission

C. AUTODYN JOB SUBMISSION

Initiation of a solution on the ARC machines is not performed directly by users, but by a scheduling engine that dynamically allocates the requested resources. Jobs are submitted to the scheduling engine via bash scripts. The dynamic allocation of resources by the scheduler poses a problem for AUTODYN, which requires that a host configuration file (parallel.cfg) be present at run time. Without foreknowledge of the hosts that will be assigned to the solution, AUTODYN cannot run in parallel. The solution is to write additional instructions within the bash script which retrieve the host names, relative processor speeds, and assigned memory per host, and create the file automatically. The bash script applied as a solution is presented below for utility in future work. While specifically applicable to HPC systems running CentOS Linux, the principle is the same for any distribution. For the sake of security, the specific ANSYS license server port is made anonymous. Development of the script was performed by the author, with significant assistance in the bash implementation and required details of ARC3 by John Hodrien of the Advanced Research Computing office.

```

#!/bin/bash
#$ -cwd -V
# job name
#$ -N job_name
# number of compute nodes and number of CPU cores per node
# whole nodes are requested to avoid conflict with ssh
#$-l h_rt=48:00:00
#$-l nodes=1,ppn=16


SLOTMEM=1000

module add ansys/18.1

export ANSYSLMD_LICENSE_FILE=<license server location>
export MPI_HOME="$ANSYS_HOME/v181/commonfiles/MPI/IBM/9.1.4.2/linx64/bin/"
export PATH="$PATH:$ANSYS_HOME/v181/autodyn/bin/"

# create head lines of parallel.cfg
echo "#@EPDEF=$ANSYS_HOME/v181/autodyn/bin/linx64" > parallel.cfg
echo "#@PPDEF arc3" >> parallel.cfg
echo "#@PPCFG arc3" >> parallel.cfg
```

```
24
25 # get MachinesCores from PE_HOSTFILE in format of host1:N:host2:N
26 MachinesCores=$(awk '{print $1 ":" $2}' $PE_HOSTFILE|paste -s -d ':')
27
28 # print hostname and relative speed in first line, then memory size,
       number of CPU cores used and number of tasks (usually equal to CPU
       cores used) in seconds line for each allotted compute node
29
30 OIFS=$IFS;
31 IFS=":";
32 MachinesCoresArray=($MachinesCores);
33 for ((i=0; i<${#MachinesCoresArray[@]}; ++i)); do
34   if [[ $((i % 2)) -eq 0 ]]; then
35     cpu=${MachinesCoresArray[i+1]}
36     let mem=cpu*SLOTMEM
37     echo "${MachinesCoresArray[i]} sp=1000" >> parallel.cfg
38     echo "#@ mem=${mem} cpu=${cpu} task=${cpu}" >> parallel.cfg
39   fi
40 done
41 FS=$OIFS;
42
43 # Start AUTODYN solver by specifying input file. It reads parallel.cfg
       automatically to run in parallel.
44 autodyn181 -I admodel_0.ad
```

References

[1] Vitali F. Nesterenko. "Shock (Blast) Mitigation by "Soft" Condensed Matter". In: *MRS Proceedings* (2011). DOI: 10.1557/proc-759-mm4.3.

[2] Sheila M. Bird and Clive B. Fairweather. "Military fatality rates (by cause) in Afghanistan and Iraq: A measure of hostilities". In: *International Journal of Epidemiology* (2007). ISSN: 03005771. DOI: 10.1093/ije/dym103.

[3] NATO. "AEP-55Ed.2 : Procedures For Evaluating The Protection Level Of Logistic And Light Armoured Vehicles. Volume 2 : Mine Threat". In: *Allied Engineering Publication* (2011).

[4] NATO. "AEP-55Ed.3 : Procedures for Evaluating The Protection Level of Armoured Vehicles. Volume 3: IED Threat". In: *Allied Engineering Publication* (2011).

[5] HFM-090 Task Group 25. *Test Methodology for Protection of Vehicle Occupants against Anti-Vehicular Landmine Effects*. Tech. rep. NATO, 2007.

[6] John. D Anderson Jr. *Modern Compressible Flow with Historical Perspective*. Third. New York: McGraw-Hill, 2003, pp. 121,264–266,297–298. ISBN: 0-07-112161-7.

[7] Fan Zhang, ed. *Shock Waves Science and Technology Library, Vol. 6*. 2012. DOI: 10.1007/978-3-642-22967-1.

[8] Darina Fišerová. "Numerical Analyses of Buried Mine Explosions with Emphasis on Effect of Soil Properties on Loading". PhD thesis. Cranfield University, 2006.

[9] Andrew Tyas. "Experimental Measurement of Pressure Loading from Near-Field Blast Events: Techniques, Findings and Future Challenges". In: *Proceedings* (2018). DOI: 10.3390/icem18-05364.

[10] Paul J. Hazell. *ARMOUR: Materials, theory, and design*. 2015. ISBN: 9781482238303. DOI: 10.1201/b18683.

[11] Sudeep Kumar Lahiri and Lee Ho. *Simulation of Rapid Structural Failure Due to Blast Loads from Conventional Weapons*. Tech. rep. Providence, RI: Dassault Systems Simula Corp, 2010. URL: https://pdfs.semanticscholar.org/9455/07c666c7c34bb12665207c6a0ef3ea3da125.pdf.

[12] P D Smith and J G Hetherington. *Blast and Ballistic Loading of Structures*. 1st. Oxford: Butterworth-Heinemann Ltd, 1994, pp. 42–47. ISBN: 0 7506 2024 2.

[13] Denis Bergeron, Robert Walker and Clay Coffey. *Detonation of 100g anti-personnel mine surrogate charges in sand: A test case for computer code validation. Technical Report DRES-SR-668*. Tech. rep. Defence Research Establishment Suffield, Canada, 1998.

[14] A. Ramasamy et al. *Blast mines: physics, injury mechanisms and vehicle protection*. 2009. DOI: 10.1136/jramc-155-04-06.

[15] Major Stanley M. Johnson. *NCG Technical Report No. 21 - Explosive Excavation Technology*. Tech. rep. Livermore, California: U.S Army Engineer Nuclear Cratering Group, 1971.

[16] F. J. Mostert. *Challenges in blast protection research*. 2018. DOI: 10.1016/j.dt.2018.05.007.

[17] A. Erdik et al. "Numerical simulation of armored vehicles subjected to undercarriage landmine blasts". In: *Shock Waves* (2016). ISSN: 09381287. DOI: 10.1007/s00193-015-0576-1.

[18] M Held and The International Ballistics Committee. "Momentum Distribution of Anti-Tank Mines". In: *20th International Symposium on Ballistics*. 2002.

[19] V. Denefeld, N. Heider and A. Holzwarth. "Measurement of the spatial specific impulse distribution due to buried high explosive charge detonation". In: *Defence Technology* (2017). ISSN: 22149147. DOI: 10.1016/j.dt.2017.03.002.

[20] S. Hlady. "Effect of Soil Parameters on Land Mine Blast". In: *18th Military Aspects of Blast and Shock (MABS)* (2004).

[21] Leo Laine and Andreas Sandvik. "DERIVATION OF MECHANICAL PROPERTIES FOR SAND". In: *the 4th Asia-Pacific Conference on Shock and Impact Loads on Structures* (2001).

[22] Amal Bouamoul et al. *An empirical model for mine-blast loading*. Tech. rep. Defence Research and Development Canada - Valcartier.

[23] L. C. Taylor et al. "Loading mechanisms on a target from detonation of a buried charge". In: *Proceedings - 24th International Symposium on Ballistics, BALLISTICS 2008*. 2008. ISBN: 9781932078930.

[24] Jinhua Huang, Helen Durden and Mostafiz Chowdhury. "Bio-inspired armor protective material systems for ballistic shock mitigation". In: *Materials and Design* (2011). ISSN: 02641275. DOI: 10.1016/j.matdes.2011.03.061.

[25] Alessandro Liberati et al. "The PRISMA statement for reporting systematic reviews and meta-analyses of studies that evaluate health care interventions: explanation and elaboration". In: *Journal of clinical epidemiology*. 2009. DOI: 10.1016/j.jclinepi.2009.06.006.

[26] Nu Ri Yun et al. "Experiments on blast protective systems using aluminum foam panels". In: *KSCE Journal of Civil Engineering* (2014). ISSN: 19763808. DOI: 10.1007/s12205-014-0092-3.

[27] Changsu Shim et al. "Mitigation of Blast Effects on Protective Structures by Aluminum Foam Panels". In: *Metals* (2012). DOI: 10.3390/met2020170.

[28] M. Liverts et al. "Mitigation of exploding-wire-generated blast-waves by aqueous foam". In: *Physics of Fluids* (2015). ISSN: 10897666. DOI: 10.1063/1.4924600.

[29] G. J. Ball and R. A. East. "Shock and blast attenuation by aqueous foam barriers: Influences of barrier geometry". In: *Shock Waves* (1999). ISSN: 09381287. DOI: 10.1007/s001930050137.

[30] B. W. Skews, M. D. Atkins and M. W. Seitz. "The impact of a shock wave on porous compressible foams". In: *Journal of Fluid Mechanics* (1993). ISSN: 14697645. DOI: 10.1017/S0022112093001788.

[31] Chengqing Wu and Hamid Sheikh. "A finite element modelling to investigate the mitigation of blast effects on reinforced concrete panel using foam cladding". In: *International Journal of Impact Engineering* (2013). ISSN: 0734743X. DOI: 10.1016/j.ijimpeng.2012.11.006.

[32] G. W. Ma and Z. Q. Ye. "Analysis of foam claddings for blast alleviation". In: *International Journal of Impact Engineering* (2007). ISSN: 0734743X. DOI: 10.1016/j.ijimpeng.2005.10.005.

[33] D. Karagiozova, G. S. Langdon and G. N. Nurick. "Blast attenuation in Cymat foam core sacrificial claddings". In: *International Journal of Mechanical Sciences* (2010). ISSN: 00207403. DOI: 10.1016/j.ijmecsci.2010.02.002.

[34] E. Del Prete et al. "Blast wave mitigation by dry aqueous foams". In: *Shock Waves* (2013). ISSN: 09381287. DOI: 10.1007/s00193-012-0400-0.

[35] M. A. Dawson. "Composite plates with a layer of fluid-filled, reticulated foam for blast protection of infrastructure". In: *International Journal of Impact Engineering* (2009). ISSN: 0734743X. DOI: 10.1016/j.ijimpeng.2009.03.008.

[36] G. W. Ma and Z. Q. Ye. "Energy absorption of double-layer foam cladding for blast alleviation". In: *International Journal of Impact Engineering* (2007). ISSN: 0734743X. DOI: 10.1016/j.ijimpeng.2005.07.012.

[37] Ryan Alberdi, John Przywara and Kapil Khandelwal. "Performance evaluation of sandwich panel systems for blast mitigation". In: *Engineering Structures* (2013). ISSN: 01410296. DOI: 10.1016/j.engstruct.2013.08.021.

[38] M. Schenk, S. D. Guest and G. J. McShane. "Novel stacked folded cores for blast-resistant sandwich beams". In: *International Journal of Solids and Structures* (2014). ISSN: 00207683. DOI: 10.1016/j.ijsolstr.2014.07.027.

[39] Linhui Zhang et al. "Dynamic response of corrugated sandwich steel plates with graded cores". In: *International Journal of Impact Engineering* (2014). ISSN: 0734743X. DOI: 10.1016/j.ijimpeng.2013.11.011.

[40] H. Arora, P. A. Hooper and J. P. Dear. "Dynamic response of full-scale sandwich composite structures subject to air-blast loading". In: *Composites Part A: Applied Science and Manufacturing* (2011). ISSN: 1359835X. DOI: 10.1016/j.compositesa.2011.07.018.

[41] E. A. Flores-Johnson et al. “A numerical study of bioinspired nacre-like composite plates under blast loading”. In: *Composite Structures* (2015). ISSN: 02638223. DOI: 10.1016/j.compstruct.2015.02.083.

[42] Srinivasan Arjun Tekalur, Arun Shukla and Kunigal Shivakumar. “Blast resistance of polyurea based layered composite materials”. In: *Composite Structures* (2008). ISSN: 02638223. DOI: 10.1016/j.compstruct.2007.08.008.

[43] George A. Christou et al. “Shock attenuation of PMMA sandwich panels filled with soda-lime glass beads: A fluid-structure interaction continuum model simulation”. In: *International Journal of Impact Engineering* (2012). ISSN: 0734743X. DOI: 10.1016/j.ijimpeng.2012.03.003.

[44] Yehia A. Bahei-El-Din, George J. Dvorak and Olivia J. Fredricksen. “A blast-tolerant sandwich plate design with a polyurea interlayer”. In: *International Journal of Solids and Structures* (2006). ISSN: 00207683. DOI: 10.1016/j.ijsolstr.2006.03.021.

[45] Yehia A. Bahei-El-Din and George J. Dvorak. “Behavior of sandwich plates reinforced with polyurethane/polyurea interlayers under blast loads”. In: *Journal of Sandwich Structures and Materials* (2007). ISSN: 10996362. DOI: 10.1177/1099636207066313.

[46] David Hui and Piyush K. Dutta. “A new concept of shock mitigation by impedance-graded materials”. In: *Composites Part B: Engineering*. 2011. DOI: 10.1016/j.compositesb.2011.05.016.

[47] Mohammad A. Al-Shudeifat et al. “Numerical and experimental investigation of a highly effective single-sided vibro-impact non-linear energy sink for shock mitigation”. In: *International Journal of Non-Linear Mechanics* (2013). ISSN: 00207462. DOI: 10.1016/j.ijnonlinmec.2013.02.004.

[48] Tanaz Rahimzadeh, Ellen M. Arruda and M. D. Thouless. “Design of armor for protection against blast and impact”. In: *Journal of the Mechanics and Physics of Solids* (2015). ISSN: 00225096. DOI: 10.1016/j.jmps.2015.09.009.

[49] O. E. Petel et al. “Blast wave attenuation through a composite of varying layer distribution”. In: *Shock Waves* (2011). ISSN: 09381287. DOI: 10.1007/s00193-010-0295-6.

[50] Mica Grujicic et al. “Shock-wave attenuation and energy-dissipation potential of granular materials”. In: *Journal of Materials Engineering and Performance* (2012). ISSN: 10599495. DOI: 10.1007/s11665-011-9954-8.

[51] A. G. Hanssen et al. “Validation of constitutive models applicable to aluminium foams”. In: *International Journal of Mechanical Sciences* (2002). ISSN: 00207403. DOI: 10.1016/S0020-7403(01)00091-1.

[52] Q. M. Li and H. Meng. “Attenuation or enhancement - A one-dimensional analysis on shock transmission in the solid phase of a cellular material”. In: *International Journal of Impact Engineering* (2002). ISSN: 0734743X. DOI: 10.1016/S0734-743X(02)00016-7.

[53] A. G. Hanssen, L. Enstock and M. Langseth. “Close-range blast loading of aluminium foam panels”. In: *International Journal of Impact Engineering* (2002). ISSN: 0734743X. DOI: 10.1016/S0734-743X(01)00155-5.

[54] Rodolfo Monti. “Normal shock wave reflection on deformable solid walls”. In: *Meccanica* (1970). ISSN: 00256455. DOI: 10.1007/BF02145653.

[55] G. J. McShane et al. “The response of clamped sandwich plates with lattice cores subjected to shock loading”. In: *European Journal of Mechanics, A/Solids* (2006). ISSN: 09977538. DOI: 10.1016/j.euromechsol.2005.08.001.

[56] M. Grujicic et al. “Concept-level analysis and design of polyurea for enhanced blast-mitigation performance”. In: *Journal of Materials Engineering and Performance* (2012). ISSN: 10599495. DOI: 10.1007/s11665-011-0117-8.

[57] BAE Systems Cam Johnston. Private Communication. 2017.

[58] G. Jourdan et al. “Attenuation of a shock wave passing through a cloud of water droplets”. In: *Shock Waves* (2010). ISSN: 09381287. DOI: 10.1007/s00193-010-0251-5.

[59] K. C. Adiga et al. “Implications of droplet breakup and formation of ultra fine mist in blast mitigation”. In: *Fire Safety Journal* (2009). ISSN: 03797112. DOI: 10.1016/j.firesaf.2008.08.003.

[60] Douglas A. Schwer and K. Kailasanath. “Numerical simulations of the mitigation of unconfined explosions using water-mist”. In: *Proceedings of the Combustion Institute* (2007). ISSN: 15407489. DOI: 10.1016/j.proci.2006.07.145.

[61] Huon Bornstein, Paul Phillips and Christopher Anderson. "Evaluation of the blast mitigating effects of fluid containers". In: *International Journal of Impact Engineering* (2015). ISSN: 0734743X. DOI: 10.1016/j.ijimpeng.2014.08.014.

[62] Li Chen et al. "Performance based investigation on the construction of anti-blast water wall". In: *International Journal of Impact Engineering* (2015). ISSN: 0734743X. DOI: 10.1016/j.ijimpeng.2015.03.003.

[63] Y. S. Shin et al. "Modeling mitigation effects of watershield on shock waves". In: *Shock and Vibration* (1998). ISSN: 10709622. DOI: 10.1155/1998/782032.

[64] M. Cheng, K. C. Hung and O. Y. Chong. "Numerical study of water mitigation effects on blast wave". In: *Shock Waves* (2005). ISSN: 09381287. DOI: 10.1007/s00193-005-0267-4.

[65] Baoxing Xu, Yu Qiao and Xi Chen. "Mitigating impact/blast energy via a novel nanofluidic energy capture mechanism". In: *Journal of the Mechanics and Physics of Solids* (2014). ISSN: 00225096. DOI: 10.1016/j.jmps.2013.09.022.

[66] Yun Chen, Wei Huang and Shlomi Constantini. "Blast shock wave mitigation using the hydraulic energy redirection and release technology". In: *PLoS ONE* (2012). ISSN: 19326203. DOI: 10.1371/journal.pone.0039353.

[67] L. Javier Malvar and James E. Tancreto. *Analytical and Test Results for Water Mitigation of Explosion Effects*. Tech. rep. Port Hueneme, California: Naval Facilities Engineering Services Center, 1998, pp. 2–5. URL: https://apps.dtic.mil/dtic/tr/fulltext/u2/a497400.pdf.

[68] A. Britan et al. "Experimental and Numerical Study of Shock Wave Interaction with Perforated Plates". In: *Journal of Fluids Engineering* (2004). ISSN: 00982202. DOI: 10.1115/1.1758264.

[69] G. S. Langdon et al. "Perforated plates as passive mitigation systems". In: *Defence Science Journal*. 2008. DOI: 10.14429/dsj.58.1644.

[70] G. S. Langdon et al. "Performance of mild steel perforated plates as a blast wave mitigation technique: Experimental and numerical investigation". In: *International Journal of Impact Engineering* (2010). ISSN: 0734743X. DOI: 10.1016/j.ijimpeng.2010.06.001.

[71] Sumil Seeraj and Beric W. Skews. "Dual-element directional shock wave attenuators". In: *Experimental Thermal and Fluid Science* (2009). ISSN: 08941777. DOI: 10.1016/j.expthermflusci.2008.11.002.

[72] Shahar Berger, Gabi Ben-Dor and Oren Sadot. "Numerical Investigation of Shock Wave Attenuation by Geometrical Means: Double Barrier Configuration". In: *Journal of Fluids Engineering* (2015). ISSN: 0098-2202. DOI: 10.1115/1.4028875.

[73] S. Berger, G. Ben-Dor and O. Sadot. "Experimental and numerical investigations of shock-wave attenuation by geometrical means: A single barrier configuration". In: *European Journal of Mechanics, B/Fluids* (2015). ISSN: 09977546. DOI: 10.1016/j.euromechflu.2014.11.006.

[74] Shachar Berger, Oren Sadot and Gabi Ben-Dor. "Experimental investigation on the shock-wave load attenuation by geometrical means". In: *Shock Waves* (2010). ISSN: 09381287. DOI: 10.1007/s00193-009-0237-3.

[75] Hadassah Naiman and Doyle D. Knight. "The effect of porosity on shock interaction with a rigid, porous barrier". In: *Shock Waves* (2007). ISSN: 09381287. DOI: 10.1007/s00193-007-0077-y.

[76] Y. Andreopoulos, S. Xanthos and K. Subramaniam. "Moving shocks through metallic grids: Their interaction and potential for blast wave mitigation". In: *Shock Waves* (2007). ISSN: 09381287. DOI: 10.1007/s00193-007-0082-1.

[77] A. Hadjadj and O. Sadot. "Shock and blast waves mitigation". In: *Shock Waves* (2013). ISSN: 0938-1287. DOI: 10.1007/s00193-012-0429-0.

[78] F. Ohtomo, K. Ohtani and K. Takayama. "Attenuation of shock waves propagating over arrayed baffle plates". In: *Shock Waves* (2005). ISSN: 09381287. DOI: 10.1007/s00193-005-0282-5.

[79] A. Chaudhuri et al. "Numerical study of shock-wave mitigation through matrices of solid obstacles". In: *Shock Waves* (2013). ISSN: 09381287. DOI: 10.1007/s00193-012-0362-2.

[80] *ANSYS^{TM} Academic Research Mechanical, Release 18.1, Help System, FLUENT Theory Guide*. ANSYS Inc. 2013.

[81] Jr John D. Anderson. *Computational Fluid Dynamics: The Basics with Applications*. 1995.

[82] Randall J. LeVeque. *Finite Volume Methods for Hyperbolic Problems*. 2002, p. 314. DOI: 10.1017/cbo9780511791253.

[83] E. Toro. *Riemann Solvers and Numerical Methods for Fluid Dynamics*. 2nd ed. Heidelberg: Springer-Verlag, 1999, pp. 47–50. ISBN: 3-540-65966-8.

[84] Gary A. Sod. *A survey of several finite difference methods for systems of nonlinear hyperbolic conservation laws*. 1978. DOI: 10.1016/0021-9991(78)90023-2.

[85] Bram van Leer. "Towards the ultimate conservative difference scheme. V. A second-order sequel to Godunov's method". In: *Journal of Computational Physics* (1979). ISSN: 10902716. DOI: 10.1016/0021-9991(79)90145-1.

[86] J. R. Edwards. *Reflections on the early development of the "AUSM family" of Riemann solvers*. 2019. DOI: 10.1007/s00193-018-0863-8.

[87] Meng Sing Liou and Christopher J. Steffen. "A new flux splitting scheme". In: *Journal of Computational Physics* (1993). ISSN: 00219991. DOI: 10.1006/jcph.1993.1122.

[88] Meng Sing Liou. "A sequel to AUSM: AUSM+". In: *Journal of Computational Physics* (1996). ISSN: 00219991. DOI: 10.1006/jcph.1996.0256.

[89] Meng Sing Liou. "A sequel to AUSM, Part II: AUSM+-up for all speeds". In: *Journal of Computational Physics* (2006). ISSN: 10902716. DOI: 10.1016/j.jcp.2005.09.020.

[90] ANSYS Inc. *ANSYS FLUENT 12.0 Theory Guide*. URL: https://www.afs.enea.it/project/neptunius/docs/fluent/html/th/main{_}pre.htm.

[91] D. G. Holmes and S. D. Connell. "Solution of the 2D Navier-Stokes equations on unstructured adaptive grids". In: *9th Computational Fluid Dynamics Conference, 1989*. 1989.

[92] Russ D. Rausch, John T. Batina and Henry T.Y. Yang. "Spatial adaptation of unstructured meshes for unsteady aerodynamic flow computations". In: *AIAA Journal* (1992). ISSN: 00011452. DOI: 10.2514/3.11057.

[93] ANSYS Inc. *ANSYS FLUENT Theory Guide (Release 17.0)*. Canonsburg, PA, 2016.

[94] K. F Riley, M. P Hobson and S. J Bence. *Mathematical Methods for Physics and Engineering*. 3rd. Cambridge: Cambridge University Press, 2006, pp. 1026–1028. ISBN: 978-0-521-67971-8.

[95] Stephen B. Pope. *Turbulent Flows*. 4th. Cambridge: Cambridge University Press, 2006, pp. 3,182–189,268,359–385. ISBN: 0 521 59886 9.

[96] B. E. Launder and D. B. Spalding. "The numerical computation of turbulent flows". In: *Computer Methods in Applied Mechanics and Engineering* (1974). ISSN: 00457825. DOI: 10.1016/0045-7825(74)90029-2.

[97] N. C. Markatos. *The mathematical modelling of turbulent flows*. 1986. DOI: 10.1016/0307-904X(86)90045-4.

[98] David C. Wilcox. "Reassessment of the scale-determining equation for advanced turbulence models". In: *AIAA Journal* (1988). ISSN: 00011452. DOI: 10.2514/3.10041.

[99] F. Menter. "Zonal Two Equation k-w Turbulence Models For Aerodynamic Flows". In: *23rd Fluid Dynamics, Plasmadynamics, and Lasers Conference*. 1993. DOI: 10.2514/6.1993-2906.

[100] Hermann Schlichting. *Boundary Layer Theory*. 6th. McGraw-Hill Inc, 1968, pp. 602–605.

[101] *ANSYS Fluent Theory Guide (version 19 R2, Online)*. Canonsburg, PA, 2019. URL: https://ansyshelp.ansys.com.

[102] ANSYS Inc. *ANSYS Theory Guide (12.0) : 4.12.4 Enhanced Wall Treatment*. URL: https://www.afs.enea.it/project/neptunius/docs/fluent/html/th/node101.htm.

[103] M. Wolfshtein. "The velocity and temperature distribution in one-dimensional flow with turbulence augmentation and pressure gradient". In: *International Journal of Heat and Mass Transfer* (1969). ISSN: 00179310. DOI: 10.1016/0017-9310(69)90012-X.

[104] B. A. Kader. "Temperature and concentration profiles in fully turbulent boundary layers". In: *International Journal of Heat and Mass Transfer* (1981). ISSN: 00179310. DOI: 10.1016/0017-9310(81)90220-9.

[105] M. L Wilkins et al. *A Method for Computer Simulation of Problems in Solid Mechanics and Gas Dynamics in Three Dimensions and Time*. Tech. rep. Livermore, California: Lawrence Livermore Laboratory, 1974. URL: https://www.osti.gov/servlets/purl/4276327.

[106] Jay P. Boris and David L. Book. "Flux-corrected transport. I. SHASTA, a fluid transport algorithm that works". In: *Journal of Computational Physics* (1973). ISSN: 10902716. DOI: 10.1016/0021-9991(73)90147-2.

[107] W. F. Noh and Paul Woodward. "SLIC (Simple Line Interface Calculation)". In: 1976. DOI: 10.1007/3-540-08004-x_336.

[108] SHARCNET. *ANSYS 17.0 Online Help*. 2016. URL: https://www.sharcnet.ca/Software/Ansys/17.0/en-us/help/exd{_}ag/exp{_}dyn{_}theory{_}expl{_}flui{_}struct{_}582.html (visited on 11/06/2019).

[109] R. Castedo et al. "Estimation of Jones-Wilkins-Lee parameters of emulsion explosives using cylinder tests and their numerical validation". In: *International Journal of Rock Mechanics and Mining Sciences* (2018). ISSN: 13651609. DOI: 10.1016/j.ijrmms.2018.10.027.

[110] B. M. Dobratz and P. C. Crawford. *LLNL Explosives Handbook - Properties of Chemical Explosives and Explosive Simulants*. 1985. DOI: 10.1177/001452468509600304.

[111] Jerko Škifić. *Sod Shocktube*. 2019. URL: https://github.com/ibackus/sod-shocktube.

[112] Bruce Fryxell. *Exact Riemann Solver*. URL: http://cococubed.asu.edu/codes/riemann/exact_riemann.f.

[113] A. Britan et al. "Shock wave attenuation by grids and orifice plates". In: *Shock Waves*. 2006. DOI: 10.1007/s00193-006-0019-0.

[114] M. Grujicic and B. A. Cheeseman. "Concurrent computational and dimensional analyses of design of vehicle floor-plates for landmine-blast survivability". In: *Journal of Materials Engineering and Performance* (2014). ISSN: 15441024. DOI: 10.1007/s11665-013-0637-5.

[115] M. Grujicic et al. *A Combined Multi-Material Euler/Lagrange Computational Analysis of Blast Loading Resulting from Detonation of Buried Landmines*. 2008. DOI: 10.1163/157361108784050086.

[116] Jovan Trajkovski, Jasenko Perenda and Robert Kunc. "Blast response of Light Armoured Vehicles (LAVs) with flat and V-hull floor". In: *Thin-Walled Structures* (2018). ISSN: 02638231. DOI: 10.1016/j.tws.2018.06.040.

[117] A. Bouamoul and G. Toussaint. "Experimental tests and numerical calculations using ale and sph approaches on mine blast effects on structure". In: *Proceedings - 24th International Symposium on Ballistics, BALLISTICS 2008*. 2008. ISBN: 9781932078930.

[118] M. Grujicic, B. Pandurangan and B. A. Cheeseman. "The effect of degree of saturation of sand on detonation phenomena associated with shallow-buried and ground-laid mines". In: *Shock and Vibration* (2006). ISSN: 10709622. DOI: 10.1155/2006/652405.

[119] ANSYS Inc. *AUTODYN Theory Manual*. 2005. URL: www.century-dynamics.com.

[120] Warren C. Lothrop and G. Richard Handrick. "The Relationship between Performance and Constitution of Pure Organic Explosive Compounds". In: *Chemical Reviews* (1949). ISSN: 15206890. DOI: 10.1021/cr60139a001.

[121] NPL. *Kaye & Laby Tables of Physical and Chemical Constants*. 2015.

[122] Sebastian Balos, Vencislav Grabulov and Leposava Sidjanin. *Future armoured troop carrying vehicles*. 2010. DOI: 10.14429/dsj.60.550.

[123] O. Igra et al. "Experimental and numerical study of the interaction between a planar shock wave and a square cavity". In: *Journal of Fluid Mechanics* (1996). ISSN: 00221120. DOI: 10.1017/S0022112096002145.

[124] O. Igra et al. "Experimental and theoretical study of shock wave propagation through double-bend ducts". In: *Journal of Fluid Mechanics* (2001). ISSN: 00221120. DOI: 10.1017/S0022112001004098.